University of Huddersfield Repository

Alwodai, Ahmed

Motor Fault Diagnosis Using Higher Order Statistical Analysis of Motor Power Supply Parameters

Original Citation

Alwodai, Ahmed (2015) Motor Fault Diagnosis Using Higher Order Statistical Analysis of Motor Power Supply Parameters. Doctoral thesis, University of Huddersfield.

MOTOR FAULT DIAGNOSIS USING HIGHER ORDER STATISTICAL ANALYSIS OF MOTOR POWER SUPPLY PARAMETERS

Ahmed Mahmoud M Alwodai

A thesis submitted to the University of Huddersfield in partial fulfilment of the requirements for the degree of Doctor of Philosophy.

University of Huddersfield

2015

DECLARATION

No portion of the work referred to in this thesis has been submitted in support of an application for another degree or qualification of this or any other university or other institute of learning.

DEDICATION

I dedicate this work to my dear father for the lifelong and boundless love that I received from him as well as his unwavering support, also dedicated to my wife and my children for their unfaltering encouragement throughout my study. Without their support, reaching this point would not have been possible.

ABSTRACT

Motor current signature analysis (MCSA) has been an effective method to monitor electrical machines for many years, predominantly because of its low instrumentation cost, remote implementation and comprehensive information contents. However, it has shortages of low accuracy and efficiency in resolving weak signals from incipient faults, such as detecting early stages of induction motor fault. In this thesis MCSA has been improved to accurately detect electrical and mechanical faults in the induction motor namely broken rotor bars, stator faults and motor bearing faults. Motor current signals corresponding to a healthy (baseline) and faulty condition on induction motor at different loads (zero, 25%, 50% and 75% of full load) were rearranged and the baseline current data were examined using conventional methods in frequency domain and referenced for comparison with new modulation signal bispectrum.

Based on the fundamental modulation effect of the weak fault signatures, a new method based on modulation signal bispectrum (MSB) analysis is introduced to characterise the modulation and hence for accurate quantification of the signatures. This method is named as (MSB-SE).

For broken rotor bar(BRB), the results show that MSB-SE suggested in this research outperforms conventional bispectrum CB significantly for all cases due its high performance of nonlinear modulation detection and random noise suppression, which demonstrates that MSB-SE is an outstanding technique whereas (CB) is inefficient for motor current signal analysis [1] . Moreover the new estimators produce more accurate results at zero, 25%, 50%, 75% of full load and under broken rotor bar, compared with power spectrum analysis. Especially it can easily separate the half BRB at a load as low as 25% from baseline where PS would not produce a correct separation.

In case of stator faults, a MSB-SE is investigated to detect different severities of stator faults for both open and short circuit. It shows that MSB-SE has the capability to accurately estimate modulation degrees and suppress the random and non-modulation components. Test results show that MSB-SE has a better performance in differentiating spectrum amplitudes due to

stator faults and hence produces better diagnosis performance, compared with that of power spectrum (PS).

For motor bearing faults, tests were performed with three bearing conditions: baseline, outer race fault and inner race fault. Because the signals associated with faults produce small modulations to supply component and high noise levels, MSB-SE is used to detect and diagnose different motor bearing defects. The results show that bearing faults can induce detectable amplitude increases at its characteristic frequencies. MSB-SE peaks show a clear difference at these frequencies whereas the conventional power spectrum provides change evidences only at some of the frequencies. This shows that MSB has a better and reliable performance in detecting small changes from the faulty bearing for fault detection and diagnosis. In addition, the study also shows that current signals from motors with variable frequency drive controller have too much noise and it is unlikely to discriminate the small bearing fault component.

This research also applies a mathematical model for the simulation of current signals under healthy and broken bars condition in order to further understand the characteristics of fault signature to ensure the methodologies used and accuracy achieved in the detection and diagnosis results. The results show that the frequency spectrum of current signal outputs from the model take the expected form with peaks at the sideband frequency and associated harmonics.

LIST OF CONTENTS

LISTOF FIGURES

LIST OF TABLES

LIST OF ABBREVIATIONS

AC	Alternating current
BRB	Broken rotor bar
CB	Conventional Bispectrum
CM	Condition Monitoring
CSI	Current Source Inverter
DFT	Discrete Fourier Transform
EMF	Electro-Motive Force
FT	Fourier Transform
FFT	Fast Fourier Transform
HOS	Higher Order Spectra
LRC	Locked Rotor Current
LRT	Locked Rotor Torque
MCSA	Motor Current Signature Analysis
MMF	Magneto Motive Force
MSB	Modulation Signal Bispectrum
MSB-SE	Modulation Signal Bispectrum based on Sideband Estimation
PS	Power spectrum
PWM	Pulse Width Modulation
VFD	Variable Frequency Drive
VSI	Voltage Source Inverters
VVI	Variable Voltage Inverter

LIST OF NOTATION

D_b	Bearing ball diameter
D_p	Pitch diameter
f_r	Rotor frequency
f_s	Fundamental supply frequency
g	Air gap length
J	Moment of inertia of the rotor
l	Effective length of the motor
L_{ms}	Magnetising inductance for a stator winding
N_b	Number of rotor bars
N_B	Number of rolling elements
N_s	Effective number of turns of any stator phase
n_r	Rotor speed
n_s	Synchronous speed
p	Number of pole pairs
P_m	Mechanical power available on the rotor shaft at full load
r	Air gap average radius
R_r	Resistance of rotor phase winding
s	Motor Slip
T_{em}	Electromagnetic torque produced by the motor
T_L	Maximum external load applied on the machine shaft
β	Contact angle
μ_o	Permeability of air=4π×10-7 H/m
ω_{rm}	Rotor speed in mechanical radian per second
θr	Angular position of the rotor with respect to the stator reference

ACKNOWLEDGEMENT

Few goals are ever achieved without the help of teachers, mentors, colleagues, family, and friends. For the assistance, support, and guidance I have received while completing my postgraduate studies I am indebted to ***Prof. Andrew Ball***, I would like to express my sincere gratitude to him. Also I would like to express my genuine appreciation to my second supervisor ***Dr. Fengshou Gu*** for his continuous direction, support and patience throughout my PhD research above and beyond the merely technical during my research, it was really my privilege to have such a supervisory team. I would like to acknowledge invaluable input and countless enlightening meetings, discussions and conversations with them.

My special thanks goes to my colleagues and friends, I was fortunate to have nice peers in my research group.

My thanks also go to the technical team for their kind help and cooperation.

CHAPTER 1
INTRODUCTION

This chapter provides a brief description of conventional condition monitoring techniques followed by a review of condition monitoring of an induction motor and explains why motor current signature analysis technique has been chosen for research into the detection and diagnosis of induction motor faults. Finally, the aim and research objectives are given in detail and the chapter ends by describing the thesis content and layout.

1.1 Overview

Induction motor based drive systems are the most widely used prime movers in industry. Any faults on the system will influence production activities and consume additional energy, and even often bring unexpected breakdowns. Therefore, condition monitoring (CM) of these systems has been increasingly investigated for developing further advanced techniques that permit on-line early detection and diagnosis of incipient faults, which will avoid any negative consequences of unexpected shutdowns. As a result correct diagnosis and early detection of incipient faults result in fast unscheduled maintenance and short down time for the process under consideration. They also avoid harmful, sometimes devastative, consequences and help reducing financial loss. A perfect diagnostic technique should take the minimum measurements necessary from a machine and by analysis extract a diagnosis, so that its condition can be inferred giving a clear indication of incipient failure modes in a minimum time.

Electrical machines and drive systems are subjected to many different types of faults. These faults include [2]:

- Stator faults which are defined by stator winding open or short-circuited
- Rotor electrical faults which include rotor winding open or short-circuited for wound rotor machines and broken bars or cracked end-ring for squirrel-cage machines.
- Mechanical faults such as bearing damage, eccentricity, bent shaft and misalignment
- Failure of one or more power electronic components of the drive system

A number of general survey papers on condition monitoring techniques for diagnosing and detecting of electrical machines faults were presented such as[3-9], providing comprehensive overview on different diagnostic procedures adopted for the most common and frequent faults occurring in induction motors.

The researches of induction motor performance during unusual condition due to presence of faults and the possibility to diagnose these irregular conditions have been a challenging issue for many electrical machine researchers [10]. Many studies have presented a number of methods of condition monitoring such as vibration, acoustic emission and thermal monitoring. However, all of these methods need some special tools and expensive instruments whereas current monitoring does not require additional devices because of the basic electrical quantities with electromechanical plants such as current and voltage which are readily measured by tapping into the existing voltage and current transformers that are always installed as a part of the protection system [10]. Consequently, current monitoring is non-invasive and might even be implemented in the motor control system remotely from the motors being monitored [11].

As shown in general review papers [3, 12, 13] there has been numerous research in recent years exploring the condition monitoring of motor drives through a wide range of approaches. Amongst all the different condition monitoring techniques, motor current signature analysis (MCSA) is still the main area of research and shows the most potential for the induction motor fault diagnosis. This is certainly due to the apparent advantages that it can be implemented using low cost instruments. MCSA can be performed with easy installation without interruption to the machine operation, through remote implementation, comprehensive diagnostic information, and with pre-existing theoretical supports, gives MCSA an advantage over the other popular methods such as vibrio-acoustic monitoring and temperature. Although there are a number of applications [14-19] of MCSA reported in the literature, currently there have not been any established approaches available for industry to benefit from using MCSA.

When a fault is present, the frequency spectrum of the line current becomes different from healthy motor. Such a fault modulates the air gap and produces rotating frequency harmonics in the self and mutual inductance of the machine. The specific harmonics component of the line current location depends on the mode of the faults [16]. Consequently this technique offers important application and economic benefits. MCSA based on method is used in this research to diagnose the common fault of induction motor namely broken bar faults, short circuit, open circuit and motor bearing faults. The proposed method in the research allows continues real time tracking of several modes of faults in the induction motor operating under full speed and different loads. The effects of various faults of the induction motor are investigated.

One of the main causes of the limited application may stem from the inherent drawback of noise inclusion in the Discrete Fourier Transform (DFT) based spectrum analysis, which is used by most of current studies to extract the weak diagnostic features in the measured signal. To overcome this inefficiency, new signal processing methods have been continuously investigated in the majority of recent studies.

Initially, alternatives to the Fourier Transform (FT) based framework must be found to avoid the problem due to DFT calculation [20]. Discrete wavelet transform (DWT) has been applied to the current during a load reduction or during the speed increasing transient process [17, 21, 22], it has been shown that DWT is effective in detecting local gear faults of varying severity. Additionally, DWT has also been used to analyse the current signals from start-up transients and new fault indicators have also been investigated [20], resulting in an impressive performance in discriminating between different motor faults. The empirical mode decomposition (EMD) has also been evaluated and found to be capable of detecting faults from motors during transient stages [23]. These achievements have shown that more accurate diagnosis can be obtained by using these newer methods rather than the traditional spectral analysis. However, more efforts need to be carried out to interpret the detection features to provide more general rules for applying this method. As an example in [24], DWT results may be preceded by DFT to gain more explainable results.

Currently, DFT based investigations are still the main focus for research because of the inherent connections of FT to the physical properties of rotating machines [25]. Of particular interest is the work which performs diagnosis to include the phase information from DFT. In [25], the phase rather than the modulus from FT of current signals is explored for broken rotor bar detection and diagnosis. The results show that the phase of FT allows the detection of one broken rotor bar when the motor operates under a low load (25% of rated load), but the method robustness decreases for a half-broken rotor bar.

Higher order spectra (HOS) are useful signal processing tools that have shown significant benefits over traditional spectral analyses because HOS have non-linear identification, phase information retention and Gaussian noise elimination properties [26, 27]. The application of HOS techniques in condition monitoring has been reported in [27, 28] based on motor vibrations and it is clear that multi-dimensional HOS measures can contain more accurate information than traditional two-dimensional spectral measures for diagnostic purposes. Recently, Saidi, et al [29, 30] tried to use the diagonal slices of a conventional bispectrum (CB) applied to induction machine stator current, which combines the information from both the magnitude and phase. It claimed that the results are more accurate in the detection of rotor broken bars even when the induction machine is rotating at a low level of shaft load (i.e. no-load condition). However, there are some doubts regarding the claim because the bispectrum slices show unconvincing peaks at the sidebands even for a load of 25% [31]. In addition, the bispectrum estimation is obtained by only averaging the signal over a few times, which is certainly not enough to obtain reliable estimations from a statistical point of view because inevitable noise contamination [1].

An earlier study by [1] made using the motor current for reciprocating compressor fault diagnosis has revealed that random noise can be suppressed with a new data processing method, named as modulation signal bispectrum (MSB). MSB is an extension of the conventional bispectrum (CB) for characterising modulation signals predominantly, which has resulted in better diagnosis than that of the power spectrum(PS), showing that MSB is an effective method to detect and quantify sidebands in current signals through its high performance in noise suppression. In particular, the application of MSB is fully supported by the motor current signal model developed in research.

Following the success of using MSB for reciprocating compressors, the method has been further improved so that the influences of the carrier-magnitude at the supply fundamental is removed in MSB slices of interest, achieving faster MSB analysis for accurate sideband estimation. This has led to attractive results in detecting and diagnosing different faults from multi stage gearboxes and electrical motors [32-35].

However, these new investigations rely mainly on the magnitude information of MSB for fault diagnosis. The use of MSB coherence, which may contain more effective information for detection and diagnosis in more complicated motor current signals from multiple rotating processes, has not yet been explored fully in the diagnosis process. Moreover, this research will explain the key differences between CB and MSB for effective selection of signal processing methods to implement MCSA. Additionally, this research develops a new MSB based sideband amplitude estimator (MSB-SE) that obtains the amplitude at sidebands with high accuracy, which allows the amplitudes at lower and higher sidebands caused by motor faults to be estimated individually and the BRB from motor current signals with inevitable noise and interferences. This new method will also apply on different faults of induction motors, namely: broken bar, stator faults and motor bearing faults.

1.2 Research Motivations

To conclude, in the following a state of the art from the reviewed articles are summarised in Table. The summary includes articles reviewed in chapters 1 to 4 and particularly those studied the MCSA.

Reference	Faults	Statistical Technique
[1]	reciprocating compressor fault	Modulation Signal Bispectrum (MSB)
[29]	broken rotor bar	Power Spectrum and Bispectrum
[30]	broken bar and motor bearing fault	Bispectrum
[36]	broken rotor bar and turn short circuit	Bispectrum
[37]	broken rotor bar and stator faults	Bispectrum
[38]	motor bearing faults	Fast Fourier Transform (FFT)
[39]	broken rotor bar	FFT

Table 1.1-The State of Art from Reviewed Articles

Hence, based on the progress on MCSA made in recent years, it has released that the following gaps

- Fault signatures is weak and has not had effective methods to extract them reliably
- Little works on the diagnosis study of variable speed drives.

Therefore, this research is set up to fill these gaps in order to achieve accurate and reliable diagnosis results.

1.3 Research Aim and Objectives

The aim of this research is to develop a condition monitoring technique capable of detecting and diagnosing electrical and mechanical faults commonly present in three-phase induction motors. Three tasks were performed to facilitate this aim:

Firstly: the Motor current signature analysis technique used to detect and diagnose induction motor faults is reviewed.

Secondly: a new MSB based on sideband estimator (MSB-SE) is introduced for obtaining the amplitude at sidebands with high accuracy.

Finally the results of MSB are compared with conventional PS.

1.4 Research Objectives

The aim of the research is to investigate the detection and the diagnosis of induction motor faults by monitoring the motor current.

The possibility of MCSA will prove to be an improvement that detects and extricates electrical and mechanical faults in the induction motor, and to introduce novel procedures for motor fault detection based on MCSA. The objectives of the research are summarised as follows:

Objective one: To design and build a comprehensive motor test facility in which to seed faults and gain experimental data on subsequent system behaviour. This work will allow CM of the system using such diverse monitoring techniques as dynamic motor current signals. It will also allow specific faults to be seeded into the induction motor: broken rotor bar, open and short circuit on stator windings and motor bearing faults.

Objective two: To enable the controlled seed of a variety of chosen fault conditions in a test facility and to seed each fault in a range of severities. These faults include the electrical and mechanical faults of induction motors, namely broken rotor bar, stator winding fault and motor bearings fault. The effect of these faults on the performance of a three-phase squirrel cage induction motor was investigated.

Objective three: To collect and analyse motor current data from a healthy motor to establish a baseline profile for use in fault detection and then compare the spectral content of the motor current signal from a healthy motor with a known fault. To categorize the differences between MCSA with and without a fault, to establish a link between specific faults and the corresponding differences in the motor current signature.

Objective four: To evaluate motor temperature influence on motor current signal.

Objective five: To examine the VFD operation mode on the motor current signals.

Objective six: To examine the motor current signature using different traditional signal processing techniques power and bispectral analysis for baseline and different motor faults and different load conditions.

Objective seven: To analyse and examine the motor current signature by the application of new methods of signal processing based on modulation signal bispectrum

Objective eight: To evaluate the possibilities of model-based fault detection and diagnosis using a mathematical model. A model for three-phase squirrel cage induction motor will be developed for normal and abnormal operating conditions. The abnormal conditions will include broken rotor faults. Each operating condition will be simulated at different load conditions.

Objective nine: To provide directions and guide lines for future research in this field.

1.5 Research Scope

This research is mainly performed for investigating the detection and diagnosis of induction motors faults using motor current signature analysis by applying higher order statistics and power spectrum. MSB based sideband amplitude estimator (MSB-SE) that obtains the amplitude at sidebands is examined on a 4Kw induction motor fed by an open loop (V/Hz), non-compensated variable frequency drive.

1.6 Research Methodology

Figure 1.1 illustrates the methodology of this research that amended from [36] to investigate the common fault diagnosis in 4kw AC induction motor.

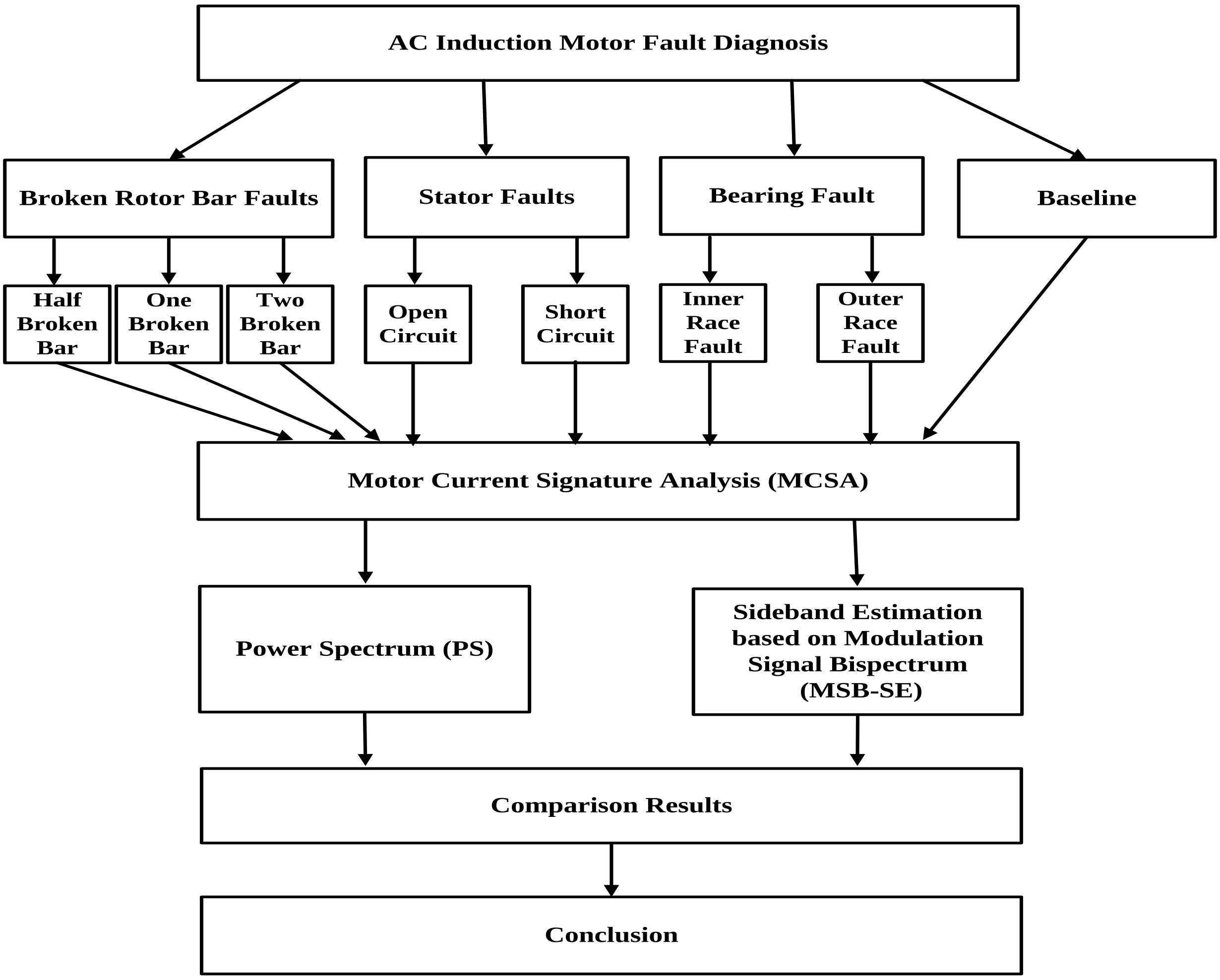

Figure 1.1-Schematic Diagram of Research Methodology used (amended form [36])

Seven experiments are performed in this thesis to diagnose the common faults of induction motors using motor current signature analysis technique. Faults include half broken bar, one broken bar, two broken bar, open circuit and short circuit in stator windings, and motor bearing faults.

The current power spectrum (PS) and modulation signal bispectrum based on sideband amplitude estimator (MSB-SE) are applied and compared at zero, 25%, 50% and 75% of full load. The results are discussed and then final conclusions are made.

1.7 Structure of Research

In this section a brief outline is given of the contents and relative emphasis of the following chapters.

Chapter 2this chapter introduces some details of principle of induction motor and AC Drives.

Chapter 3 presents a basic description of the physical phenomena related to induction motors, and induction motor fault, as well as it presents some reviews on induction motor fault detection. Moreover, it explains the physical phenomena of faulty induction motors with broken rotor bars; inter-turn short-circuits and open-circuit in the stator windings and motor bearing faults by Motor Current Signature Analysis (MCSA).

Chapter 4 this chapter presents some of conventional diagnostic techniques using frequency domain current signal. The FFT is used to get amplitude spectrum and power spectrum (PS).Moreover, the chapter describes some HOS techniques such as Conventional Bispectrum (CB) and modulation signal bispectrum (MSB).Finally, the chapter presents a new method that is based upon modulation signal bispectrum estimation (MSB-SE). This method is applied on motor current signal to diagnose motor faults.

Chapter 5 presents the induction motor test rig on which the experimental investigations were carried out. A description of the faults to be seeded and how they were introduced into the test rig.

Chapter 6 reports the analysis of the motor data collected using conventional methods and the MSB technique developed by the author to determine whether it is suitable for use with induction motor condition monitoring. The results presented include baseline tests under conventional method such as amplitude spectrum and power spectrum. Additionally, the chapter presents effects of motor temperature on the current signal. After that it provides some comparisons between conventional bispectrum and modulation signal bispectrum under broken bar case in 3D graphs. Finally it presents comparison results of motor current using PS and MSB-SE under different motor health. The result shows that MSB-SE has a better capability than PS for induction motor fault diagnosis.

Chapter 7 describes, in detail, a mathematical model for a 4kW, 400V, 4 poles, and 50Hz squirrel cage induction motor. To implement and identify the full potential of the phase current approach, three operating conditions (healthy, one broken bar and two broken bars) were simulated for different loads. The model parameters estimation was presented and the correlation between the simulated and measured results of broken bar current signature was made.

Chapter 8 outlines the conclusions drawn and the suggestions for future work.

1.8 Summary of Chapter 1

This chapter provides comprehensive overview on induction motor condition monitoring. Different diagnostic processes applied for the most common and frequent faults occurring in induction motors. Therefore an accurate diagnosis and early detection of incipient faults result in short down time, avoid harmful and help reducing financial loss. Many studies have presented a number of methods of condition monitoring such as vibration, acoustic emission, thermal monitoring and motor current signature analysis (MCSA). MCSA is still the main area of research and shows the most potential for the induction motor fault diagnosis due to its easy installation and low cost.

MCSA based on method is used in this research to diagnose the common fault of induction motor. Seven experiments are performed in this thesis to diagnose the common faults of induction motors using motor current signature analysis technique. The faults included half broken bar, one broken bar, two broken bar, open circuit and short circuit in stator windings, and motor bearing faults. Based on the fundamental modulation effect of the weak fault signatures, a new method based on modulation signal bispectrum (MSB) analysis is introduced to characterise the modulation and hence for accurate quantification of the signatures. This method is named as (MSB-SE).

This chapter also presents the structure of the research and provides brief description for each chapter.

CHAPTER 2
INDUCTION MOTOR AND AC DRIVE

The induction motor can only run efficiently at close to the synchronous speed of the rotating field. The best method of speed control must therefore provide for continuous smooth variation of the synchronous speed, which in turn calls for variation of the supply frequency. This is achieved using an inverter to supply the motor. Therefore this chapter will introduce some details of principle of induction motor and AC Drives.

2.1 Induction Motor

Induction motors are complex electro-mechanical devices used worldwide in industrial processes to convert electrical energy into mechanical energy. Such motors are widespread because they are robust, easily installed, controlled, and adaptable for many industrial applications, including pumps, fans, air compressors, machine tools, mixers, and conveyor belts, as well as many other industrial applications [40]. Moreover, induction motors may be supplied directly from a constant frequency sinusoidal power supply or by an AC variable frequency drive. These drives are discussed in the Section 2.2.

2.1.1 Construction of Three-Phase Induction Motors

The stator is composed of three parts: frame, lamination core and windings. The frame mechanically supports the stator and the rotor shaft bearings. The windings are composed of three equally distributed coils along the stator lamination core, which are connected to the three-phase power supply as shown in Figure 2.1. The energy for the rotor is delivered by the synchronous rotation of the stator magnetic field. The name of the “induction motor” is thus derived from this phenomenon. It should be pointed out that there is a space between the stator and the rotor which is called the air gap [41].

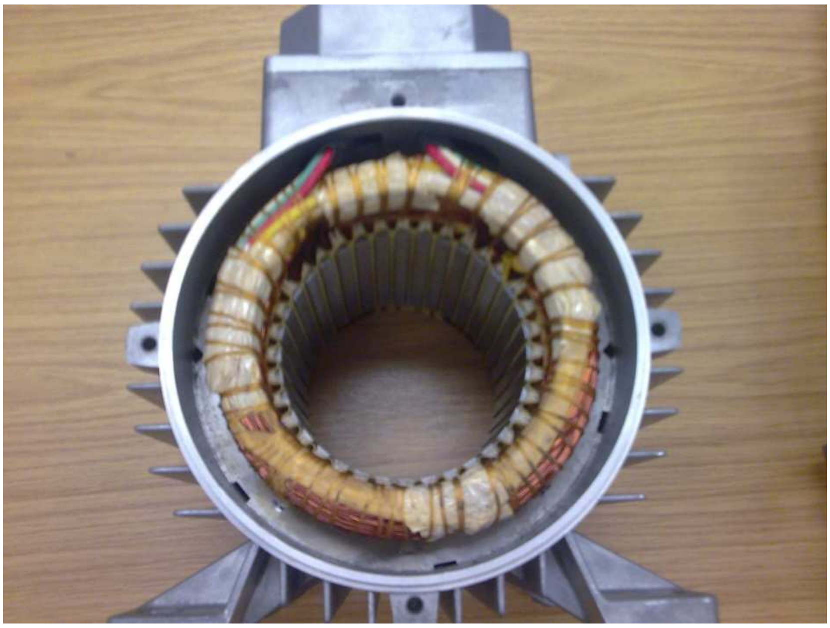

Figure 2.1-Photo of Induction Motor Stator used

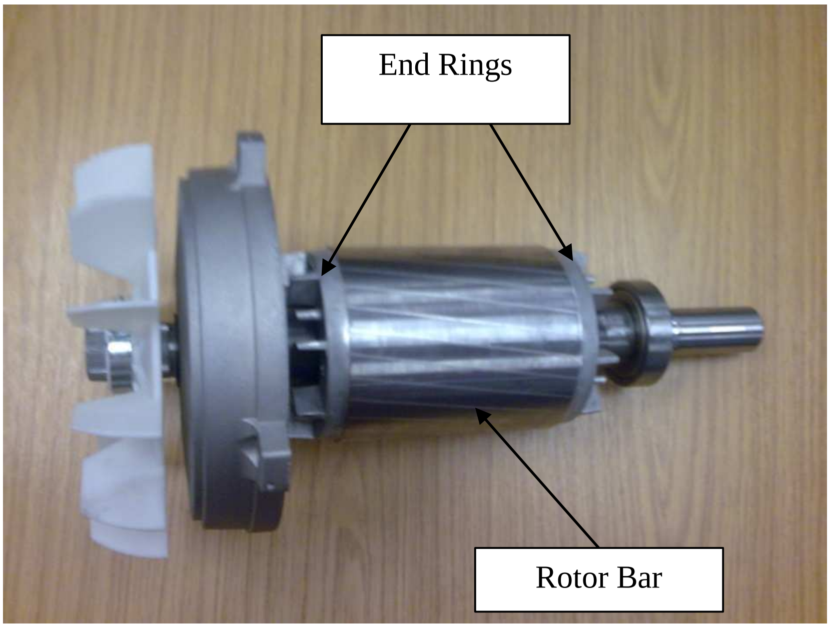

Figure 2.2-Photo of Squirrel cage rotor used

The rotor is composed of a squirrel cage, a shaft, and a lamination stack as shown in Figure 2.2. The main part of the rotor is the squirrel cage, which is composed of bars and two end rings. The conductive rotor bars are short-circuited on both sides by the end rings. For small and medium size motors the rotor bars and slip rings end are made of die-cast aluminium [42-44]. Consequently, the electric current can circulate from one side to other side of the squirrel cage [40]. The bars are enveloped by a laminated iron core, which concentrates the magnetic flux from the stator windings in the rotor. This lamination also mechanically supports the rotor shaft. The bearings on both sides of the rotor shaft allow the rotor to spin freely inside the stator [40].

2.1.2 Operation of the Induction Motor

The stator windings are arranged on the stator poles in a way that results in magnetic flux lines that seem to rotate. The operation of three phase induction motor is based on Faraday's law, as shown in Figure2.3 when AC current passes through stator windings which displaced by an electrical phase difference of 120° a magnetic field will induced [45]. The direction of the magnetic field depends on the phase sequence, so that if phase sequence is ABC the rotation direction of the magnetic field is clockwise direction. However, change in stator windings connection will effect on the magnetic field direction and then rotor rotation direction. At the starting the rotor is stationary and the slip ($s=1$) and rotor and stator frequency are the same. Under the normal operation condition the slip is between 3% and 10% at full in case of squirrel cage induction motors [41, 43, 46].When the motor operates under no-load condition the difference between synchronous speed and rotor speed is usually 0.1% of synchronous speed [46].

The magnetic field is created and rational speed known as synchronous speed which given by this formula:

$$n_s = \frac{60\, f_s}{p} \tag{2.1}$$

where $n_s$is synchronous speed, f_s is power source frequency (50 HZ in the UK), and P is the number of pole pairs per phase.

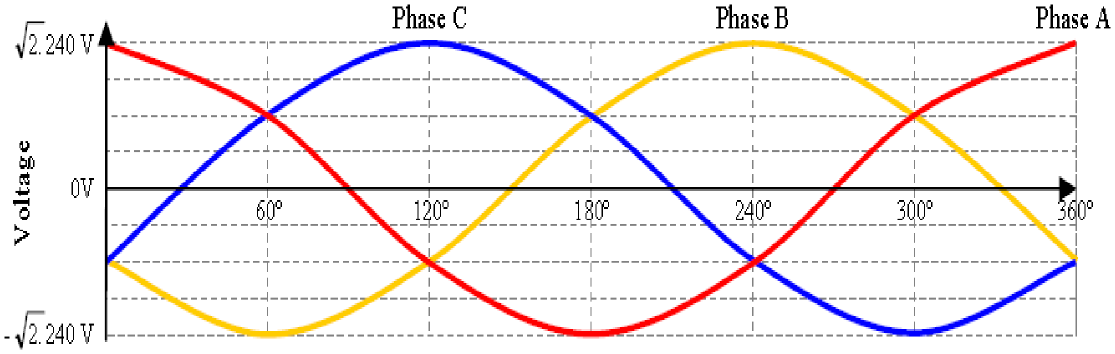

Figure 2.3-Representation of Three-Phase Currents in Induction Motor [45]

At start-up, as the magnetic field is rotating and the rotor is initially stationary, a voltage is induced in the closed-loop (shorted at the end-rings) rotor bars. The induced electromotive force (EMF), E, is governed by Faraday's Law of electromagnetic induction [45]:

$$E = Blv \tag{2.2}$$

where *B* is the magnetic flux density which measured in Webers per square meter [Wb/m^2], which is equivalent to Teslas [T], *l* is the active length of the conductors in the magnetic field (in metres), and *v* is the relative speed of the conductors (in metres per second). As the magnitude of induced voltage varies proportionally with the relative speed between the rotor and the stator fields, a relatively large current up to 6-8 times that experienced during steady-state operation flows in the shorted rotor bars [47].

Thus the current-carrying conductors being within the magnetic field, a force known as Lorentz force (*F*) is experienced on each conductor [43]:

$$F = BlI \tag{2.3}$$

where I is the current flowing in each conductor.

However, if the field stops to rotate then no current would flow in the conductors. Similarly, the rotor cannot operate at synchronous speed because then the relative field would be zero and no current would flow in the conductors. In practice, the relative speed between the rotor and stator field decreases as the rotor approaches synchronous speed. This causes a consequential reduction in induced rotor voltage, rotor bar current and hence torque [43].

As a result, if the mechanical load is applied to the induction motor the rotor speed will decrease and the magnetic field will cut the rotor bars at higher rate speed, the induced voltage and the resulting current will increase as well. The rotor speed never reaches to the synchronous speed, actually if the rotor turns at the same as the synchronous speed the flux will not cut the rotor bars and induced voltage and resulting current will be zero[43]. The difference between synchronous speed n_s and rotor speed n_r is called slip speed .The slip can be expressed in per unit by the flowing formula [43, 46]:

$$s = \frac{n_s - n_r}{n_s} \tag{2.4}$$

The voltage and frequency induced in the rotor conductors depends on slip which described by these equations[43]:

$$\begin{aligned} f_r &= s\, f_s \\ E_r &= s\, E_{oc} \end{aligned} \tag{2.5}$$

Where

f_s and f_r are frequencies of source and rotor respectively.

E_r is the induced voltage in the rotor at slip s.

E_{oc} is the induced open circuit voltage in the rotor.

2.1.3 Torque Production

As it was discussed in Section 2.1.2 if the rotor of induction motor is initially stationary, its conductor will be subjected to a sweeping magnetic field, produced by stator’s current, inducing current in the short-circuit rotor with same frequency. The interaction of air gap flux and rotor Magnetomotive force (MMF) produces torque [40]. At synchronous speed, the rotor cannot have any induced currents and; therefore, torque cannot be produced. At any other speed, there will be a difference between the rotating field speed (synchronous speed n_s) and the shaft speed n_r, which is called slip speed. The slip speed will induce current and torque in the rotor. The rotor will move in the same diction as that of the rotating magnetic field to reduce the induced current [40].

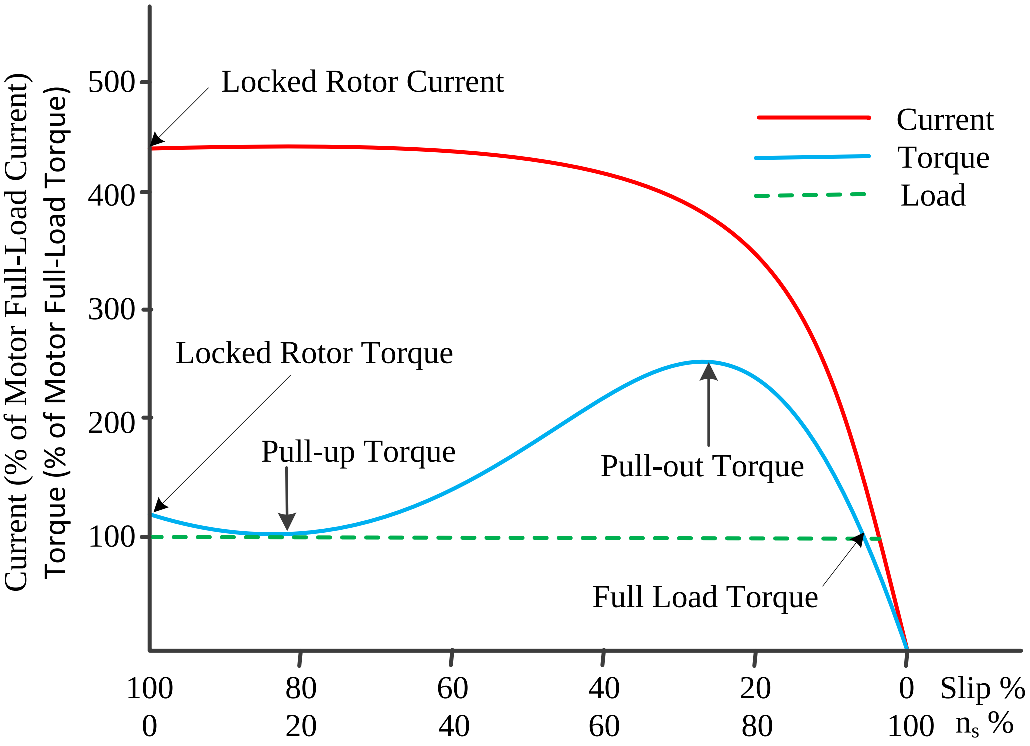

Figure 2.4-Typical Torque-Speed and Current-Speed Curves for Squirrel Cage Motors (amended from [48])

The torque is produced by the interaction between the radial flux wave and the axial currents in the rotor. The torque acts in the same direction of the rotating and causes to drag the rotor along by the field. The rotor as a result will never reach the synchronous speed as there is no rotor current, no EMF and no torque. A typical torque-speed and current-speed curves for squirrel cage motors are shown in Figure 2.4 [48].

When starting the induction motor by connecting into a fully supply voltage, a very high starting current is induced into the rotor known as the locked rotor current (LRC). This current develops a great amount of induced EMF in the rotor, which generates the starting or locked rotor torque (LRT). However, as the rotor accelerates both current and torque typically is likely to alter slightly with the rotor speed; and if the supply voltage remains constant, the torque reaches to its minimum value which is referred to as the Pull-up torque. As the rotor speed increases and gets close to the full speed (about 80% of synchronous speed), the torque grows to the maximum point which is known as the pull-out or breakdown torque; while slight drop notice in the current.[42] As the rotor accelerates further and about to reach the rated motor speed, with no load, both current and torque would rapidly fall to minimal values. Finally, the motor speed stabilises when loaded to the full load torque. During normal operation conditions the motor runs at a lower slip, the number of the stator poles determines the nominal motor speed [40, 49].

2.2 AC Drive

The majority of inverters used in motor drives are voltage source inverters (VSI), in which the output voltage to the motor is controlled to suit the operating conditions of the motor.

To achieve variable speed, an induction motor is supplied by an inverter based on IGBT (Insulated Gate Bipolar Transistor) technology, which is fed by pulse width modulation from a voltage source inverter (PWM-VSI). PWM-VSI induction motors are usually more reliable than those operated directly online [50-53].

However, when a motor is fed by a VFD, the maximum power supplied to the motor is restricted by the output limit of the drive. Figure 2.5 depicts how the induction motors generally are connected with VFDs [53].

An inverter-driven motor system controls the rotational speed of an alternating current (AC) electric motor by controlling the frequency and voltage of the electrical power supplied to the motor. This system is also called variable frequency drive (VFD), adjustable-frequency drive (AFD), and variable-speed drive (VSD) [52]. Variable-frequency drives are widely used in ventilation systems, pumps, elevators, conveyors, machine tools, etc. There are three basic design types of VFDs that are described briefly in next section.

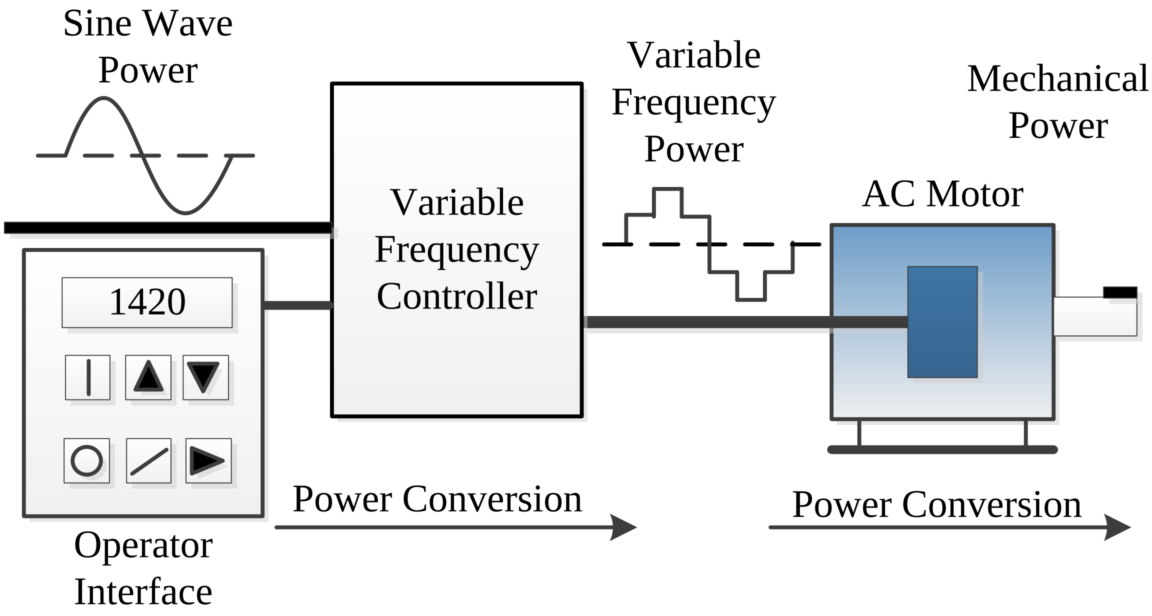

Figure 2.5-Induction Motor Fed by VFD [53]

2.3 General Structure of Variable Frequency Drives

The AC variable frequency drive consists of three main components as shown in Figure 2.6

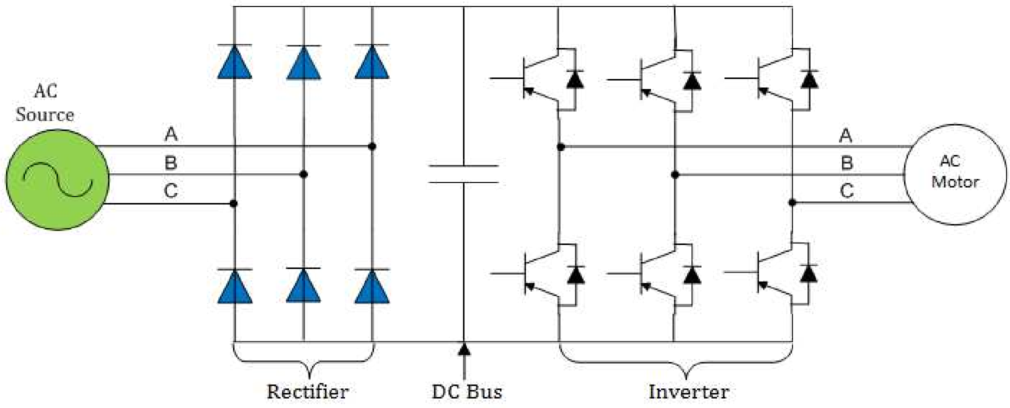

.

Figure 2.6-Structure of Variable Frequency Drive [54]

2.3.1 Rectifier:

The rectifier is connected to the supply network and generates a DC voltage supply which feeds the main DC link elements. The mains rectifier consists of a bridge circuit which converts the supply network from AC to DC. The DC voltage resulting from this always corresponds to the peak value of the connected mains voltage [55].

Where

$$V_{peak} = \sqrt{2}V_{rms} \tag{2.1}$$

Rectifiers can use diodes, silicon controlled rectifiers (SCR), or transistors to rectify power. Diodes are the simplest device and allow power to flow any time when the voltage of the proper polarity is present [55].

2.3.2 DC Bus:

After the power flows through the rectifiers it is stored on a DC bus. The DC bus contains capacitors to accept power from the rectifier, store it, and later deliver that power through the inverter section. The DC bus may also contain inductors, DC links, chokes, or similar items that add inductance, thus smoothing the incoming power supply to the DC bus. The DC voltage feeds the inverter (now commonly with insulated gate bipolar transistors (IGBTs)) which regulate both voltage and frequency to the motor to produce a near sine wave like output [55].

2.3.3 Inverter

The last part of the VFD is an inverter. The inverter contains transistors that distribute power to the motor. There are three basic types of inverters commonly employed in adjustable AC drives[55]:

1. The variable voltage inverter (VVI), or square-wave six-step voltage source inverter (VSI), receives DC power from an adjustable voltage source and adjusts the frequency and voltage.

2. The current source inverter (CSI) receives DC power from an adjustable current source and adjusts the frequency and current.
3. The pulse width modulated (PWM) inverter is the most commonly chosen. It receives DC power from a fixed voltage source and adjusts the frequency and voltage. (PWM types cause the least harmonic noise).

The pulse width modulated inverter is used in this research. Therefore it will be studied in details.

2.4 Pulse Width Modulated Inverter

2.4.1 General Concepts of the PWM

The Insulated Gate Bipolar Transistor (IGBT) is a common option in modern VFDs. The IGBT can switch on and off several thousand times per second and accurately control the power sent to the motor. The IGBT uses a method named pulse width modulation (PWM) to provide a current sine wave of the desired frequency to the motor[56, 57].

Pulse Width Modulation is extremely popular because it is affordable, highly reliable and reflects the least amount of harmonics back into its power source. The AC line supply voltage is the input signal for the converter (with diodes and large DC capacitors) which creates and maintains a stable DC bus voltage as shown in Figure 2.7 [49].

PWM means that each transition of the alternating voltage output is actually a series of short pulses of varying widths. By varying the width of the pulses in each half cycle, the average power produced has a sine-like output. The number of transitions from positive to negative per second determines the actual frequency to the motor. The main advantages of PWM are: excellent input power factor; no motor cogging; high efficiency 92-96% and lower initial cost [2] .However there are also several disadvantages: motor heating and insulation breakdown in some applications; non-regenerative operation; line-side power harmonics.

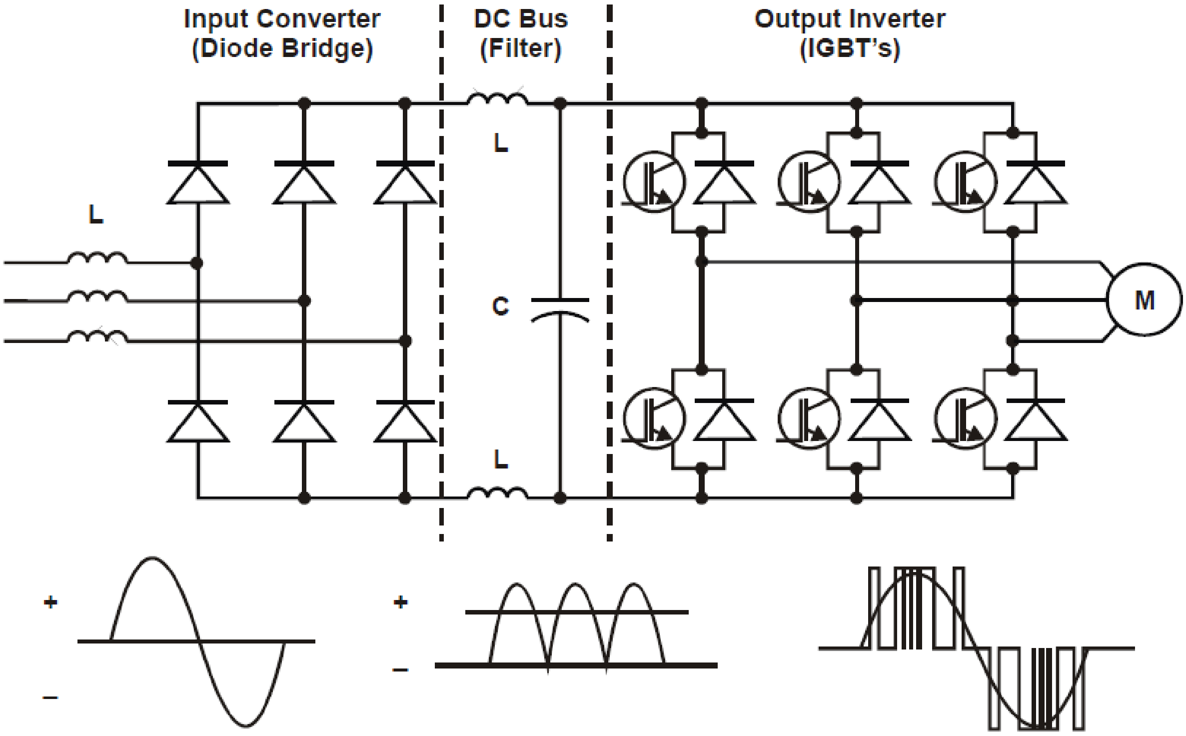

Figure 2.7-Block Diagram of a PWM Drive as an Example of VSDs [49]

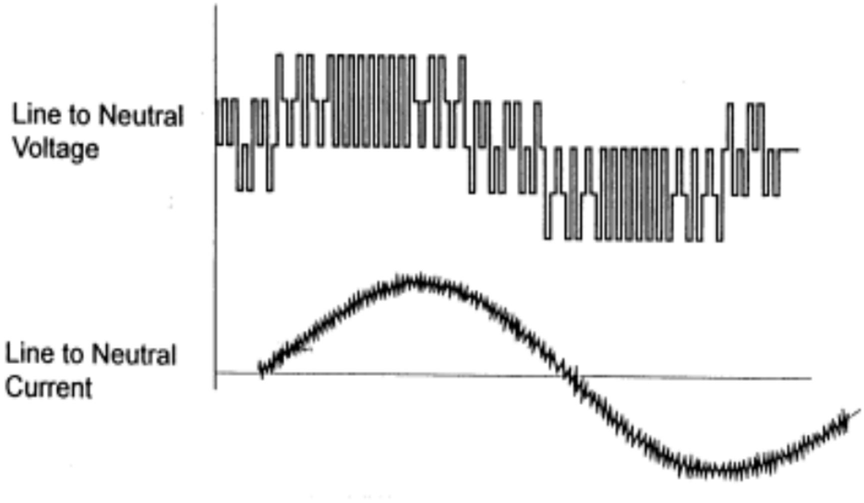

Figure 2.8-PWM Inverter Output Switching Waveform[58]

Observing Figure 2.8, it can be seen that the output of the PWM drive does not provide an exact model of the AC input sine waveform. Instead, it provides voltage pulses that are at constant amplitude [58].

2.4.2 PWM Drive Characteristics

Comparing with other types of inverters the PWM has the following characteristics[59]

- VFD drive DC link voltage is constant.
- Lower resultant voltage is created by more and narrower pulses.
- Pulse amplitude is constant over entire frequency range and equal to the DC link voltage.
- Higher resultant voltage is created by fewer and wider pulses.
- Even though the voltage consists of a series of square-wave pulses, the motor current will very closely approximate a sine wave. The inductance of the motor acts to filter the pulses into a smooth AC current waveform.
- Alternating current (AC) output is created by reversing the polarity of the voltage pulses.
- Voltage and frequency ratio remains constant from 0 - 50 Hz. For a 415 motor this ratio is 8.3 volts/Hz. To calculate this ratio, the motor voltage divided by 50 Hz. At low frequencies the voltage will be low, as the frequency increases the voltage will increase. (Note: this ratio may be varied somewhat to alter the motor performance characteristics such as providing a low-end boost to improve starting torque).

2.5 Operation Modes of VFD

A VFD system can operate under three basic modes: open-loop, slip compensation and closed-loop. Under both the slip compensation and closed-loop modes, the motor can run at the required speed accurately whereas under the open-loop, the speed of the motor reduces as load increases due to the slip effect of induction machines [54]. The slip is usually about 0.03 at rated frequency, resulting in an effect which can be neglected in many applications [54, 60, 61].

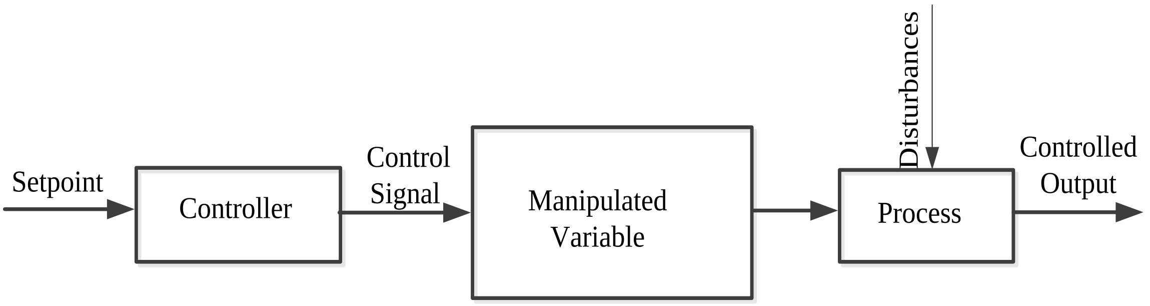

Figure 2.9-Input-Output Configuration of Open-loop Control System [62]

Figure 2.9 represents a block diagram of an open-loop control system, where the controller receives the desired value and adjusts the manipulated variable which affects the process and changes the controlled variable. There is no contact between the controller and the controlled variable[62]

The system structure in Figure 2.10 illustrates the block diagram of a closed loop control system. It shows that a feedback line was added to the open loop path which allows the controller to measure the controlled variable and compares it with the reference or setpoint. An error signal is produced as a result from the comparator which sends the error signal to the controller algorithm to produce the control signal[62].

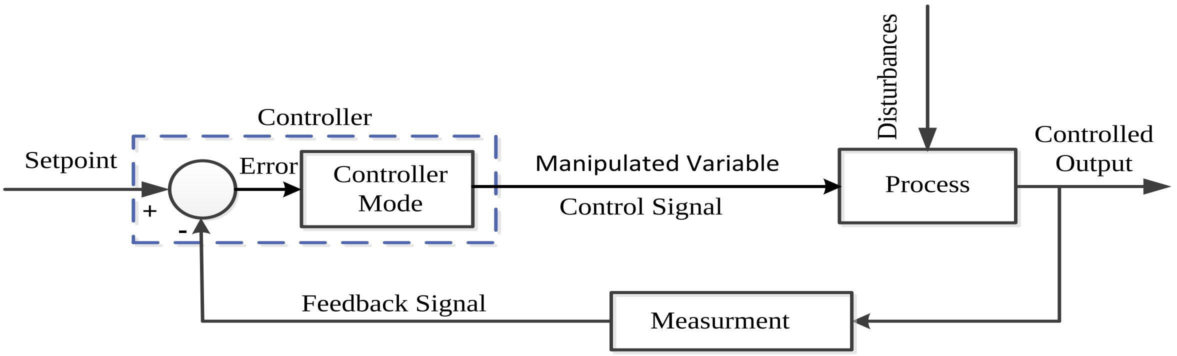

Figure 2.10-Block Diagram of Closed-Loop Control System [62]

For variable-frequency operation, however, the slip for constant torque varies inversely proportional to the frequency. When the frequency decreases, the slip becomes significantly large and it can no longer be ignored. At very low frequencies this effect becomes so important that if not sufficiently compensated for the motor will not be capable to provide the load torque and will stop[63].

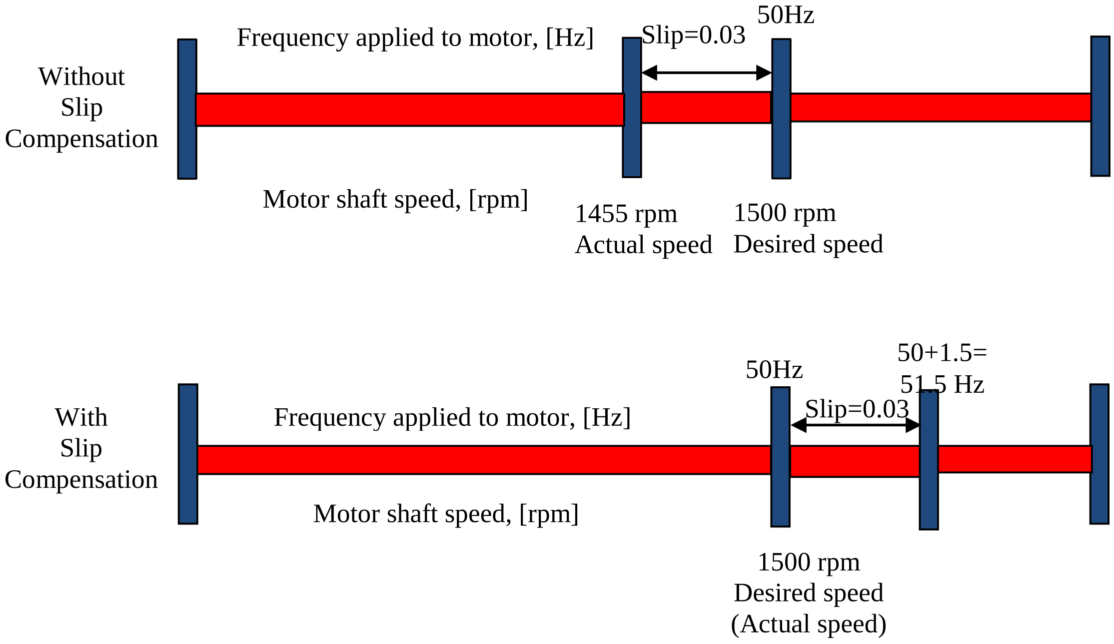

Figure 2.11-Slip Frequency Compensation[54]

Figure 2.11 shows a function that needs the motor to provide full torque at 1500 RPM. The top part of the figure illustrates what occurs without slip compensation. The applied frequency is 50Hz, but the motor actual shaft RPM, due to slip, has a value of 1455 [54].

The bottom part of Figure 2.11 illustrates how slip compensation automatically compensates for this condition by applying 1.5Hz of additional output frequency to the existing output frequency of 50Hz, resulting in a new output frequency of 51.5Hz. The motor shaft still slips back, but now the actual shaft speed is the desired 1500rpm[54].

For more understanding of the function of slip compensation at open loop driver operation, Figure 2.12 illustrates the current phase spectra of 4kw, 4 poles induction motor which is fed by VFD with non-slip compensation. One can see from the figure main supply frequency component at 50 Hz under all loads. The motor actual speed changes as load changes, for example, the speed was 1447.9 rpm under 75% full load while slip was 0.035.

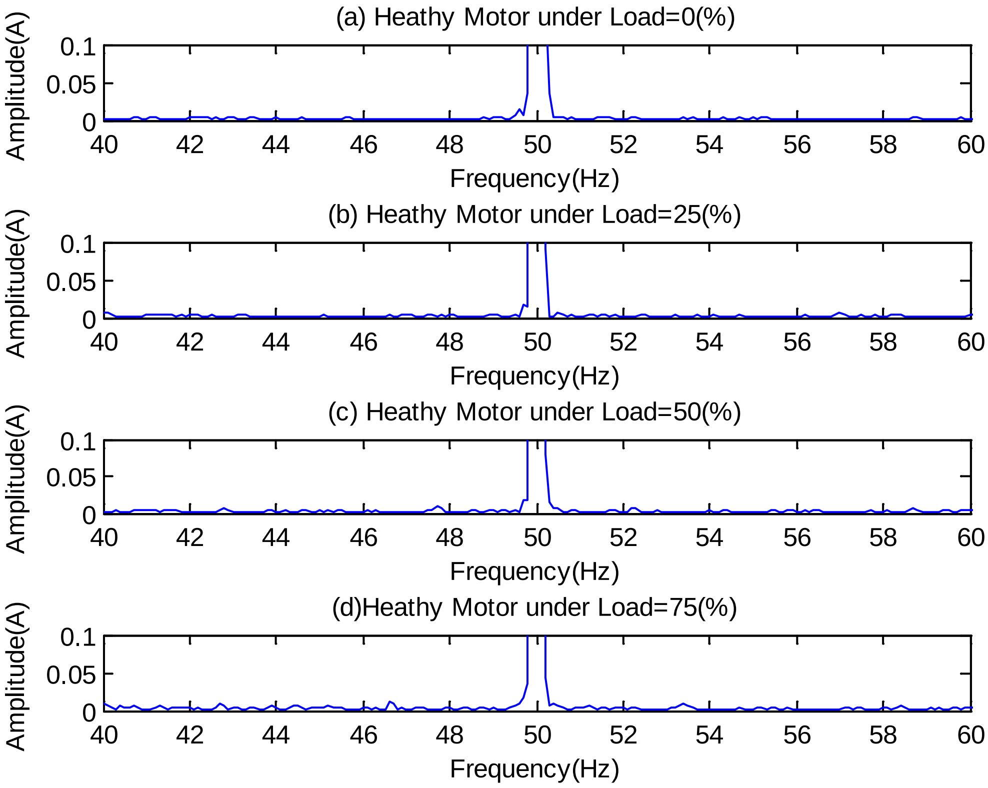

Figure 2.12-Phase Current Spectrum with Non-slip Compensation (from experimental study in chapter 6)

Figure 2.13 shows phase current spectrum under healthy condition with slip compensation. As can be seen from the figure as the load increases, the speed decreases and supply frequency shafted to the right side. For instance the motor speed was 1475.3 rpm under 75% full load while the slip was 0.04.

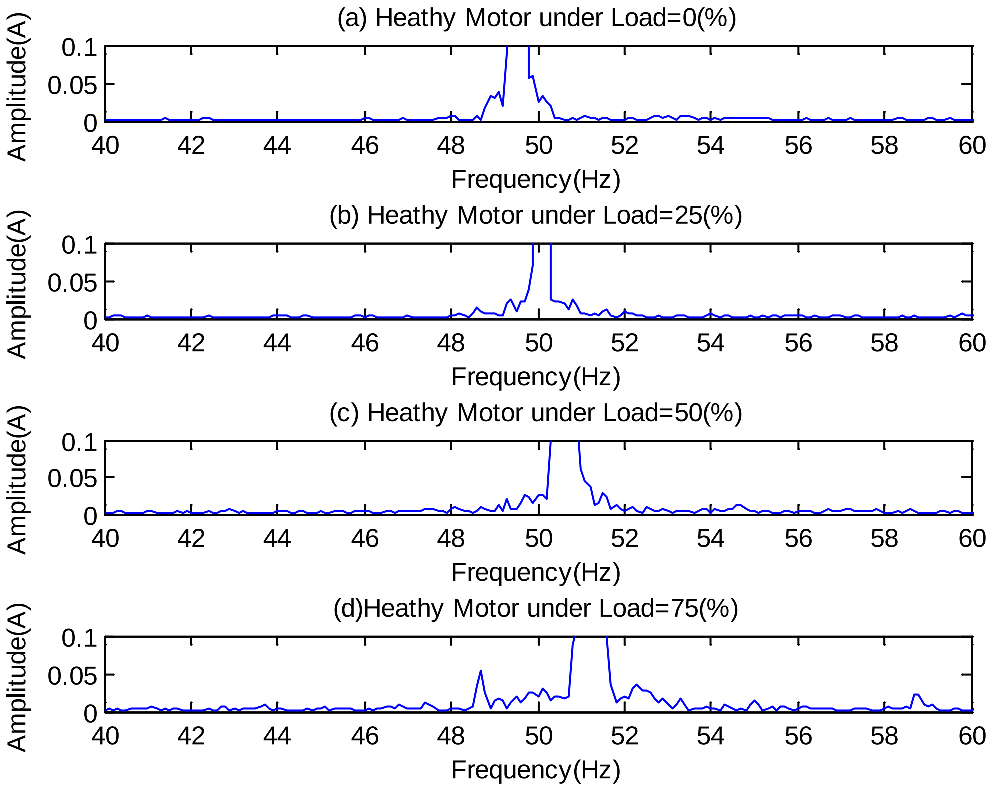
(a) Heathy Motor under Load=0(%)

(b) Heathy Motor under Load=25(%)

(c) Heathy Motor under Load=50(%)

(d)Heathy Motor under Load=75(%)

Figure 2.13-Phase Current Spectrum with Slip Compensation (from experimental study in chapter 6)

	Motor Speed [rpm]				Supply Frequency[Hz]				Slip [Per Unit]			
	Zero-load	25% load	50%Load	75% load	Zero-load	25% load	50%Load	75% load	Zero-load	25% load	50%Load	75% load
Without Slip Compensation	1493	1480	1464.8	1447.9	50	50	50	50	0.005	0.013	0.024	0.035
With Slip Compensation	1475.6	1476.1	1476.8	1475.3	49.5	50.1	50.6	51.2	0.006	0.018	0.027	0.040

Table 2.1-Comparison of Results under Healthy Condition (from experimental study in chapter 6)

Table 2.1 exhibits the comparison of results of motor speeds with slip compensation and without slip compensation under different loads (see chapter six for more details).

2.6 Benefits of Variable Frequency Drives

According to [63, 64]variable frequency drives offer the following benefits:

- Simple installation
- Low motor starting current
- High power factor
- Energy savings
- Lower kVA
- Reduction of thermal and mechanical stresses on the motor during starts

2.7 Summary of Chapter 2

This chapter introduces some details of principle of induction motor and AC Drives. An inverter-driven motor system controls the rotational speed of an alternating current (AC) electric motor by controlling the frequency and voltage of the electrical power supplied to the motor. This system is also called variable frequency drive (VFD). Variable-frequency drives are widely used in ventilation systems, pumps, elevators, conveyors, machine tools, etc.

The induction motor can only run efficiently at close to the synchronous speed of the rotating field. The best method of speed control must therefore provide for continuous smooth variation of the synchronous speed, which in turn calls for variation of the supply frequency. This is achieved using an inverter to supply the motor. The majority of inverters used in motor drives are voltage source inverters (VSI), in which the output voltage to the motor is controlled to suit the operating conditions of the motor. The pulse width modulated (PWM) inverter is the most commonly chosen. It receives DC power from a fixed voltage source and adjusts the frequency and voltage. PWM types cause the least harmonic noise.

CHAPTER 3

ANALYTIC MODELS FOR INDUCTION MOTOR FAULTS

This chapter presents a basic description of the physical phenomena related to induction motors, and induction motor fault, as well as presenting some reviews on induction motor fault detection. Moreover, it explains the physical phenomena of faulty induction motors with broken rotor bars; inter-turn short-circuits and open-circuit in the stator windings, air-gap eccentricity and motor bearing faults by MCSA.

3.1 Induction Motor Faults

In recent years, condition monitoring as well as fault diagnostics of squirrel-cage induction machines received considerable attention from both industry and academe. A number of different techniques that address various types of the most common failures have been developed and implemented [49, 65, 66]. Researchers were able to gain a better insight into the mechanisms of these failures and use this knowledge to both improve the design of the machine itself and develop the means to diagnose machine faults more effectively.

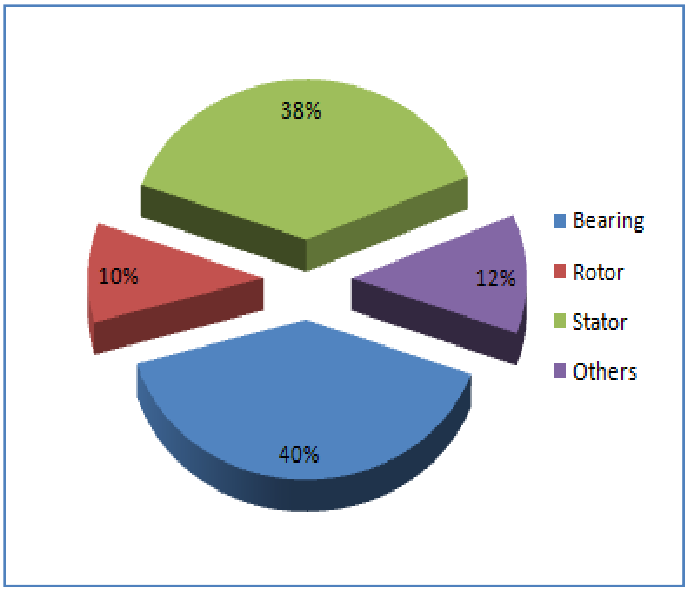

Figure 3.1-Common Faults in Induction Motors[54]

Induction machine failures are commonly divided based on the main machine components, into three main groups, namely, stator, rotor and bearing faults [5]. As can be seen in Figure 3.1, around 40% of faults associated with induction machines are due to bearing failures, whereas faults associated with stator windings account for 38% of induction machine failures, and failures associated with rotors account for approximately 10% of induction machine failures[54].

These faults produce one or more of the symptoms as follows [67, 68]:

(a) unbalanced air-gap voltages and line currents
(b) increased torque pulsations
(c) decreased average torque
(d) increased losses and reduction in efficiency
(e) excessive heating

For the purpose of detecting such fault-related signals, many diagnostic methods have been developed so far. These methods to identify the above faults may involve several different types of fields of science and technology. They can be described as follows [11]:

(a) motor-current signature analysis (MCSA)
(b) model, artificial intelligence, and neural-network-based techniques
(c) noise and vibration monitoring
(d) chemical analysis
(e) electromagnetic field monitoring, search coils, coils wound around motor shafts (axial flux-related detection)
(f) temperature measurements
(g) infrared recognition
(h) radio-frequency (RF) emissions monitoring
(i) acoustic noise measurements

This thesis is focused on three types of induction motor faults, namely: inter-turn short circuits in stator windings, open circuit, and broken rotor bars and motor bearing faults. These categories of faults in induction motors are discussed in this chapter as well as MCSA is used to detect such faults.

3.2 Electrical Faults

3.2.1 Rotor Faults

Induction motors are the most widely used prime movers in industry. Broken rotor bars (BRB) in motors are a common fault which often brings unexpected breakdowns and leads to loss of productivity. In recent years, this type of fault has been increasingly studied for developing advanced techniques that permit on-line early detection and diagnosis of motor faults to avoid any negative consequences of unexpected shutdowns [69].

There are three major types of faults that can be associated with squirrel-cage rotor structures, firstly, inter-laminar currents, sometimes referred to as inter-bar currents caused by shorts through the rotor core laminations, secondly rotor end-ring connector breakages; and finally, rotor-bar breakages. These faults may result from a wide variety of stresses as well as manufacturing defects [70, 71]. Recurrent overloading, both thermal and electrical, in addition to excessive vibrations due to supply voltage unbalances, load variations, and frequent starting transients may result in accelerated failures of squirrel-cage rotor bars and other structural components [69].

The rotor current in a cage winding produces an effective three phase magnetic field that has the same number of poles as the stator field. However, it is rotating at the slip frequency with respect to the rotor. When rotor asymmetry occurs there will be a resultant backward rotating field at the slip frequency with respect to the forward rotating rotor. This one induces one additional frequency in the stator current at $(1-2s)f_s$ [72-76]:

$$f_{brb} = (1-2s)f_s \tag{3.1}$$

where f_s is the stator supply frequency and s is the slip.

This returning current variation causes a torque pulsation at the twice slip frequency $2sf_s$ and a speed oscillation [72, 77]. This one induces in the stator winding an upper side hand current component at $(1+2s)f_s$ which depends on the load inertia. Therefore the broken rotor bars induce in the stator additional frequencies defined by [8, 78-85]:

$$f_{brb} = (1 \pm 2ks)f_s \tag{3.2}$$

Where a harmonic integer *k*=1, 2, 3 …. n

3.2.1.1 Sideband Current Signal Estimation under Broken Rotor Bar

When a motor drive is operating under healthy conditions, the ideal electromagnetic relationship of the driving motor can be examined by using just one of the three phases. For example, the effect due to asymmetric rotor cases such as broken rotor bar and misaligned shafts can be modelled by only using phase A. By neglecting the higher order harmonics of the mains supply and inherent errors of rotor systems, the current signal in phase A for a healthy motor drive can be expressed as[31, 86, 87]

$$i_A = \sqrt{2}I\cos(2\pi f_s t - \alpha_I) \tag{3.3}$$

Correspondingly, the magnetic flux in the motor stator is [86]

$$\emptyset_A = \sqrt{2}I\cos(2\pi f_s t - \alpha_\emptyset) \tag{3.4}$$

The electrical torque produced by the interaction between the current and flux can be expressed as [86]

$$T = 3p\emptyset I\sin(\alpha_I - \alpha_\emptyset) \tag{3.5}$$

where I and ϕ denote the root mean squared (RMS) amplitudes of the supply current and the linkage flux respectively, α_I and α_ϕ are the phases of the current and flux respectively referring to the phase of supply voltage signal, f_s is the fundamental frequency of the electrical supply and P is the number of pole pairs.

If there is a fault on the rotor such as a broken rotor bar, there will be an additional current component, denoted as i_f, in the stator winding to interact with the main magnetic fields between stator and rotor [65, 86]. Supposing that the additional current is a sinusoidal wave with a frequency f_F, an associated current wave with BRB amplitude I_F and phase angle α_F can be expressed as [31]

$$i_f = \sqrt{2} I_F \cos(2\pi f_F t - \alpha_F) \tag{3.6}$$

Correspondingly, an oscillatory electric torque due to its interaction with the fundamental flux can be derived using electric torque equation $T_e = Im\left(p\widehat{\emptyset}\hat{I}_F\right)$as [31]:

$$\Delta T = 3p\emptyset I_F \sin[2\pi f_F t - \alpha_\emptyset + \alpha_F] \tag{3.7}$$

which causes the motor rotor to produce a corresponding angular speed oscillation due to $J\frac{d}{dt}\left({}^{\Delta\omega}/{}_{p}\right) = \Delta T$ and hence angular displacement oscillation as [31]:

$$\Delta\emptyset(t) = \int \Delta\omega dt = -\frac{3p^2\emptyset I_F}{4\pi^2 f_F^2 J}\sin[2\pi f_F t - \alpha_F] \tag{3.8}$$

where J is the inertia of the rotor system of the motor. This angular oscillation modulates the phase of the linkage flux in Equation (3.4) and yields [31]:

$$\begin{aligned} \emptyset_A^F &= \sqrt{2}\emptyset \cos[2\pi f_s t - \alpha_\emptyset + \Delta\theta(t)] \\ &\approx \sqrt{2}\emptyset \cos(2\pi f_s t - \alpha_\emptyset) + \sqrt{2}\Delta\emptyset_F \cos[2\pi(f_s - f_F)t - \alpha_F] \\ &\quad -\sqrt{2}\Delta\emptyset_F \cos[2\pi(f_s + f_F)t - 2\alpha_\emptyset + \alpha_F] \end{aligned} \tag{3.9}$$

Where $\Delta\emptyset_F = \frac{3p^2\emptyset^2 I_F}{4\pi^2 f_F^2 J}$

The derivative of the first term of the flux is the fundamental electromotive force (EMF), while the derivative of the other two terms produces two new EMFs [31]:

$$\begin{aligned} \mathrm{E}_A^F &= -\sqrt{2}\emptyset\, 2\pi f_s \sin(2\pi f_s t - \alpha_\emptyset) \\ &\quad -\sqrt{2}\Delta\emptyset_F 2\pi(f_s - f_F)\sin[2\pi(f_s - f_F)t - \alpha_F] \\ &\quad +\sqrt{2}\Delta\emptyset_F (f_s + f_F)\sin[2\pi(f_s + f_F)t - 2\alpha_\emptyset + \alpha_F] \end{aligned} \tag{3.10}$$

If the equivalent winding impedance at supply frequency is $z = Ze^{\alpha_\phi}$ and assuming that it changes with frequency shifts relative to the supply frequency, the impedances at the two sideband components are $z_l = (Z - \Delta Z_l)e^{(\varphi_Z + \Delta\varphi_{Zl})}$ and $z_r = (Z + \Delta Z_r)e^{(\varphi_Z - \Delta\varphi_{Zr})}$, which means that the modulus of impedance increases with the increase in frequency and the phase decreases with frequency. These EMFs will lead to new motor phase currents as follows [31]:

$$\begin{aligned} \mathrm{I}_A^{FS} &= -\frac{\sqrt{2}\emptyset 2\pi f_s}{Z}\sin(2\pi f_s t - \alpha_\emptyset - \alpha_\mathrm{Z}) \\ &\quad -\frac{\sqrt{2}\Delta\emptyset_F 2\pi(f_s - f_F)}{Z - \Delta Z_l}\sin[2\pi(f_s - f_F)t - \alpha_F - \varphi_Z - \Delta\varphi_{Zl}] \\ &\quad +\frac{\sqrt{2}\Delta\emptyset_F 2\pi(f_s + f_F)}{Z + \Delta Z_r}\sin[2\pi(f_s + f_F)t - 2\alpha_\emptyset + \alpha_F - \varphi_Z + \Delta\varphi_{Zr}] \end{aligned} \tag{3.11}$$

The difference between ΔZ_l and ΔZ_r becomes larger with the increase in loads due to the increase in slip and so do the two phases. In addition, for higher order harmonics, these effects will be more significant. So this change is kept in this study to explain the asymmetric sidebands in the spectrum when large frequency shifts are examined for rotor misalignments, which is approximately a 50% difference relative to the fundamental, rather than not taken into account as in [39, 86].

Combining Equation (3.6) with Equation (3.11) yields the final current signal under rotor faulty conditions:

$$\begin{aligned} i_A^F = i_A^{FS} + i_f &= -\sqrt{2}I\sin(2\pi f_s t - \alpha_\emptyset - \varphi_\mathrm{Z}) \\ &\quad +\sqrt{2}\mathrm{I}_F\cos[2\pi(f_s - f_F)t - \alpha_F] \\ &\quad +\sqrt{2}I_{Fl}\sin[2\pi(f_s - f_F)t - \alpha_F - \varphi_Z - \Delta\varphi_{Zl}] \end{aligned} \tag{3.12}$$

$$-\sqrt{2}I_{Fr}\sin[2\pi(f_s+f_F)t-2\alpha_{\emptyset}+\alpha_F-\varphi_Z+\Delta\varphi_{Zr}]$$

where $I_{Fl}=2\pi(1-2s)f_s\,\Delta\phi/(Z-\Delta Z)$ and $I_{Fr}=2\pi(1+2s)f_s\,\Delta\phi/(Z+\Delta Z)$ are the modulus of sideband components due to speed oscillations which are caused originally by BRB currents in Equation (3.6). It shows that the current signal of the faulty case exhibits three new additional components, compared with that of a normal operation. Two of these are the lower sideband components at the same frequency, but with different phases, and the other is the upper sideband component with a phase different from the previous two. To see the possible connection of these components Equation (3.12) can be expressed using phase shift relationships: $\cos(\pi/2+\theta)=-\sin(\theta)$ and $\cos(\pi+\theta)=-\cos(\theta)$

$$\begin{aligned} i_A^F &= \sqrt{2}I\cos\left(2\pi f_s t-\alpha_{\emptyset}-\varphi_{\mathrm{Z}}+\frac{\pi}{2}+\pi\right) \\ &+\sqrt{2}\mathrm{I}_F\cos[2\pi(f_s-f_F)t-\alpha_F] \\ &+\sqrt{2}I_{Fl}\cos\left[2\pi(f_s-f_F)t-\alpha_F-\varphi_Z-\Delta\varphi_{Zl}+\frac{\pi}{2}+\pi\right] \\ &+\sqrt{2}I_{Fr}\cos\left[2\pi(f_s+f_F)t-2\alpha_{\emptyset}+\alpha_F-\varphi_Z+\Delta\varphi_{Zr}+\frac{\pi}{2}\right] \end{aligned} \tag{3.13}$$

Furthermore, the two lower sidebands in Equation (3.13) can be combined to yield [31]

$$i_l=\sqrt{2}\sqrt{I_F^2+I_{Fl}^2-2I_FI_{Fl}\sin(\varphi_Z+\Delta\varphi_{Zl})}\cos[2\pi(f_s-f_F)t-\alpha_F-\delta] \tag{3.14}$$

where the amplitude of lower sideband in RMS value is

$$I_L=\sqrt{2}\sqrt{I_F^2+I_{Fl}^2-2I_FI_{Fl}\sin(\varphi_Z+\Delta\varphi_{Zl})} \tag{3.15}$$

The phase angle is [31]

$$\cos\delta=\frac{\sqrt{2}I_F-\sqrt{2}I_{Fl}\sin(\varphi_Z+\Delta\varphi_{Zl})}{\sqrt{2I_F^2+2I_{Fl}^2-4I_FI_{Fl}\sin(\varphi_Z+\Delta\varphi_{Zl})}} \tag{3.16}$$

It shows that the lower sideband amplitude appearing in PS is combined from two different types of underlying physical processes. Alternatively, the BRB current interferes with the current component due to speed oscillation.

Substituting Equation (3.14) into i_A^F in Equation (3.13) yields a more concise expression of the current signal for asymmetrical rotor faults [31]:

$$\begin{aligned} i_A^F \approx{} & \sqrt{2}I\cos\left(2\pi f_s t - \alpha_\emptyset - \varphi_{\mathrm{Z}} + \frac{\pi}{2} + \pi\right) \\ & + \sqrt{2}I_L\cos[2\pi(f_s - f_F)t - \alpha_F - \delta] \\ & + \sqrt{2}I_{Fr}\cos\left[2\pi(f_s + f_F)t - 2\alpha_\emptyset + \alpha_F - \varphi_Z + \Delta\varphi_{Zr} + \frac{\pi}{2}\right] \end{aligned} \tag{3.17}$$

From the above derivation and discussion it can be concluded that [31]:

a) The BRB leads to additional current components which will be the lower and upper sideband components at $(1 \pm 2s)f_s$ shown in the spectrum of phase current signal.

b) The amplitudes of these sidebands are influenced by rotor inertia, load variation, power factor and machine impedance. Especially, the amplitude of the original BRB current i_f shown at the lower sideband interferes with that due to speed oscillations. This means that the interference needs to be eliminated to obtain the amplitude of i_f for accurate and reliable prediction of fault severity.

c) The phases of sidebands are not only related to the same factors as their amplitude, but also the phase variation of the fault current. However, it will be shown in Section 4.6 that an appropriate phase combination between sidebands and the carrier of fundamental supply can eliminate the phase variation in order to achieve reliable and accurate sideband estimation.

3.2.2 Stator Faults

As illustrated in Figure 2.1 there are four typical stator faults: winding short turn, open circuit, phase to phase short circuit and phase to ground fault [45, 46, 88, 89]. These asymmetric stator faults are usually related to insulation failures which result from different reasons such as overloading, poor connection etc. As a result, the different types of winding faults and their causes are summarised below[90]:

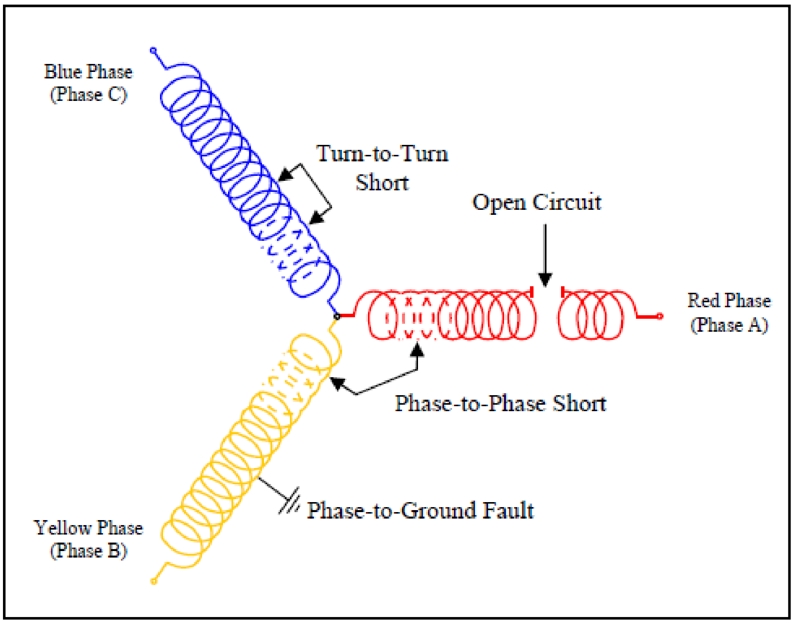

Figure 3.2-Different three-phase stator winding faults[45]

- Inter-turn short circuits between turns of the same phase, winding short circuits, short circuits between winding and stator core, short circuits on the connections, and short circuits between phases are usually caused by stator voltage transients and abrasion.
- Inter-turn short circuits are also due to voltage transients and can be caused by the successive reflection resulting from cable connection between motors and AC drives. Such AC drives produce extra voltage stress on the stator windings due to the inherent pulse width modulation of the voltage applied to the stator windings[91]. Again, long cable connections between a motor and an AC drive can induce motor over voltages. This effect is caused by successive reflections of transient voltage.
- Short circuits in one phase are usually due to an unbalanced stator voltage. An unbalanced voltage is caused by an unbalanced load in the power line, a bad connection of the motor terminals, or bad connections in the power circuit. Moreover, an unbalanced voltage means that at least one of the three stator voltages is under or over the value of the other phase voltages.

It has been reported in [14] that about 38% of all reported induction motor failures fall into these fault modes. Because of this high fault rate, stator fault diagnosis has been studied extensively and a range of papers published on the analysis of air gap, axial flux and terminal current signals to understand possible fault mechanisms for finding effective and reliable features in measured current signals. Figure 3.3 illustrates short circuit in one of a stator coil [64].

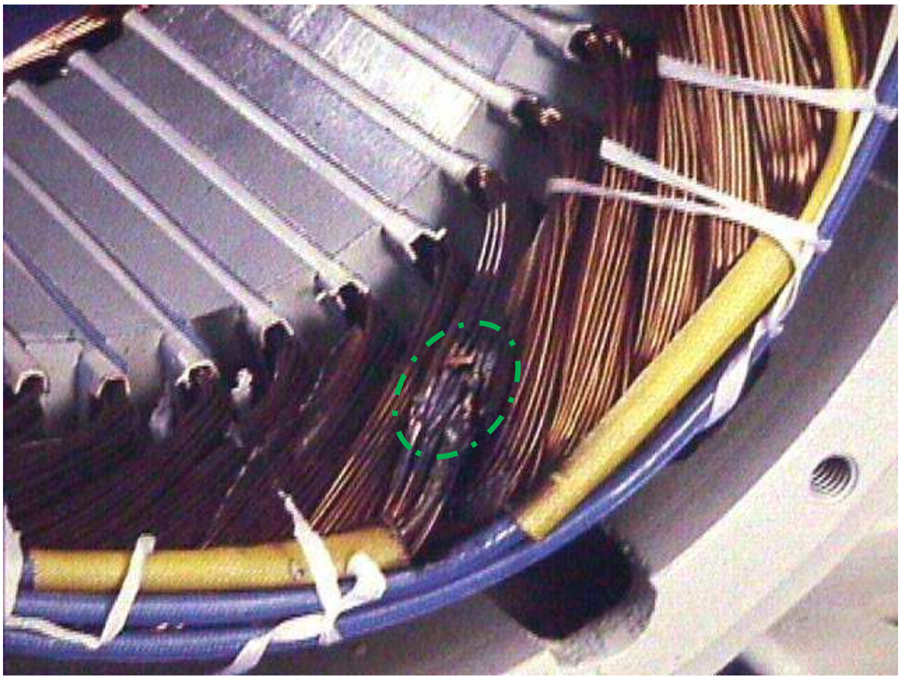

Figure 3.3-Short Circuit in Stator Coil [64]

3.2.2.1 Stator Fault Detection by Stator Current Analysis

overall, stator faults cause uneven distribution of the air-gap flux waveform around the stator cross section, which makes the stator currents to be modulated by rotor slot frequency and the feature frequencies in current signals can be found at characteristic frequencies [33, 66, 92-96]

$$f_{sf}=f_s\left[1\pm mN_b\left[\frac{1-s}{p}\right]\right] \tag{3.18}$$

To be convenient for field engineers, Equation (3.18) can be expressed in terms of rotor frequency as [97]

$$f_{sf}=f_s\pm mN_bf_r \tag{3.19}$$

where f_s supply frequency, f_r rotor speed, s the motor slip, N_b number of rotor bars, p number of pole-pairs and m= 1, 2, 3… is the harmonics orders.

The motor stator faults were seeded for both open circuit and short circuit as shown in section 5.3.2. Modulation signal bispectrum technique was applied on motor current signals to detect and diagnose open and short circuit on stator windings.

3.3 Mechanical Faults

3.3.1 Motor Bearing Faults

Studies have shown that the common faults in induction motors (about 40%–50%) happen in rolling bearings, depending on the type of installation, the motor size, and the supply voltage [98-100]. In general it is due to manufacturing faults, lack of lubrication, installation errors and wear and tear. According to the affected elements, shown in Figure 3.4, bearing faults can be classified as inner ring, outer ring, ball element and cage faults[101].

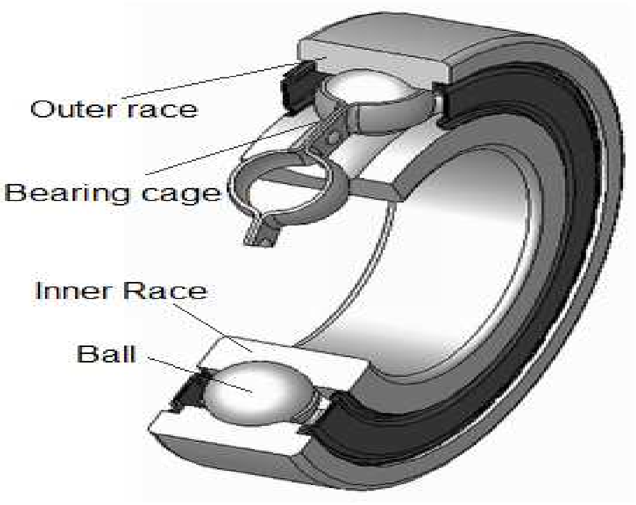

Figure 3.4-Components of the Rolling Ball Bearing [101]

The inner ring is mounted on the shaft of the machine and is usually the rotating part whereas the outer ring is fixed in the housing of the machine and in most cases it does not rotate. The rolling elements may be balls, cylindrical rollers, spherical rollers, tapered rollers or needle rollers. They rotate against the inner and outer ring raceways and transmit the load acting on the bearing via small surface contacts separated by a thin lubricating film. The cage separates the rolling elements to prevent metal-to-metal contact between them during operation. Seals are important for the protection of bearing from contamination and to keep the lubricant inside the bearing surroundings.

3.3.1.1 Bearing Fault Modes

This thesis considers rolling-element bearings with a geometry shown in Figure 3.5. The bearing consists essentially of the outer and inner raceways, the balls, and the cage, which keeps the distances between the balls equals. The number of balls is N_B, their diameter is D_b, and the pitch diameter is D_p. The point of contact between a ball and the raceway is characterised by the contact angle β [101].

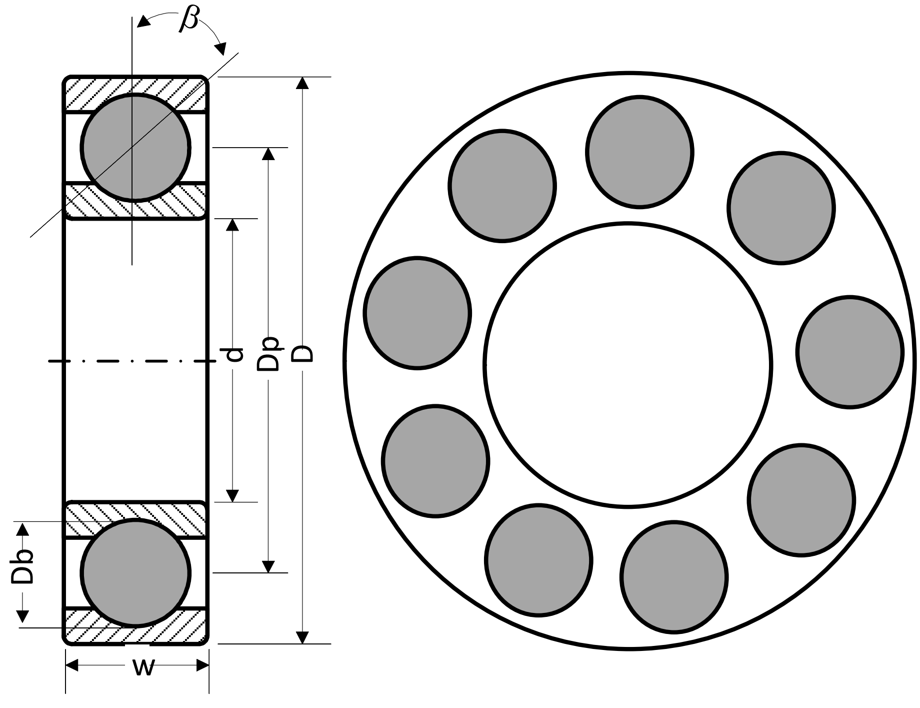

Figure 3.5-Geometry of a Rolling-Element Bearing [101]

Bearing faults can be classified into distributed and localised defects [102]. Distributed defects affect a whole region and are difficult to characterise by distinct frequencies. On the other hand, single-point defects are localised and can be classified according to the following affected element [102]:

- Outer raceway defect
- Inner raceway defect
- Ball defect
- Cage defect

With each type of bearing fault, a characteristic frequency can be associated. This frequency is corresponding to the periodicity by which an irregularity appears due to the existence of the fault. The characteristic frequencies are functions of the bearing geometry and the mechanical rotor frequency f_r. For the four considered fault types, the characteristic frequency takes the following expressions [38, 103-105]:

$$f_o = \frac{N_b}{2} f_r(1 - \frac{D_b}{D_p}\cos\beta) \tag{3.20}$$

$$f_i = \frac{N_b}{2} f_r(1 + \frac{D_b}{D_p}\cos\beta) \tag{3.21}$$

$$f_b = \frac{D_p}{D_b} f_r(1 - \frac{{D_b}^2}{{D_p}^2} cos^2\beta) \tag{3.22}$$

$$f_c = \frac{1}{2} f_r(1 - \frac{D_b}{D_p} cos\,\beta) \tag{3.23}$$

Where f_o is the outer race fault frequency, f_i is the inner race fault frequency, f_b is the ball fault frequency and f_c is cage fault frequency.

The characteristic fault frequencies are the result of the absolute motion (vibration) of the machine. The stator current is not affected by the absolute motion of the machine, but rather by a relative motion between the stator and rotor (i.e., changes in the air gap). In the instance of a bearing fault, the characteristic fault frequencies are essentially modulated by the electrical supply frequency.

3.3.1.2 Bearing Fault Detection by Stator Current Analysis

The most often mentioned model studying the influence of bearing damage on the induction machine stator current was presented by[106]. The authors consider the generation of rotating eccentricities at bearing fault characteristic frequencies f_v, which leads to periodical changes in the machine inductances. This should produce additional frequencies f_{bf} in the stator current, which can be predicted by [101, 107, 108]:

$$f_{Bf} = |f_s \pm k f_v| \qquad (3.24)$$

where f_s is the electrical supply frequency, f_v is one of the four characteristic fault frequencies defined by Equation 3.1 through Equation 3.4and k = 1, 2, 3...

This model has been used in several recent works [106, 109, 110]. In [106], two types of faults were tested, namely a hole drilled through the outer race and indentation produced in both the inner and outer surfaces. For both faults, the vibration and current spectra are analysed in both loaded and unloaded motor cases. The first faulty condition (outer race defect) is characterised by f_o and $2f_o$components in the vibration spectrum and $|f_s \pm f_o|$ and $|f_s \pm 2f_o|$ components in the current spectrum. The second fault (inner race defect) is highlighted by f_o, $2f_o$, and f_i components in the vibration spectrum and $|f_s \pm f_o|$, $|f_s \pm 2f_o|$, and $|f_s \pm f_i|$ components in the current spectrum. The authors claim that the characteristic fault frequency components are relatively small when compared to the rest of the current spectrum. The largest components occur at multiples of the supply frequency and are caused by saturation, winding error distribution, and supply voltage changes. However, an evaluation of the amplitude of these largest components in different cases (healthy and two types of fault condition) is not shown. In[109], two inner race faults (spalls and drilled hole) are analyzed, and the authors point out a problem related to the experimental simulation of bearing faults: The act of disassembling, remounting, and realigning the test motor can significantly alter the vibration and current spectra. The results show that, for both defects, the characteristic fault-frequency components are clearly visible only in the vibration spectrum and not in the current spectrum. Both inner and outer raceway defects are analysed in[110]. They show some differences in the amplitudes of the current spectrum of a 1.5 kW induction motor at full load, but the characteristic fault-frequency components do not stand out clearly.

A new analytical model was suggested by [38] to take into account the load-torque variations caused by bearing faults in addition to the effect of relative motion between rotor and stator. In this way, new frequencies in the current spectrum are identified for the defects in the inner raceway.

$$f_i' = |f_s \pm f_r \pm k f_i| \tag{3.25}$$

In [111] a three-phase 2.2-kW two-pole induction motor was used and the motor is equipped with two rolling ball bearings, type 6205Z, with nine balls, lubricated with grease. The research presents four different types of bearing defects namely, crack in the outer race, hole in the outer race, deformation of the seal, and corrosion. The tests are performed under no load and full-load.

The faults in the outer race have noticeable effects on the current spectrum, both in load and no-load conditions; the result shows a considerable increase of the third and seventh harmonic components at no load, and an increase of the even harmonics at high frequencies in the load condition [111].

In general previous studies have demonstrated the capability of current power spectrum based bearing fault signatures to detect bearing faults and produced diagnostic features of different bearing faults. However, because of high background noise levels of the current signals, especially when the motor is supplied by a variable frequency drive (VFD), the features are often very weak [101].

This research will examine the motor current spectra of healthy, outer race faults and inner race faults of an unloaded machine supplied with and without a VFD. To confirm the existences of the bearing characteristic frequencies, the motor is disconnected from the test rig and connected to an independent power supply directly to reduce the noise which is caused by the inverter and drive couplings as can be seen in Chapter 6. The current signals are analysed by both power spectrum (PS) and modulation signal bispectrum (MSB), The latter analysis technique is a modified bispectrum analysis and has been demonstrated in previous studies to have good performance in noise reduction [33]and is expected to produce more reliable bearing fault detection than that of power spectrum.

3.3.2 Air-gap Eccentricity

Induction motors might fail because of air-gap eccentricity. Air-gap eccentricity happens due to shaft deflection, inaccurate positioning of the rotor with respect to stator, bearing wear, stator core movement etc. Air-gap eccentricity creates unbalanced radial forces and hence unbalanced magnetic pull that might cause rotor-to-stator scrub, and finally results in damage of the stator core and stator windings. As a result the difference in air gap can result in the variation magnetic field distribution on the rotor, so that the direction of magnetic force is on the smallest air gap, which so called unbalanced magnetic pull. As well as eccentricity can lead to vibration and harmonics in current signal. Eccentricity can be caused by defective bearings, manufacturing faults and unbalanced rotor shaft [112, 113].

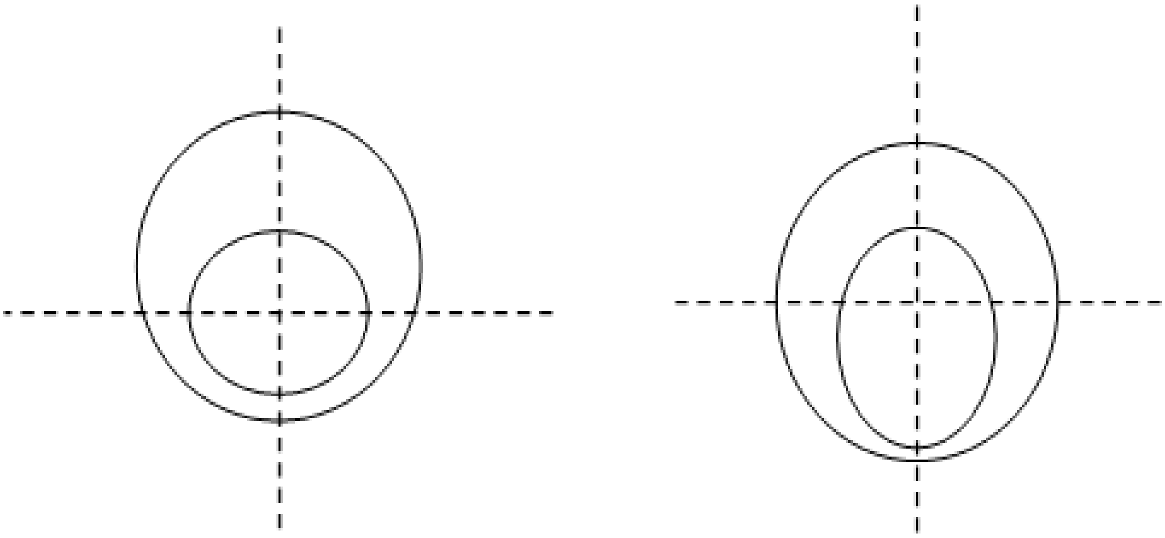

(a) Oval Stator

(b) Oval Stator

Figure 3.6-Air-gap Eccentricity

Eccentricity can be classified in two groups, static eccentricity and dynamic eccentricity[114]. The static eccentricity is a situation in which rotor rotation centre is removed to a more remote place in parallel to stator centre. The smallest air gap is always stationary and the magnetic pull force occurs in this side. An oval stator is considered as an example of static eccentricity as shown in Figure 3.6(a).

However, the dynamic eccentricity occurs when the rotator rotates around the stator centre but it does not rotate around its centre, so that magnetic pull force rotates with the rotor[115]. As an example of this type of eccentricity, there is an oval rotator as in Figure 3.6(b).

3.3.2.1 Air-gap EccentricityDetection by Motor Current Signature

As a result of presence variation of eccentricity, sideband components appear around the slot harmonics in the stator line current frequency spectrum. The frequency components in the stator currents of an induction machine with to air-gap eccentricity are given by [4, 103, 116-120]

$$f_{ecc} = \left[(kN_b \pm n_d)\frac{1-s}{p} \pm m\right] f_s \qquad (3.26)$$

where is the fundamental supply frequency, k an integer, $N_b$number of rotor bars, n_d eccentricity order number, (static eccentricity is n_d=0, dynamic eccentricity is n_d=1), $p$isthe number of pole-pairs,$m$is the order of the stator time harmonics that are present in the power supply driving the motor, given by ±1, ±3, ±5, …etc., and $s$the slip.

If both static and dynamic eccentricities exist together, spectral components can be observed around the fundamental, which are given by [121-126]

$$f_{mix} = (f_s \pm \mathrm{m} f_r) \qquad (3.27)$$

where m = 1,2,3,... , $f_r = (1-s)f_s/p$ the mechanical rotational frequency and p number of pole pairs.

3.4 Summary of Chapter 3

This chapter provides a basic description of the physical phenomena related to induction motors, and induction motor fault. Moreover, it describes the three electrical and mechanical faults most commonly presented in three-phase induction motors: shorted stator turns and broken rotor bars, stator faults, motor bearing faults and air-gap eccentricity. The possible sources and causes for each fault are presented in detail.

Broken rotor bars (BRB) in motors are a common fault which often brings unpredicted breakdowns and leads to loss of productivity. In recent years, this type of fault has been increasingly studied for developing advanced techniques that permit on-line early detection and diagnosis of motor faults to avoid any negative consequences of unexpected shutdowns. There are three major types of faults that can be associated with squirrel-cage rotor structures, firstly, inter-laminar currents, sometimes referred to as inter-bar currents caused by shorts through the rotor core laminations, secondly rotor end-ring connector breakages; and finally, rotor-bar breakages.

There are four typical stator faults: winding short turn, open circuit, phase to phase short circuit and phase to ground fault. These asymmetric stator faults are usually related to insulation failures which result from different reasons such as overloading, poor connection etc. Normally, stator faults cause uneven distribution of the air-gap flux waveform around the stator cross section, which makes the stator currents to be modulated by rotor slot frequency and the feature frequencies in current signals can be found at characteristic frequencies.

Bearing faults can be classified into distributed and localised defects. Distributed defects affect a whole region and are difficult to characterise by distinct frequencies. On the other hand, single-point defects are localised and can be classified according to the following affected element: outer raceway defect, inner raceway defect, ball defect and cage defect. With each type of bearing fault, a characteristic frequency can be associated. This frequency is corresponding to the periodicity by which an irregularity appears due to the existence of the fault. The characteristic frequencies are functions of the bearing geometry and the mechanical rotor frequency f_r.

Air-gap eccentricity creates unbalanced radial forces and hence unbalanced magnetic pull that might cause rotor-to-stator scrub, and finally results in damage of the stator core and stator windings. As a result the difference in air gap can result in the variation magnetic field distribution on the rotor, so that the direction of magnetic force is on the smallest air gap, which so called unbalanced magnetic pull. Moreover, eccentricity can lead to vibration and harmonics in motor current signal.

CHAPTER 4

STATISTICAL TECHNIQUESIN CONDITION MONITORING

This chapter presents some of conventional diagnostic techniques using frequency domain current signal. The FFT is used to get both amplitude spectrum and power spectrum (PS).Moreover the chapter describes some HOS techniques such as Conventional Bispectrum (CB) and modulation signal bispectrum (MSB).Finally the chapter presents a new method that is based on modulation signal bispectrum estimation (MSB-SE). This new method is applied to motor current signal to diagnose motor faults.

4.1 Introduction

This chapter reviews Higher-Order Statistics (HOS) and its relation to conventional second-order statistics. The first- and second-order statistics, for instance, mean, variance, autocorrelation and power spectrum, are accepted signal-processing implements and are used widely in data analysis. However, second-order statistics are suitable for describing Gaussian and linear processes. In practice, there are many situations where the processes deviate from Gaussianity and linearity. The generalised concept of HOS was introduced by Tukey and Brillinger in the early 1960s and in recent years these methods have produced a large number of research actions[127].

The HOS can be used in the following reasons[100]:

- Detecting deviations from Gaussianity.
- Extracting non-minimum phase information.
- Detecting and characterising non-linearity.

As a result time domain is a good source of information. There are a large number of statistical measures, for example, moments, cumulants and auto-correlation. The signal is often assumed stationary in statistical analysis.

Consequently transforming the signal from time to frequency domains can describe the periodicities of the signal; detect nonlinearities present in the signal and support understanding of the signal generating process. The discrete Fourier Transformer can play the main role for this type of transformer.

The power spectrum and bispectrum are special cases of the nth order spectrum.

4.2 Amplitude Spectrum

In many industry-standard, hand-held, data collection devices the time data is transformed to the frequency domain (at which point the data is called a spectrum) and the original time data discarded to minimise the data storage requirements. The frequency domain allows identification and tracking of individual frequency components, and identification of frequency and amplitude modulation, distortion and also noise levels. It therefore permits close correlation with physical machine characteristics.

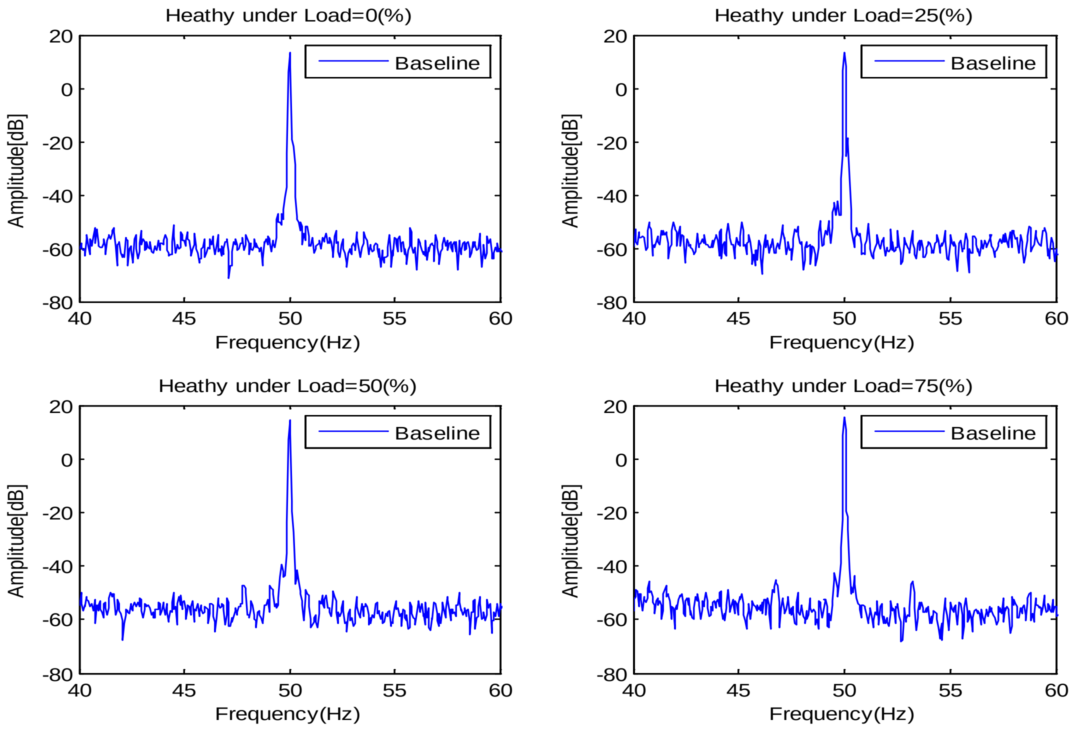

Figure 4.1-Phase Current Spectrum under Healthy Condition (from experimental study in chapter 6)

The background to Fourier transformation (FT) is a mathematical one based on Fourier series analysis of continuous and infinite functions which discussed in detailed in most high-level mathematics textbooks such as [128]. In practice, data is sampled in time and thus digitised. To achieve a Fourier transformation for this case, a Discrete Fourier Transform (DFT) is required. This is usually achieved using a Fast Fourier Transform (FFT) which has a greatly reduced number of arithmetic operations compared with a direct DFT method [129]. The FFT is particularly important for condition monitoring and therefore this section provides detail on its practical application.

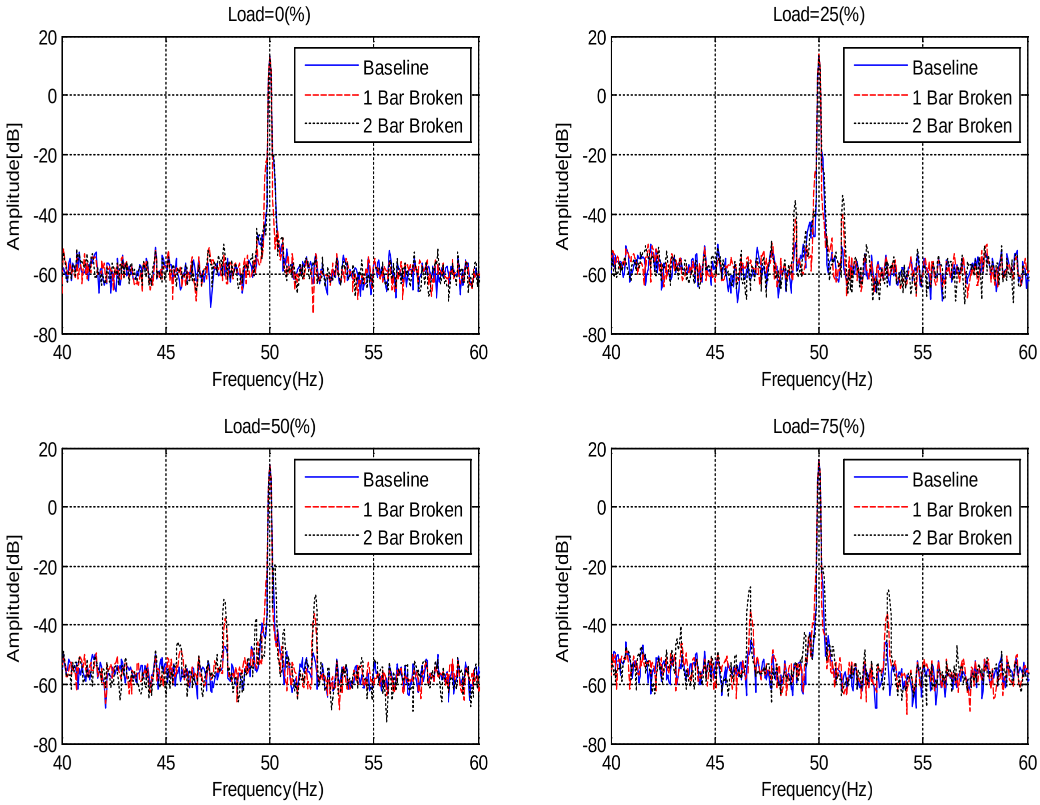

Figure 4.2-Phase Current Spectrum under Healthy and Broken Bar Condition (from experimental study in chapter 6)

By applying Fast Fourier Transform (FFT) to the signal in time domain, the amplitude of spectrum can be achieved. Figure 4.1 shows phase current spectra of healthy motor under different loads.

The spectra of current signals, shown in Figure 4.2 display a high degree of amplitude feature. The carrier components at the supply frequency 50 Hz have very high amplitudes and the sideband components under 75% full load and at 50±3.25 Hz, which correspond to the broken bar and speed fluctuation, are clearly visible.

In the spectra, the sideband amplitudes for broken bar are higher when compared with the spectrum of the healthy condition. Therefore the amplitude of sidebands changes with severity of the faults. As a result the current signals contain sufficient information for motor fault detection and diagnosis.

4.3 Power spectrum

Fora discrete time current signal $x(t)$, and its Discrete Fourier Transform (DFT) $X(f)$, is defined as[130]:

$$X(f) = DFT[x(t)] = \sum_{t=-\infty}^{+\infty} x(t)\, e^{-j2\pi ft} \tag{4.1}$$

Where *DFT* denotes to Discrete Fourier Transform

The second order measure of power spectrum (PS) of $x(t)$, can be estimated by the formula[131, 132]:

$$P(f) = E\{X(f)X^{*}(f)\} \tag{4.2}$$

where $X^{*}(f)$ is the complex conjugate of $X(f)$and $E\{\ \}$ the expectation operator showing that a statistical averaging is necessary in the spectrum estimation process.

Power spectrum can be calculated by Matlab and Figure 4.3 shows steps of the calculation [133].

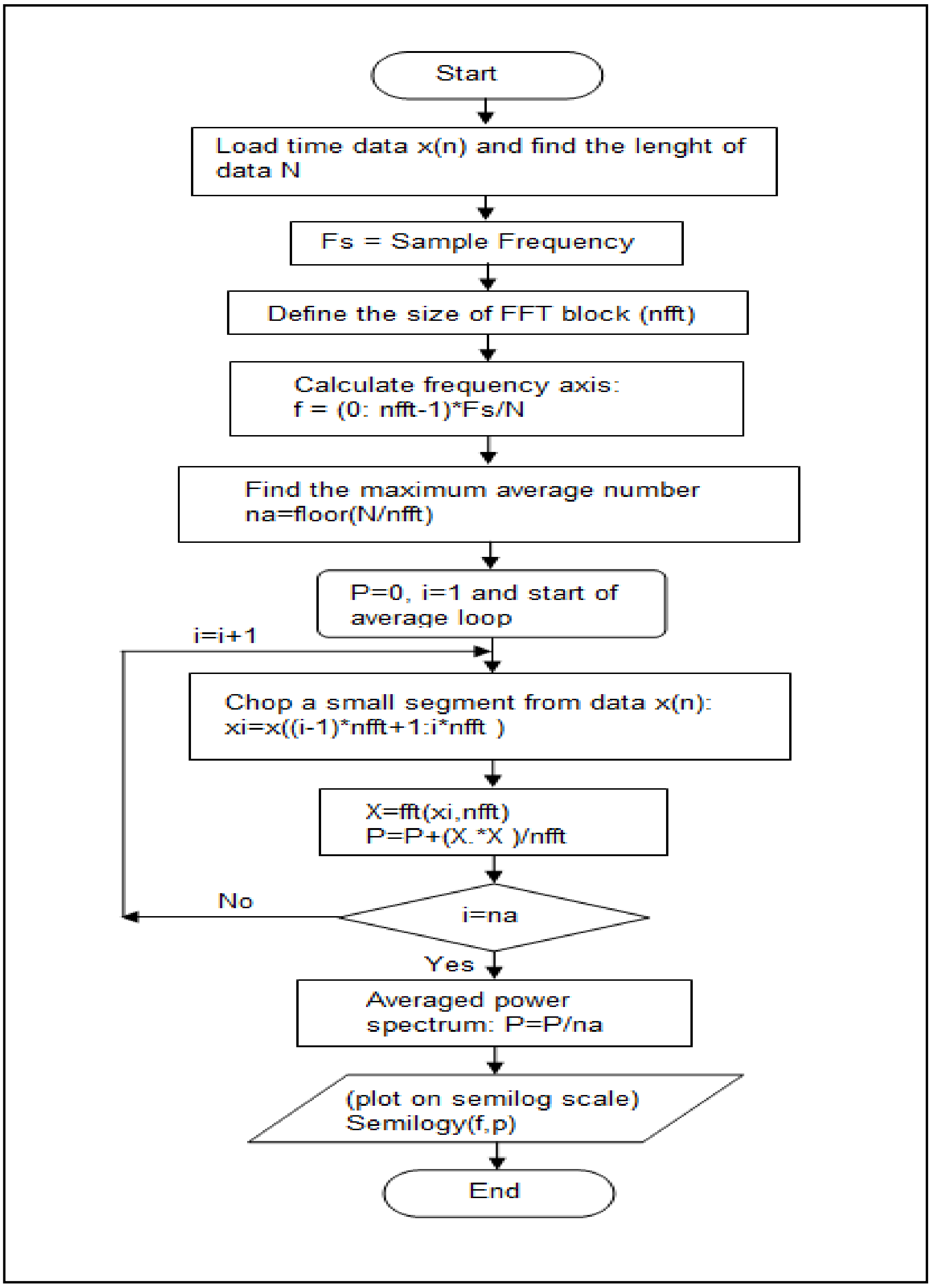

Figure 4.3-Flowchart of Calculating Power Spectrum in Matlab amended from [133]

Figure 4.4 shows power spectrum of phase current signal under different loads and health conditions. Comparing Figure 4.2with Figure 4.4, one can see the power spectrum is considered as the amplitude square of spectrum.

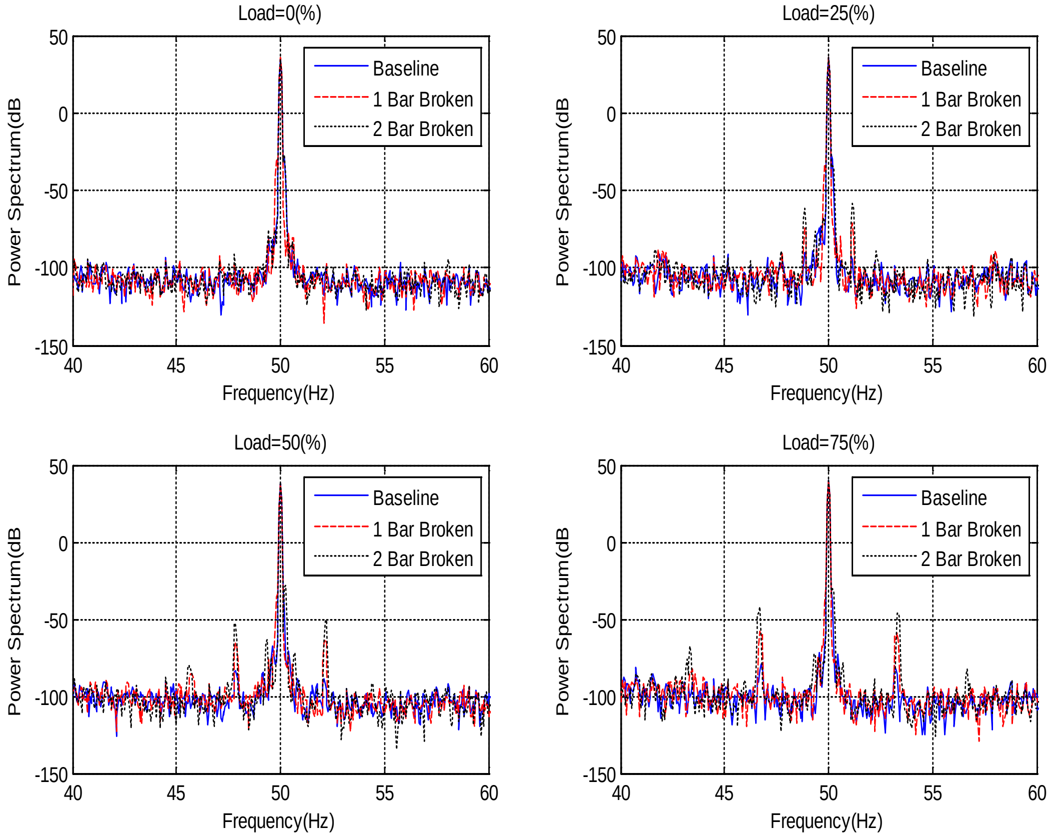

Figure 4.4-Phase Current Spectrum under Healthy and Broken Bar Condition (from experimental study in chapter 6)

4.4 Conventional Bispectrum and its Estimation

The bispectrum analysis is a type of higher order spectra (HOS), which is used by a large number of researches since the 1980s [134].

The power spectrum which as defined in Equation 4.2is a linear transform and is a function of the frequency index *f*. Extending this definition to take the measurements of the third-order gives rise to the estimation of conventional bispectrum (CB) [36, 37, 135].

$$B(f_{1,}f_2) = E\{X(f_1)\, X(f_2)X^*(f_1 + f_2)\} \tag{4.3}$$

Note that, unlike second-order measures, the third-order measure is a complex quantity, in that it contains both magnitude and phase information about the original time signal *x(t)*. If the frequency components at f_1, f_2 and $(f_1 + f_2)$ are independent components, each frequency will be characterised by statistically independent random phases distributed over (-π, π) uniformly. Upon the statistical averaging denoted by the expectation operator *E{}*in Equation 4.3, the bispectrum will tend towards zero due to the random phase mixing effect. In this way random noise and non-coupling contents can be suppressed significantly to obtain an optimised estimation of the triple product when the original signal is contaminated with a random noise and with non-coupling interference. This means that a lengthy data must be required to achieve sufficient averages for the realisation of these unique properties of CB.

On the other hand, if the three spectral components f_1, f_2 and $(f_1 + f_2)$ are non-linearly coupled to each other, the total phase of the three components will not be random at all, even though each of the individual phases are random, in particular, the phases have the following relationship[36, 37]:

$$\emptyset(f_2) + \emptyset(f_1) = \emptyset(f_2 + f_1) \tag{4.4}$$

Consequently, the statistical averaging will not lead to a zero value in the bispectrum. This nonlinear coupling is indicated by a peak in the bispectrum at the bifrequency B (f_1,f_2).

To measure the degree of coupling between coupled components, a normalised form of the bispectrum or bicoherence is usually used and defined as [1, 136, 137]

$$b^2(f_1, f_2) = \frac{|B(f_1, f_2)|^2}{E\left\{|X(f_1)X(f_2))|^2\right\} E\{|X(f_1+f_2)|^2\}} \tag{4.5}$$

The bicoherence is independent of the amplitude of the triple product of the DFT amplitudes and its values are bounded between 0 and 1. The bicoherence is close to 1 if there are nonlinear interactions among frequency combinations, f_1, f_2 and $f_2 - f_1$. On the other hand, a value of near 0 means an absence of interactions between the components. Therefore, based on the amplitude of bicoherence the nonlinear interactions can be detected and the interaction degrees can be also measured between the coupling components.

4.5 Modulation Signal Bispectrum and Its Estimation

CB in Equation 4.3 allows phase information between different component to be taken into account and shows unique performance in examining the presence of possible quadratic phase coupling (QPC) from the harmonically related frequency components of f_1, f_2 and $(f_2 + f_1)$. However, it neglects the possibility that the occurrence of $(f_2 - f_1)$, the lower sideband in PS, may be also due to the nonlinear relationship between the two components of f_1 and f_2. Because of this, it is not adequate to describe modulation signals such as the motor current signal in Equation3.17. To improve the performance of CB in characterising the motor current signals, a new variant of the conventional bispectrum, named as a modulation signal bispectrum (MSB) is examined in [1, 32-35] as follows:

$$MSB(f_{1,}f_2) = E\{X(f_2 + f_1)X(f_2 - f_1)X^*(f_2)X^*(f_2)\} \qquad (4.6)$$

Unlike the CB in Equation (4.3), this definition takes into account both $(f_2 + f_1)$ and $(f_2 - f_1)$ synchronously for characterising the nonlinear coupling in modulation signals. It shows that a bispectral peak will be presented clearly at bifrequency $MSB(f_{1,}f_2)$ if $(f_2 + f_1)$ and $(f_2 - f_1)$ are both due to nonlinear coupling between f_1 and f_2. This is more accurate and effective in representing the modulation signals.

The overall phase of MSB in Equation (4.6) is

$$\emptyset_{MSB}(f_1, f_2) = \emptyset(f_2 + f_1) + \emptyset(f_2 - f_1) - \emptyset(f_2) - \emptyset(f_2) \qquad (4.7)$$

when two components f_1 and f_2 are in coupling, their phases are related by

$$\emptyset(f_2 + f_1) = \emptyset(f_2) + \emptyset(f_1),\ \emptyset(f_2 - f_1) = \emptyset(f_2) - \emptyset(f_1) \qquad (4.8)$$

By substituting Equation (4.8) into Equation (4.7) the total phase of MSB will be zero and its amplitude will be the product of the four magnitudes, which is the maximum of the complex product. Therefore, a bispectral peak will appear at (f_1, f_2).Equation (4.6) now includes both $(f_2 + f_1)$ and $(f_2 - f_1)$ simultaneously for measuring the nonlinearity of modulation signals. If $(f_2 + f_1)$ and $(f_2 - f_1)$ are both due to a nonlinear effect between f_1 and f_2 a bispectral peak will appear at bifrequency$\left(f_{1,}f_2\right)$. This is more accurate and apparent in representing the sideband characteristics of modulation signals.

With this definition, the MSB phase of motor BRB current signals presented in Equation3.17 can be obtained as

$$\begin{gathered}\emptyset_{MSB}(f_{\mathrm{F}}, f_{\mathrm{s}}) = \emptyset(f_s + f_{\mathrm{F}}) + \emptyset(f_{\mathrm{s}} - f_{\mathrm{F}}) - \emptyset(f_{\mathrm{s}}) - \emptyset(f_{\mathrm{s}}) \\ = -2\alpha_{\emptyset} - \varphi_Z + \Delta\varphi_{Zr} + \frac{\pi}{2} - \delta - 2(-\alpha_{\emptyset} - \varphi_Z + \frac{\pi}{2} + \pi) \\ = \varphi_Z + \Delta\varphi_{Zr} - \delta - \frac{\pi}{2}\end{gathered} \tag{4.9}$$

Equation 4.9 shows that the MSB phase of current signals relates only to the machine parameters including the impedance phase $\varphi_Z + \Delta\varphi_{Zr}$ and fault amplitude induced phase δ , but not fault phase α_F and magnetic flux phase α_{ϕ}. This means that the phase of MSB will be a constant when the motor is operating under steady conditions. In other words, MSB is independent of the angular position of the motor rotor or the start point of a signal segment acquired. This will allow sufficient averages in MSB estimation to be performed using a data set collected or framed at any time through a Welch method. The average in turn will suppress random noise and non-modulating components to obtain a reliable estimation of MSB and of the hidden modulating signal.

It is worth noting that the phase of conventional bispectrum applied to signals expressed in Equation 3.17 is not independent of signal segments used. This means that an average process in estimating CB will lead to an uncertain result. Instead, it will change with segment sequences used, in an extreme case, CB magnitude will be close to zeroes if the phases of data segments distribute uniformly between 0 and 2π . Therefore, CB is not suitable for analysing motor current signals.

For the case when the fault is due to pure speed oscillation, such as a misaligned shaft and rotor eccentricity, the MSB phase is simplified by excluding the second term in Equation3.13 as

$$\emptyset_{MS}(f_F, f_s) = \Delta\varphi_{Zr} - \Delta\varphi_{Zl} - \pi \tag{4.10}$$

As a result the phase will be closer to π . Especially, when the impedance phase changes are in the sample amplitude, the MSB phase will be a constant value of π, showing that the modulation due to pure speed oscillation is close to the phase modulation process.

4.6 Sideband Estimator using MSB

Because a motor current signal with electrical and mechanical faults contains a series of sideband components which appear mainly around the supply component, a bispectrum slice at the supply frequency will be sufficient to characterise these sidebands for fault detection and diagnosis. By setting f_2 in Equation 4.6 into a constant frequency value such as the fundamental $f_2 = f_s =$50 Hz, MSB slice at supply frequency can be expressed as [33, 92, 101]:

$$MSB(f_{1,}f_{\mathrm{s}}) = E\{X(f_{\mathrm{s}} + f_1)X(f_{\mathrm{s}} - f_1)X^*(f_{\mathrm{s}})X^*(f_{\mathrm{s}})\} \qquad (4.11)$$

In fault diagnosis it is the amplitude of the sideband or modulator that is useful for both detection and diagnosis. However, the magnitude of $MSB(f_{1,}f_{\mathrm{s}})$ from Equation 4.6 or Equation 4.11 is a combination of sideband and supply components. The diagnostic results will be influenced by the amplitude at supply frequency, i.e. the results are too sensitive to load conditions [31].

Considering that the amplitude of supply frequency is predominant in current signals and it can be identified easily in the frequency domain, an MSB slice based sideband estimator, abbreviated as MSB-SE, can be introduced as [33, 92, 101]

$$\text{MSB-SE}\left(f_{1,}f_{\mathrm{s}}\right) = E\left\{X\left(f_{\mathrm{s}}+f_1\right)X\left(f_{\mathrm{s}}-f_1\right)\frac{X^*(f_s)}{|X(f_{\mathrm{s}})|}\frac{X^*(f_s)}{|X(f_{\mathrm{s}})|}\right\} \qquad (4.12)$$

To calculate the combined effect of sidebands only, but not the carrier at the supply frequency, because the magnitude of $X^*(f_s)/|X(f_s)|$ is unity, in the form of magnitude-phase, the sideband estimator is[31]:

$$\text{MSB-SE}\left(f_{1,}f_{\mathrm{s}}\right) = E\{|X(f_{\mathrm{s}}+f_1)||X(f_{\mathrm{s}}-f_1)|\}e^{j\emptyset_{MSB}(f_1,f_{\mathrm{s}})} \qquad (4.13)$$

Displaying that the phase information of $f_s$still taken into account in the estimation process and hence the noise suppression property is well maintained by MSB-SE.

Equations 4.12and 4.13 show that the magnitude of MBS-SE peaks is determined purely by the magnitude product of sideband components. It means that the product of two symmetrical sidebands$|X(f_s+f_1)||X(f_s-f_1)|$ is equal to either$|X(f_s-f_1)||X(f_s-f_1)|$ or $|X(f_s+f_1)||X(f_s+f_1)|$in the PS expression of Equation 4.2 provided that the two sidebands have the same amplitude and the signal is noise free. This shows that the unit of MSB-SE has the same unit as that of PS and hence they can be compared easily [33].

However, the amplitude from Equation 4.12 or Equation 4.13 is obtained by including phase effects which highlights components with the same phases, and suppress any components with phase inconsistency such as random noise. On the other hand, the sideband amplitude from PS includes noise influences because the estimation of power spectrum does not take into account phase information [101].

In addition, MSB-SE can also have its coherence function to confirm the coupling effects between sidebands and carrier and to check the degree of random noise influence, which allows confirmation of the existence of SMS-SE peaks for the detection of modulation process in noise measurements.

According to Gu et al[1]and Equation (4.12), MSB-SE coherence can be obtained by [33, 92, 101]

$$b^2_{MSB-SE}(f_1, f_s) = \frac{|BMS-SE(f_1,f_2)|^2}{E\{|X(f_1+f_s)X(f_1-f_s)|^2\}} \qquad (4.14)$$

4.7 Summary of Chapter 4

This chapter reviews Higher-Order Statistics (HOS) and its relation to conventional second-order statistics. The first and second-order statistics, for instance, mean, variance, autocorrelation and power spectrum, are accepted signal-processing implements and are used widely in data analysis. Particularly, second-order statistics are suitable for describing Gaussian and linear processes. In practice, there are many situations where the processes deviate from Gaussianity and linearity and then more advanced technique is used such as bispectrum.

In this chapter the bispectrum is used to display the induction motor current signals. Due to a motor current signal with electrical and mechanical faults contains a series of sideband components which appear mainly around the supply component, a bispectrum slice at the supply frequency will be sufficient to characterise these sidebands for fault detection and diagnosis.

The phase of conventional bispectrum (CB) applied to signals is not independent of signal segments used. This means that an average process in estimating CB will lead to an uncertain result. Instead, it will change with segment sequences used in an extreme case, CB magnitude will be close to zeroes if the phases of data segments distribute uniformly between 0 and 2π Therefore, CB is not suitable for analysing motor current signals. To improve the performance of CB in characterising the motor current signals.

To extract additional components caused by motor faults in current signals, a new MSB-SE estimator can be applied for obtaining a more accurate measure of the modulation. MSB-SE analysis is particularly effective as it takes into account the sideband phase information and results in a more accurate estimation of the sideband magnitudes by suppressing the random noise influences from the motor operation and the measurement process.

CHAPTER 5

INDUCTION MOTOR FAULT SEEDING AND TEST FACILITY

This chapter details the test rig facility and fault seeding for the experimental study of induction motor current. It starts by describing the test rig components and the main specifications of the motor. It then explains the instrumentation of the current measurements. Finally, the chapter describes motor fault seeding by explaining each fault.

5.1 Test System

Figure.5.1 shows the test rig facilities which used by [138] to develop and test an accurate and sensitive Micro – Electro Mechanical Systems (MEMS) wireless accelerometer suitable for application to a rotating shaft. The test rig employed in this research to examine induction motor faults.

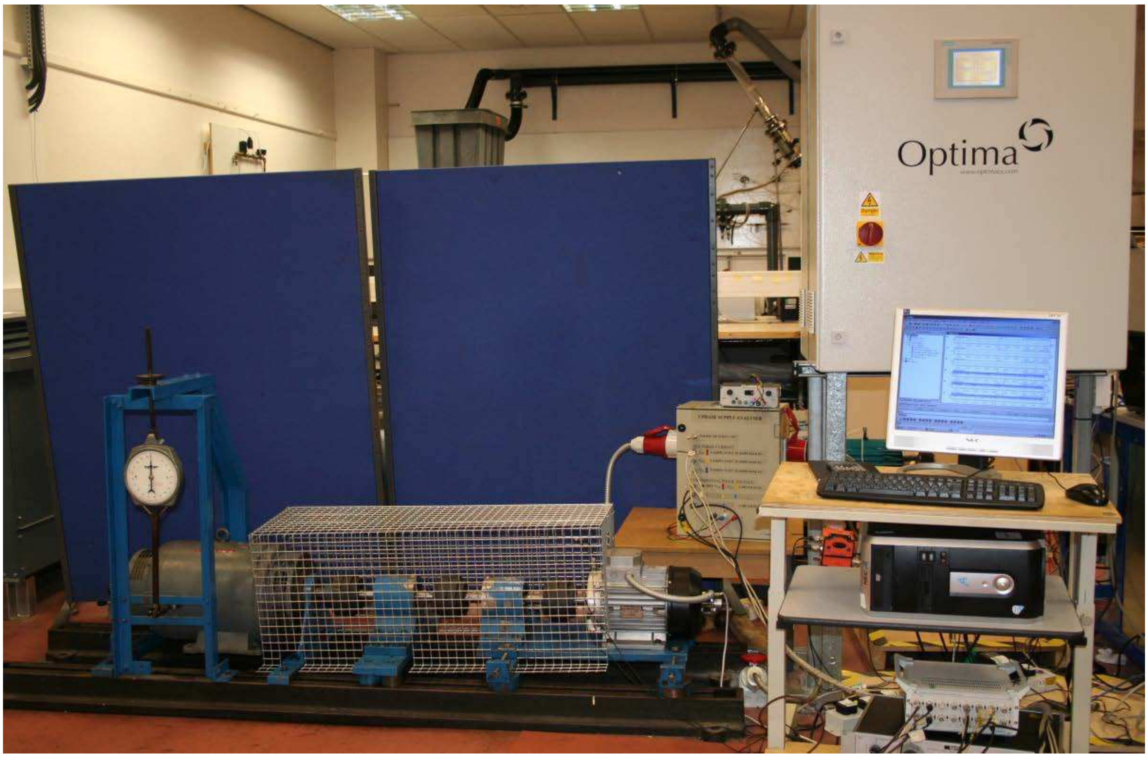

Figure 5.1-Photo of the Induction Motor Test Facility Used [138]

The system consists of an induction motor, variable speed controller, supporting bearings, couplings and DC generator as a load. The test motor is a three-phase induction motor with rated output power of 4 kW at speed 1420 rpm (two-pole pairs), 28 rotor bars and 36 stator slots. The schematic diagram of the test facilities used in this research is shown in Figure 5.2 [32].

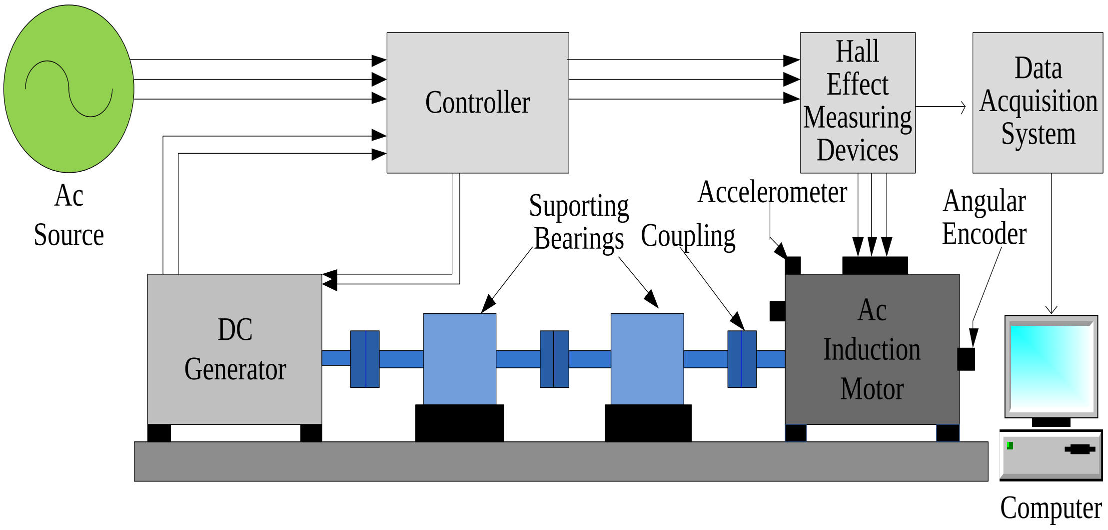

Figure 5.2-Schematic of the Induction Motor Test Facility [32]

Rated voltage (Δ/Y)	230/400 V
Rated current (Δ/Y)	15.9/9.2 A
Motor power	4 kW
Number of phases	3
Number of poles	4 poles/phase
Supply frequency	50 Hz
Motor rated speed	1420 rpm
Number of stator slots	36
Number of rotor bars	28
Power factor	0.8

Table 5.1-Induction Motor Specification

The details of the induction motors placed into the test facility are presented in Table5.1. It can be seen that relatively small, low-voltage, motors were used.

A total of six motors were purchased with identical name-plate specifications at an approximate cost of £200 each. These motors were labelled sequentially so that the source of any data collected could later be identified. As a result, the first motor which was used in a healthy motor and open circuit test was marked in (M1), while the second motor that was used in a half broken rotor bar was labelled in (M2), motor (M3) was for one broken bar, motor (M4) was for two broken bars, motor (M5) was for a short circuit test; finally the last motor (M6) was used as a motor bearing test.

5.2 Instrumentations

Ten measurement parameters were regularly recorded from the induction motor test facility, so that their relative potential in facilitating condition monitoring could be investigated. Each parameter was measured by a different type of measurement transducer. Every transducer was connected to a data acquisition system via coaxial BNC cables, which are high quality and provide low noise levels, and produced a voltage output corresponding to the amplitude of the measured parameter.

5.2.1 Current and Voltage Transducers

Figure 5.3 shows the power supply measurements box, which was designed to measure motor voltages and currents using voltage and current transducers shown in Figure 5.3. Every transducer produced a voltage output corresponding to the amplitude of the measured parameter, and was connected to the data acquisition system (DAS).The inputs of the measurement box are the three line voltages and currents while the outputs are the three line voltages and currents.

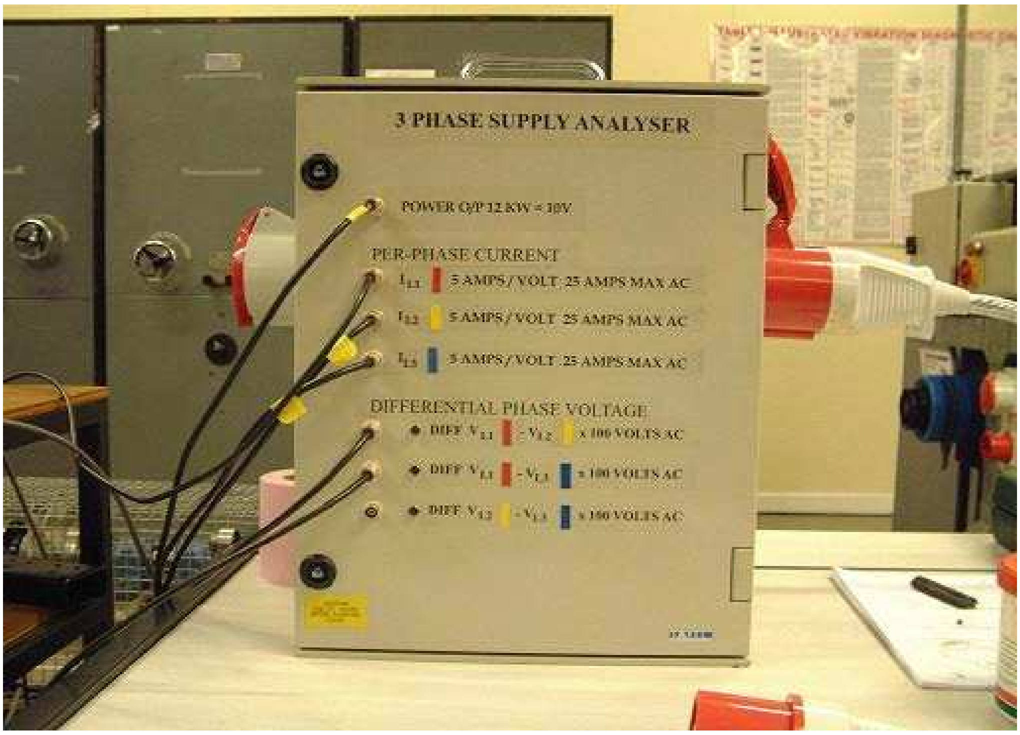

Figure 5.3-Power Supply Measurements Box

Phase current A connected to DAS through Channel 9 while phase B and Phase C were connected to channel 10 and channel 11 respectively. Similarly, Phase voltage A, B and C were connected to DAS through channels 12, 13, 14 respectively.

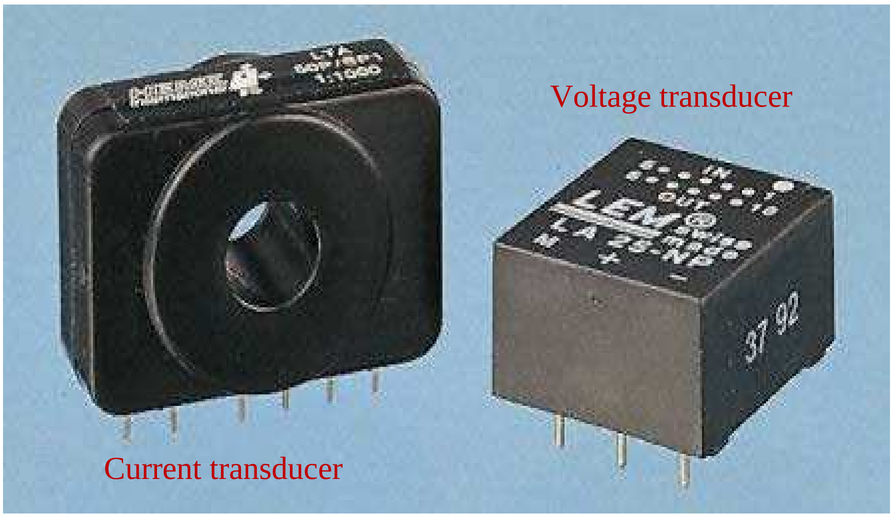

Figure 5.4-Current and Voltage Transducers

Electrical current signals of the testing motor in three phases were measured by a hall-effect sensor with a linear frequency response from DC to 4 kHz and measurement range 0 to 25A, which allows the content in a wide frequency range, especially around the supply fundamental of 50Hz, to be measured accurately. Figure 5.4 shows the Hall Effect current and voltage transducer which used in this research.

5.2.2 Accelerometers

To confirm the motor bearing fault characteristics the accelerometers mounted on the bearing end-caps to measure vibration of the motor casing. They were placed horizontally and vertically on the drive and were each connected to the data acquisition system (DAS). Figure 5.2 shows the accelerometers and their places on the motor where accelerometer (A) measures the vertical motor vibration while accelerometer (B) measures the horizontal motor vibration. Accelerometer (A) has a sensitivity 5.106 mv/ms-2 which connected to DAS via channel 3, while accelerometer (B) a sensitivity 4.960 mv/ms-2 which connected to DAS via channel 4.

5.2.3 Shaft Encoder

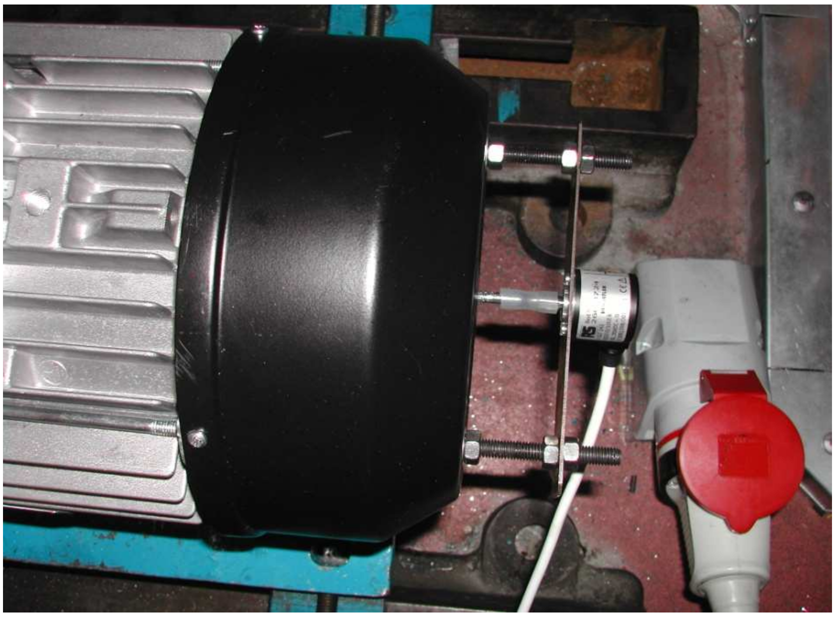

Figure 5.5-Hengstler Shaft Encoder

The device measures instantaneous angular speed (IAS) which can be achieved by analysis of its data and an average speed of the motor shaft. The measurement produced a square pulse output every angular degree and 100 square pulses every complete revolution. Figure 5.5 shows Hengstler shaft encoder which was connected to shaft rotor by a torsional rigid rubber coupling. The outputs of the encoder connected to DAS by channel 1 and channel 2.

5.3 Induction motor fault seeding

5.3.1 Rotor Fault Seeding

The typical failure mechanism is a breakage or cracking of the rotor bars where they join the end-rings which can be due to thermal or mechanical cycling of the rotor during operation. This mode of failure is common in many industrial applications. The broken bar results in severe vibration and declines accelerating torque. When the rotor bar cracks, it overheats around the crack due to losses. The broken bar may affect the adjacent bars also, and this can happen during the start operation with any given load, so that the adjacent bars carry higher current and then higher thermal stresses will occur. The high thermal stresses may lead to damage of the rotor laminations. The rotor failures are accounted for about 10% of all electrical machine faults [139-142].

Three BRB cases with different BRB severities and one baseline case were tested under the same operating conditions. As illustrated in Figure 5.6(a), the first BRB case is a motor with half BRB which was created by drilling a hole into one of the 28 bars up to the half depth of a bar. The second is one complete bar breakage created by drilling the hole to the full depth of the bar. And the third is two continuous bar breakage which was induced by drilling two bars side by side to their full depth as shown in Figure 2 (b). These three fault cases were induced in three different motors with the same specifications as shown in Table 5.1 and they were tested to have close baseline signatures before the faults were created on their rotors.

(a) Rotor with One Bar Broken (b) Rotor with Two Bars Broken

Figure 5.6-Illustrative photos for Broken Rotor Bar Fault Seeding

5.3.2 Stator Fault Seeding

5.3.2.1 Open Circuit Fault Seeding

One of the most common faults in the electrical motors is the inter-turn short circuit in one of the stator coils. Many researchers presented this mode of stator fault [16, 143, 144].They modified the stator circuit by joining tapes on the windings across a selected number of turns after that connected an external resistance to the tapes terminals [145].This fault is usually cause by contaminants, abrasion, vibration or voltage surge. The turn-to-turn failures lead to the reduction of the resistance between two winding turns in the same phase. This research presents the stator faults which are based on the motor design. As a result the motor test has a stator winding connection as shown in Figure 5.7. As can be seen from the figure, the stator windings consist of three conductors which connected in parallel winding.

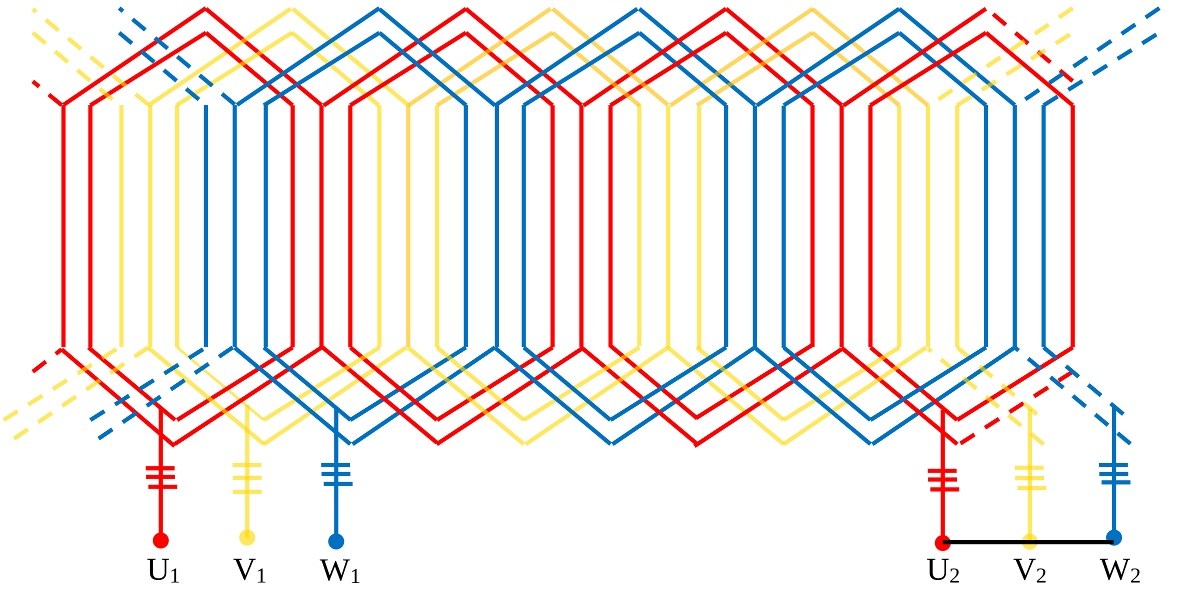

Figure 5.7-Stator winding connections

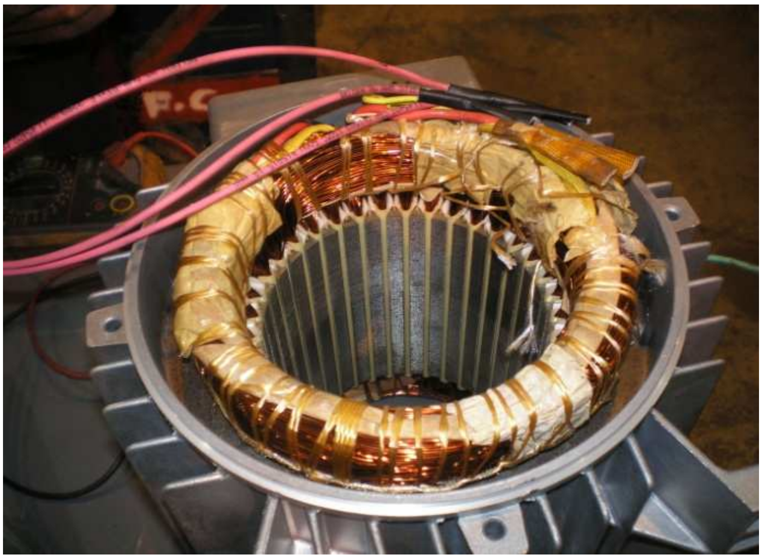

Figure 5.8-Soldered Tappings into One Phase

To seed this fault, insulation of copper of three conductors was scraped-off at the end of the same phase of an end stator winding and then a length of additional wire was soldered to each of these points, and these joints were subsequently reinsulated as can be seen in figure 5.8. The three wires were sent to the other terminal box, this box was fixed on the motor (see Figure 5.9). This work was made by Lawton Electrical Services LTD (LESL).

The terminal box contains a main phase supply and three conductors of the phase were marked by points 4, 5 and 6. The phase supply came from main box of the motor.

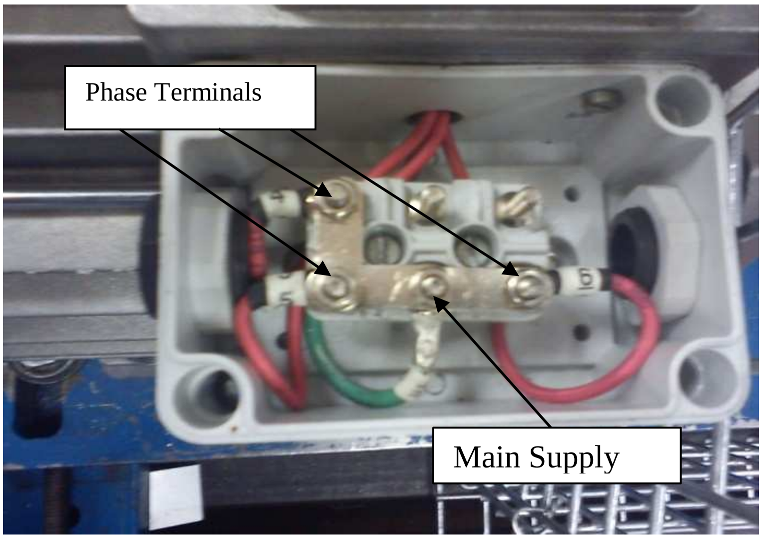

Figure 5.9-Terminal Connection Box

In order to simulate the mode of fault, points 4 and 5 were connected to the main supply while point 6 was out. In this condition the resistance of the phase increased to 1.5 times of normal situation resistance (in health condition R_s=1.4Ω).

Other fault of stator windings can be simulated in this research by connecting point 4 only while points 5 and 6 were out. This means that the resistance of the phase increased three times over the health condition.

5.3.2.2 Short Circuit Fault Seeding

To evaluate the performance of spectrum analysis, current signals were collected under two different stator winding configurations: firstly a healthy motor; two inter turn short circuit in first coil in phase A under two successive load conditions: zero and 25% of full load. This allows the diagnostic performance to be examined at different loads and avoid any possible damages of the test system at the full load when the faults are simulated as shown in Figure 5.10.

Figure 5.10-Two-turn Shorted in First Coil of Phase A

5.3.3 Bearing Fault Seeding

Two types of common bearing faults have been tested in this research. Both bearings are rolling ball bearings, type 6206ZZ deep groove ball bearing measuring 30x62x16mm, with nine balls (N_b=9),D_b=9.52mm and D_p=46.0 mm, which used to support the rotor .The first one, an abrasive wear in the outer race has been considered; which models that caused by friction between ball and outer race surfaces due to lack of lubrication as shown in Figure 5.11(a), while the second case of fault is an inner race defect as shown in Figure 5.11(b).

(a) Outer race fault

(b) Inner Race Fault

Figure 5.11-Illustrative Photos for Motor Bearing Fault Seeding

To analyse the current signals, a dataset is acquired in a motor rig under different seeded fault cases and operating conditions.

5.4 Data Acquisition System

Figure 5.12 shows theYE6232B from Global Sensor Technology, a high-performance data acquisition system (DAS) used in the laboratory for capturing and analysing experimental data.

Figure 5.12-Global Sensor Technology YE6232B DAS

This type of DAS is capable of analysing data in different ways such as time domain or frequency domain via a Fast Fourier Transform. It was only used for data acquisition and recording. More complicated signal processing techniques were carried out using MATLAB. During the data acquisition process, the number of data points and the sampling frequency were set to 1920000 points and 96 kHz respectively. For such setting the required time to collect this length of data is found to be twenty seconds [127, 134, 146, 147].

The YE6232B data acquisition system holds the following main features [148]:

- A 24-bit A/D parallel data acquisition system based on USB 2.0 interface,
- Voltage/IEPE input; 16 channel, built-in programmable gain amplifier and real-time digital filters,

- Supporting smart transducers (IEEE1451.4),
- Supporting multi-equipment cascading connection; suitable for multi-point testing,
- Built-in programmable gain amplifier and anti-filtering,
- Sampling frequency can be chosen by the software and varies from 375 Hz to 96000Hz.

Table 5.2 shows detailed specifications of DAS.

DAQ system manufacturer	Global Sensor Technology YE6232B
Number of Channels	16 (selectable)
A/D Conversion resolution	24 bit
Sampling rate (maximum)	96kHz per channel, Parallel sampling
Input range	±10 V
Gain	×1, ×10, ×100
Filter	Anti-aliasing
Interface	USB 2.0
Dimensions (mm)	426W×88H×300D(H)
Software	YE7600 General test & analysis software
Weight	4 Kg

Table 5.2-Technical Specifications of the DAS [148]

5.5 Data Acquisition Control Software

YE7600 is general purpose data acquisition, conditioning and analysis software. It supports all instruments manufactured by SINOCERA and allows set up parameters for sampling, conditioning data format and signal sources. It has highly efficient data storage and fast data conversion to other formats such as MATLAB, Excel, etc., [149]. It is capable of time-domain analysis as well as frequency-domain. YE7600 contains various sampling triggers: manual, signal, hardware and from the waveform showing on the screen. The channels to be sampled could be set according to choice; the refreshing speed of the screen waveform is adjustable [149].

5.6 Experimental Setting

The research was carried out based on a laboratory setup. The choice of laboratory experimental was in addition to the cost, due to the ability to control the environmental and unknown variables. Additionally, laboratory work setting allow to replicate different type of faults within nearly the same conditions. The results from this experimental research study can be generalised as the equipment used for the study were industrial and real type. Almost all equipment used are made for real industrial applications [150]. Hence the results from this research study can be generalised to the 4Kw AC induction motor.

The experiment was performed on baseline, broken rotor bar, stator faults and motor bearing faults by using test rig which discussed in section 5.1. Different loads were used to investigate the system behaviour under these conditions. The test was carried out by setting up the steps which are displayed on the screen of control panel (see Figure 5.13).

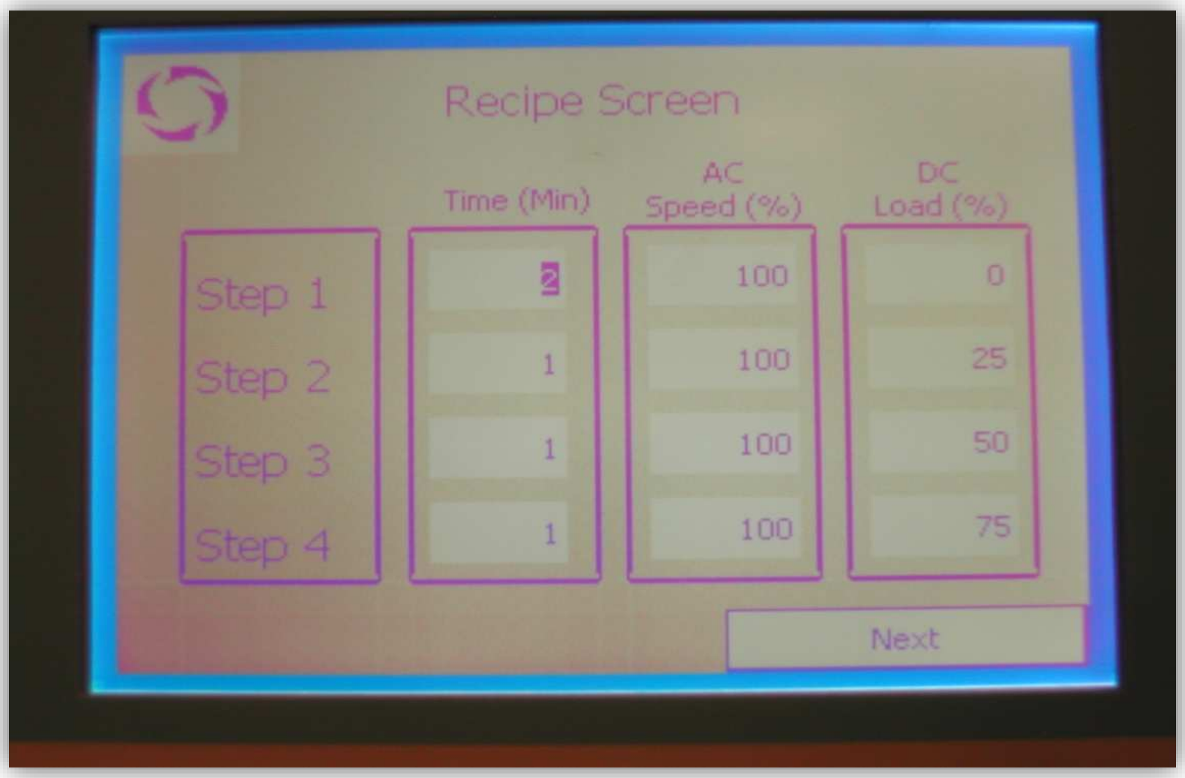

Recipe Screen

	Time (Min)	AC Speed (%)	DC Load (%)
Step 1	2	100	0
Step 2	1	100	25
Step 3	1	100	50
Step 4	1	100	75

Figure 5.13-Control Panel Screen

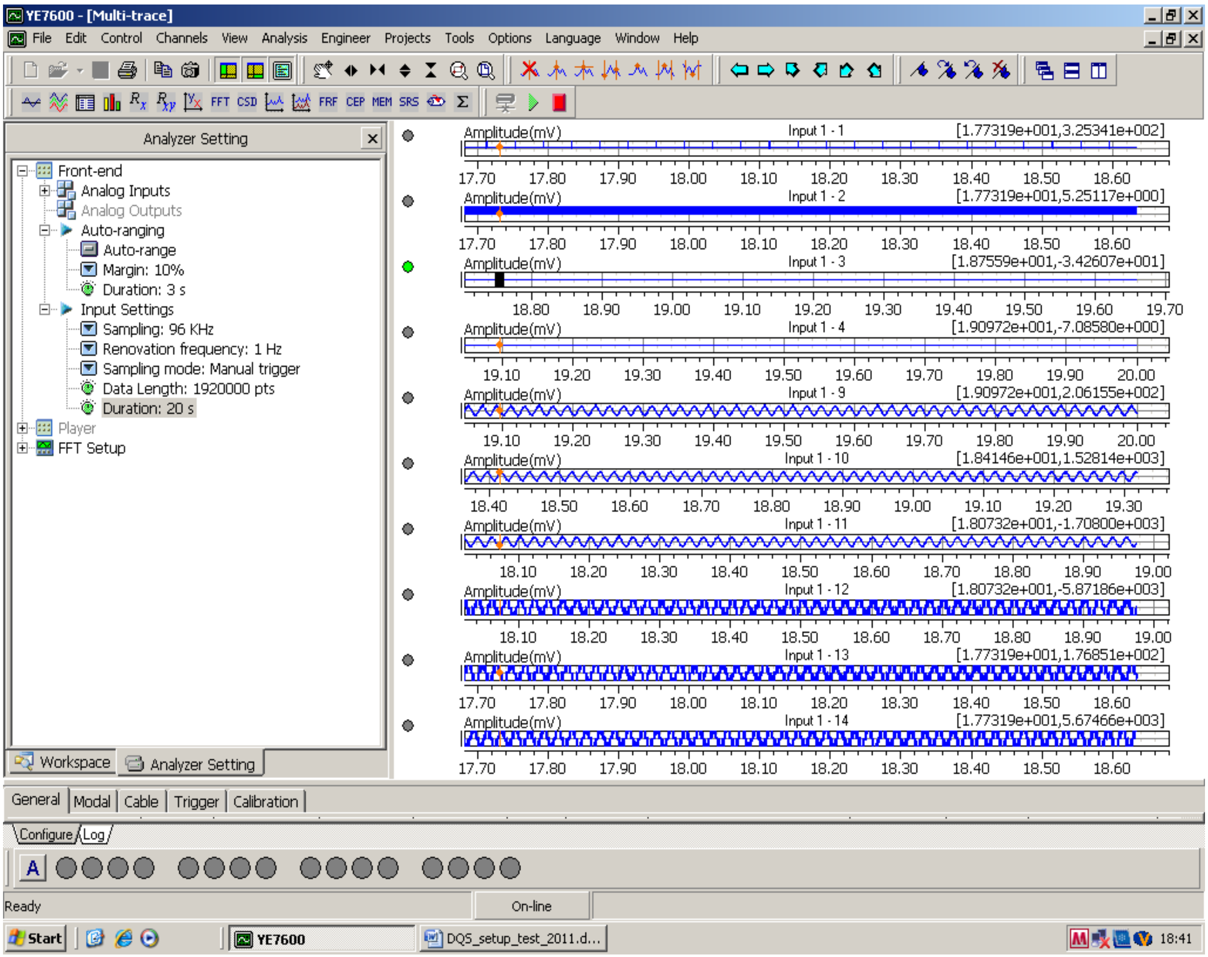

YE7600 - [Multi-trace]

Analyzer Setting

- Front-end
  - Analog Inputs
  - Analog Outputs
  - Auto-ranging
    - Auto-range
    - Margin: 10%
    - Duration: 3 s
  - Input Settings
    - Sampling: 96 KHz
    - Renovation frequency: 1 Hz
    - Sampling mode: Manual trigger
    - Data Length: 1920000 pts
    - Duration: 20 s
- Player
- FFT Setup

Input 1 - 1 [1.77319e+001,3.25341e+002]

Input 1 - 2 [1.77319e+001,5.25117e+000]

Input 1 - 3 [1.87559e+001,-3.42607e+001]

Input 1 - 4 [1.90972e+001,-7.08580e+000]

Input 1 - 9 [1.90972e+001,2.06155e+002]

Input 1 - 10 [1.84146e+001,1.52814e+003]

Input 1 - 11 [1.80732e+001,-1.70800e+003]

Input 1 - 12 [1.80732e+001,-5.87186e+003]

Input 1 - 13 [1.77319e+001,1.76851e+002]

Input 1 - 14 [1.77319e+001,5.67466e+003]

Ready

On-line

Figure 5.14-Raw Data Acquired from the Test Rig

Ten parameters (two speeds of encoder and three voltages, two vibration signals and three currents) were measured and recorded regularly from the induction motor test facility, so that their relative usefulness in effective CM could be investigated. In each test the raw data was acquired and displayed on a computer monitor in a form of plots as shown in Figure 5.14. This allows examining the data before storing it.

To examine the influence of the operating condition on fault diagnosis performance, electrical current signals were measured under loads: 0%, 25%, 50% and 75% of the full operating load. In addition, to perform a sufficient number of averages in MSB estimation and obtain reliable results, data acquisition for each operation was repeated at least three times.

The MSB program has been developed by one of the research groups in the Centre for Efficiency and Performance Engineering (CEPE) at the University of Huddersfield [1]. Part of this research includes the development of this algorithm as to improve its detecting performance and the capability of calculating the sidebands across the fundamental supply frequency. The developed algorithm referred to as Modulation Signal Bispectrum based on Sideband Estimation (MSB-SE).

All of the measurements were sampled simultaneously with a high speed data acquisition system at a sampling rate of 96 kHz per channel. This high rate ensures that the speed obtained by the encoder is of sufficient accuracy for slip estimation. The system has a data resolution of 24bits. With this high dynamic data range the small components due to modulation and the large components at supply frequency can be measured concurrently. Moreover, a data length of 20 seconds was acquired for each acquisition in order to achieve a good average in calculating MSB while maintaining sufficient frequency resolution.

5.7 Summary of Chapter 5

This chapter presented the test facilities and relevant instrumentation that would be used in data acquisition as well as induction motor faults which seeded in the lab.

The test motor is one of the most commonly used in industry. Although the motor is set in the test lab the motor faults were seeds as real and at real conditions as accurately as possible. As a result the results achieved form the test can be similar to that results got in industry. On the test rig, transducers and instrumentation are mounted which are capable of collecting some common types of signals for general analysis purposes.

The power supply measurements box, which was designed to measure motor voltages and currents using voltage and current transducers. Every transducer produced a voltage output corresponding to the amplitude of the measured parameter, and was connected to the data acquisition system (DAS). A Hengstler shaft encoder which was connected to shaft rotor by a torsional rigid rubber coupling to measure motor speed and then motor slip. To confirm the motor bearing fault characteristics the accelerometers mounted on the bearing end-caps to measure vibration of the motor casing. They were placed horizontally and vertically on the drive and were each connected to the data acquisition system (DAS). All of these sensors have a high sensitivity and frequency response range so that they can be suitable for the research purpose of this work.

The test rig was developed in the lab to examine induction motor faults. The system consists of an induction motor, variable speed controller (VFD), supporting bearings, couplings and DC generator as a load. The test motor is a three-phase induction motor with rated output power of 4 kW at speed 1420 rpm (two-pole pairs), 28 rotor bars and 36 stator slots. The induction motor is fed by a variable frequency drive to control motor speed using open loop control. Six motor tested under different motor faults such as broken rotor bar, stator faults and motor bearing fault and results were compared by baseline.

Sinocera YE6232B data acquisition system was used to analyse motor current and motor vibration signals. The data acquisition system is supported by general purpose YE76000 software for data acquisition, conditioning and analysis as part of the data acquisition system. This software allows the user to set up parameters for data acquisition and it converts data to Matlab format. Additionally and records all data at a sampling rate of 96 kHz. The Data export to the computer and analyse it by Matlab.

A Matlab code was developed to calculate current power spectrum PS, conventional bispectrum CB and modulation signal bispectrum MSB. The current signals were processed under baseline, broken bars and stator faults and at zero, 25%, 50% and 75% of full load. Finally all motor fault data was compared with baseline.

CHAPTER 6

EXPERIMENTAL RESULTS

This Chapter reports the analysis of the motor data collected using conventional methods and the MSB technique developed by the author to determine whether it is suitable for use with induction motor condition monitoring. The results presented include baseline tests under conventional methods such as amplitude spectrum and power spectrum. Additionally, the chapter presents the effects of motor temperature on the current signal. After that it provides some comparisons between conventional bispectrum and modulation signal bispectrum under broken bar case in 3D graphs. Finally it presents comparison results of motor current using PS and MSB-SE under different motor health. The result shows that MSB-SE has a better capability than PS for induction motor fault diagnosis.

6.1 Effect of Motor Temperature on Motor Slip

To show the motor temperature effects on motor slip, a k-type 100 mm long mineral insulated plug mounted probe is connected to the motor as shown in Figure 7.1

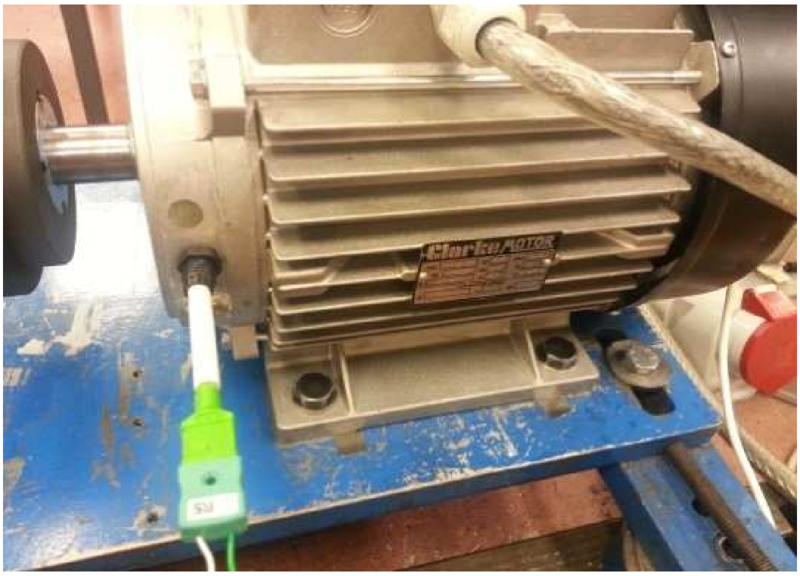

Figure 6.1-Temprature Sensor Connected to the Motor

The temperature sensor measures the air temperature around the stator windings and the rotor bars.

The relationship between motor slip and motor temperature can be determined by [151]

$$s_s = s_t \frac{(t_s+k_1)}{(t_t+k_1)} \tag{6.1}$$

where s_s is the slip corrected to specified stator temperature t_s, s_t is the slip measured at stator winding temperature t_t, t_s is the specified temperature which is based on the class of the insulation system (see [151]for more details), t_t is the observed stator winding temperature during load test, and the constant k_1 is 225 for aluminum rotor conductors.

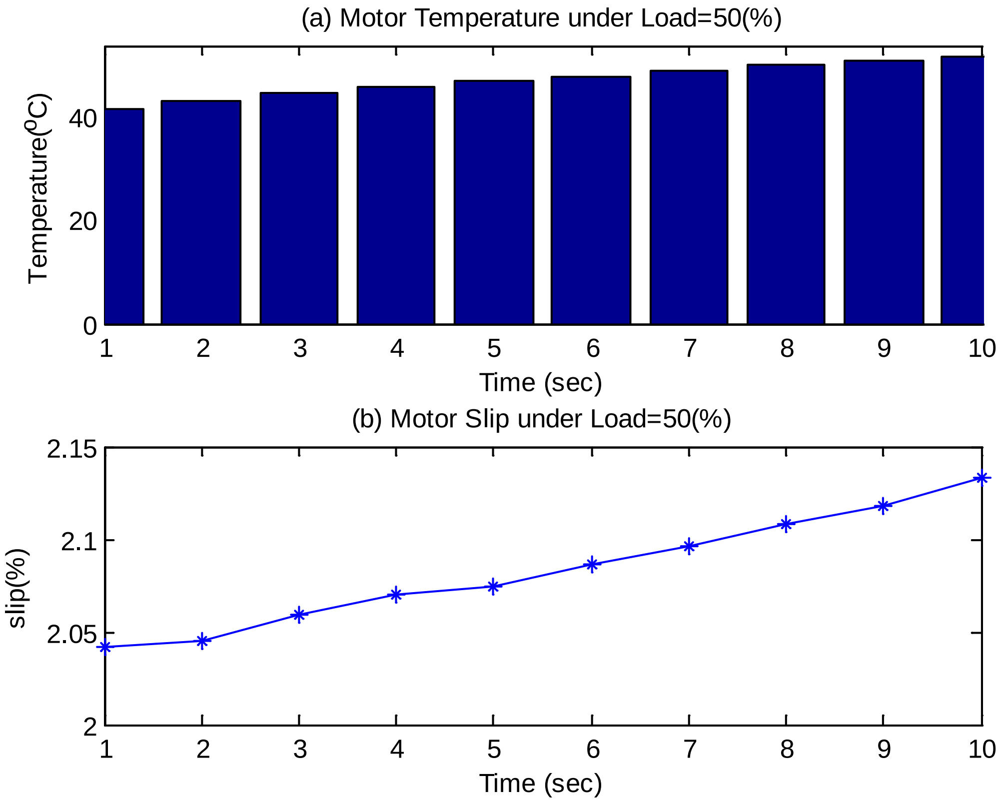

Figure 6.2-Healthy Motor Temparature and Slip under 50% Full Load

To demonstrate the relationship between slip and temperature of the induction motor, motor temperature test was performed in the lab. The healthy motor ran at full speed and 50% full load for ten minutes and data was collected each minute as shown in Figure 6.2.

Figure 6.2(a) shows motor temperature collected under 50% load for the healthy motor in ten minutes. The temperature gradually increases during the test. The motor slip shown in Figure 6.2(b) increases as well.

6.2 Baseline of Current Spectrum

6.2.1 Baseline Power Spectrum

Figure 6.3 shows three-phase current spectra under different load namely zero, 25%, 50% and 75% full load and at 100% full speed. As can be seen from the figure all phase currents are identical. Therefore, only one phase was used to detect all induction motor fault detection which was presented in this thesis.

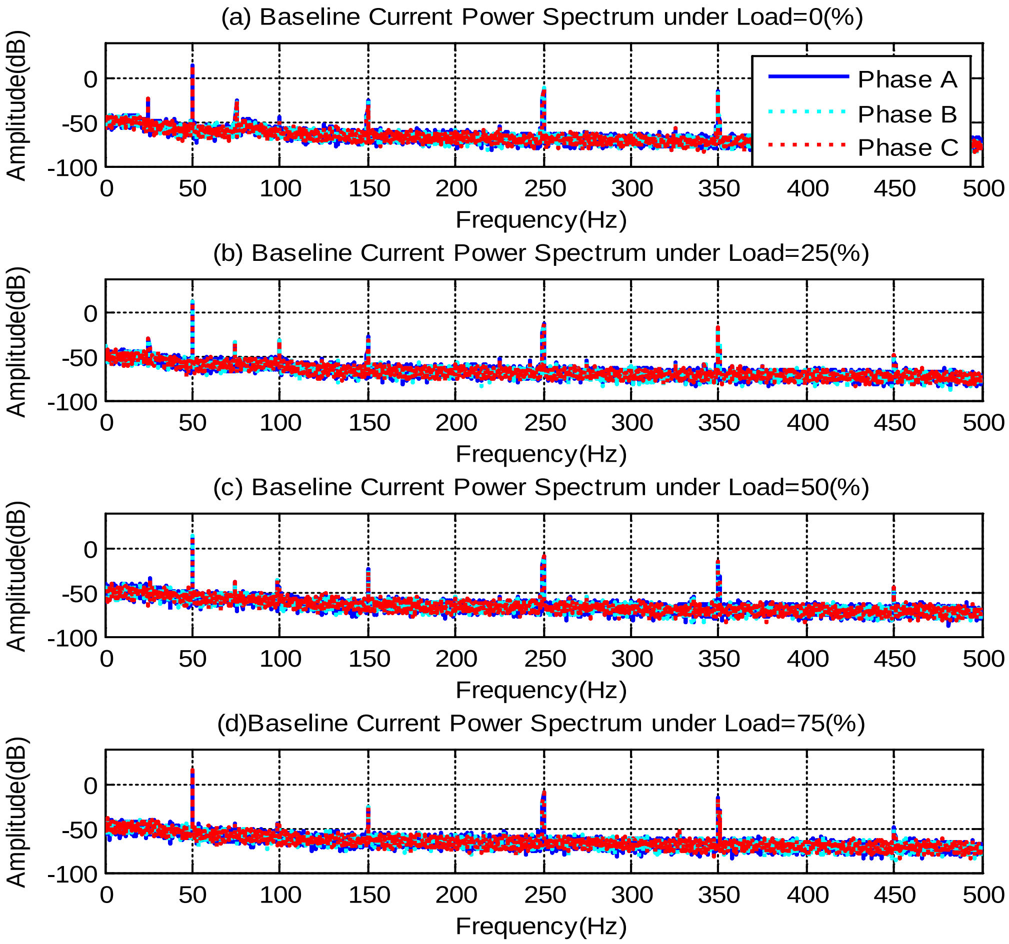

Figure 6.3-Current PS under Different loads and Healthy Condition

6.2.2 Baseline of Current MSB-SE

Figure 6.4shows a typical MSB for current signal under 75% of the full load when the motor is healthy. As shown in Figure 6.4(b) the 50Hz supply component in the power spectrum is eliminated completely in MSB. This makes easier and more reliable to examine components that relate to motor heath conditions. For example, the sideband components: (50-3.4)Hz and (50+3.4)Hz around the 50Hz shown by power spectrum of Figure 6.4(b), arisen by rotor asymmetric errors, are combined into a single bispectral peak at frequency 3.4 Hz, which is much easier to be identified and hence MSB allows a significant reduction of the efforts in spectrum analysis.

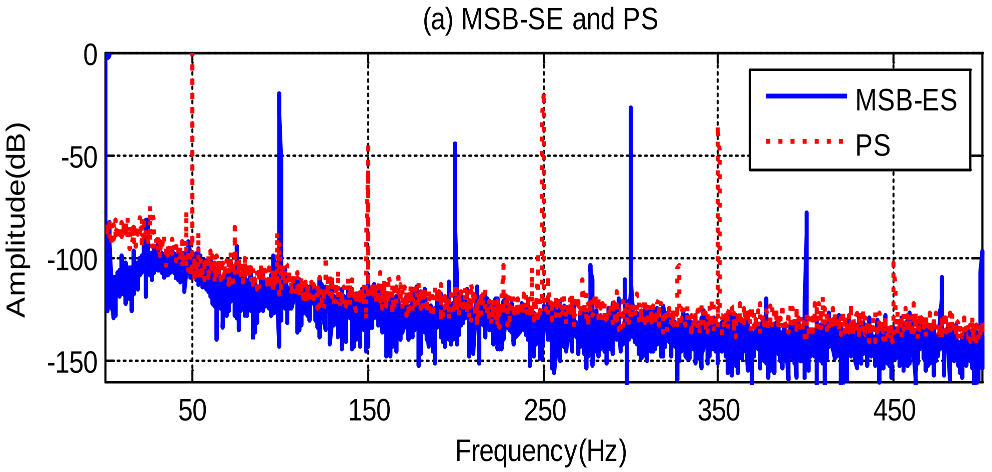
(a) MSB-SE and PS

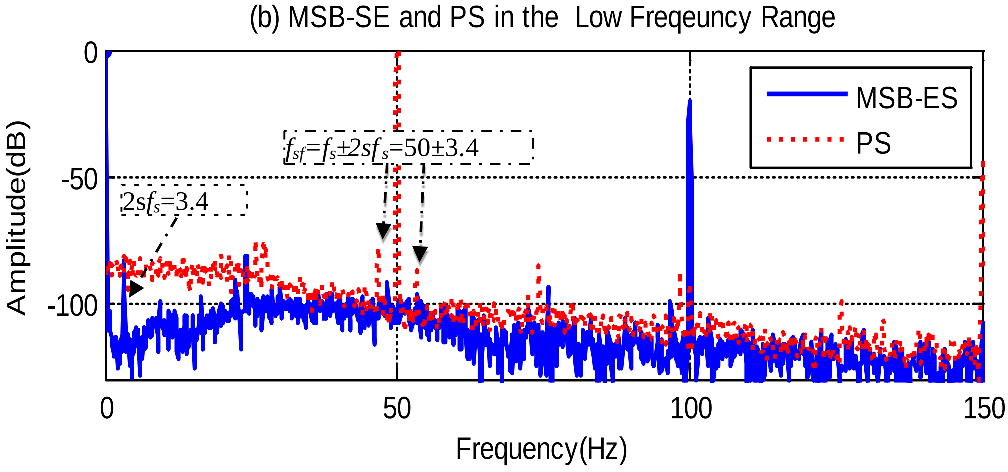
(b) MSB-SE and PS in the Low Freqeuncy Range

Figure 6.4-MSB-SE and PSSpectrum Characteristics For Baseline Motor

Moreover, MSB-SE shows very good performance in noise reduction. Comparing it with power spectrum, as shown in Figure.6.4 (a), it can be found that the spectrum noise floor is about a 10dB lower than that of power spectrum. This makes spectral peaks such as that due to rotor faults in the high frequency range to be estimated more accurately and hence to obtain more accurate and better diagnostic results.

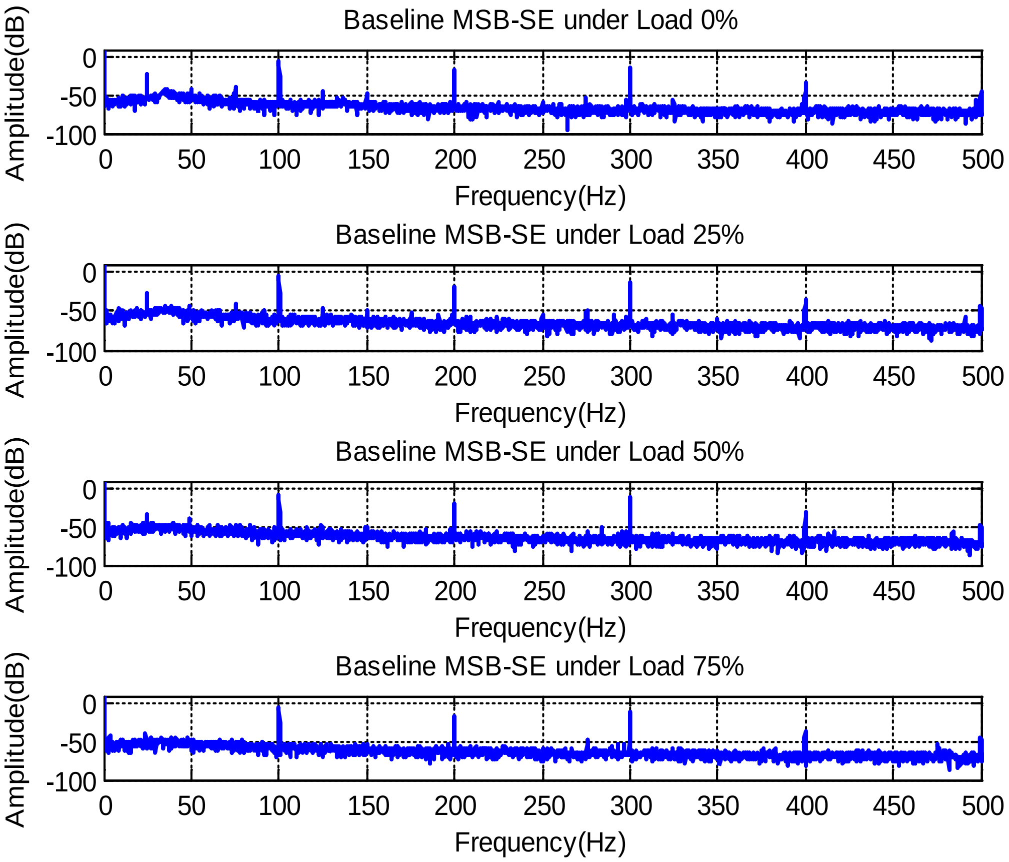

Figure 6.5-Current MSB-SE under Different loads and Healthy Condition

Figure 6.5 shows phase current MSB-SE under zero, 25%, 50% and 75% of full load and at 100% full speed after taking slice at 50 Hz. As can be seen from Figure 6.5 the 50Hz supply component in the power spectrum is eliminated completely in MSB. This makes easier and more reliable to examine components that relate to motor heath conditions.

6.3 Detection and Diagnosis of Broken Rotor Bar in Induction Motors

6.3.1 Experimental Evaluations

In order to evaluate motor current signals behaviour in frequency domain (see Appendix A for more details on motor current analysis in time domain), the three analysis methods, three different datasets are processed to obtain MSB-SE, CB and PS simultaneously for comparisons. In calculating DFT, a Hanning data window is applied to the data segment to minimise the side lobes of DFT and spectrum leakage. In addition, a 40% overlap between segments is used; the number of averages is set to more than 100, in order to effectively suppress noise and interference. Moreover, a single Matlab function is developed to calculate PS, CB and MSB simultaneously according to Equations 4.2, 4.3 and 4.12 respectively, which ensures their performance to be compared under the same base. The results of CM and MSB are examined within a frequency range from 0 to 80Hz, which is common for detection rotor faults, and are presented as a proper surface graphs to give effective representation of the key features in the results.

6.3.2 Influence of Slip-Compensation

6.3.2.1 Detection under Non-slip Compensation

Figure 6.7 shows phase current spectrum under different load and at 100% rated speed with non-slip compensation under healthy and one broken rotor bar condition. The computed values of lower sideband frequencies under broken bar condition were50.51, 51.39, 52.40and 53.54Hz, while the upper sideband frequencies were 49.49, 48.61, 55.02, 47.60 and 46.46 Hz and under zero, 25%, 50% and 75% rated load, respectively.

As can be seen from Figure 6.6the detection of the slip frequency sidebands at no-load (and also at little loads) is too difficult, since the current in the rotor bars is small. The most expressive results were obtained at great loads, especially near the rated load.

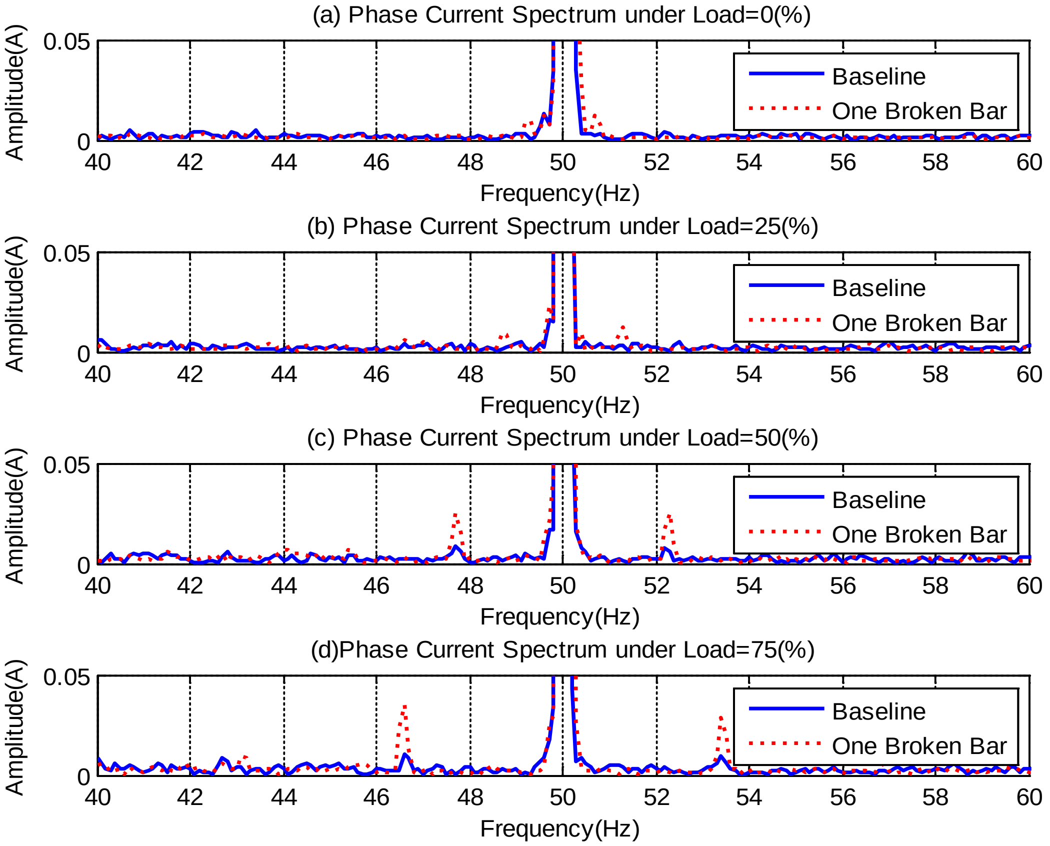

Figure 6.6-Phase Current Spectra with Non-slip Compensation

	Healthy Motor						One Broken Bar					
Load	f_s (Hz)	f_r (Hz)	Lower sideband	Upper sideband	Slip (s)	$2sf_s$	F_s (Hz)	F_r (Hz)	Lower sideband	Upper sideband	Slip (s)	$2SF_s$
0%	50	24.88	49.53	50.46	0.005	0.50	50	24.87	49.49	50.51	0.005	0.50
25%	50	24.67	48.67	51.33	0.013	1.30	50	24.65	48.61	51.39	0.013	1.30
50%	50	24.41	47.65	52.35	0.024	2.40	50	24.40	47.60	52.40	0.024	2.40
75%	50	24.13	46.53	53.47	0.035	3.5	50	24.11	46.46	53.54	0.035	3.50

Table 6.1-Test Results of Healthy and One Broken Bar with Non-slip Compensation

Table 6.1 shows the test results speeds for the healthy motor and one broken bar with non- slip compensation. The shaft speeds are changing at different loads. For instance the motor shaft speeds are 24.88 Hz (1493 rpm) and 24.13 Hz (1448 rpm) at zero and 75% rated load, respectively.

6.3.2.2 Detection under Slip Compensation

The slip compensation technique of speed control does not monitor the actual shaft speed for speed adjustment; relatively, it uses drive output current transducers to monitor the current drawn by the motor and alters the main frequency so that the motor speed can maintain desired speed as steady as possible. However, because of inevitable load fluctuations the main supply frequency realised in this way will have some fluctuations accordingly, or it is not as stable as that without slip compensation.

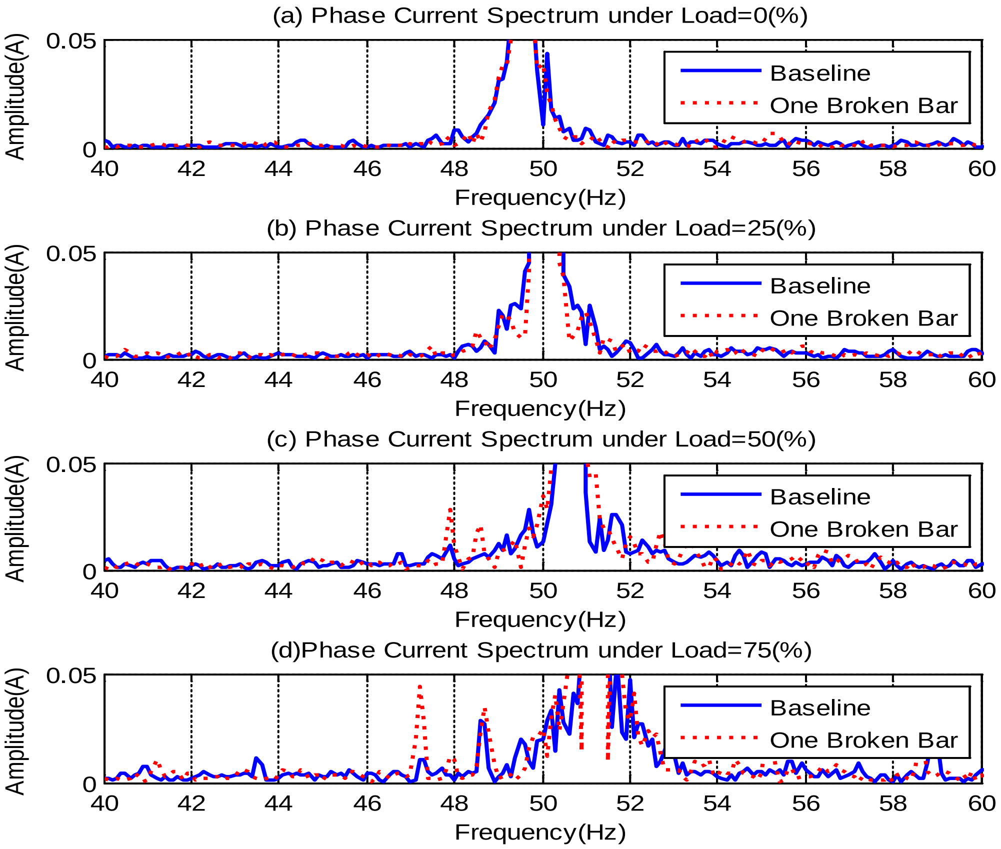

Figure 6.7-Phase Current Spectra with Slip Compensation

Figure 6.7 shows phase current spectra under different load and at 100% rated speed with slip compensation under healthy and broken rotor bar condition. The computed values of lower sideband frequencies under broken bar condition were47, 41, 47, 46.38 and 45.73 Hz, while the upper sideband frequencies were 51.79, 53.20, 55.02, and 56.67 Hz and under zero, 25%, 50% and 75% rated load, respectively.

It seems clear that from the figure, the speeds are consistent at different load. For example the motor shaft speeds were 1455 rpm and 1454 rpm at zero and 75% rated load, respectively. Therefore the results showed the advantage of variable frequency drive with slip compensation.

On the other hand the current spectrum cannot show the frequency sidebands with slip compensation technique. This is because of the harmonics that appear on current spectrum. To avoid this problem other technique has open loop with nonslip controller was used in this thesis.

Table 6.2 shows the test results speeds for the healthy motor and one broken bar with slip compensation and under different loads.

	Healthy Motor						**One Broken Bar**					
Load	F_s (Hz)	F_r (Hz)	Lower sideband	Upper sideband	Slip (S)	$2SF_s$	F_s (Hz)	F_r (Hz)	Lower sideband	Upper sideband	Slip (S)	$2SF_s$
0%	49.5	24.57	48.74	50.39	0.008	0.82	49.5	24.23	47.40	51.67	0.022	2.13
25%	50.1	24.59	48.27	51.92	0.018	1.82	50.1	24.26	46.94	53.26	0.032	3.16
50%	50.6	24.60	48.83	53.37	0.027	2.77	50.6	24.26	46.41	54.86	0.042	4.22
75%	51.2	24.65	47.04	55.36	0.041	4.16	51.2	24.22	45.70	56.70	0.054	5.50

Table 6.2-Test Results of the Healthy and One Broken Bar with Slip Compensation

6.3.3 Characteristics of MSB-SE and CB

Figure 6.8 presents typical MSB results under two broken bars. As it can be seen in Figure 6.8(a) MSB-SE shows a distinctive peak at bifrequency (3.4,50)Hz in the bispectrum domain. Clearly, this peak is relating to $2sf_s$ and can be relied on to detect and diagnose BRB. In addition, this peak is also distinctive in MSB-SE coherence in Figure 6.8(c), confirming that it is from modulation processes between $2sf_s$ and f_s.

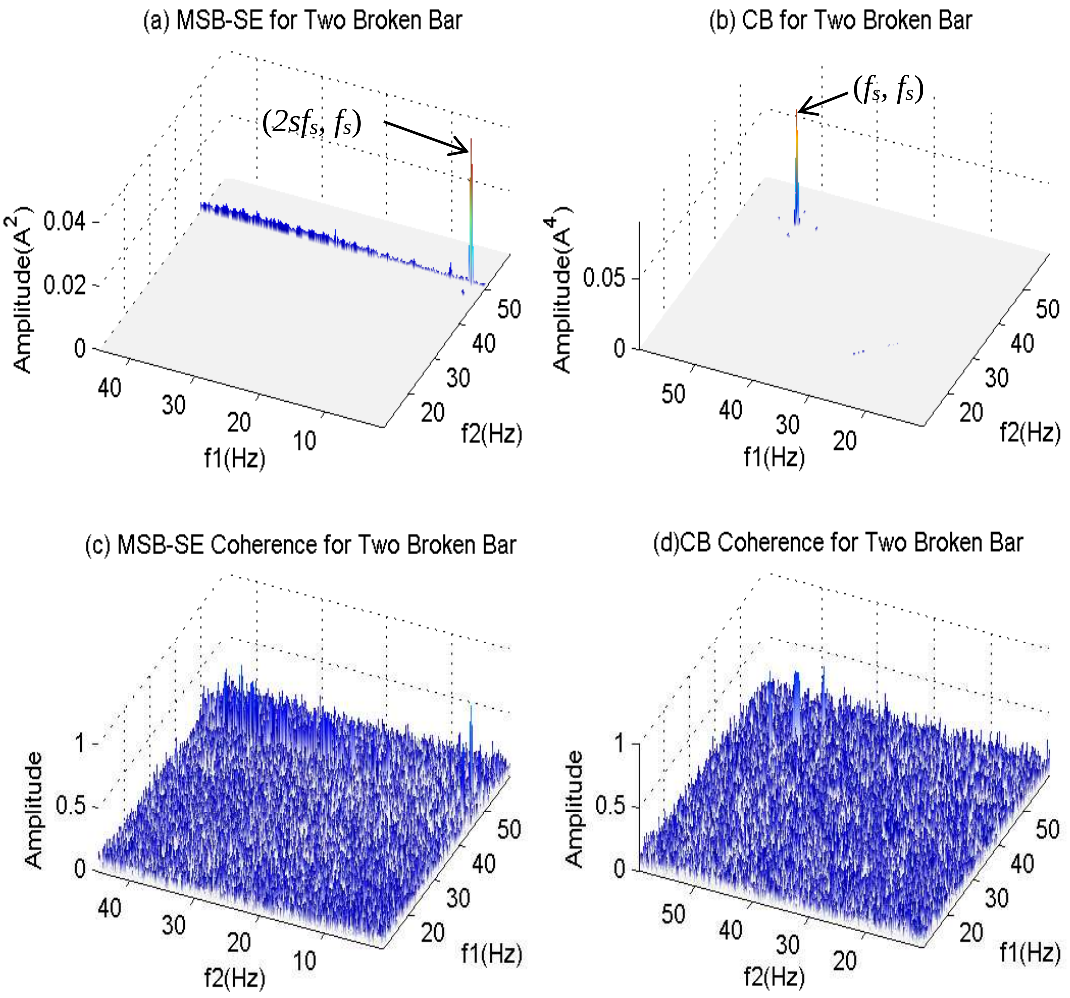

Figure 6.8- Characteristics of MSB-SE and CB for a Two Broken Bar Case at75% Load

On the other hand, the CB in Figure 6.8(b) shows a single peak at bifrequency (50, 50) Hz. This frequency does not show any connections to BRB at $2sf_s$. Moreover, CB coherence in

Figure 6.8(d) is predominated by background noise in the whole domain of interest. It means that the peak at (50, 50) Hz is not from real nonlinear coupling, but is due to the very high amplitudes at 50Hz in the original signal. For more details on MSB-SE and CB feature more results were shown in Appendix B.

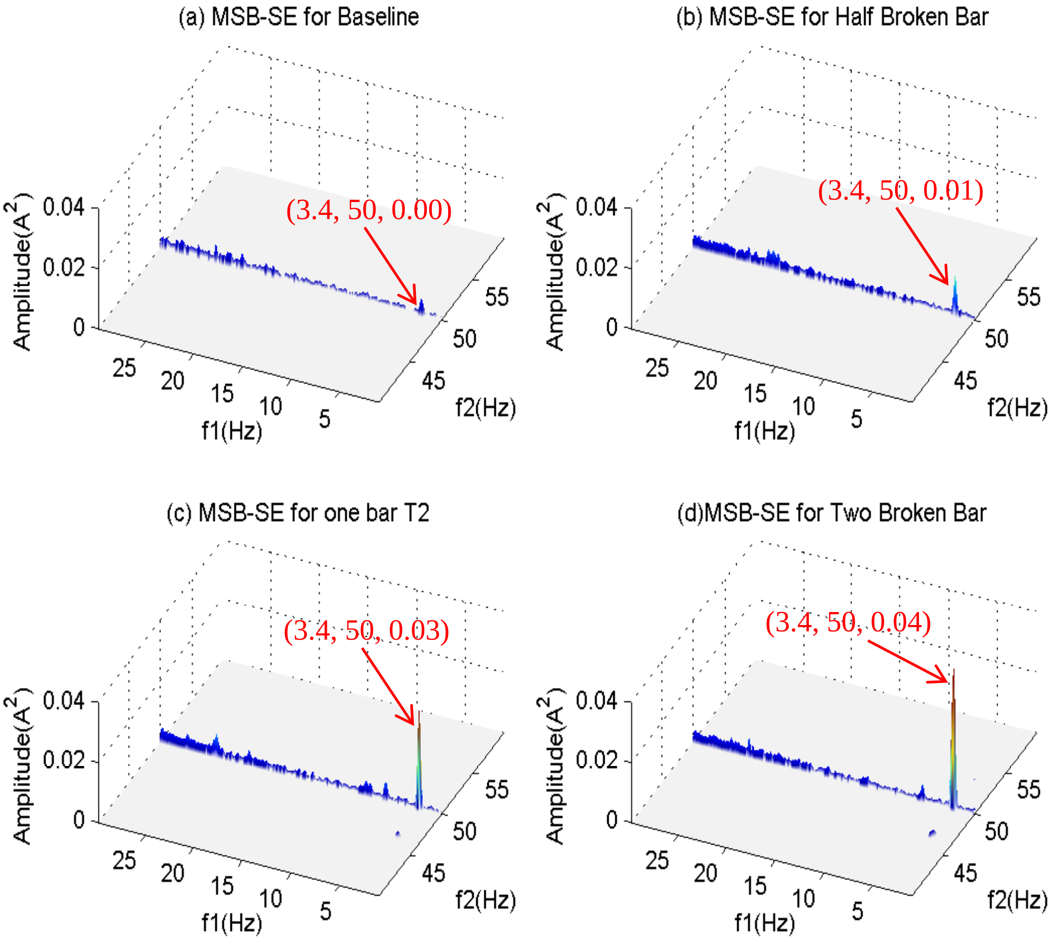

Figure 6.9-MSB-SE for Baseline Motor and BRB Cases under 75% of Full Load

Figure 6.9 shows the MSB-SE results for the four cases, presented with z-axis magnified to show the small peaks of the small faults. The three coordinates in the figure denote $f1$, $f2$, MSB values respectively. It can be seen that that the characteristic MSB-SE peaks at the bifrequency of $(2sf_s, f_s)$= (3.4, 50) Hz for the baseline is relatively small. Its existence is because of the inherent rotor asymmetry arisen from the manufacture process. Comparatively, the half BRB show a very significant peak at the bifrequency of (3.4, 50) Hz, allowing it to be differentiated easily from the baseline. Moreover, the magnitude for all the four cases increases monotonically with the fault severity.

6.3.4 Broken Rotor Bar Diagnosed By PS

Typical stator current PS are shown in Figure 6.10 for the current signals from different loads and motor health cases. It is clear that from the figure, the peaks appear at characteristic frequency ($f_s \pm 2sf_s$). As a result the amplitude of Ps increase as fault severity increases and load increases.

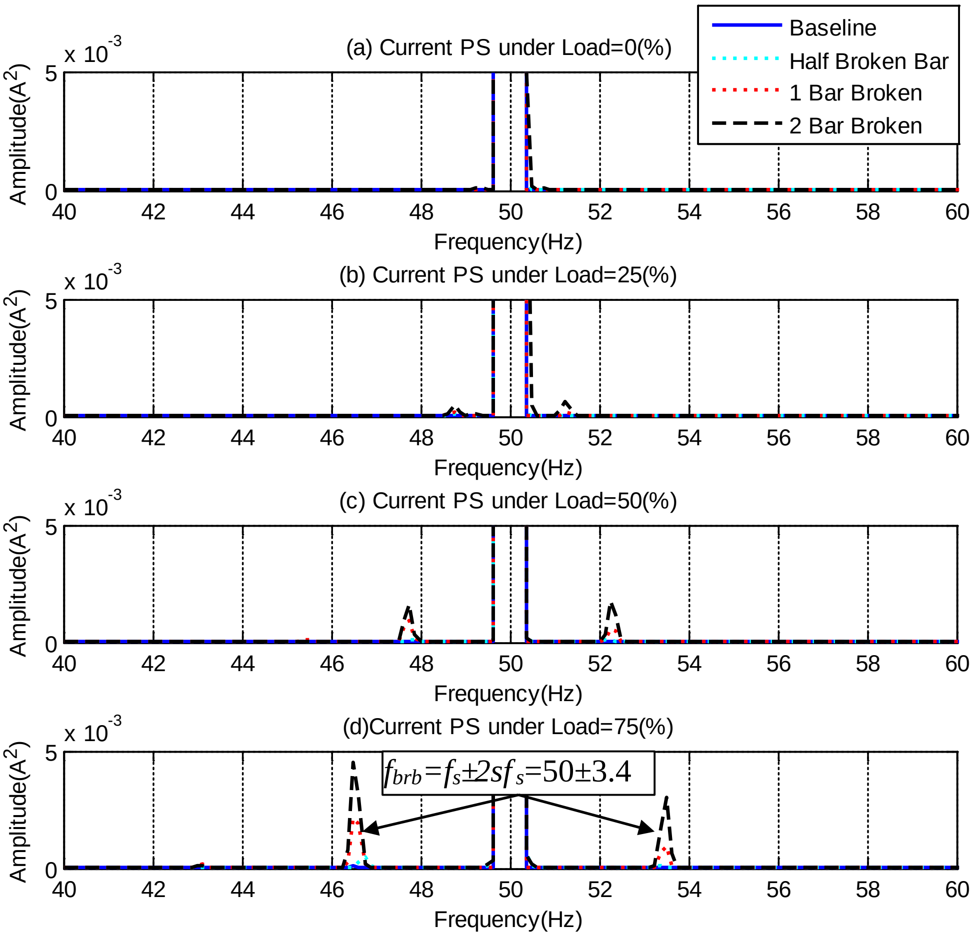

Figure 6.10-Current PS for baseline and Rotor Broken Bar Cases

6.3.5 Broken Rotor Bar Diagnosis by MSB-SE

Figure 6.11 shows the MSB-SE results for the four cases, presented with slice at 50Hz to compare the result with PS. It can be seen that that the characteristic MSB peaks appear at the bifrequency of($2sf_s$)for all broken bar condition and at 25%, 50%, 75% of full load. Moreover, the magnitude for all the four cases increases monotonically with the fault severity.

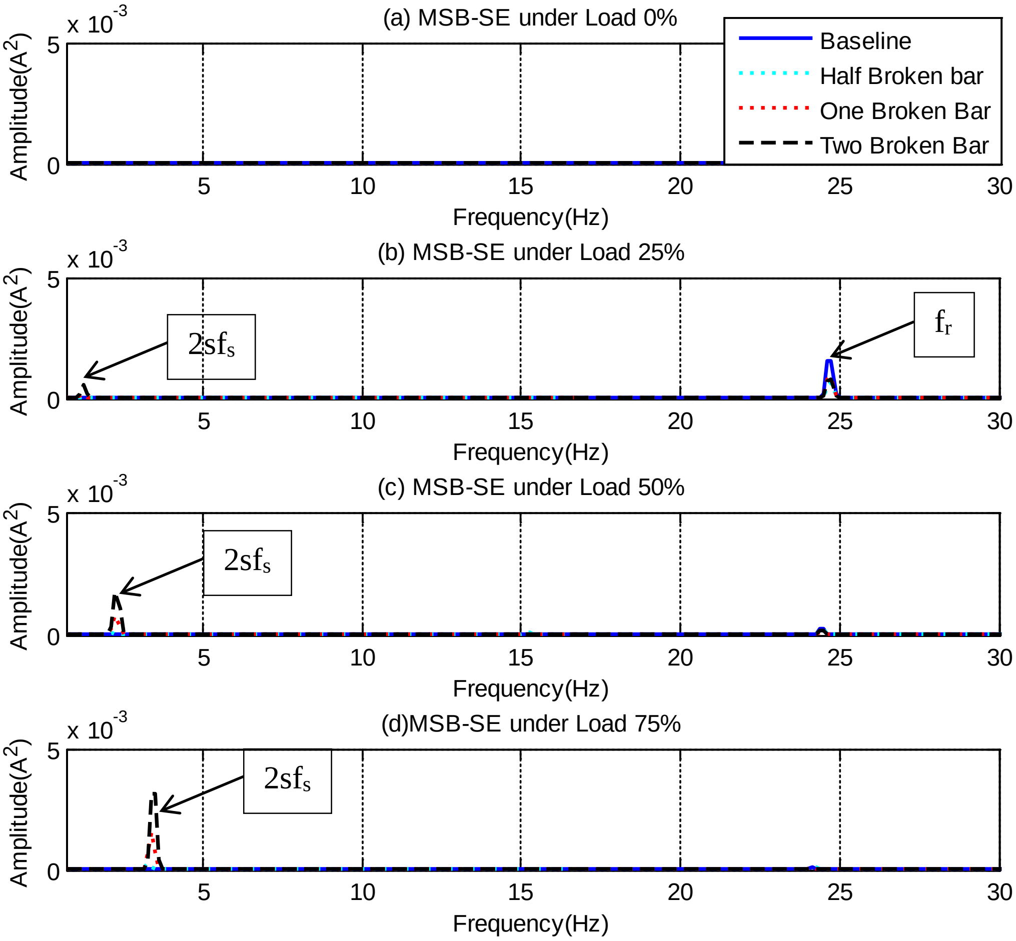

Figure 6.11-Current MSB-SE for Baseline and Rotor Broken Bar Cases

The quality of MSB-SE peaks can be further assessed by their corresponding coherences. As shown in Figure 6.12 the MSB-SE under baseline and different broken bar cases. Coherence values at the characteristic bifrequency ($2sf_s$) which have amplitude near one. This means that

MSB-SE amplitude estimation have a very high accuracy and thus confirms the reliability of BRB detection and diagnosis.

In addition the coherences show a peak at bifrequency (f_r), due to shaft speed fluctuations.

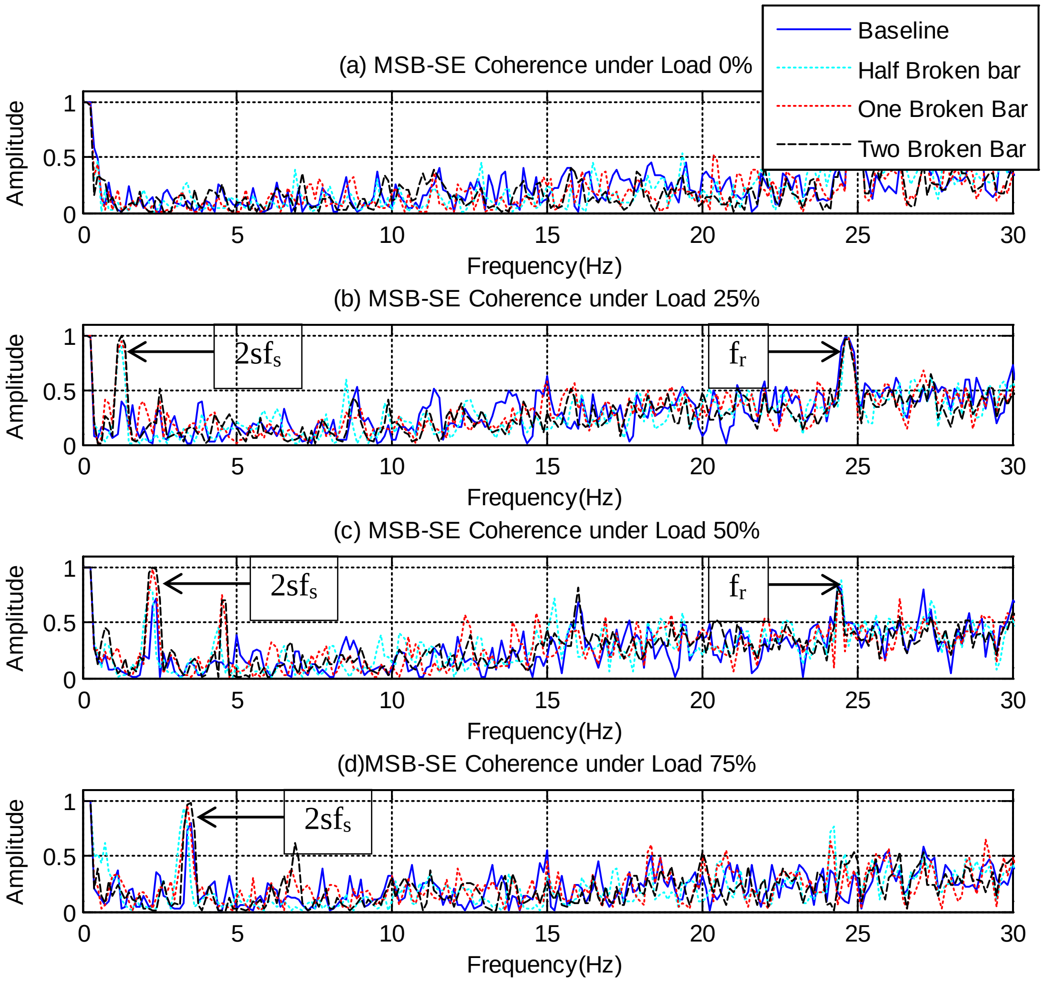

Figure 6.12-MSB Coherences for Baseline Motor and BRB Cases

6.3.6 Comparison between MSB and PS for Broken Bar Detection

To show the capability of MSB in suppressing random noise for measured signals, a comparison is made between MSB-SE and PS based on the same data sets above. Figure 6.13 shows an MSB-SE which is plotted on top of the PS by a frequency shift mirrored about 50Hz. As seen in the graph, the floor noise level of MSB-SE is nearly 10dB lower than that of PS in the frequency range from 0 to 10Hz. Because of the good noise suppression capability, the higher order harmonics of $2sf_s$ can be resolved much more easily. Similarly, the components at f_r and even $2f_r$ can be identified without any difficulty. However, there may be a problem in identifying $2f_r$ by PS because the peak at $(f_s - 2f_r)$ is invisible due to high noise level. This demonstrates that MSB has a good noise reduction capability, which leads to a more accurate amplitude of the modulating components. In addition, Figure 6.13 also shows that MSB-SE produces a sparse representation of current spectrum. It makes the identification and extraction of fault components much easier and more reliable.

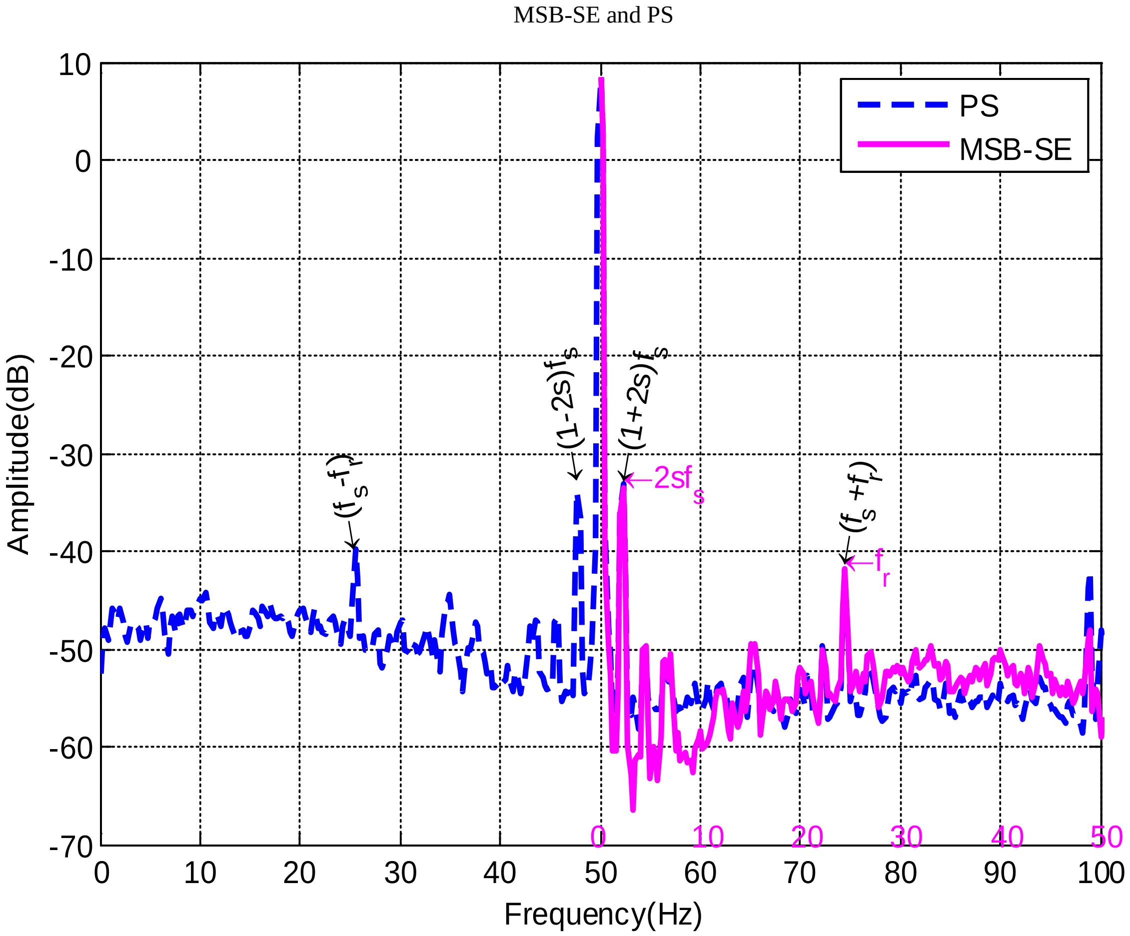

Figure 6.13-Comparison between MSB-SE and PS for Two Broken Bar under 50% Load

6.4 Detection and Diagnosis of Stator Faults

To show the performance of MSB bispectrum in analysing current signals, a dataset is acquired in a motor rig under different simulated fault cases and operating conditions as shown in Figure 5.1 and Figure 5.2. The system consists of an induction motor, variable speed controller, supporting bearings, couplings and DC generator as a load. The test motor is a three-phase induction motor with rated output power of 4 kW at speed 1420 rpm (two-pole pairs) and 28 rotor bars. To change the speed of the testing motor, a digital variable speed controller is attached to the test rig between the power line source and the motor. The controller can be programmed to any specific shaft rotation speed between 0 and 1500rpm. The induction motor is directly coupled with a loading DC generator. The field of the generator is connected to a DC source through controller while the generated power was fed back to the mains electrical grid and the load in the induction motor can be adjusted by changing the field resistance of the DC generator. The operating load can be varied from no load to full load via the control panel.

A power supply measurement unit is designed to measure instantaneous AC voltages, currents and power, using hall-effect voltage and current transducers and a universal power cell. A shaft encoder, mounted on the shaft end produces 100 pulses per revolution for measuring the motor speed.

During tests all the data was acquired using a GST YE6232B high speed data acquisition system as shown in Figure 5.13. This system has 16 channels, each with a 24 bit analogue-digital converter at a maximum sampling frequency of 96 kHz, which allows the details of the 50Hz component, the high order supply harmonics, rotor bar pass frequency, stator bar pass frequency to be recorded for further analysis.

6.4.1 Detection and Diagnosis Open Circuit in the Stator Winding

To evaluate the performance of MSB analysis under open circuit in stator windings, current signals were collected under three different stator winding configurations: healthy motor, one coil removal and two-coil removal under four successive load conditions: zero, 25%, 50% and

75% of full load, which allows the diagnostic performance to be examined at different loads and avoid any possible damages of the test system at the full load when the faults are simulated.

The dataset is processed off-line by using a Matlab program which implements FT calculation to obtain both power spectrum using Equation 4.2 and MSB-SE using Equation 4.12 simultaneously. During the calculation it uses a rectangular FT window of the same size for both power spectrum and MSB-SE, which results in a frequency resolution of 0.125Hz, and the same average times (100 times), so that they can be compared directly in their performance of identifying fault characteristic frequencies and quantifying spectral peaks. In addition, a MSB slice only at 50Hz is presented for direct comparison because this slice gives full information about the modulation characteristics.

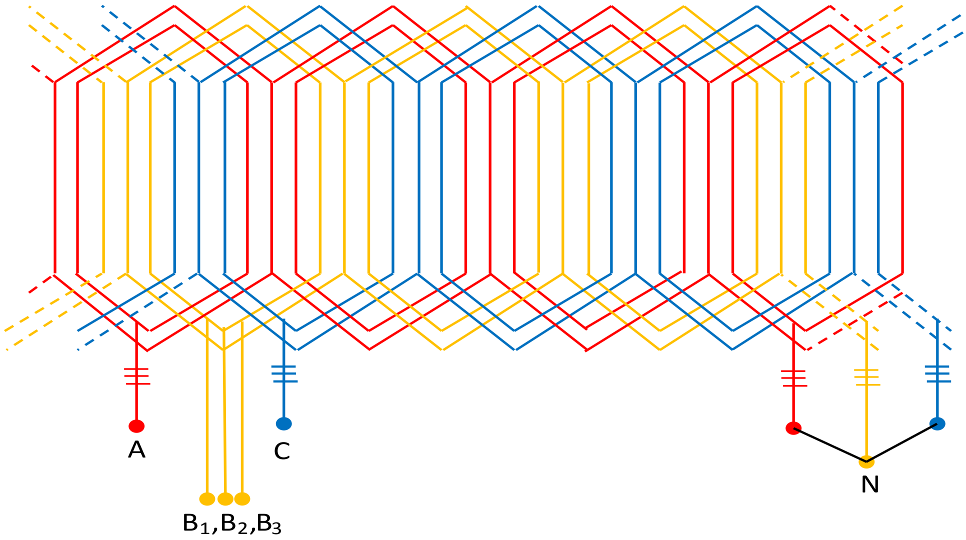

Figure 6.14-Schematic of Stator Fault Seeding in Phase B

As shown in Figure 6.14, there are three parallel coils in each phase. By reconfiguring the terminals of the phase terminals, it allows rewiring the three coils in phase B in three different ways: supply to B1-B2-B3 for the healthy case, supply B1-B2 for the case of one coil removal which represents a smaller fault and supply to B1 only for two conductor removal which represents a larger fault. Obviously, these coil removals could be a simulation of asymmetric stator which will increase the motor equivalent impedance and hence degrade motor performance.

6.4.1.1 Open Circuit Diagnosis by Power Spectrum

Figure 6.15 shows typical power spectra for the current signals collected under different loads namely zero load, 25% load, 50% load and 75% load. For the healthy case the characteristic frequency values shift lower and the peak amplitude goes higher with increasing in loads. The existence of the characteristic frequencies in the healthy case is due to inevitable manufacturing tolerances or inherent errors that lead to a clear asymmetric distribution between the three stator phases.

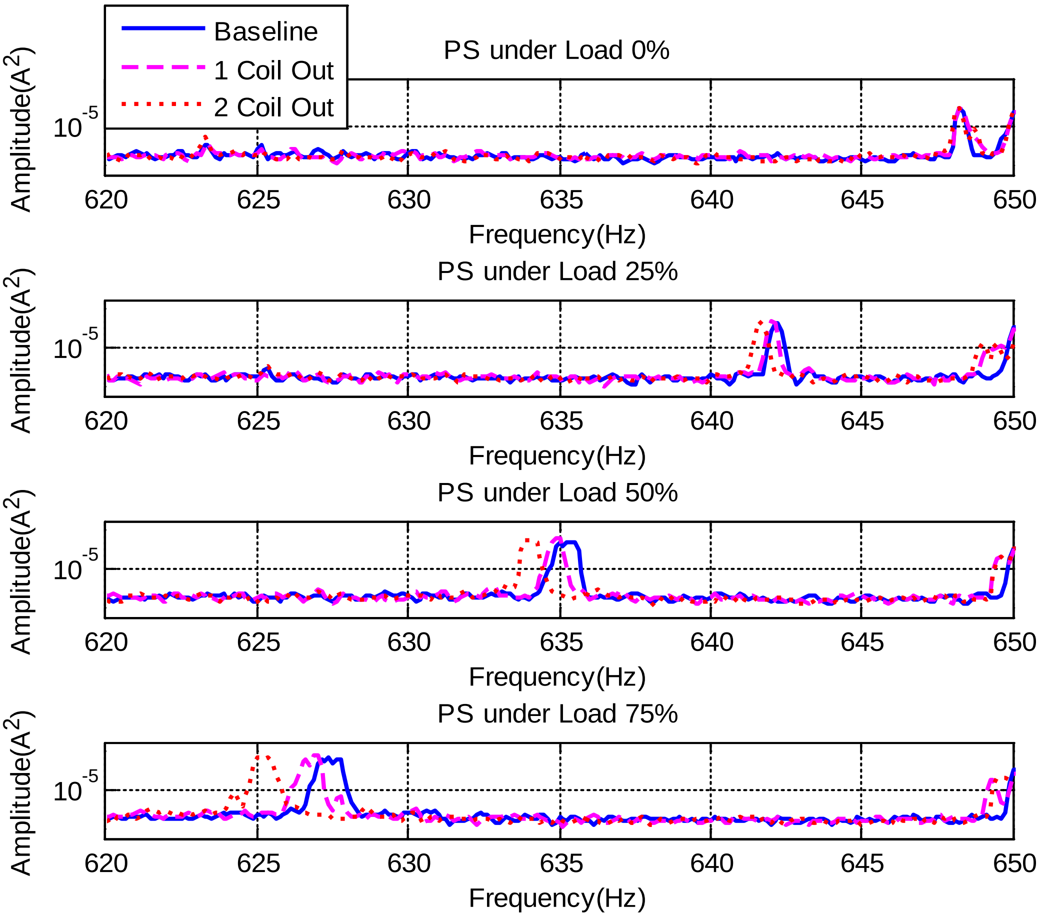

Figure 6.15-Current Power Spectrum Zoomed aroundLower Sidebands of Bar-pass-frequency under Different Loads and Stator Cases.

However, as the asymmetry becomes worse due to the fault, the amplitude increases slightly and the frequency shifts also becomes slightly larger when comparing the results under different motor fault cases, which is consistent with that the faults result in weaker magnetic field and more rotor slip. Thus these changes may be used for separating different health cases.

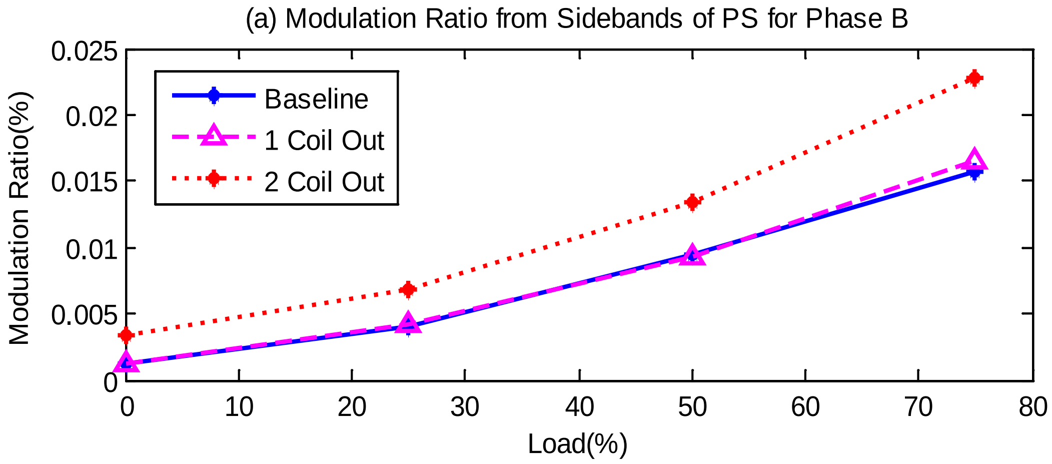
(a) Modulation Ratio from Sidebands of PS for Phase B

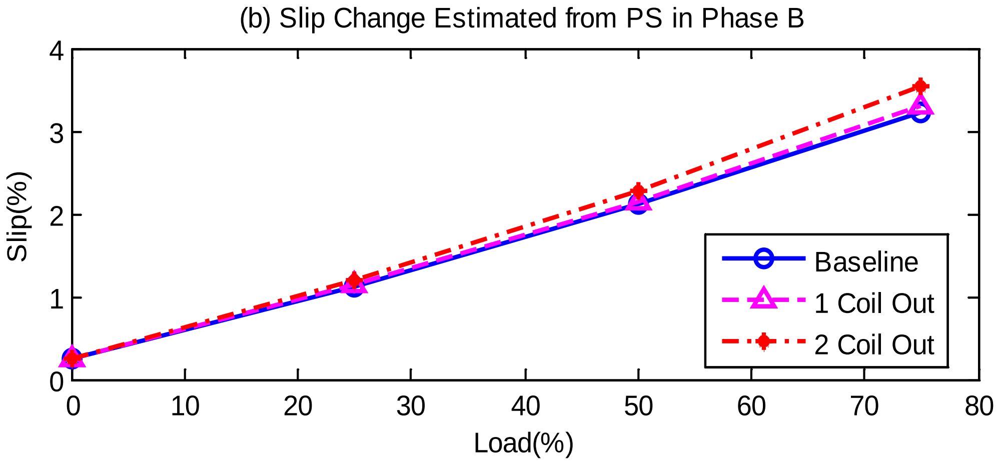
(b) Slip Change Estimated from PS in Phase B

Figure 6.16-Diagnosis by Amplitude Changes and Slip Changes from PS

Figure 6.16 presents the diagnostic results based on the change in the amplitude and frequency estimated from power spectrum using dataset from phase B. The modulation ratio used in Figure 6.16(a) is calculated by normalising the mean value of two sideband amplitudes with the root mean square (RMS) values of current signals whereas the slip is estimated using the frequency values extracted from power spectrum based on Equation 3.18. As shown in Figure 6.16, the relative amplitude change and frequency change increase with increasing loads and fault levels, which is consistent with the operating principles of induction motors. However, these load trends makes it impossible to separate the healthy motor and the one coil removal case under load conditions below 50%. It means that a full separation can be reached only at 75% load, although its difference between healthy motor and one-coil removal is very small.

In addition, the amplitude changes can give a full separation under different load conditions when it has two coil removals on the stator, which shows that amplitude changes are less sensitive to loads and can be a useful feature for power spectrum based diagnosis.

6.4.1.2 Open Circuit Diagnosis by MSB-SE

Typical stator current MSB are shown in Figure 6.17 for the current signals from different loads and motor health cases. Similar to the characteristics observed from power spectra in Figure 6.15, MSB peak amplitudes at the characteristic frequencies increases and the frequency value shifts lower as load increases. However, the amplitude increases more significantly with the progression in fault severity. In addition, bispectral peaks in Figure6.17 appear at frequency values that have a 50Hz difference from that of power spectrum, showing the effect of MSB-SE demodulation.

In the same way as that of power spectrum, the healthy case exhibits a frequency shift toward to lower value and an amplitude increase as the load increases. However, for the faulty cases, MSB-SE amplitudes increase more significantly and the frequency shifts also becomes slightly larger as the fault severity becomes higher. Especially, the larger changes in amplitudes with fault cases demonstrate that MSB has very effective noise reduction, which allows small amplitudes to be estimated accurately and hence produce accurate modulation estimation.

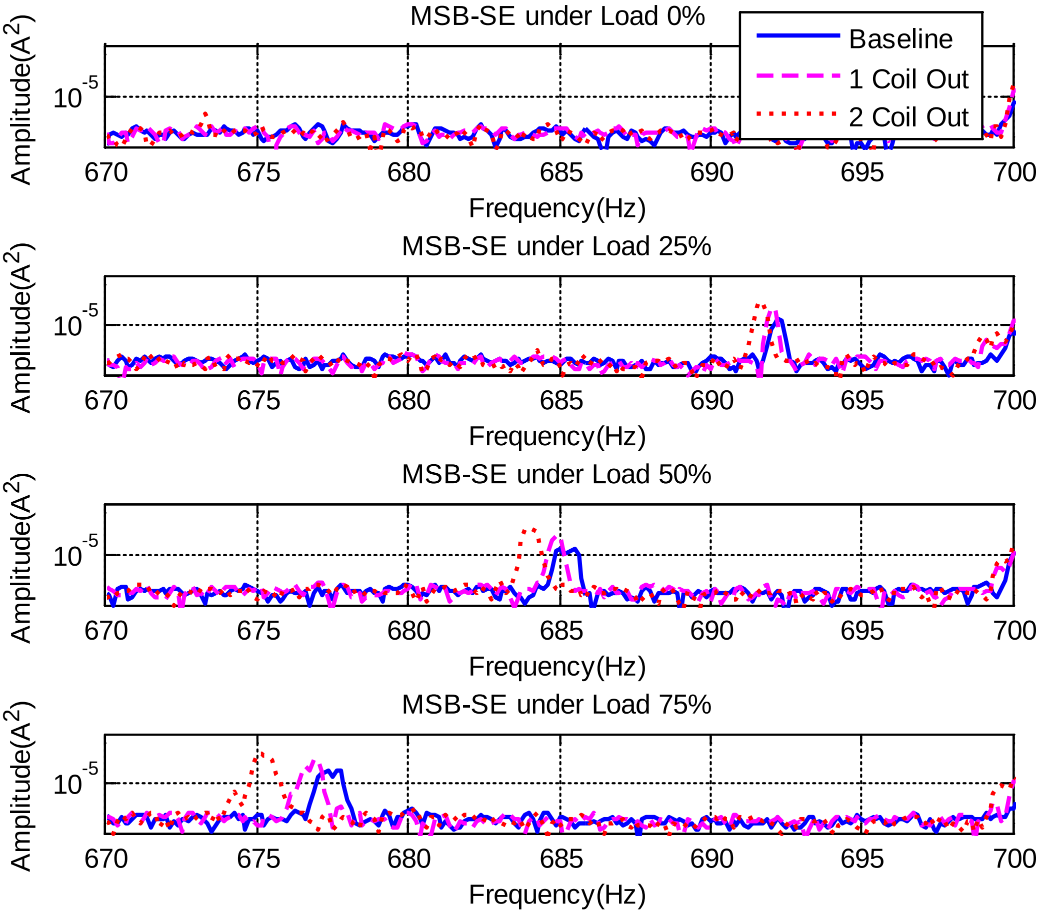

Figure 6.17-Current MSB-SE under Different Loads and Stator Health Cases

To give an overall assessment of using MSB for fault diagnosis, results are presented in the same way as in the power spectrum, to show relative amplitude changes and frequency changes in Figure 6.18. Obviously, the frequency change based diagnosis of Figure 6.18(b) shows the same results as that of power spectrum because both MSB and bispectrum are calculated using the same frequency resolution. However, it can be seen that the amplitude change based diagnosis shows nearly full separation results, demonstrating that MSB-SE have a much better performance in diagnosing the stators faults.

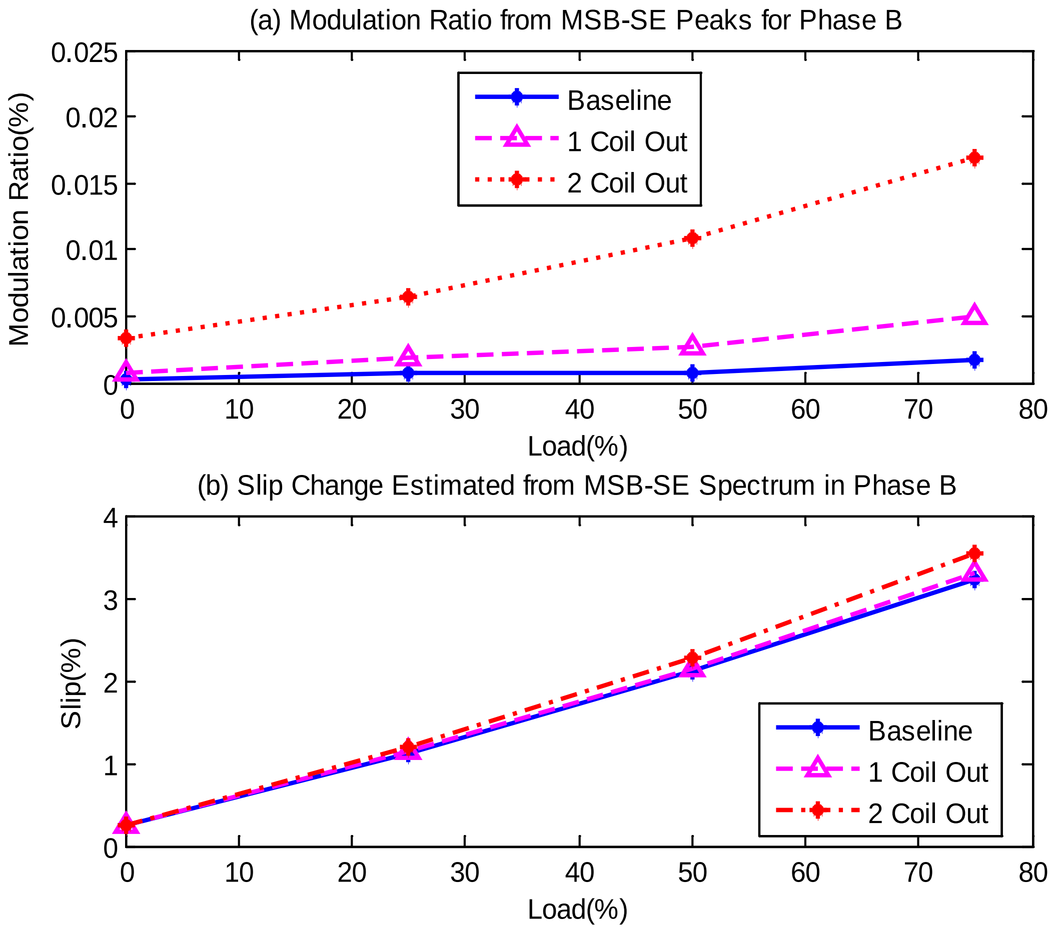

Figure 6.18-Diagnosis by Amplitude Changes and Slip Changes from MSB-SE Analysis

6.4.2 Detection and Diagnosis Open Circuit in the Stator Winding

To evaluate the performance of MSB analysis, current signals were collected under two different stator winding configurations, firstly a healthy motor, two inter turn short circuit in first coil in phase A under two successive load conditions: zero and 25% of full load. This allows the diagnostic performance to be examined at different loads and avoid any possible damages of the test system at the full load when the faults are simulated as shown in Figure 6.19.

The dataset is processed off-line by using a Matlab program which implements FT calculation to obtain both power spectrum using Equation 4.2 and MSB-SE using Equation 4.12 simultaneously. During the calculation it uses a rectangular FT window of the same size for both power spectrum and MS bispectrum, which results in a frequency resolution of 0.25Hz, with the same average times (100 times) so that they can be compared directly in their performance of identifying fault characteristic frequencies and quantifying spectral peaks. In the meantime, only the current signal in phase A is examined as the fault is induced to this phase and it produces the most significant changes between the three phases. In addition, a MSB slice only at 50Hz is presented for direct comparison because this slice provides the full information about the modulation characteristics.

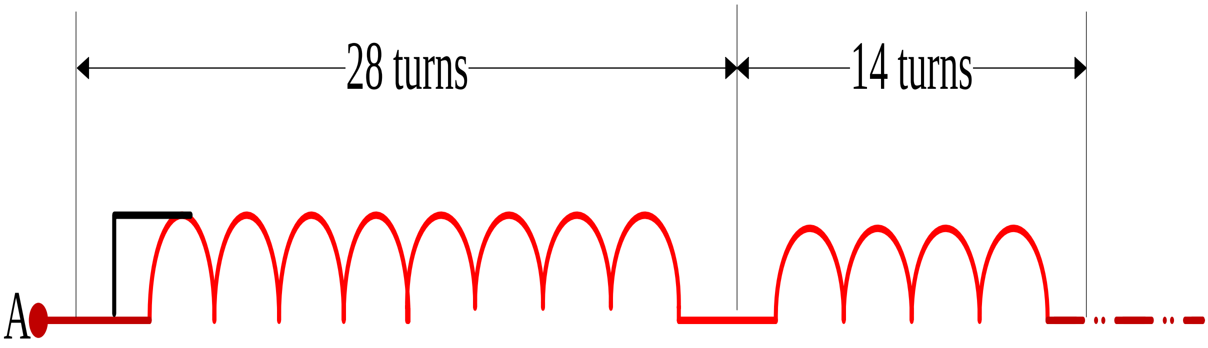

Figure 6.19-Two-turn Shorted in First Coil of Phase A

6.4.2.1 Inter-Turn Short Circuit Diagnosis by PS

Figure 6.20shows typical power spectra for the current signals collected under different loads, namely zero load and 25% load. For the healthy case the characteristic frequency values shift lower and the peak amplitude goes higher with increasing in loads. The existence of the characteristic frequencies in the healthy case is due to inevitable manufacturing tolerances or inherent errors that lead to a clear asymmetric distribution between the three stator phases.

However, as the asymmetry becomes worse due to the fault, the amplitude increases slightly and the frequency shifts also become slightly larger when comparing the results under different motor fault cases, which is consistent with the faults resulting in a weaker magnetic field and more rotor slip. Thus these changes may be used for separating different health cases.

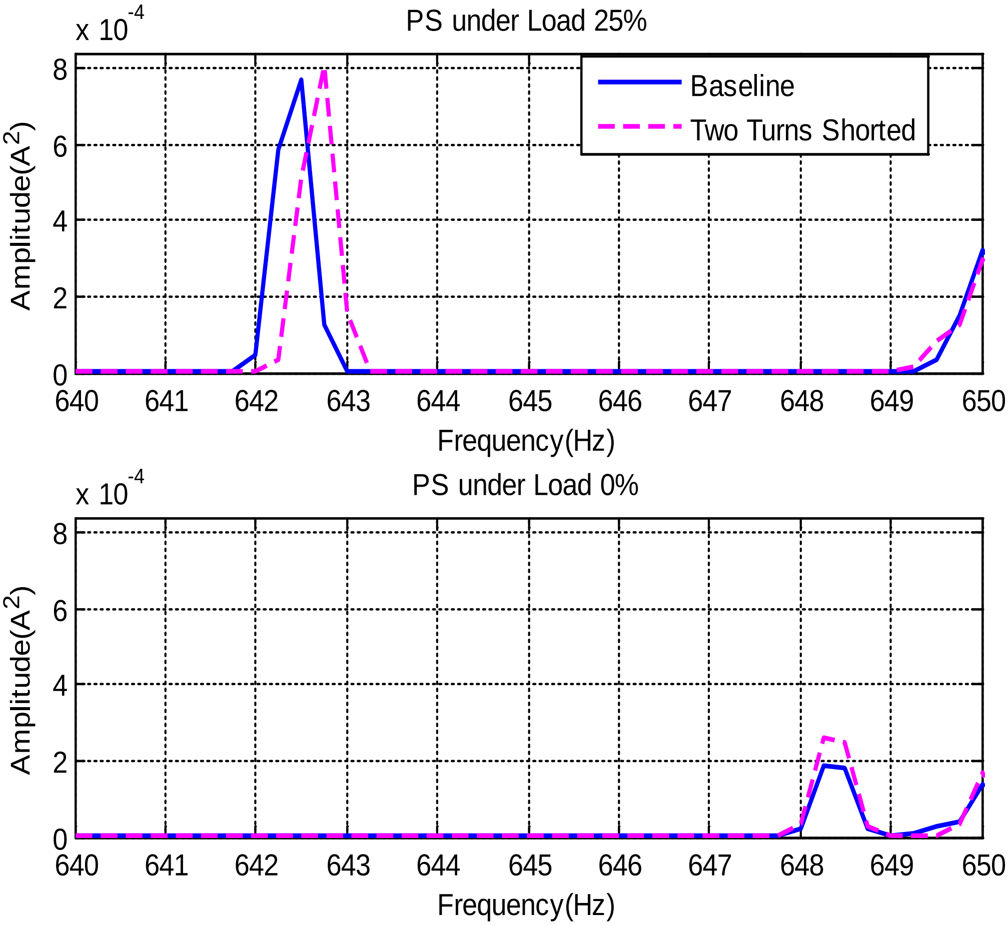

Figure 6.20-Current PS Zoomed around Lower Sidebands of Bar-pass-frequency under Different Loads and Stator Cases

Figure 6.21 presents the diagnostic results based on the change in amplitude and frequency estimated from power spectrum using dataset from phase A. The modulation ratio used in Figure 6.21(a) is calculated by normalising the mean value of two sideband amplitudes with the root mean square (RMS) values of current signals, whereas the slip is estimated using the frequency values extracted from power spectrum based on Equation 3.18. As shown in Figure 6,21(a), the relative amplitude change increases with increasing loads and fault levels, whereas frequency change is due to a change in stator winding temperature, which is consistent with the operating principles of induction motors. As a result, one can see in Figure 6.21(b) that the slip is higher in the case of healthy motor under 25% load, whereas it identifies the turn shorted case and under zero-load. This is because of changes in the stator winding temperature.

In addition, the amplitude changes can give a full separation under different load conditions when it has two-turn shorted on the stator, which shows that amplitude changes are less sensitive to loads and can be a useful feature for power spectrum based diagnosis.

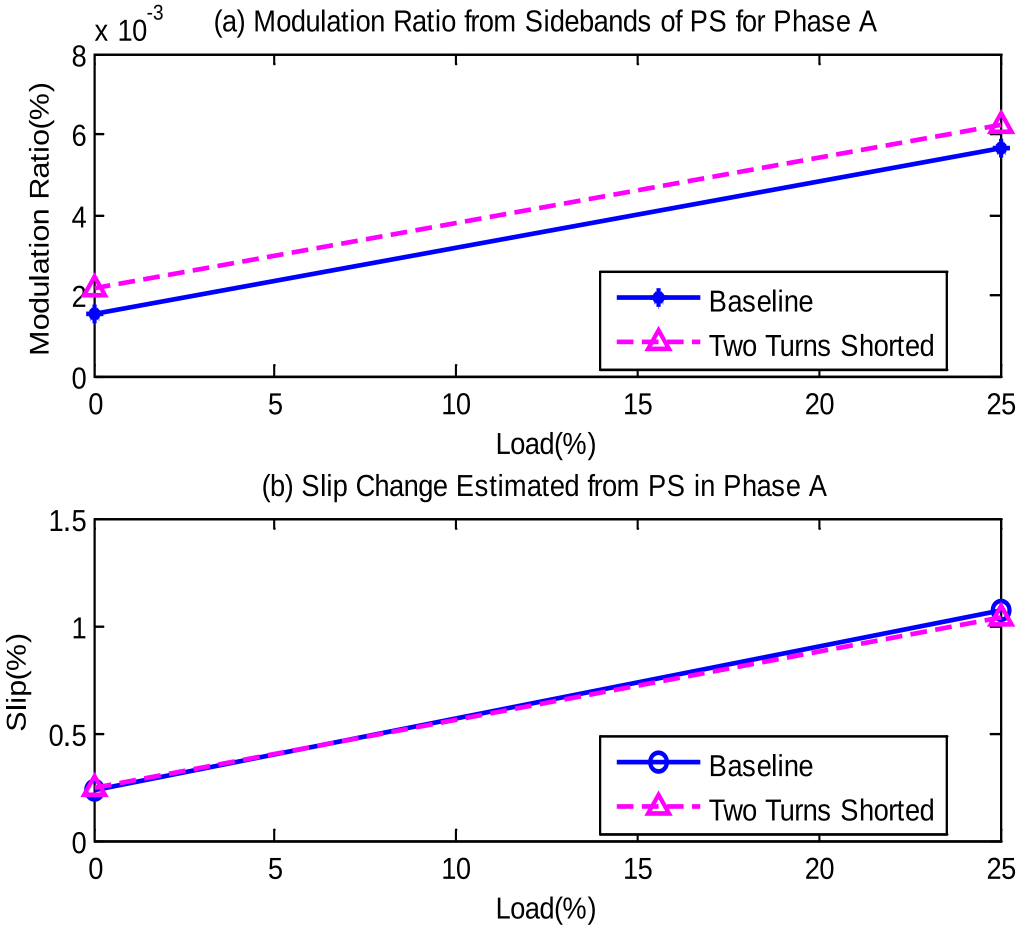

Figure 6.21-Diagnosis by Amplitude Changes and Slip Changes from PS

6.4.2.2 Inter-Turn Short Circuit Diagnosis by MSB-SE

Typical stator current MS bispectra are shown in Figure 6.22 for the current signals from different loads and motor health cases. Similar to the characteristics observed from power spectra in Figure 6.20, MSB peak amplitudes at the characteristic frequencies increases and the frequency value shifts lower as the load increases. However, the amplitude increases more significantly with progression in fault severity. In addition, bispectral peaks in Figure

6.22appear at frequency values that have a 50Hz difference from that of the power spectrum, showing the effect of MSB demodulation.

In the same way as that of power spectrum, the healthy case exhibits a frequency shift towards the lower value and an amplitude increase as the load increases. However, for the faulty cases, as the fault severity become higher, MSB amplitudes increase more significantly and the frequency shifts also becomes slightly larger. Moreover, the larger changes in amplitudes with fault cases demonstrates that MSB has very effective noise reduction, which allows small amplitudes to be estimated accurately and hence produce accurate modulation estimation.

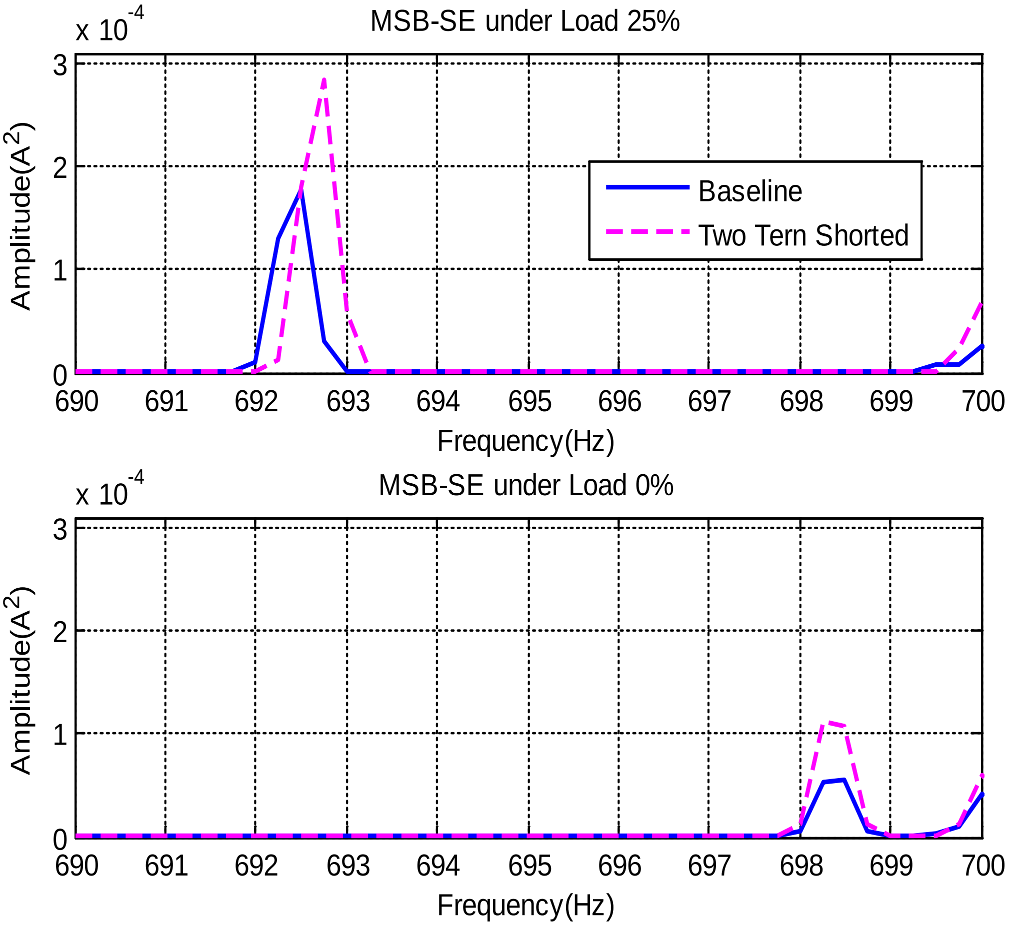

Figure 6.22-Current MSB-SE under Different Loads and Stator Health Cases

To give an overall assessment of using MSB-SE for fault diagnosis, results are presented in the same way as in power spectrum to show relative amplitude changes and frequency changes in

Figure 6.23. Obviously, the frequency change based diagnosis of Figure 6.23(b) shows the same results as that of power spectrum, this is because both MSB and bispectrum are calculated using the same frequency resolution and the same motor temperature which effects on motor slip. However, it can be seen that the amplitude change based diagnosis show nearly full separation results, demonstrating that MSB has a much better performance in diagnosing the stators faults.

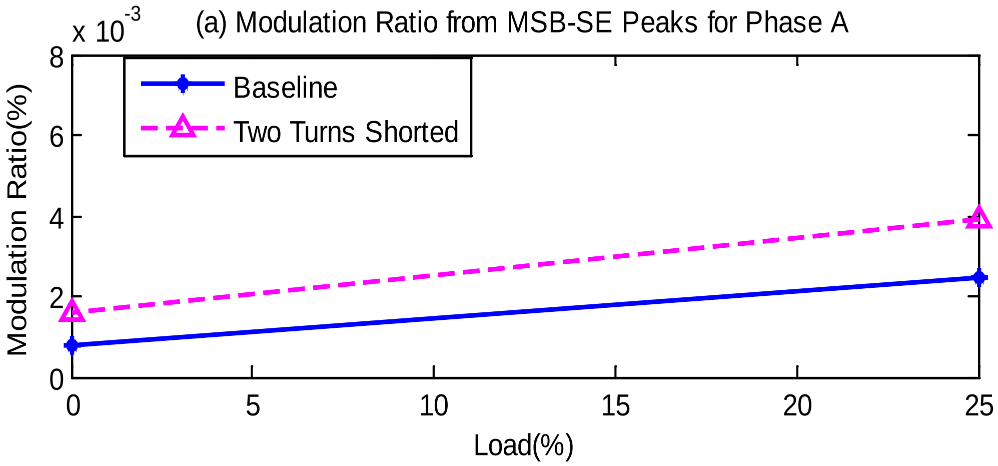

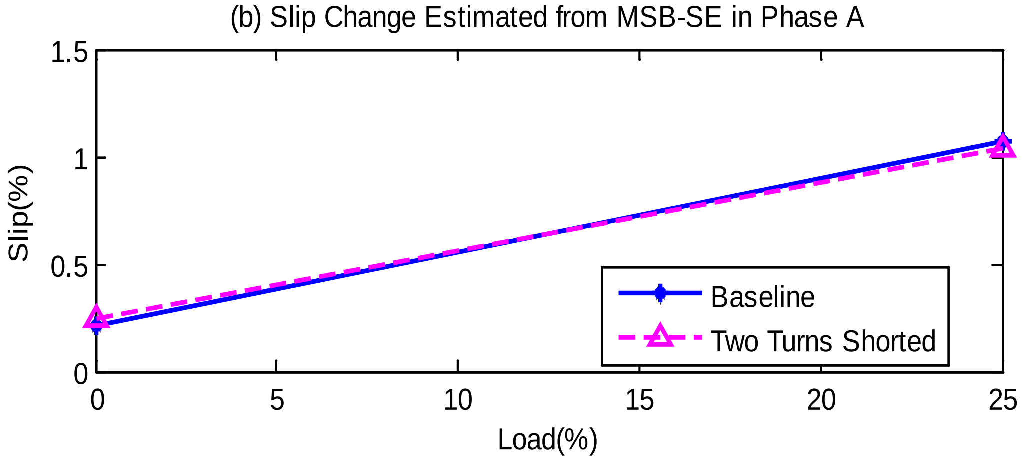

Figure 6.23-Diagnosis by Amplitude Changes and Slip Changes from MSB-SE Analysis

6.5 Detection and Diagnosis of Motor Bearing Faults

6.5.1 Test setup

Two types of common bearing faults have been tested in this study. The first one, an abrasive wear in the outer race has been considered; which models that caused by friction between ball and outer race surfaces due to lack of lubrication, while the second case of fault is an inner race defect as shown in Figure 5.11.

To analyse the current signals, a dataset is acquired in a motor rig under different simulated fault cases and operating conditions. The schematic diagram of the test facility employed to examine motor stator faults was illustrated in Figure 5.1. The system consists of an induction motor, variable speed controller, supporting bearings, couplings and DC generator as a load. The test motor is a three-phase induction motor with rated output power of 4 kW at 1420 rpm (two-pole pairs). The motor has 28 rotor bars and 36 stator slots. Two rolling ball bearings, type *6206ZZ* deep groove ball bearing measuring 30x62x16 mm, with nine balls ($N_b=9$), $D_b=9.52$ mm and $D_p=46.0$ mm, are used to support the rotor . To change the speed of the test motor, a digital variable speed controller is attached to the test rig between the power line source and the motor. The controller can be programmed to any specific shaft rotation speed between 0 and 1500rpm. The induction motor is directly coupled with a DC generator. The field of the generator is connected to a DC source through a controller while the generated power was fed back to the mains electrical grid via an inverter and the load on the induction motor can be adjusted by changing the field resistance of the DC generator. The operating load can be varied from no load to full load via the control panel.

A power supply measurement unit was designed to measure the instantaneous AC voltages, currents and power, using hall-effect voltage and current transducers and a universal power cell by the University staff. A shaft encoder, mounted on the shaft end produces 100 pulses per revolution for measuring the motor speed. A piezoelectric accelerometer, mounted on the bearing end-caps, is used to measure vibration of the motor. The accelerometer has a sensitivity of 5.0 mV/ms2 with a frequency range from 0.5 to 5000Hz, the current transducer has a sensitivity of 5 A/mv and a measurement range of 25A which allows the small changes of current and vibration to be measured with adequate accuracy.

During the tests the data was acquired using a GST YE6232B high speed data acquisition system. This system has 16 channels, each with 24 bit resolution, a maximum sampling frequency of 96 kHz, which allows the details of the 50Hz component, the high order supply harmonics, rotor bar pass frequency, stator bar pass frequency and motor bearing frequency to be recorded for further analysis.

To evaluate the performance of PS and MSB-SE analysis, current signals were collected under three different motor conditions: healthy motor, outer race fault and inner race fault and under four successive load conditions: zero, 25%, 50% and 75% of full load, which allows the diagnostic performance to be examined at different loads and avoid any possible damage to the test system at the full load when the faults are simulated. However, because of noises which are caused by controller, the characteristic bearing fault frequencies were difficult to differentiate from complex spectrum patterns. The motor was then disconnected from the loading system and the test was carried out with and without the controller and the results will be discussed in next section.

In the meantime vibration signals were also measured under healthy and two bearing faults to confirm the effectiveness of fault induced based on the vibration frequencies values which calculated by Equation 3.20 to Equation 3.23.

The dataset is processed off-line using a Matlab program which implements PS and MSB-SE calculations simultaneously with 100 times of average. In this way they can be compared directly in the performance of identifying the characteristic frequencies and quantifying their spectral peaks.

6.5.2 Effect of Controller

The phase current signal is firstly examined under different supply cases (with and without controller). Before exploring the current spectrum, vibration signals are examined to confirm the introduction of the faults. Figure 6-24 shows the vibration spectrum for both the outer race and inner race faults. The characteristic frequency and their harmonics are clearly shown. In addition, the amplitude at the fundamental frequency f_i is higher than that of f_o, indicating that the fault from inner race may be higher than that of the outer race. These then shows that the two types of faults have been induced with sufficient severity so that the vibration based method can detect them.

(a) Vibration Signal Without Controller

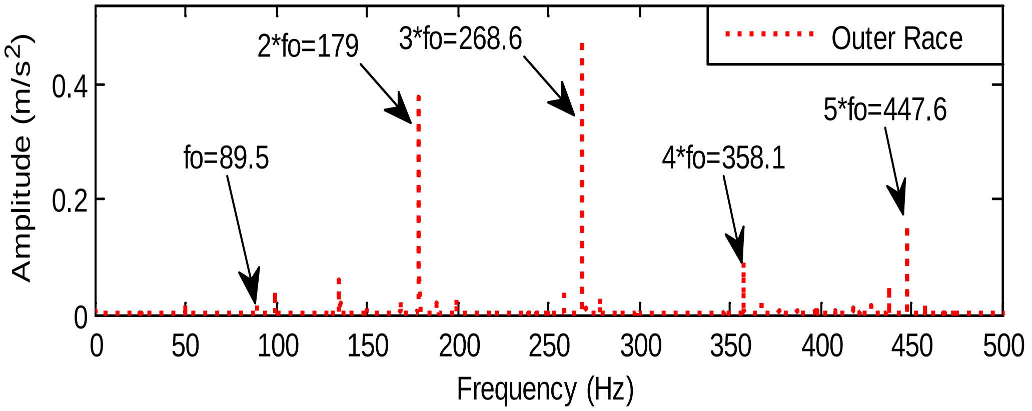

(b) Vibration Signal Without Controller

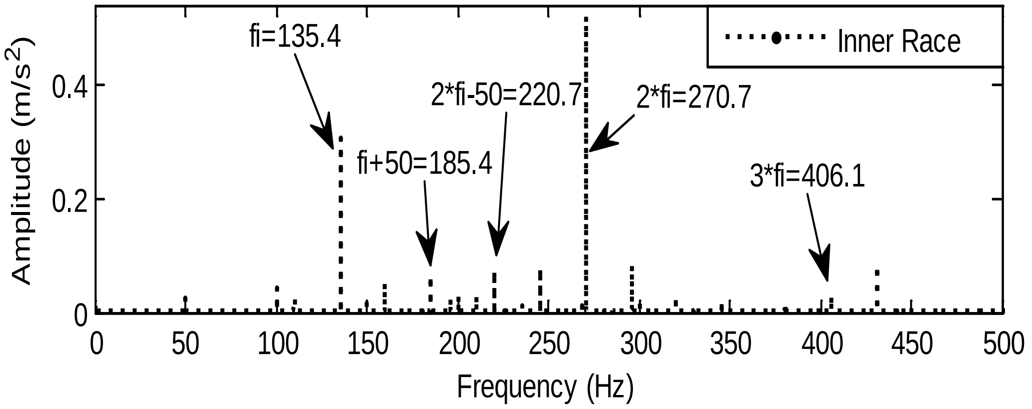

Figure 6.24-Spectrum of Vibration for Faulty Bearings

Figure 6-25 shows a comparison of current spectrum between a healthy case and two faulty bearings under four different loads with the VFD controller. To highlight the small components, the Y-scale is fixed to 0.4A. It is difficult to find the spectrum components at the characteristic frequencies suggested in Equation 3.24 due to bearing faults for all load conditions. Instead there are clear peaks at frequencies ($f_s \pm f_r$) which become higher with faults. In addition the peak values decrease with the increase of load. These changes show that there is noticeable eccentricity which may be induced to the rotor system when refitting the faulty bearings. It may indicate that the eccentricity induced changes mask the changes due to bearing faults. In addition, the controller will cause high level ofnoise because VFD provides a pulse width modulated signal source, which may also mask the small component at bearing characteristic frequencies.

(a) Current Spectrum under Load=0(%)

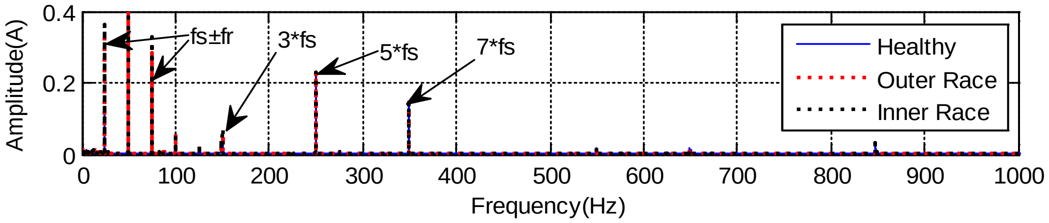

(b) Current Spectrum under Load=25(%)

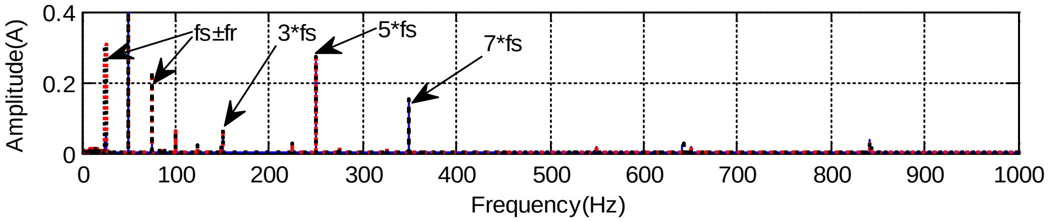

(c) Current Spectrum under Load=50(%)

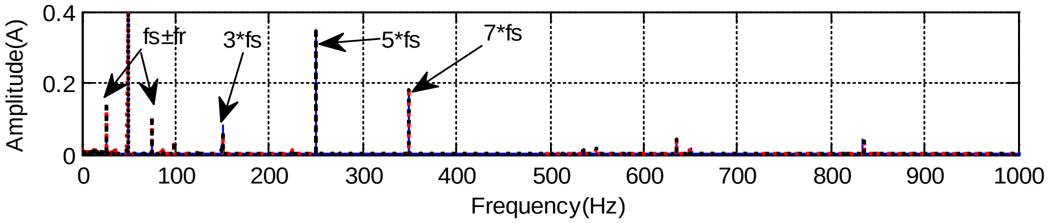

(d) Current Spectrum under Load=75(%)

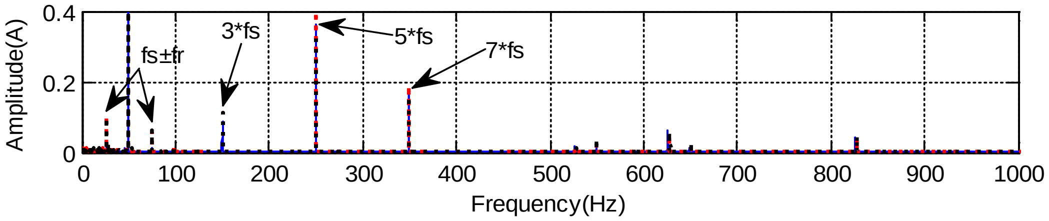

Figure 6.25-Current Spectra of Healthy Bearing, Outer Race and Inner Race Faults with Controller

To eliminate these two types of noise and other possible influences caused by downstream components such as generators and couplings, the motor was disconnected from the control system and connected directly to a main power supply. The unloaded machine was then tested under three corresponding conditions, namely, healthy, outer race and inner race faults. Figure 6.26 presents the spectrum of the phase current from the unloaded motor with and without the controller.

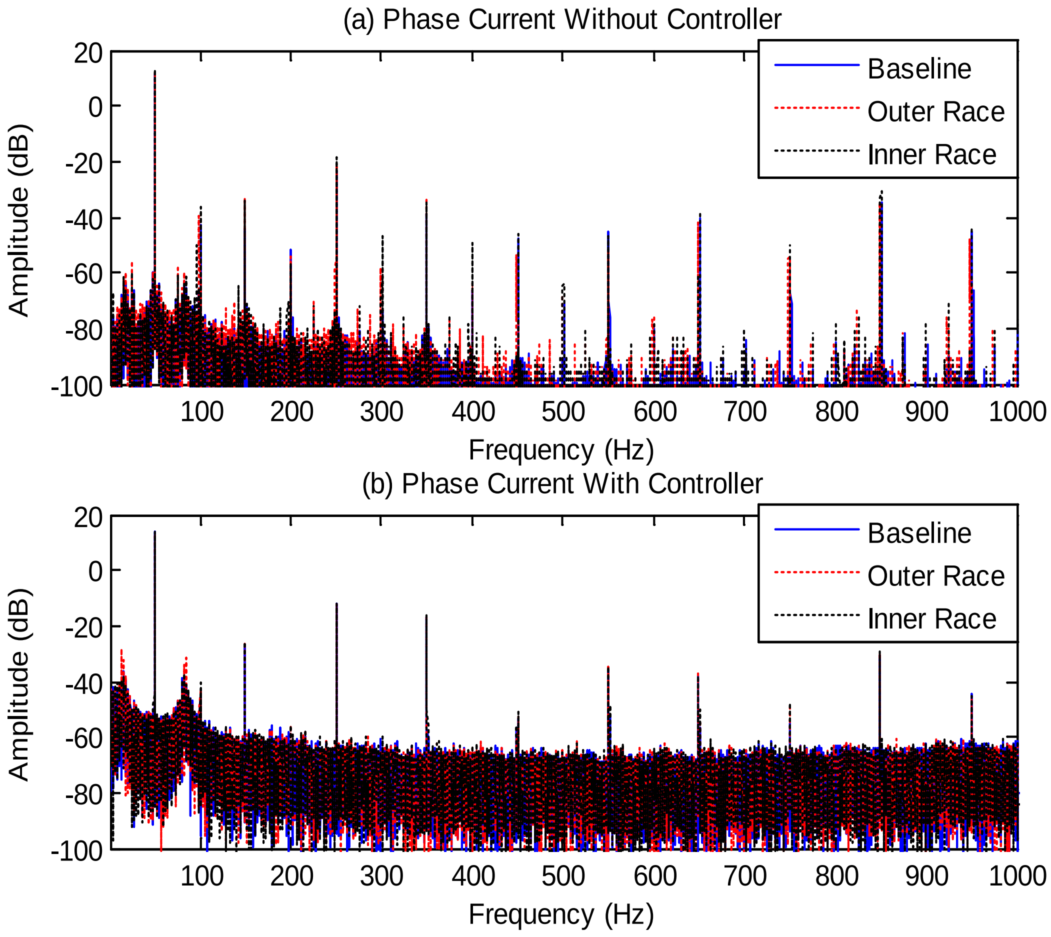

Figure 6.26-Current Spectra with Controller and without Controller

The spectrum with controller shown in Figure 6.26(a) has very rich frequency components which include not only the harmonics of supply frequency but also distinctive components at 100Hz, 200Hz etc. The latter indicates a certain degree of the imbalance of the supply system. Moreover, the background noise level is more than 40dB higher than that of the case without the controller. This shows that it is likely the bearing fault frequency is masked by the background noise. Therefore, further study of current signature analysis is carried out under the condition of no-controller and no-load. Considering the small components and complicated spectrum pattern due to bearing faults and high order harmonics, more advanced MSB analysis (MSB-SE) along with PS analysis will be used to process the measured signals.

6.5.3 Outer Race Fault Detection and Diagnosis

Figure 6-27 shows the results of MSB and PS analysis for both the healthy and faulty outer race cases in the frequency ranges around the first two harmonics of bearing fault frequency. For the healthy case both types of spectra do not show significant peaks at the characteristic frequencies of $f_s \pm f_o$ and $f_s \pm 2f_o$ for PS or f_o and $2f_o$ for MSB-SE. For the faulty case clear peaks can be observed at some of these frequencies. MSB-SE shows distinctive peaks at both f_o and $2f_o$. However, from PS spectra only one spectral peak at f_s-$2f_o$ can be discriminated in Figure 6.27(b2) and the rest of three peaks cannot be determined due to high background noise level. This shows that MSB-SE have better capability to separate the small bearing features from noisy measurement.

To show more details of the spectrum changes, Table 6.3 summarises the peak values at the characteristic frequencies of interest. For comparison, the peak values at corresponding frequency are also listed even if they are not very distinctive in the spectrum. The table shows the peaks for the faulty one are higher than that of the healthy one, showing that faulty bearings cause more fluctuation in the current signal, which is consistent with that predicted in theory.

Moreover, MSB peaks shows higher percentage increases at both of the peaks compared with that of PS. This demonstrates that MSB has a better diagnosis capability. Especially, it shows that the peak increase at $2f_o$ is higher than at f_o, which shows is agree with the spectrum results of vibration shown in Figure 6.27(a) in that the fault induce higher amplitude in the second harmonic component.

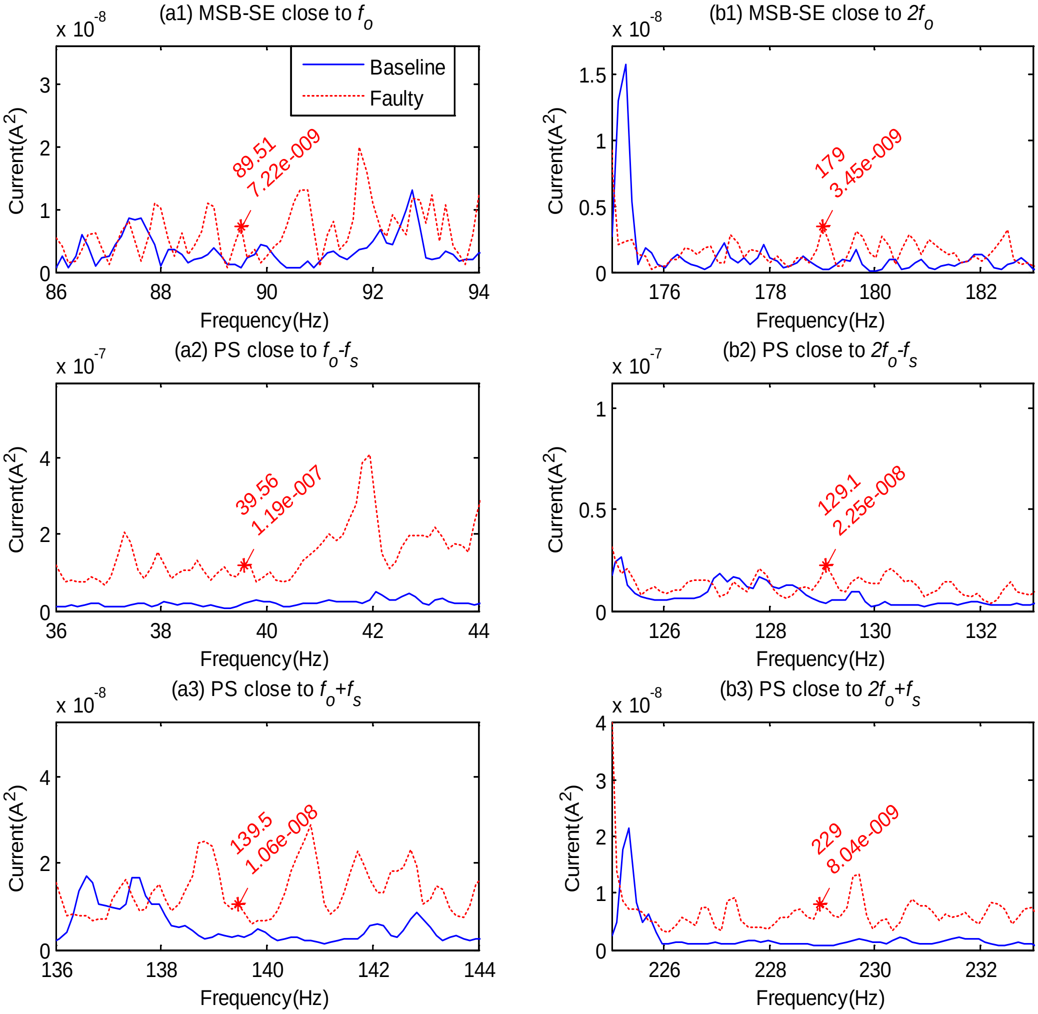

Figure 6.27-Spectrum in the Frequency Range Close to f_o and $2f_o$

Spectral Peak	Healthy[1E-6]	Faulty[1E-6]	Δ[1E-6]	Δ[%]
MSB atf_o	0.0007	0.0072	0.0065	916
PS at f_s- f_o	0.0182	0.1191	0.1009	553
PS at f_s+ f_o	0.0032	0.0106	0.0074	231
MSB *at* $2f_o$	0.00015	0.00345	0.00330	2154
PS at f_s- $2f_o$	0.00342	0.02254	0.01912	559
PS at f_s+ $2f_o$	0.00082	0.00804	0.00722	877

Table 6.3-Comparison of Spectral Peaks for Outer Race Fault

6.5.4 Inner Race Fault Detection and Diagnosis

Figure 6.28 shows the results of MSB and PS analysis for both the healthy and faulty inner race cases in the frequency ranges around the first two harmonics of bearing fault frequency. For the healthy case both types of spectra do not show significant peaks at the characteristic frequencies of $f_s \pm f_i$ and $f_s \pm 2f_i$ for PS or fi and $2fi$ for MSB. For the faulty case clear peaks can be observed at most of these frequencies. MSB shows distinctive peaks at both f_i and $2f_{i,}$. Especially, the peak at $2f_i$isquitedistinctive as shown in Figure 6.28(b1). Without double, the presence of the inner race fault can be detected by MSB analysis. From PS spectra, three peaks can be determined at Figure 6.28(a2), (b2) and (b3). However, the peak at f_s+f_i in Figure 6.28 (a3) cannot be resolved properly and has higher amplitude than that of healthy case. Because at least one set of sideband can be found, it is possible now to detect the inner race fault by SP analysis. This also shows that PS is able to detect the fault when the severity is higher, which is confirmed by the vibration spectrum shown in Figure 6.24(b). In other words, PS is less reliable in detecting this inner race compared with MSB analysis.

To show more details of the spectrum changes, the peak values at characteristic frequencies of interest are also summarised, shown in Table 6.4. For comparison, the peak value at f_s+f_i is also listed even though it is not distinctive and has higher amplitude than the healthy case in the spectrum. The table shows that the peak values for the faulty one are higher than that of the healthy one except for the peak at f_s+f_i, showing that faulty bearings cause more fluctuation in the current signal, which is consistent with that predicted in theory.

Moreover, MSB-SE peaks shows higher percentage increases at both of the peaks compared with that of PS. This demonstrates that MSB-SE has a better diagnosis capability. Especially, it shows that the peak increase at $2f_i$ is higher than at f_i, which is in agreement with the spectrum results of vibration shown in Figure 6.24(b), in that the fault induces higher amplitude in the second harmonic component.

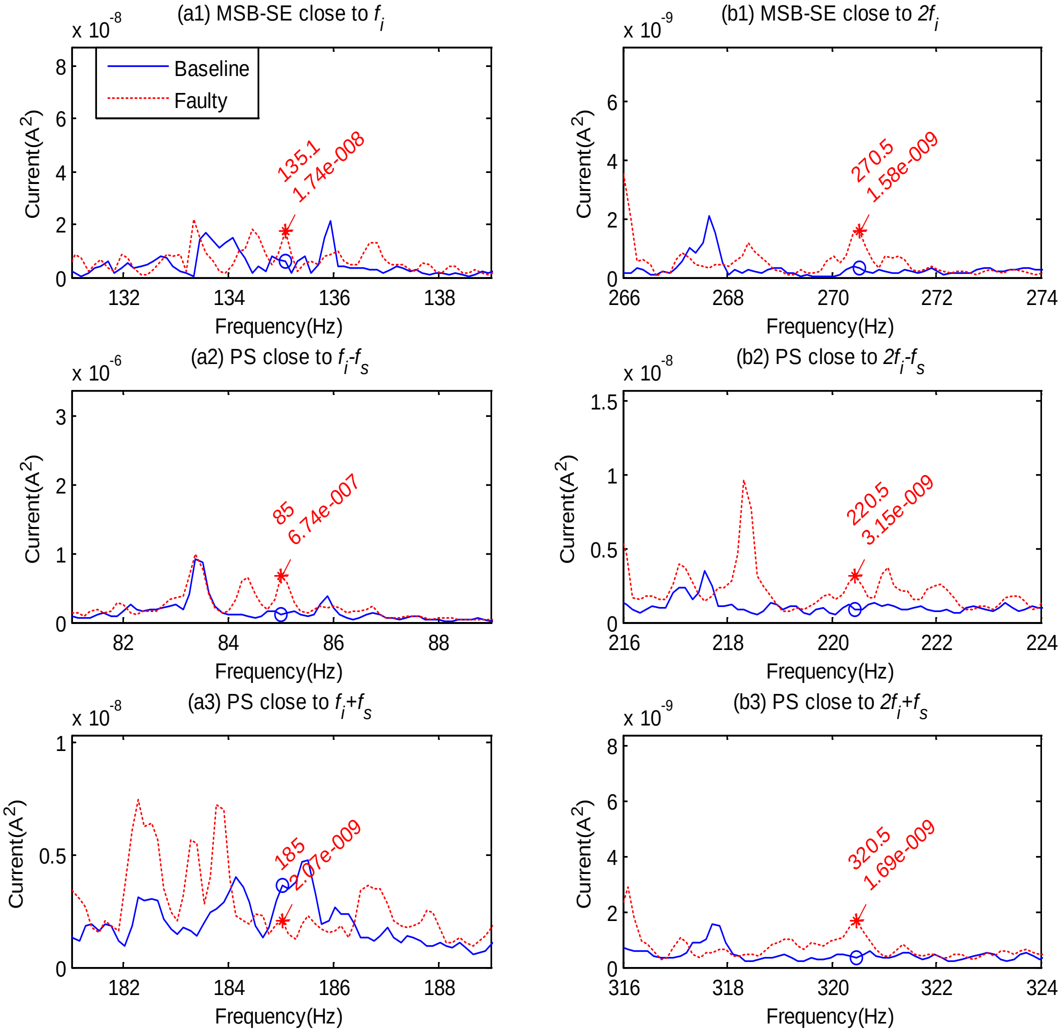

Figure 6.28-Spectrum in the Frequency Range Close to f_i and 2 f_i

However, comparing the amplitude increases between Table 6.3 and Table 6.4has found that the amplitudes of the inner race fault are smaller than that of outer race fault. This is not very consistent with that of vibration results shown in Figure 6.24. However, these less amplitude changes may be due to the higher attenuation in the high frequency range of the induction motor, which can be understood in the spectra of Figure 6.26 in which the spectral amplitude has a monotonic decrease trend with the increasing of frequency. Based on these frequency response characteristics, the amplitude changes at f_i and its harmonics will be lower because f_i is higher than f_o.

Spectral Peak	Healthy[1E-6]	Faulty[1E-6]	Δ[1E-6]	Δ[%]
MSB atf_i	0.0058	0.0174	0.0116	200
PS at f_s- f_i	0.1075	0.6741	0.5666	527
PS at f_s+ f_i	0.0036	0.0021	-0.0016	-43
MSB *at* $2f_i$	0.000294	0.001578	0.001284	437
PS at f_s- $2f_i$	0.000901	0.003153	0.002252	249
PS at f_s+ $2f_i$	0.000309	0.001685	0.001376	445

Table 6.4-Comparison of Spectral Peaks for Inner Race Fault

6.6 Summary of Chapter 6

This Chapter presents the analysis of the motor data collected using conventional bispectrum CB and MSB based sideband amplitude estimator (MSB-SE) that obtains the amplitude at sidebands to determine whether it is suitable for use with induction motor condition monitoring. To illustrate the performance of MSB, PS in analysing current signals, a dataset is acquired in a motor rig under healthy motor, broken rotor bar, stator faults and motor bearing faults and at zero, 25%, 50% and 75% of full load. The test motor is a three-phase induction motor with rated output power of 4 kW at speed 1420 rpm (two-pole pairs) and 28 rotor bars. To change the speed of the testing motor, a digital variable speed controller is attached to the test rig between the power line source and the motor. The controller can be programmed to any specific shaft rotation speed between 0 and 1500rpm. During tests all the data was acquired using a GST YE6232B high speed data acquisition system.

For broken rotor bar detection, power spectrum, spectral peaks appear at frequencies at ($f_s \pm 2sf_s$) and increase as the load and fault increases. In a similar way, the phase current bispectrum also increase in amplitudes with load and fault severity but they appear at ($2sf_s$). Moreover, MSB-SE allows the three different severities of BRB to be detected and diagnosed by using the change of MSB magnitudes. However, CB is unable to capture any of these faulty components by either its magnitude or coherence results.

In case of stator fault, power spectrum peaks appear at bar passing frequencies at ($f_s \pm N_b * f_r$) and increase as the load and fault increases. In addition, the frequency values decrease slightly as the fault severity increases because of changing in flux due to motor temperature. In a similar way, the phase current bispectrum sidebands also increase in amplitudes with load but they appear at ($N_b * f_r$). It can be concluded that MSB-SE has no modulation influences which shows the faults more clearly, which would make it easier to identify and more accurate to quantify the characteristic frequency of different stator fault to produce more accurate diagnostic results.

Similarly, MSB-SE analysis is evaluated using motor current signals to detect and diagnose motor bearing faults. From its spectrum presentations, it can be found that MSB shows a simpler spectrum structure compared with the power spectrum. It means that MSB shows peaks only at kf_o and kf_i for outer race and inner race faults respectively, whereas power spectrum shows peaks at ($f_s \pm kf_o$) and ($f_s \pm kf_i$) which can cause difficulty to identify them when the spectrum components are rich. Moreover, MSB produces a more accurate amplitude estimate due to its capability of noise reduction and non-modulation component removal. In additional MSB-SE produces a reliable difference at these frequencies whereas PS only provides change evidences at some of the frequencies. This shows that MSB has a better performance in extracting small changes from the faulty bearing for fault detection and diagnosis.

CHAPTER 7
DYNAMIC MODELOF INDUCTION MOTORS

This chapter describes the three-phase induction motor model, explaining the voltage equations and flux linkage equation. Furthermore, it introduces the equations required for mechanical dynamic system modelling. In addition, it develops the healthy induction motor mathematical model in full. After that the mathematical model is described for broken rotor bar cases. Finally, the mathematical equations are solved numerically in a MATLAB environment to predict motor current signals. These predicted results are then compared with the equivalent measurements taken during the experimental tests. The agreement between measurement and prediction suggests the model is precise enough to be used for further simulation research.

7.1 Introduction

An accurate model is very useful for monitoring and diagnosis of induction motors. As a result such models are usually used to predict and extract fault signatures.

The mathematical modelling of three phase induction motors is to describe them as coupled stator and rotor poly-phase circuits in terms of so-called phase variables, namely stator currents i_{sa}, i_{sb}, i_{sc} rotor currents i_{ra}, i_{rb}, i_{rc}, the rotor speed ω_r ; and the angular displacement θr between stator and rotor windings as shown in Figure 7.1. The magnetic coupling is expressed in terms of an inductance matrix which is a function of position θr [152]. The matrix expression of the machine equations are readily formulated in Matlab as it can be seen later.

The model is built considering that both stator and rotor are consisting of multiple inductive circuits coupled together, and the current in each circuit is considered as an independent variable. The analysis is based on the following assumptions[153]:

- Infinity iron permeability.
- Sinusoidal distributed stator windings.

- Saturation is neglected.
- Uniform air gap.
- Neglecting inter-bar currents.
- Evenly distributed rotor bars.
- Stator windings of different poles are connected in series.

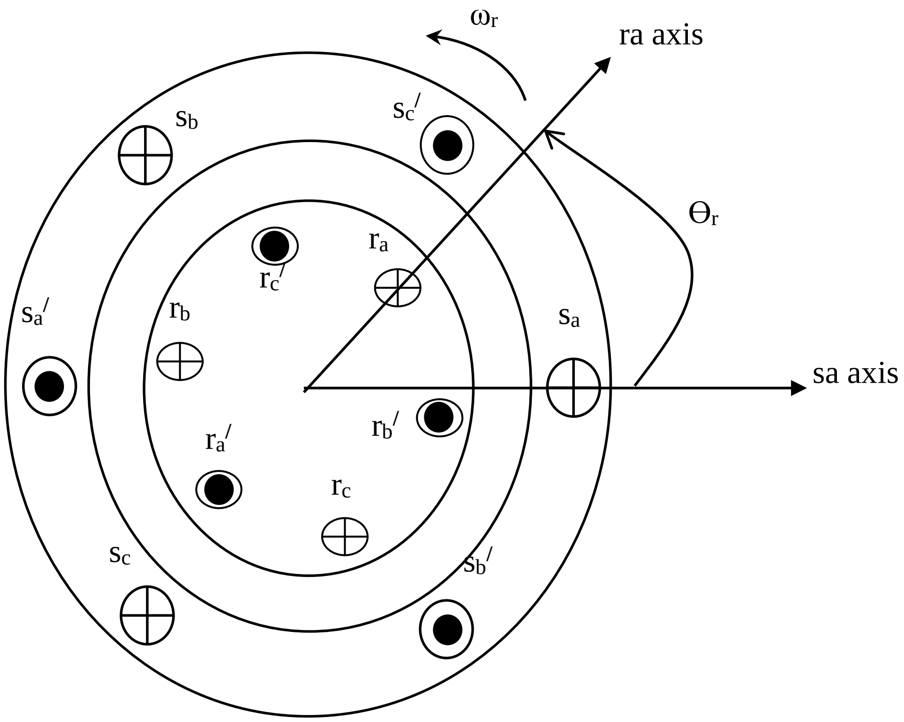

Figure 7.1-Circuit Model of the Induction Motor

7.2 Motor Modelling in Healthy Operation Condition

As can be seen from Figure 7.2 Matrices [I_s] and [I_r] represent three phase stator current and n+1 rotor current, respectively. Therefore, the rotor current matrix is composed of n loops that equal the number of rotor bars, while the additional loop represents the end-ring loop.

The stator and the rotor voltage equations can be expressed in terms of currents and flux linkage as follows [154-157].

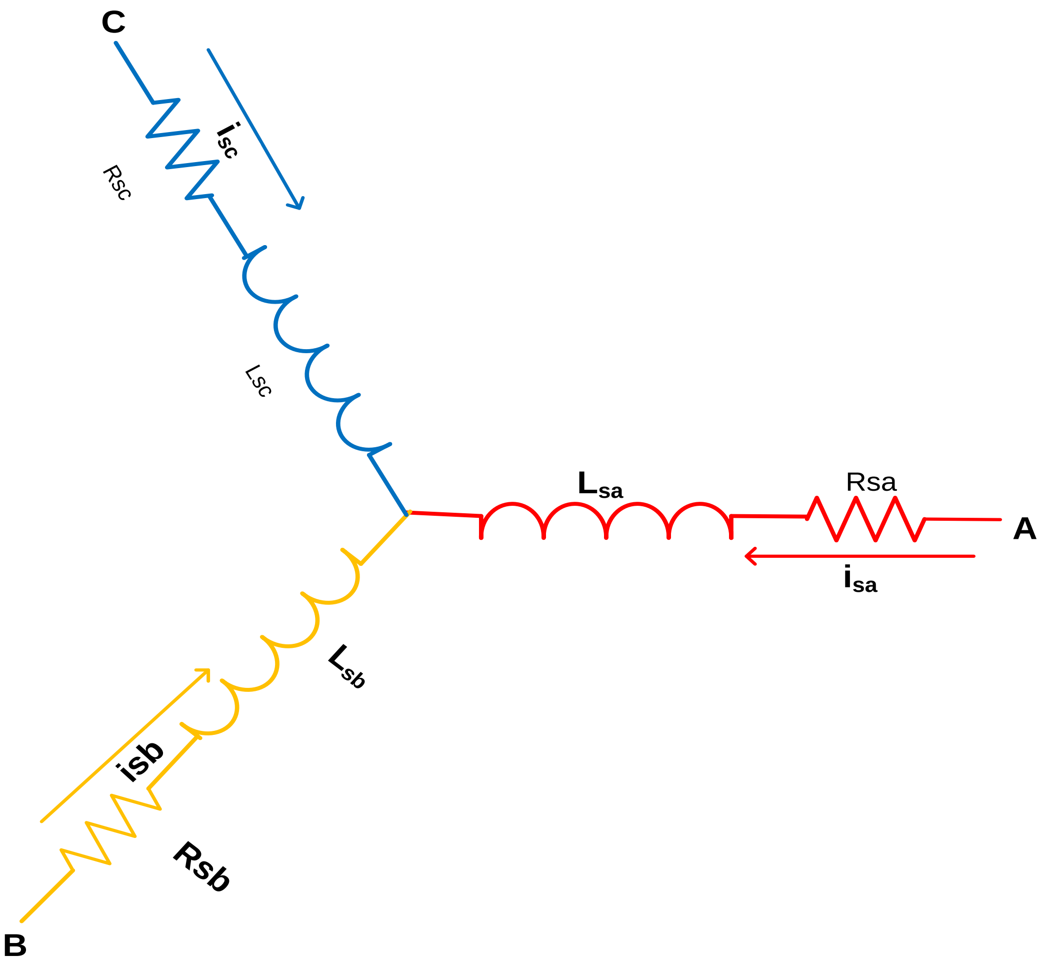

Figure 7.2-Stator Winding Y-connection

As can be seen from Figure 7.2, the stator voltage equations can be written as follows

$$[V_s] = [R_s]\,.\;[I_s] + \frac{[d\lambda_s]}{dt} \tag{7.1}$$

Where V_s is the stator voltages vector, I_s is the stator currents vector, R_s is the stator windings resistances matrix and λ_s is the total flux linkage by stator windings. Therefore,

$$[V_s] = [v_{sa} \quad v_{sb} \quad v_{sc}]^t \tag{7.2}$$

$$[I_s] = [i_{sa} \quad i_{sb} \quad i_{sc}]^t \tag{7.3}$$

The stator windings matrix can be given by

$$R_s = \begin{bmatrix} R_{sa} & 0 & 0 \\ 0 & R_{sb} & 0 \\ 0 & 0 & R_{sc} \end{bmatrix} \tag{7.4}$$

The flux linkage by stator windings can be written in matrix form as [158, 159]

$$[\mathrm{\lambda_s}] = [\mathrm{L_s}][\mathrm{I_s}] + [\mathrm{L_{sr}}][\mathrm{I_r}] \tag{7.5}$$

The stator windings inductance matrix L_s can be expressed as:

$$L_s = \begin{bmatrix} L_a + L_{ls} & L_{ab} & L_{ac} \\ L_{ba} & L_b + L_{ls} & L_{bc} \\ L_{ca} & L_{cb} & L_c + L_{ls} \end{bmatrix} \tag{7.6}$$

Note that for a healthy induction motor, the stator windings are identical and have the same resistance and inductance ($R_{sa}= R_{sb}= R_{sc}$ and $L_a= L_b= L_c$),

The stator to rotor mutual inductances matrix L_{sr} is a 3 by N_r which can be written as

$$L_{sr} = \begin{bmatrix} L_{a1} & L_{a2} & \dots\dots & L_{an} \\ L_{b1} & L_{b2} & \dots\dots & L_{bn} \\ L_{c1} & L_{c2} & \dots\dots & L_{cn} \end{bmatrix} \tag{7.7}$$

From Equation (7.1) to Equation (7.7), the stator phase voltage equations can be written as:

$$v_{sa} = R_s i_{sa} + (L_a + L_{ls})\frac{di_{sa}}{dt} + L_{ab}\frac{di_{sb}}{dt} + L_{ac}\frac{di_{sc}}{dt} + \frac{d}{dt}(L_{a1}i_{r1} + L_{a2}i_{r2} + \cdots + L_{an}i_{rn} + \\ + L_{ae}i_e) \tag{7.8}$$

$$v_{sb} = R_s i_{sb} + L_{ba}\frac{di_{sa}}{dt} + (L_b + L_{ls})\frac{di_{sb}}{dt} + L_{bc}\frac{di_{sc}}{dt} + \frac{d}{dt}(L_{b1}i_{r1} + L_{b2}i_{r2} + \cdots + L_{bn}i_{rn} + \\ + L_{be}i_e) \tag{7.9}$$

$$v_{sb} = R_s i_{sc} + L_{ca}\frac{di_{sa}}{dt} + L_{cb}\frac{di_{sb}}{dt} + (L_c + L_{ls})\frac{di_{sc}}{dt} + \frac{d}{dt}(L_{c1}i_{r1} + L_{c2}i_{r2} + \cdots + L_{cn}i_{rn} + \\ + L_{ce}i_e) \tag{7.10}$$

where:

v_{sa}, v_{sb}, and v_{sc} are the stator phase voltages,

i_{sa}, i_{sb} and i_{sc} are the stator phase currents,

L_a, L_b and L_c are the stator phase self-inductances

L_{ab}, L_{bc} and L_{ca} are the stator phase to phase mutual inductances

L_{ls} is the stator leakage inductance

(i_{r1}, i_{r2},… i_{rn}) are the rotor loops currents, Ie is the end ring current,

(L_{a1}, L_{a2}… L_{an}, L_{ae}) are phase A to rotor loops mutual inductances,

(L_{b1}, L_{b2},… L_{bn}, L_{be}) are phase B to rotor loops mutual inductances, and (L_{c1}, L_{c2}, …, L_{cn}, L_{ce}) are phase C to rotor loops mutual inductances.

7.2.1 Rotor Voltage Equations

$$[V_r] = [R_r]\,.\;[I_r] + \frac{[d\lambda_r]}{dt} \tag{7.11}$$

Where, I_r is the rotor loops currents vector, R_r is the rotor resistances matrix and λ_r is the total flux linkage by rotor loops.

Therefore

$$[V_r] = [0\;\;0\;\;0\;0\;0\;\;\dots\dots\;\;0\;0]^t \tag{7.12}$$

$$[I_r] = [i_1 i_2 i_3 \dots\dots\; i_n i_e]^t \tag{7.13}$$

The equivalent rotor loop resistance matrix can be given by [160]

$$[R_r] = \begin{bmatrix} R_l & -R_b & \dots & -R_b \\ -R_b & R_l & \dots & 0 \\ \vdots & \vdots & \ddots & \vdots \\ -R_b & 0 & \dots & R_l \end{bmatrix} \tag{7.14}$$

Where $R_l = 2(R_b + R_e)$

The flux linkage by rotor loops can be written in matrix form as [158, 159]

$$[\lambda_r] = [L_r][I_r] + [L_{sr}][I_s] \tag{7.15}$$

Where L_s is the stator windings inductances matrix, L_r is the rotor inductances matrix of rotor loops and L_{sr} is the stator to rotor mutual.

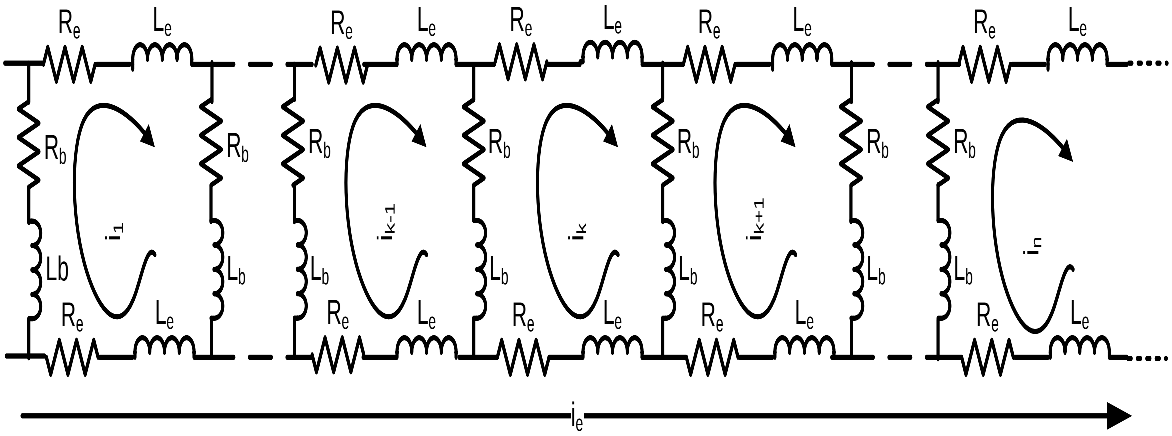

Figure 7.3-Equivalent Circuit of Squirrel Cage Rotor

By application of Kirchhoff's laws on the circuit described in Figure 7.3, the structure of rotor resistance matrix [R_r] and the rotor inductance matrix [L_r] can be simply derived. It seems clear that from the circuit below, the number of rotor loops are *n*+1(n loops + 1 end ring loop). These loops are coupled to each other and to stator phases. On the other hand, the end-ring loop does not couple with the stator phases and couples with the rotor loops only through the end-ring segment leakage inductance L_e and the end-ring segment resistance R_e. This because the end rings produce only axial fluxes (L_{ae}=L_{be}=L_{ce}=0).

With the aid of Figure 7.3 and From Equations (7.11) to (7.14), the voltage equation for any rotor loop k can be written as:

$$0 = 2(R_b + R_e).i_{rk} - R_b\left(i_{r(k-1)} + i_{r(k+1)}\right) - R_e i_e + 2(L_b + L_e)\frac{di_{rk}}{dt} - L_b\left(\frac{di_{r(k-1)}}{dt} + \frac{di_{r(k+1)}}{dt}\right) + \left(L_{k1}\frac{di_{r1}}{dt} + L_{k2}\frac{di_{r2}}{dt} + \cdots + L_{kk}\frac{di_{rk}}{dt} + \cdots + L_{kn}\frac{di_{rn}}{dt}\right) - L_e\frac{di_e}{dt} + \frac{d(L_{ak}i_a + L_{bk}i_b + L_{ck}i_c)}{dt} \tag{7.16}$$

It seems clear that for the symmetrical rotor, the steady state value of $i_e = 0$. Therefore the end ring voltage equation can be written as follows:

$$0 = nR_e i_e - R_e(i_{r1} + i_{r2} + \cdots + i_{rn}) + nL_e\frac{di_e}{dt} - L_e\left(\frac{di_{r1}}{dt} + \frac{di_{r2}}{dt} + \cdots + \frac{di_{rn}}{dt}\right) \tag{7.17}$$

7.2.2 Inductance Determination

The inductances formulas can be calculated by using winding function theory [161, 162]. The role of this method is to calculate motor inductance in terms of rotor angular speed. Therefore the motor inductances can be written as

$$L_a = L_b = L_c = \left(\frac{N_s}{2p}\right)^2\left(\frac{\pi\mu_o Lr}{g}\right) = L_{ms} \tag{7.18}$$

Where: L_{ms} is the magnetising inductance of the stator windings.

The mutual inductance between stator phases can be defined by:

$$L_{ab} = L_{bc} = L_{ca} = -\left(\frac{N_s}{2p}\right)^2\left(\frac{\pi\mu_o Lr}{2g}\right) = -\frac{L_{ms}}{2} \tag{7.19}$$

The self-inductance of the k^th^ loop can be written as

$$L_{kk} = \left(\frac{\alpha_r\mu_o Lr}{g}\right)\left(1 - \frac{\alpha_r}{2\pi}\right) \tag{7.20}$$

The mutual inductance between the kth and other loops

$$L_{k1} = L_{k2} = \cdots = L_{kn} = L_{ki} = -\left(\frac{\mu_o Lr}{g}\right)\frac{\alpha_r{}^2}{2\pi} \tag{7.21}$$

$$L_{ak} = L_m\cos\left(p(\theta_r + (k-1)\alpha_r + \delta)\right) \tag{7.22}$$

$$L_{bk} = L_m \cos\left(p(\theta_r + (k-1)\alpha_r + \delta) - \frac{2\pi}{3}\right) \tag{7.23}$$

$$L_{ck} = L_m \cos\left(p(\theta_r + (k-1)\alpha_r + \delta) + \frac{2\pi}{3}\right) \tag{7.24}$$

$$L_m = \left(\frac{4}{\pi N_s}\right) L_{ms} \sin\left(\frac{\alpha_r}{2}\right) \tag{7.25}$$

Where

$\alpha_r = (2\pi/n)$ = angle between any two adjacent bars and $\delta = \alpha r/2$.

$\theta_k = \theta_r + (k-1)\alpha_r$ = bar k angular position.

L_{ms} is the magnetising inductance for a stator winding

N_s is the effective number of turns of any stator phase

p is the number of pole pairs

μo is the permeability of air=$4\pi\times10^{-7}$ H/m

L is the effective length of the motor

r is the air gap average radius,

g is the air gap length

7.2.3 Mechanical Dynamic Equations

The mechanical system can be represented by the rotor speed equation. This equation depends on the characteristics of the load. For simplicity, the electromagnetic torque produced by the motor can be assumed to be the sum of an external and an inertial torque. Therefore the mechanical equation can be expressed as follows [163-167]

$$\frac{d\omega_{rm}}{dt} = \frac{T_{em} - T_L}{J} \tag{7.26}$$

Where:

ω_{rm} is the rotor speed in mechanical radian per second

J is the moment of inertia of the rotor (kg m^2)

T_{em} is the electromagnetic torque produced by the motor (N.m)

$T_L = \frac{P_m}{\omega_{rm}}$ is the maximum external load applied on the machine shaft (N.m), and

P_m is the mechanical power available on the rotor shaft at full load.

The electromagnetic torque T_{em} can be obtained by using the basic principle of energy conversion. This type of the torque can be determined by considering the change in co-energy W_{co} of the system produced by a small change in rotor position. As a result the electromagnetic torque can be expressed by deriving the co-energy to the rotor angle in the mechanical radian[168]:

$$T_{em} = \frac{dW_{CO}}{d\theta_{rm}} \tag{7.27}$$

Therefore the electromagnetic torque can be written as:

$$T_{em} = [i_s]^T \frac{\partial [L_{sr}]}{\partial \theta_r} [i_r] \tag{7.28}$$

$$T_{em} = \frac{1}{2} \begin{bmatrix} [I_s] \\ [I_r] \end{bmatrix}^T \frac{d}{d\theta} \begin{bmatrix} [L_s] & [L_{sr}] \\ [L_{rs}] & [L_r] \end{bmatrix} \begin{bmatrix} [I_s] \\ [I_r] \end{bmatrix} \tag{7.29}$$

Figure 7.4 shows the comparison between measured phase current signal and predicted signal of healthy motor under no-load condition and steady state.

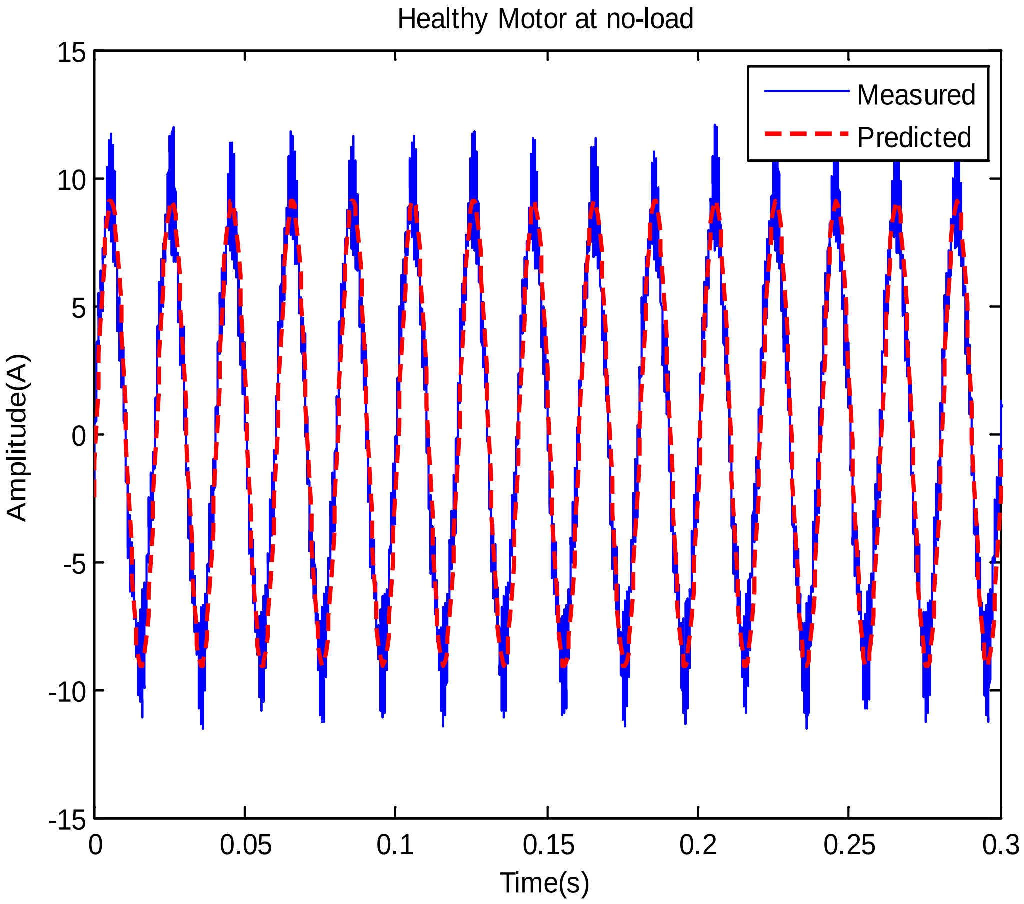

Figure 7.4-Measured and predicted value of phase current under no-load

7.3 Modelling of Broken Rotor Bar

7.3.1 Motor Modelling with One Broken Bar

As can be seen from Figure 7.5, the modelling of a broken bar or a ring segment of a short circuit occurs by increasing the value of its resistance so that the current crossing is the most close as possible to zero in steady state.

This is introduced in the matrix of resistances by the addition of the matrix of the rotor resistance [R_r] with one broken bar matrix [R_{1bb}]. In this study, the method of modelling by increasing the resistance of the broken bar, the value of this resistance is multiplied by a factor of $M = 10^3$ as well as bar k is assumed to be broken. Therefore all the elements in Equation

7.14 which relate to the broken bar k will be affected by this change. For this circumstance the resistance of broken bar (bar k) is given by [168, 169]:

$$R_{bk}=M\,R_b \tag{7.30}$$

The total resistance of the k and k-1 loops can be given by:

$$R_{k,k}=R_{k-1,k-1}=R_b(M+1)+2R_e \tag{7.31}$$

The matrix resistance of one broken bar can be expressed as follows:

$$[R_{1bb}]=\begin{bmatrix} 0 & 0 & 0 & \cdots & 0 \\ \vdots & 0 & 0 & \cdots & \vdots \\ \vdots & R_{k-1,k-1} & R_{k-1,k} & 0 & \vdots \\ 0 & R_{k,k-1} & R_{k,k} & 0 & \vdots \\ 0 & \cdots & \cdots & 0 & 0 \end{bmatrix} \tag{7.32}$$

The rotor bar inductance has only a small effect compared to the resistance and so this effect is ignored. This is because the rotor bar reactance is a function of the rotor frequency (f_r) which is very small during the steady state [170].

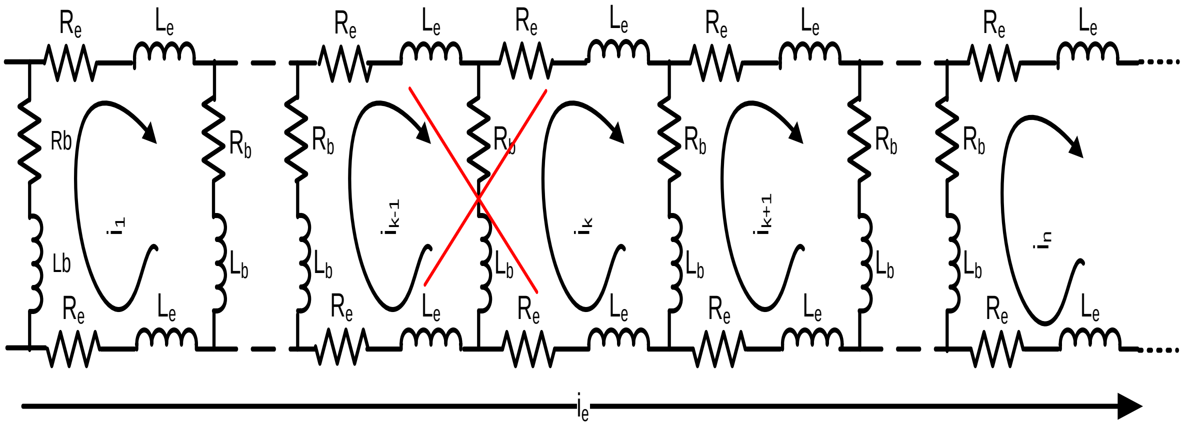

Figure 7.5-Equivalent Circuit of Rotor with One Broken Bar

7.3.2 Motor Modelling with Two Broken Bars

Figure 7.6 shows the modelling of two broken bars. As can be seen from the figure three loops are affected by the type of fault, namely loop k-1, k and k+1.

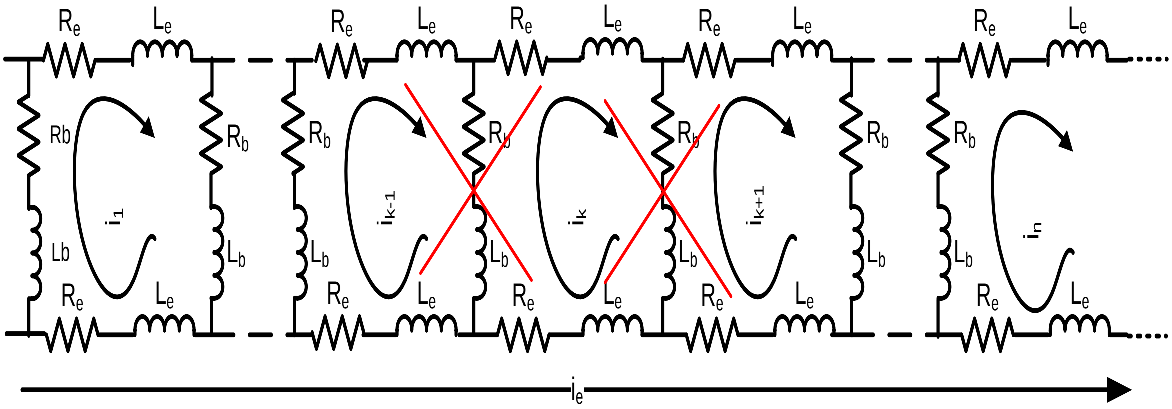

Figure 7.6-Equivalent Circuit of Rotor with Two Broken Bars

Therefore all the elements in Equation (7.14) which relate to the broken bar k and k+1 will be affected by this change. For this circumstance, the resistance of broken bar (bar k and bar k+1) is given by

$$R_{bk} = R_{bk+1} = M\,R_b \tag{7.33}$$

The total resistance of the k-1, k and k+1 loops can be given by:

$$R_{k-1,k-1} = R_{k,k} = R_{k+1,k+1} = R_b(M+1) + 2R_e \tag{7.34}$$

The matrix resistance of two broken bars can expressed as follows:

$$[R_{2bb}] = \left[\begin{array}{c|ccc|c} 0 & 0 & 0 & \cdots & 0 \\ \vdots & 0 & 0 & \cdots & \vdots \\ \cline{2-4} \vdots & R_{k-1,k-1} & R_{k-1,k} & 0 & \vdots \\ 0 & R_{k,k-1} & R_{k,k} & R_{k,k+1} & \vdots \\ 0 & 0 & R_{k+1,k} & R_{k+1,k+1} & 0 \\ \cline{2-4} 0 & \vdots & \vdots & \vdots & 0 \\ 0 & 0 & \cdots & 0 & 0 \end{array}\right] \tag{7.35}$$

7.4 Comparison of Model Based and Experimental Results

7.4.1 Model Parameters Estimation

Figure 7.7 shows the section of three phase induction. As can be seen from the figure the motor elements are seen clearly. As a result some of parameters of the motor can be measured easily.

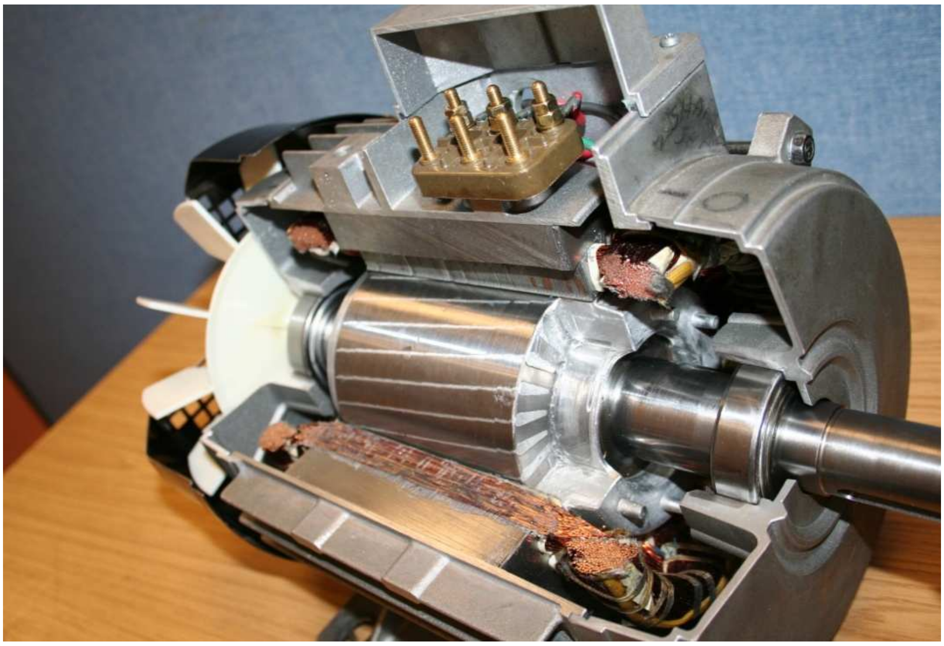

Figure 7.7-Induction Motor Section

The number of turns in a whole phase was determined by counting the number of copper turns in a slot (found to be 84 turns) dividing this number by 3 (as one phase consists of three conductors connected in parallel) and multiplying this result by half the number of slots per phase (as one complete winding turn occupies two stator slots):

$$\frac{84 \text{ turns per slot}}{3} \times \frac{1}{2} \times \frac{36}{3} \text{slots per phase} = 168 \text{ turns per phase} \qquad (7.36)$$

The proposed model in section 7.2 and section 7.3 is used as well as winding function theory to calculate inductances of the stator and the rotor; however some of the parameters are estimated. Table 7.1 illustrates the 4 kW induction motor parameters which were estimated and measured by help of motor section (see figure 7.7).

Parameter	value
Input supply phase voltage	240 V
Input supply frequency	50Hz
Number of stator slots	36
Effective number of Stator winding turns: Ns	168
Stator windings resistance: R_s	1.4 Ω
Stator windings leakage inductance: L_{ls}	0.007 H
Number of pole pairs: p	2
Number of rotor bars: N_b	28
Rotor bar resistance: R_b	98 μΩ
End ring segment resistance: R_e	7 μΩ
Rotor bar self-inductance: L_b	0.29 μH
End ring segment self-inductance: L_e	0.083 μH
Air gap average radius: r	51 mm
Air gap length: g	0.365 mm
Rotor effective length: L	120 mm
Power factor	0.8
Inertia: J	0.089N.sec^2

Table 7.1-Induction Motor Parameters

7.4.2 Monitoring the Motor Current under Healthy Condition

Figure 7.8, Figure 7.9, Figure 7.10 and Figure 7.11 show phase current signals in time domain of a healthy motor under different load, namely zero, 25%, 50% and 75% full load. As can be seen from the figures, as the load increases the current value increases as well. However, it seems clear that there is much noise in the measured value compared with predicted current value that is due to inverter processes converters.

Figure 7.12, Figure 7.13, Figure 7.14 and Figure 7.15 present the predicated and measured phase stator current spectrum of healthy motor under different loads. One can see from figures, the difference in amplitude of current spectra increase as the load increase.

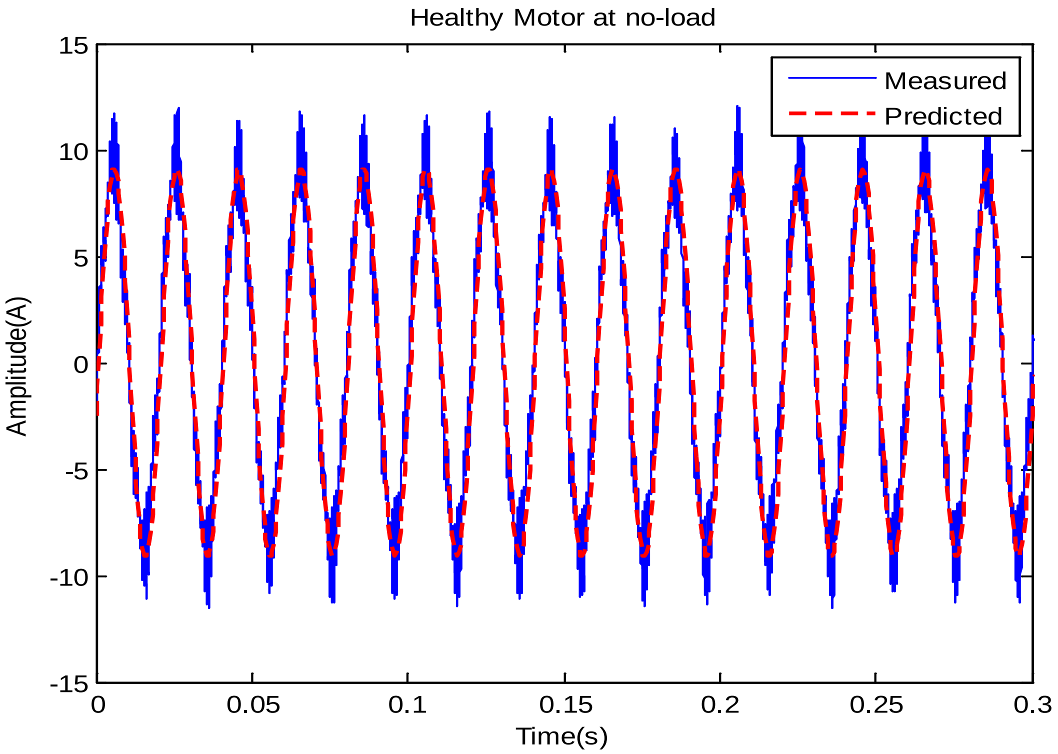

Figure 7.8-Phase Current of Healthy Motor under No-load

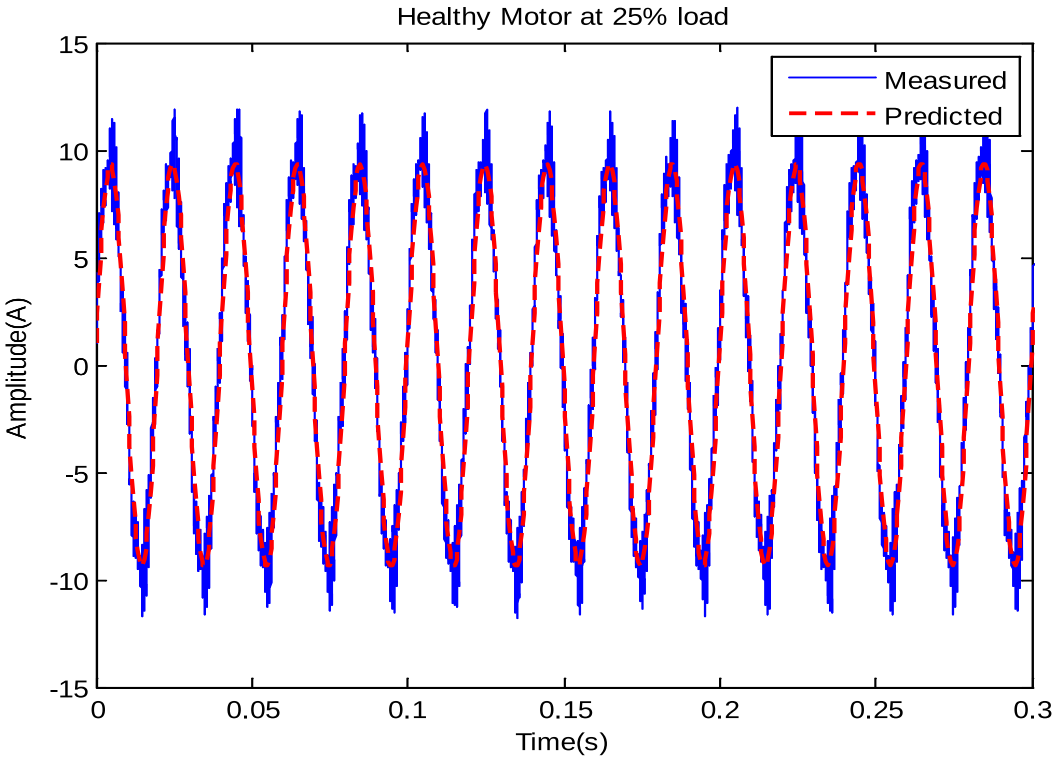

Figure 7.9-Phase Current of Healthy Motor under 25% Full Load

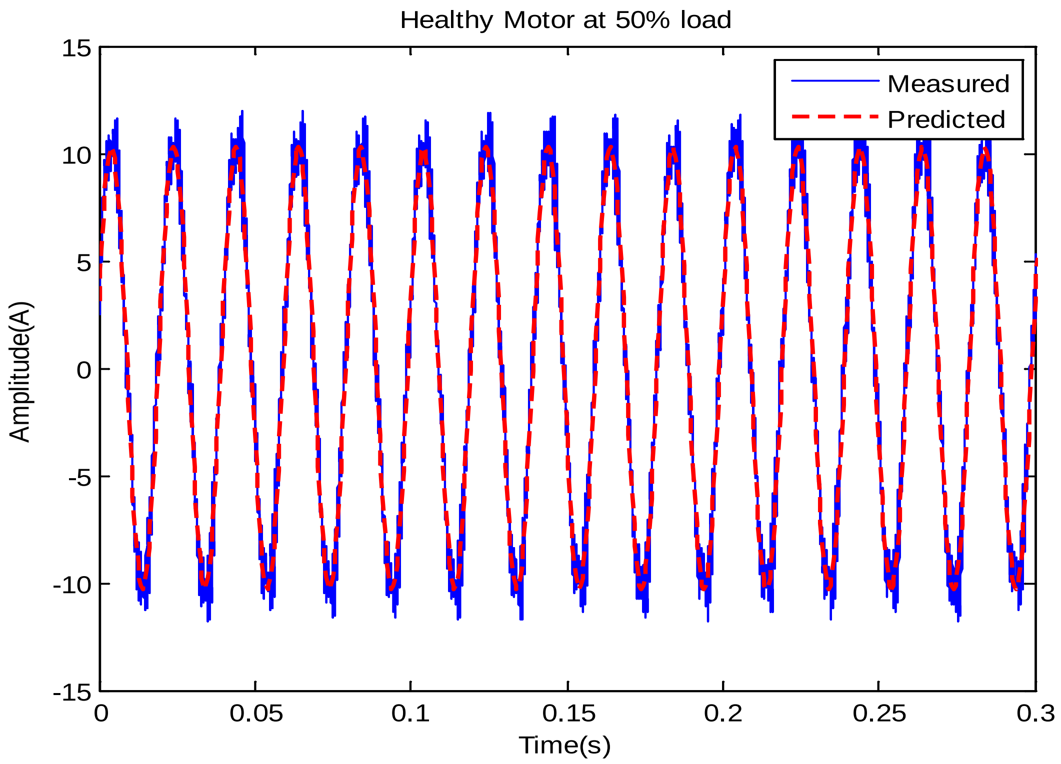

Figure 7.10-Phase Current of Healthy Motor under 50% Full Load

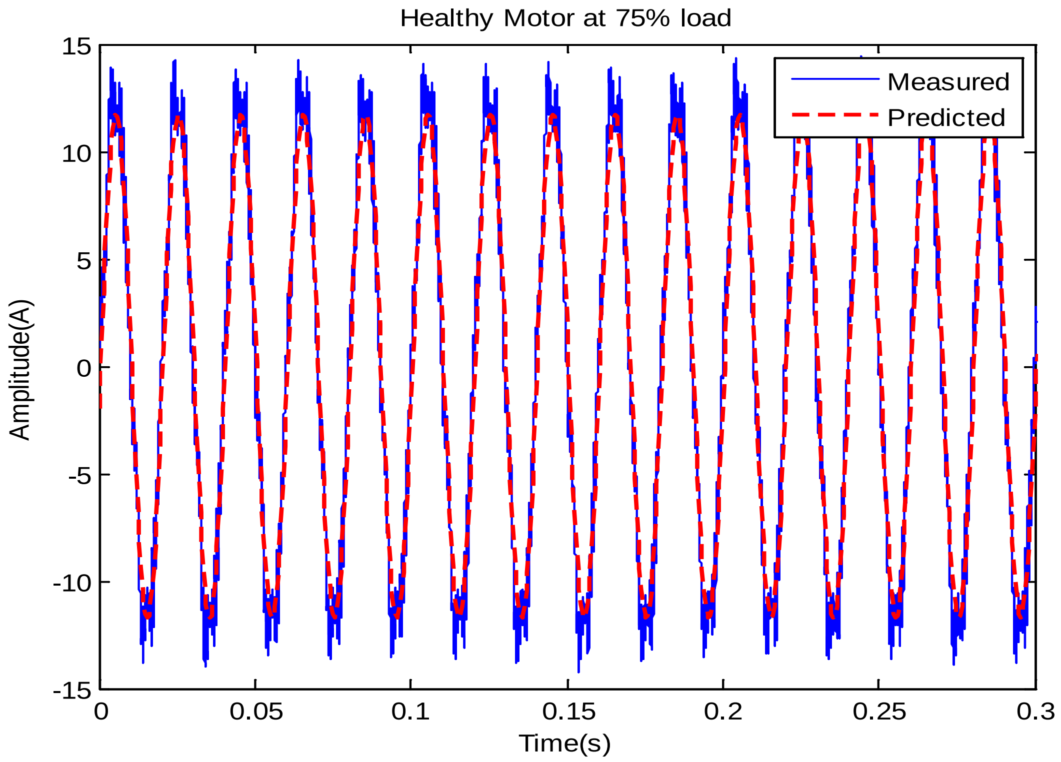

Figure 7.11-Phase Current of Healthy Motor under 75% Full Load

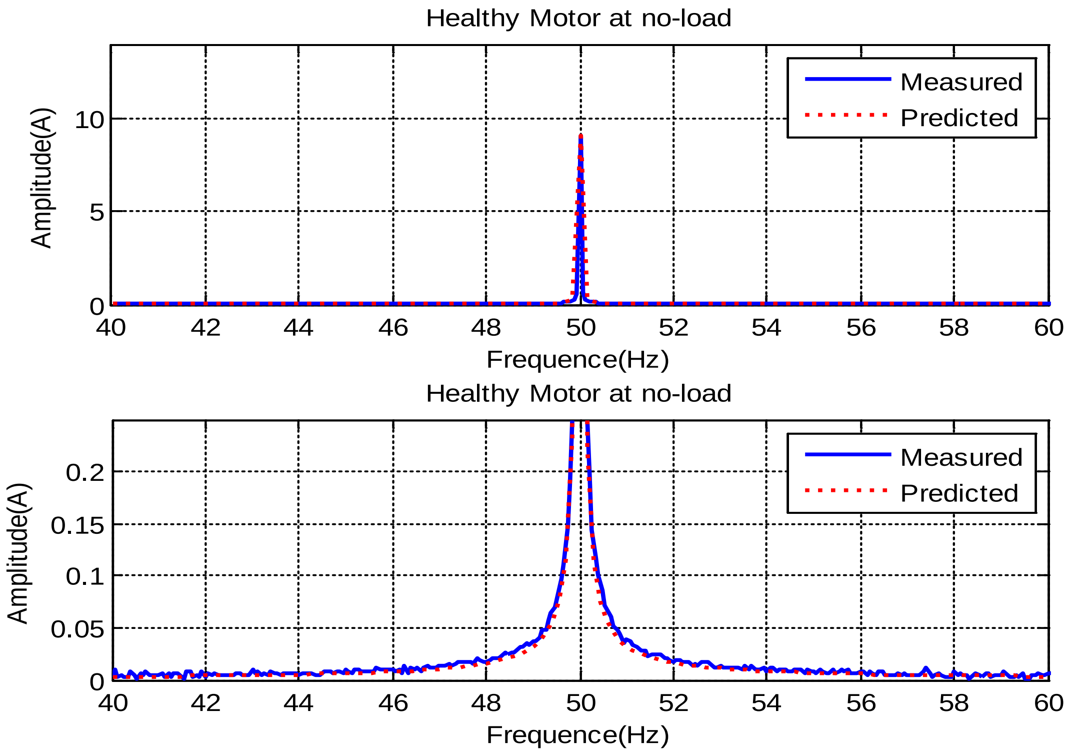

Figure 7.12-Phase Current Spectrum of Healthy Motor under No-load

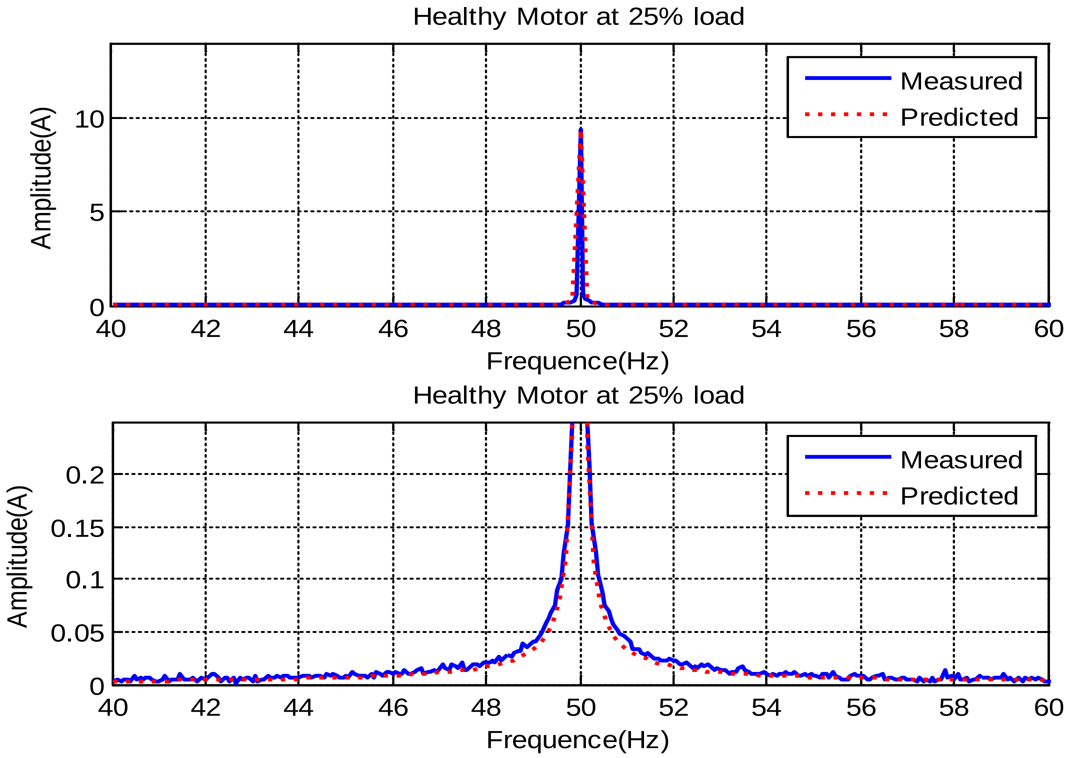

Figure 7.13-Phase Current Spectrum of Healthy Motor under 25% Full Load

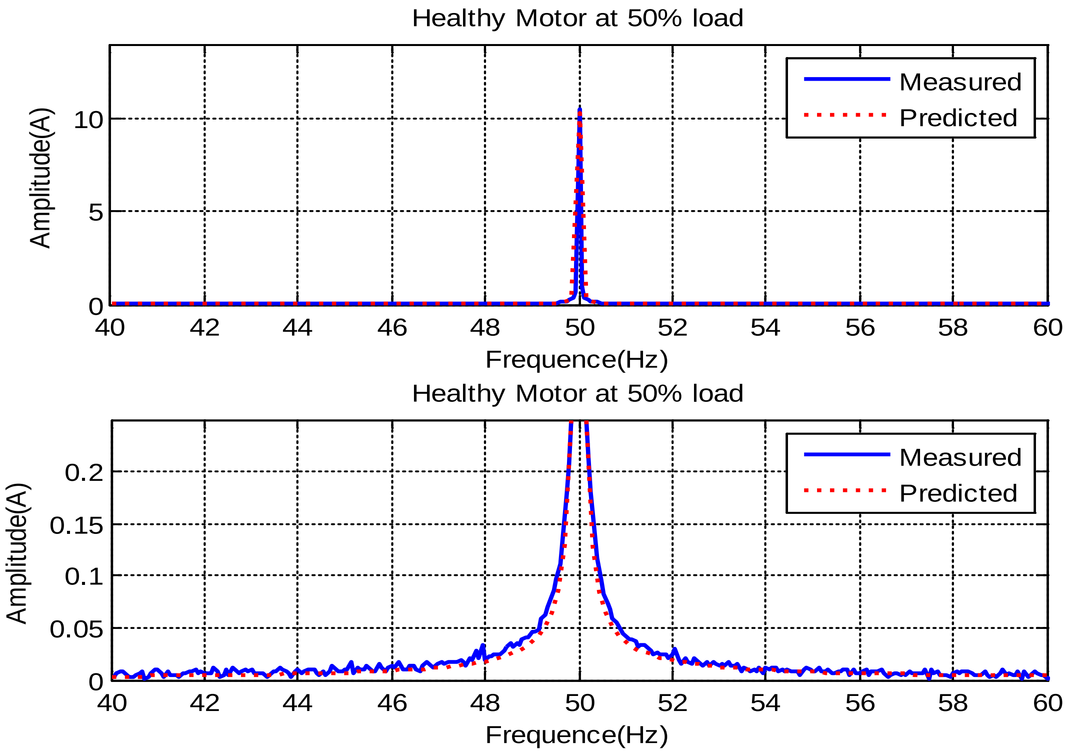

Figure 7.14-Phase Current Spectrum of Healthy Motor under 50% Full Load

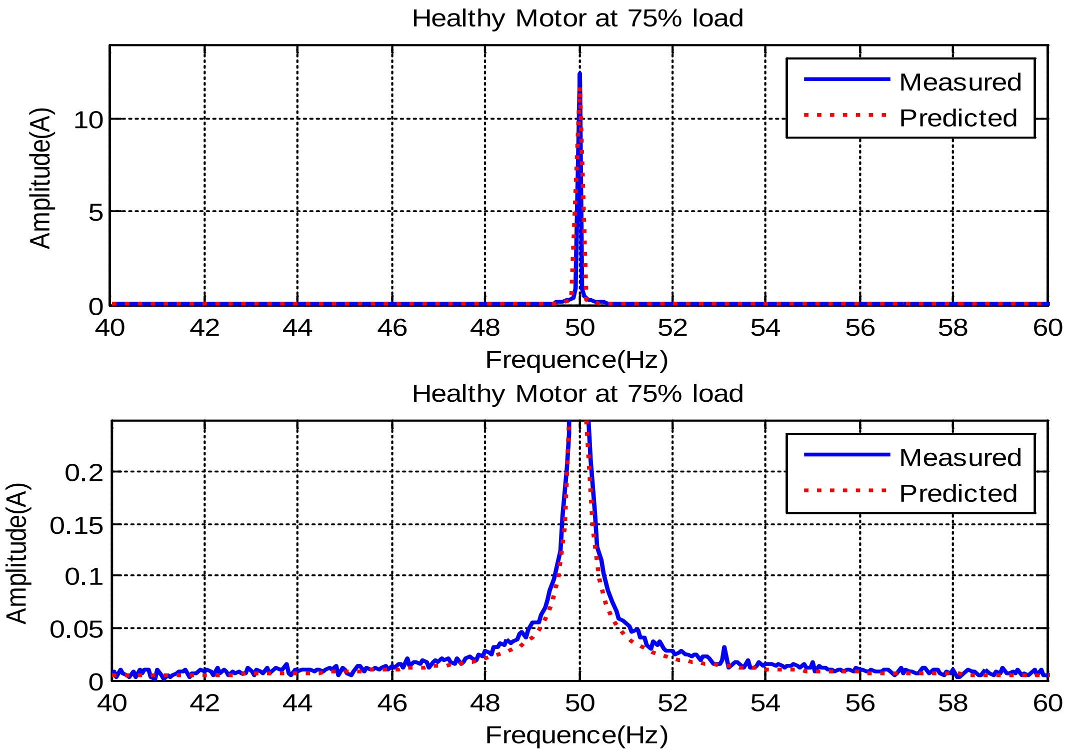

Figure 7.15-Phase Current Spectrum of Healthy Motor under 75% Full Load

7.4.3 Monitoring the Motor Current under Broken Bar Condition

7.4.3.1 One Broken Bar Current Signature

Figure 7.16, Figure 7.17, Figure 7.18 and Figure 7.19 show phase current signals in time domain of one broken bar motor under different load, namely zero, 25%, 50% and 75% full load. As can be seen from the figures, as load increases the current value increases as well. However, it seems clear that there is much noise in measured value compared with predicted current value that because of the inverter processes converters.

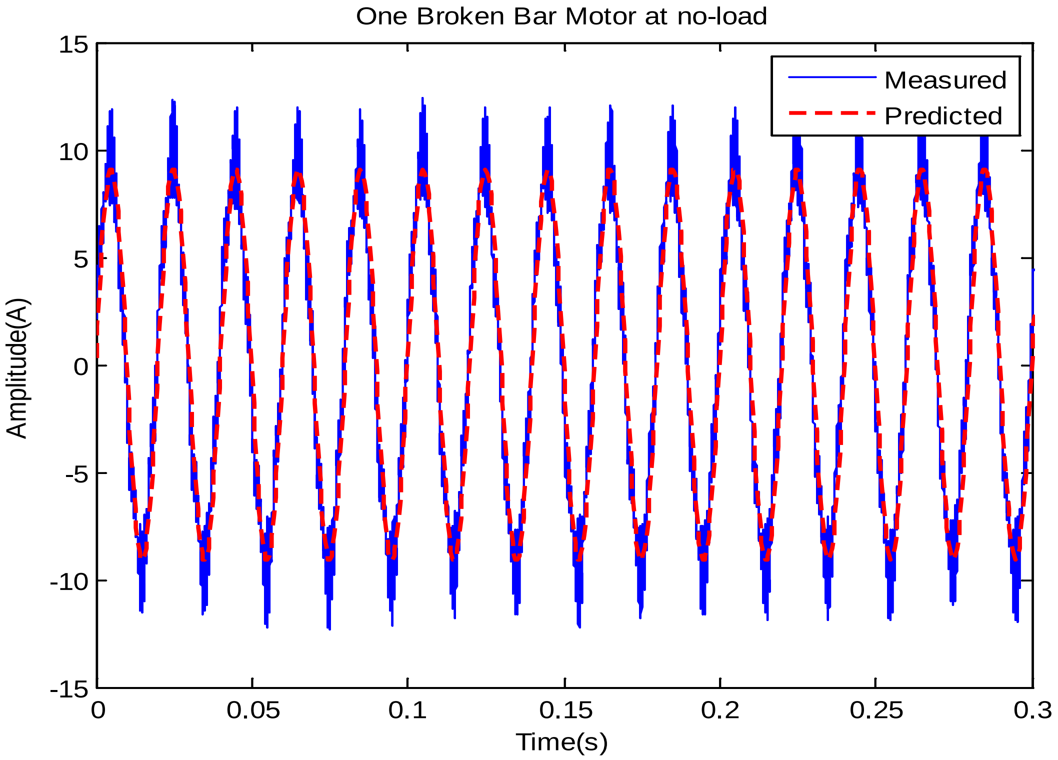

Figure 7.16-Phase Current of One Broken Bar Motor under No-load

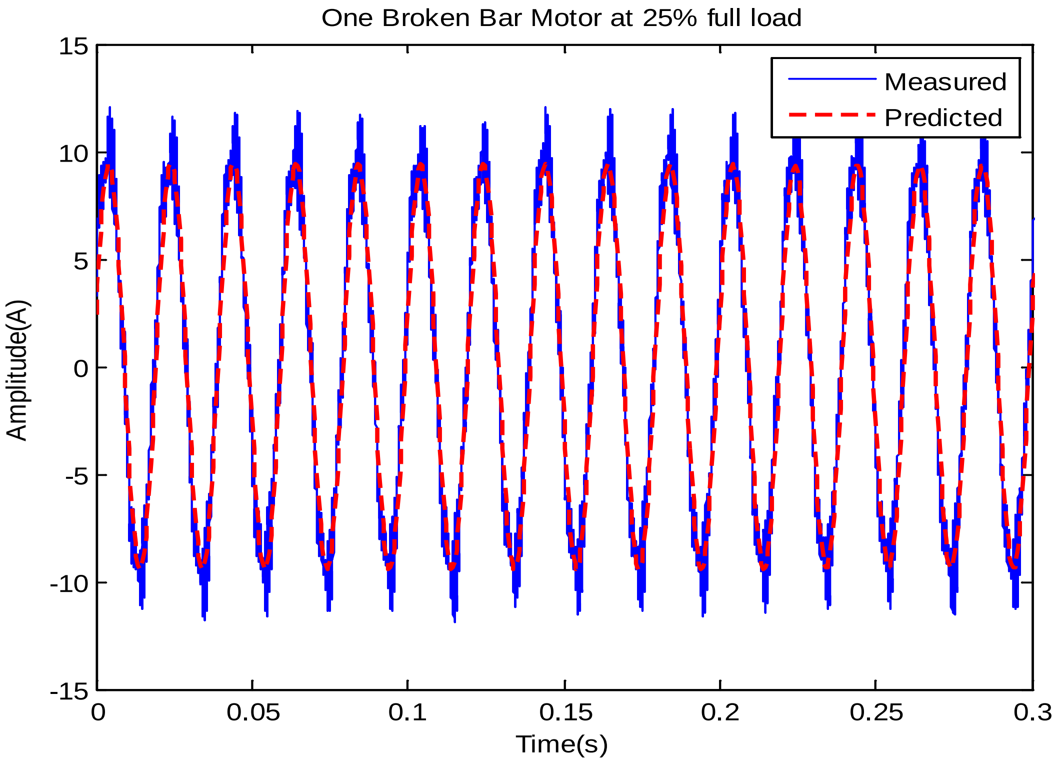

Figure 7.17-Phase Current of One Broken Bar Motor under 25% Full Load

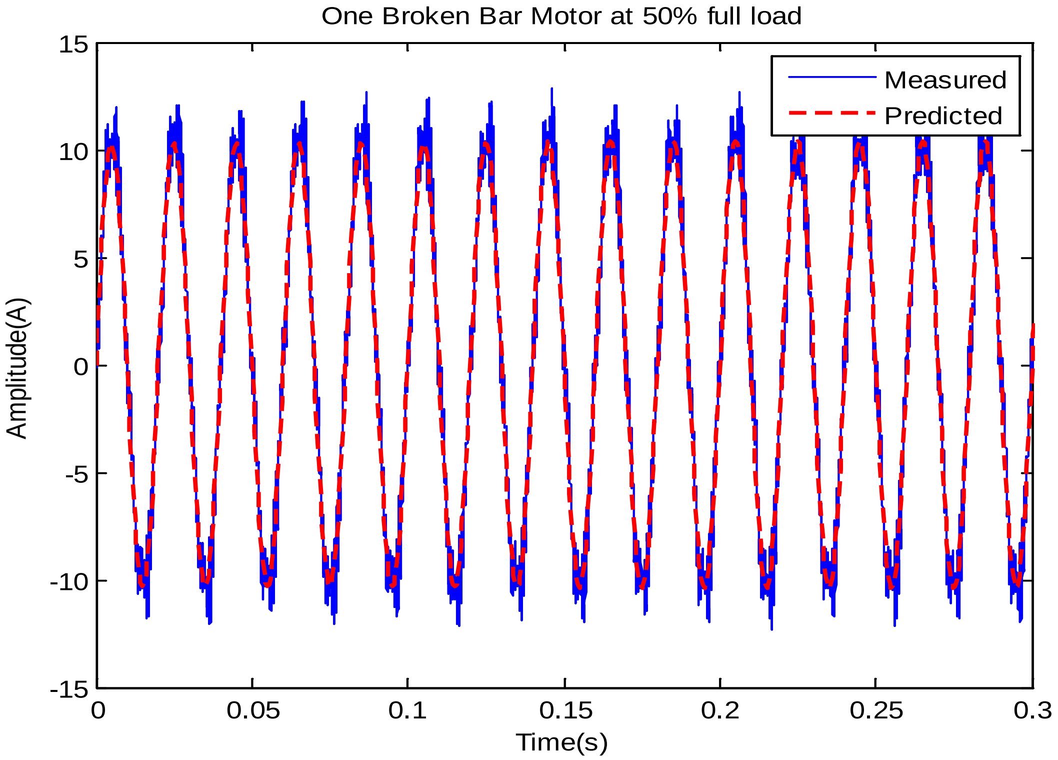

Figure 7.18-Phase Current of One Broken Bar Motor under 50% Full Load

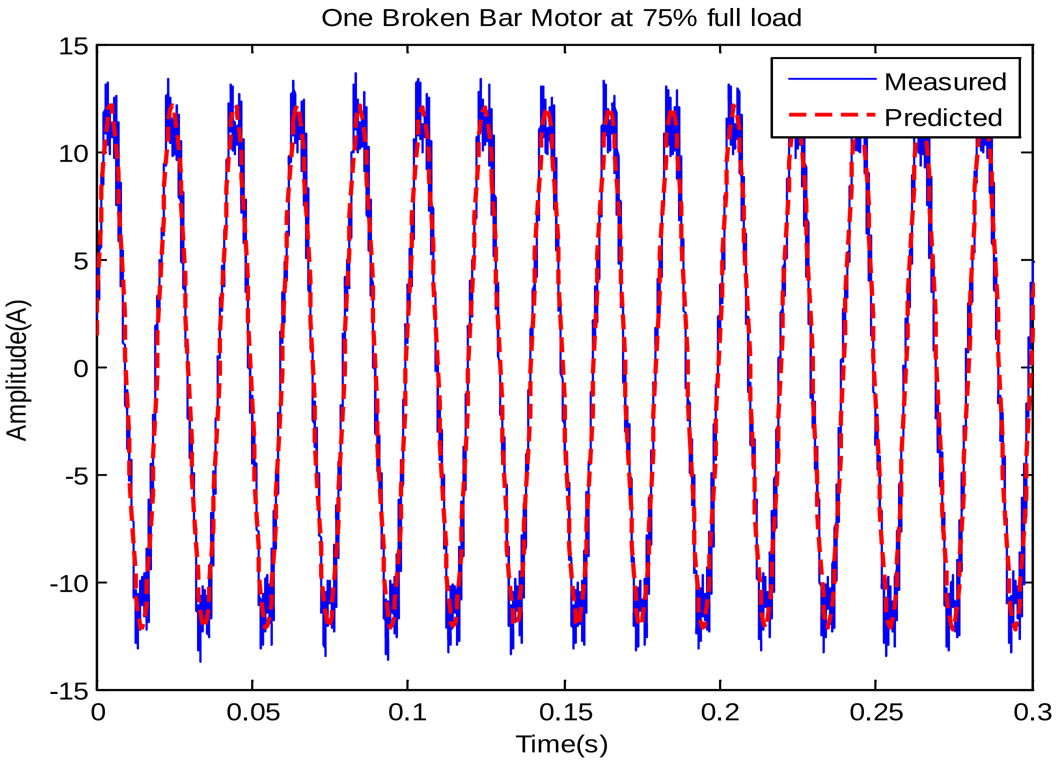

Figure 7.19-Phase Current of One Broken Bar Motor under 75% Full Load

Figure 7.20, Figure 7.21, Figure 7.22 and Figure 7.23 present the predicated and measured phase stator current spectrum of one broken rotor bar motor under different loads. It can be seen from the figures, the difference in amplitude of current spectra increase as the load increase.

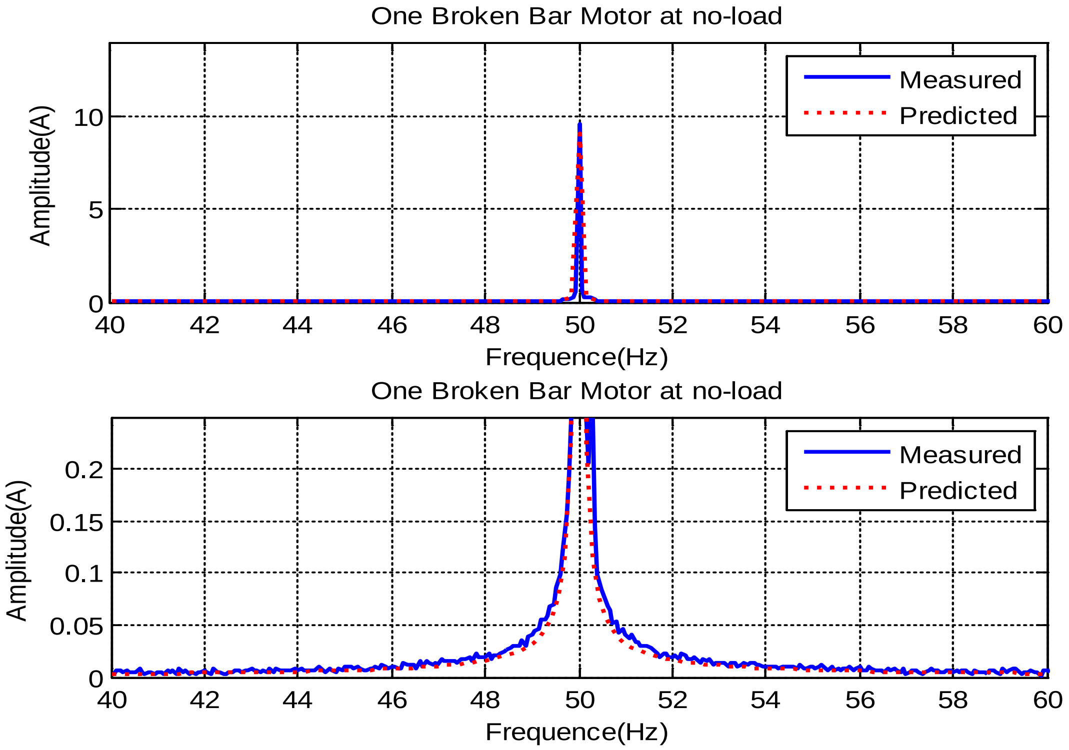

Figure 7.20-Phase Current Spectrum of One Broken Bar Motor under No-load

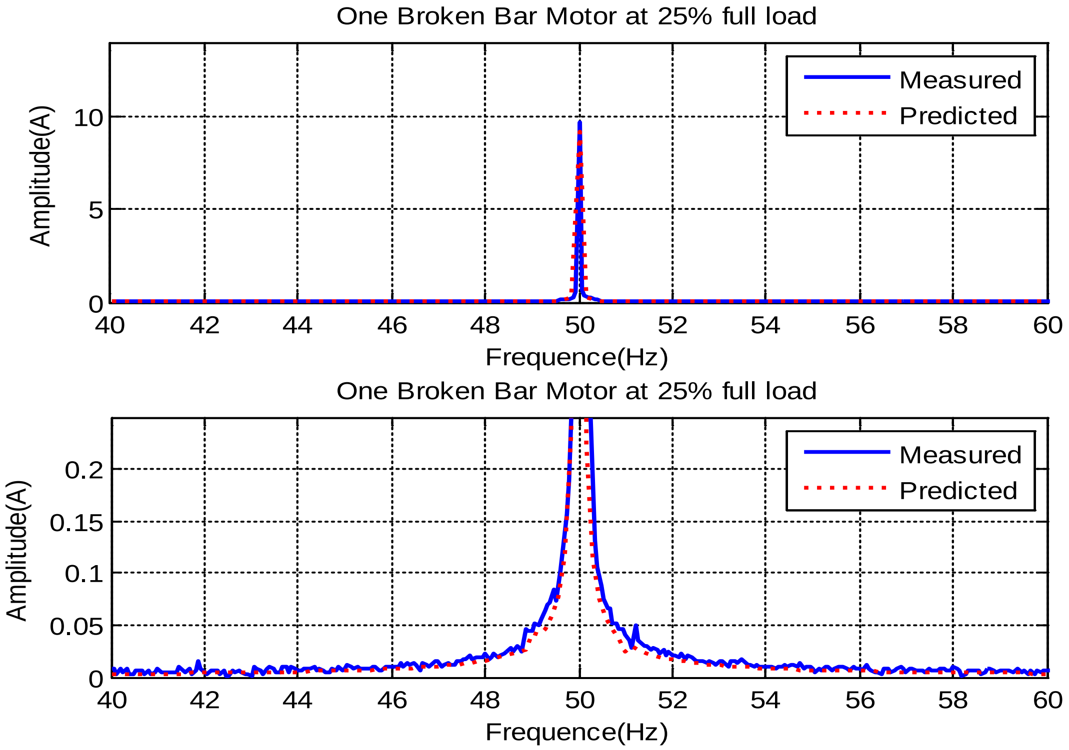

Figure 7.21-Phase Current Spectrum of One Broken Bar Motor under 25% Full Load

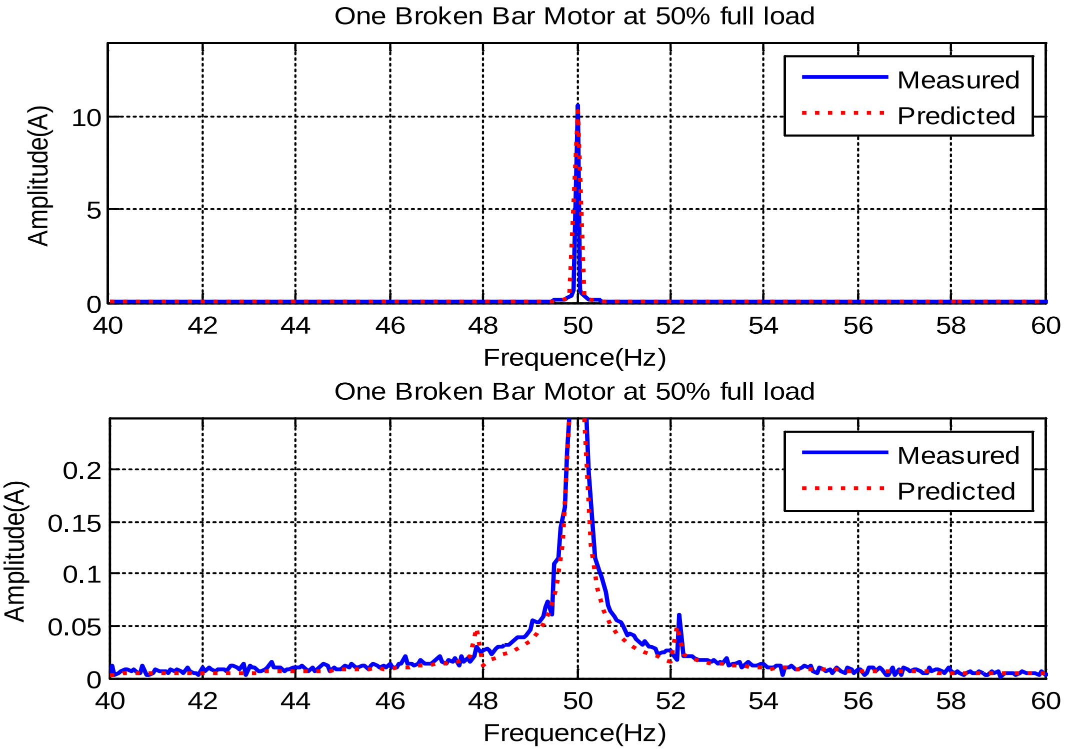

Figure 7.22-Phase Current Spectrum of One Broken Bar Motor under 50% Full Load

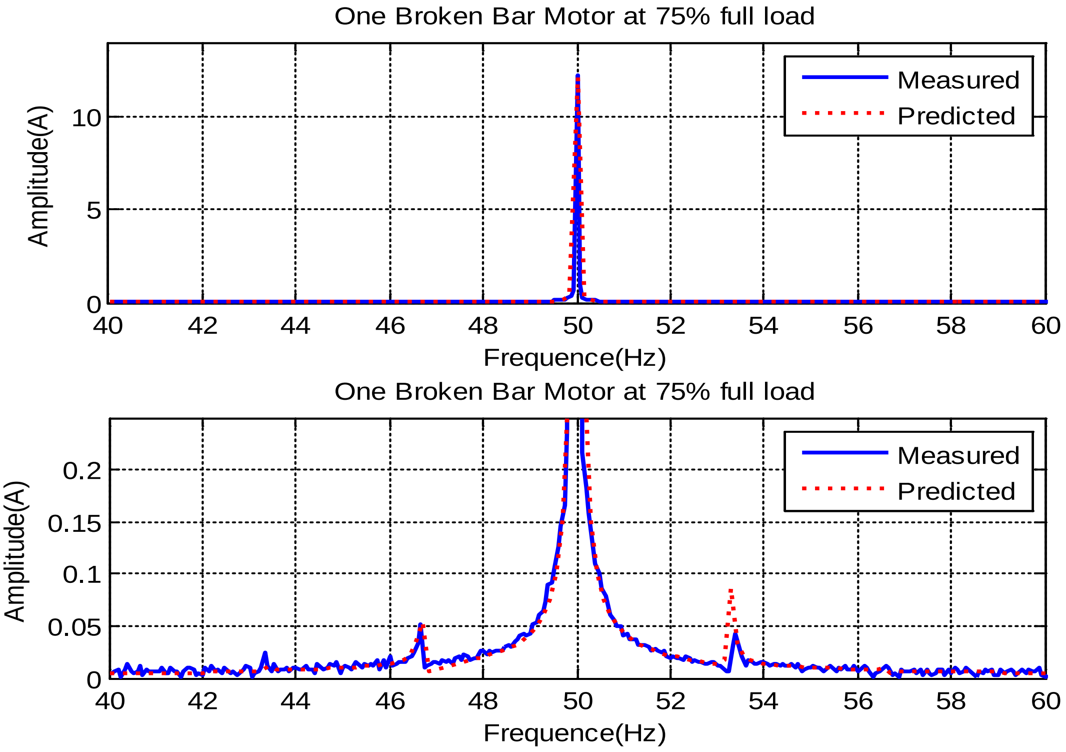

Figure 7.23-Phase Current Spectrum of One Broken Bar Motor under 75% Full Load

7.4.3.2 Two Broken Bar Current Signature

Figure 7.24, Figure 7.25, Figure 7.26 and Figure 8.27 show phase current signals in the time domain for a two broken bar case when the motor is under incremental loads: 0%, 25%, 50% and 75% of the rated load. As can be seen from these figures, the current values also increase with loads. However, it seems clearly that there is much noise in measured value compared with predicted current value that might be due to inverter processes converters.

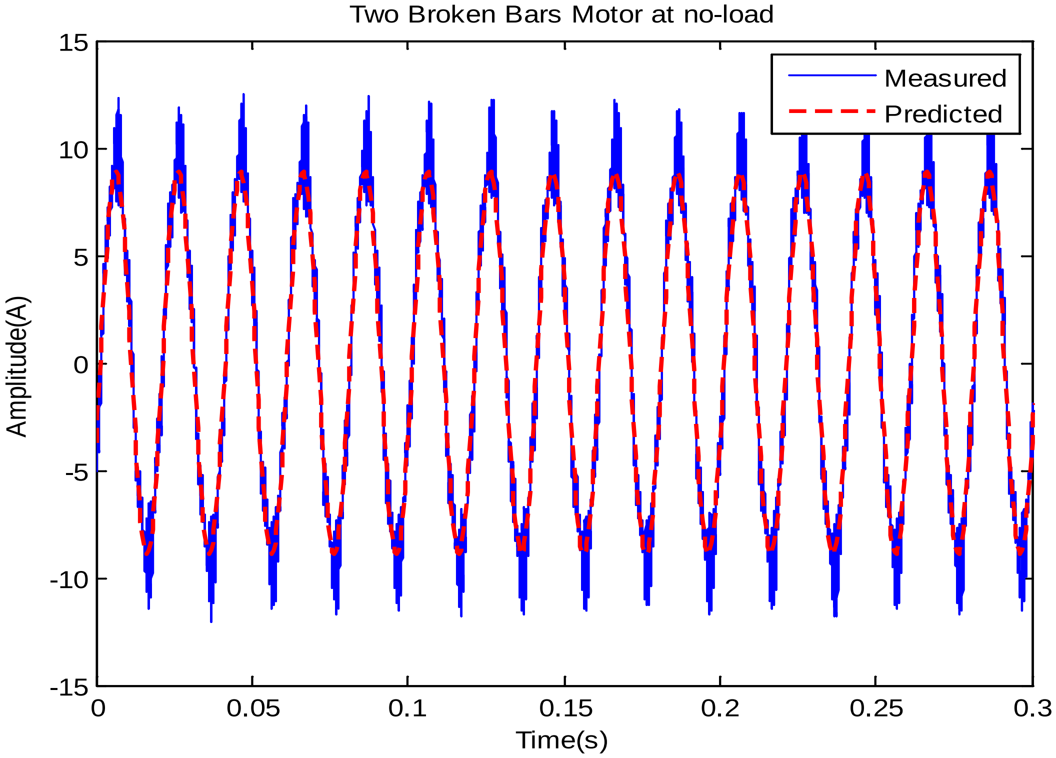

Figure 7.24-Phase Current of Two Broken Bars Motor under No-load

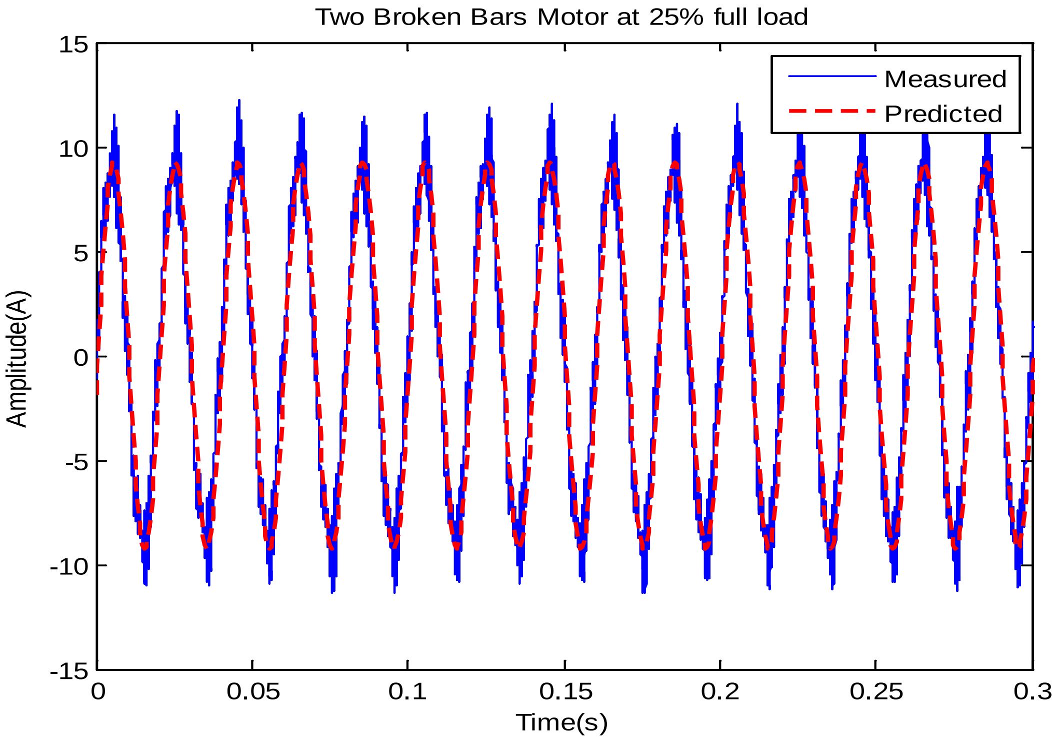

Figure 7.25-Phase Current of Two Broken Bars Motor under 25% Full Load

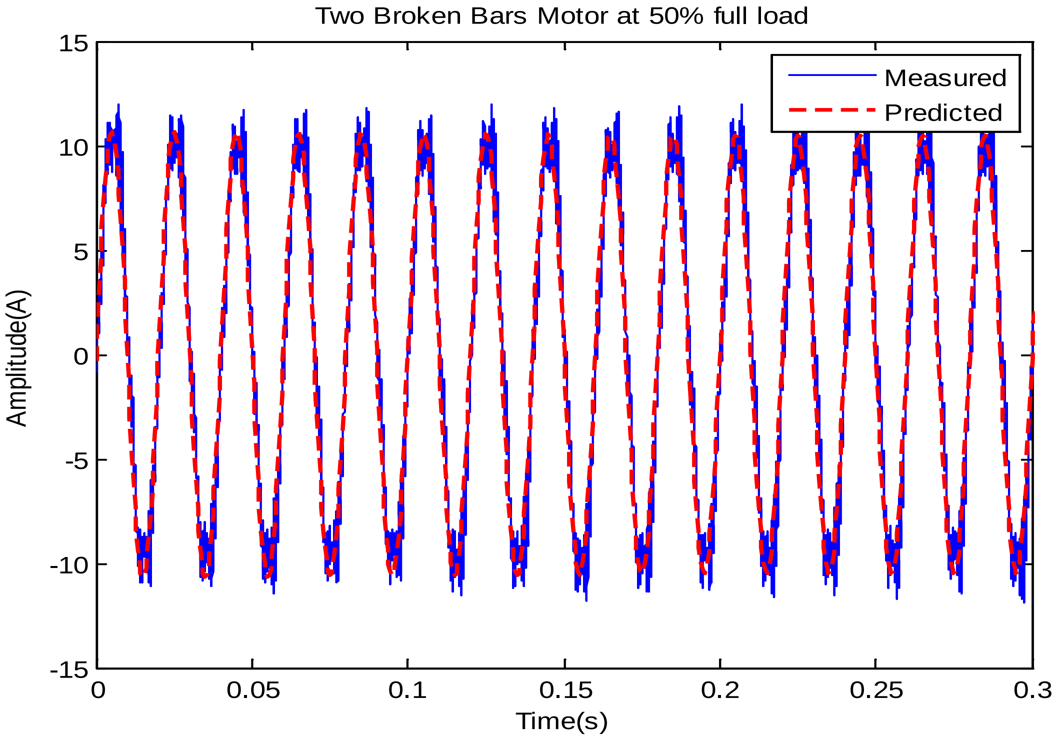

Figure 7.26-Phase Current of Two Broken Bars Motor under 50% Full Load

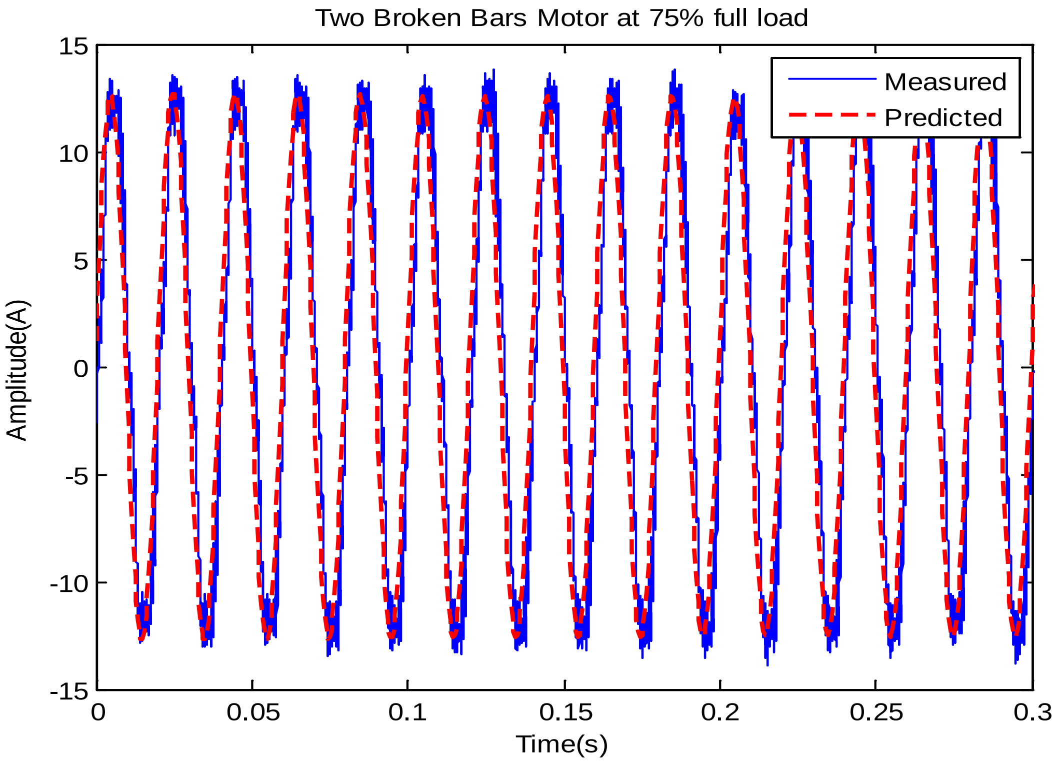

Figure 7.27-Phase Current of Two Broken Bars Motor under 75% Full Load

Figure 7.28, Figure 7.29, Figure 7.30 and Figure 7.31 present the predicated and measured phase stator current spectrum of two broken rotor bars motor under different loads. It can be seen from the figures, the difference in amplitude of current spectra increase as the load increase. However comparing with one broken bar figures, one can see the difference between current spectrums. Consequently, the amplitude of current spectra in the case of two broken bars was bigger than that in case of one broken bar.

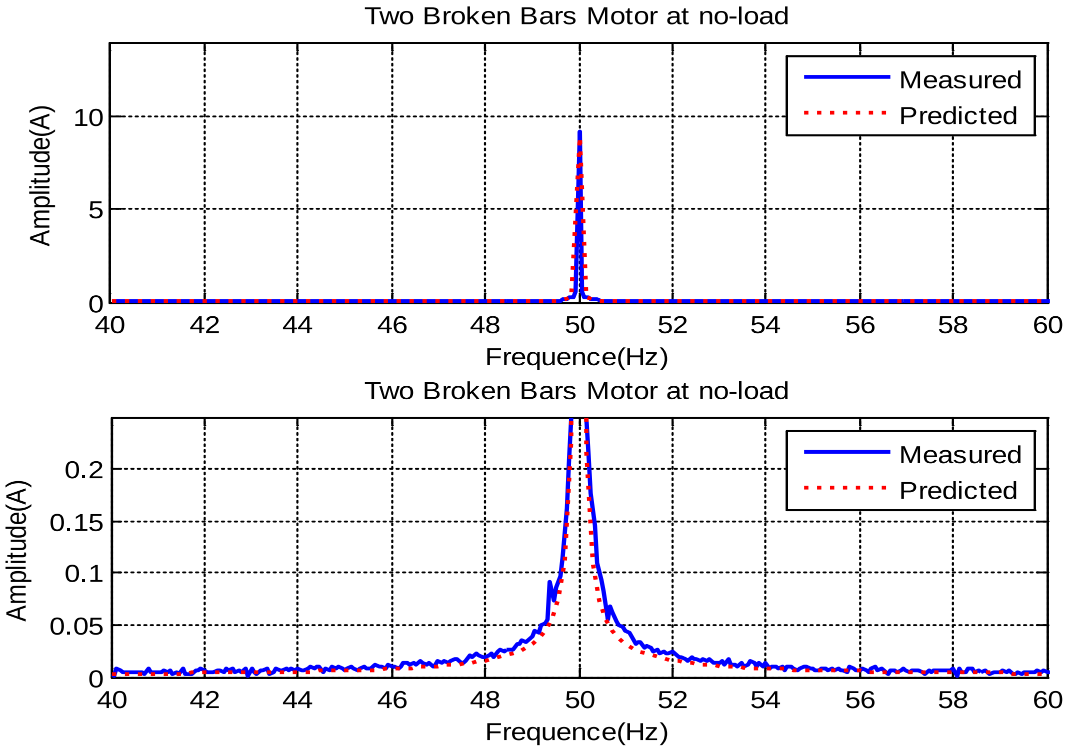

Figure 7.28-Phase Current Spectrum of Two Broken Bars Motor under No-load

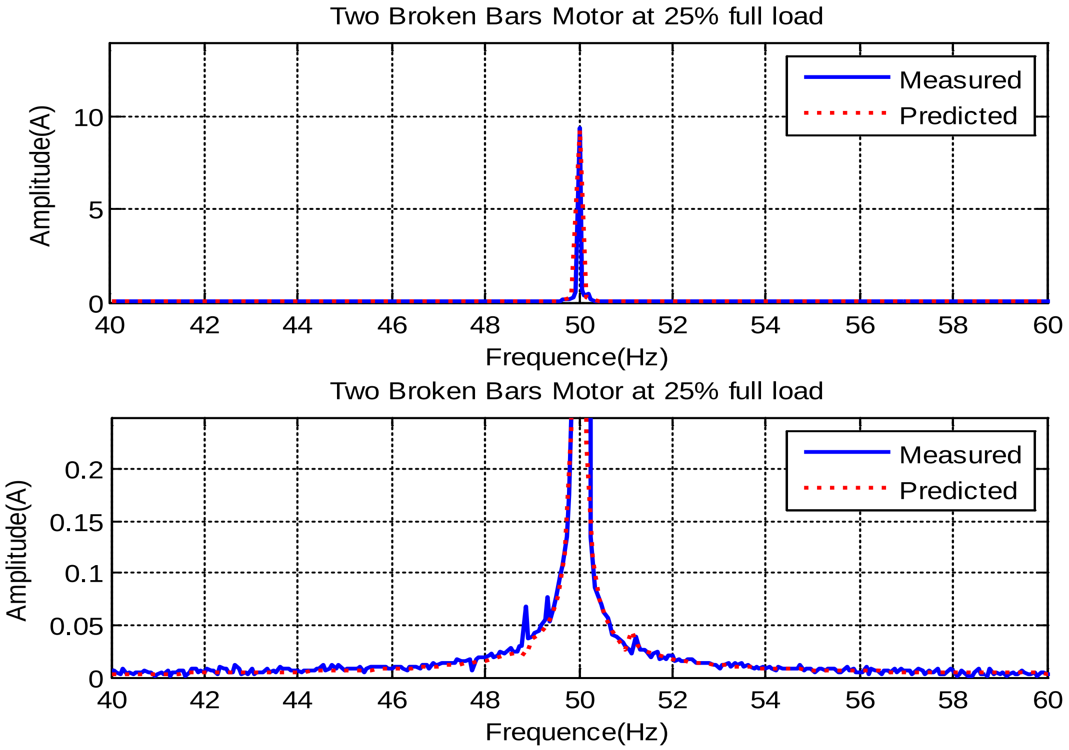

Figure 7.29-Phase Current Spectrum of Two Broken Bars Motor under 25% Full Load

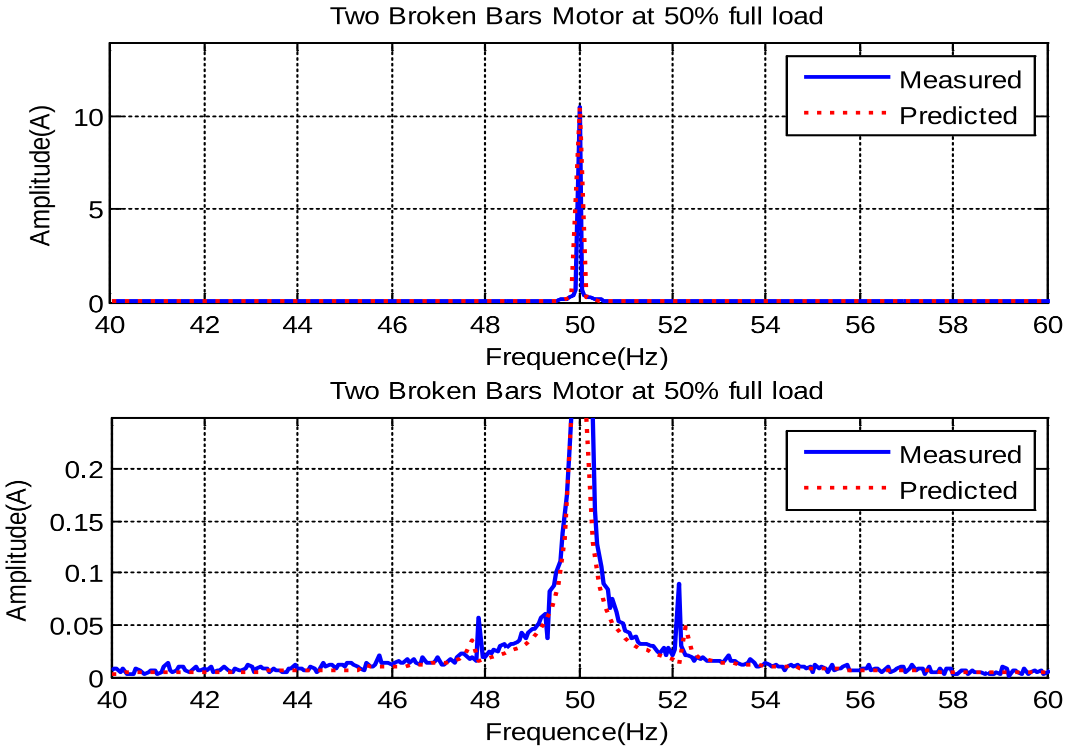

Figure 7.30-Phase Current Spectrum of Two Broken Bars Motor under 50% Full Load

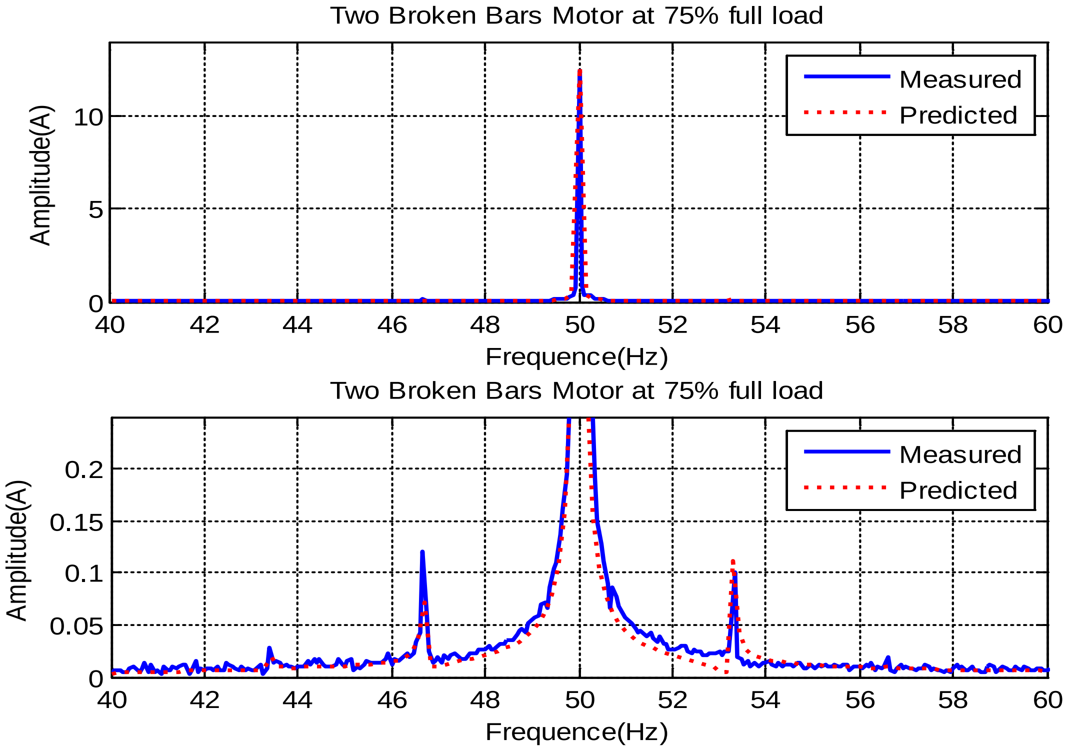

Figure 7.31-Phase Current Spectrum of Two Broken Bars Motor under 75% Full Load

7.5 Summary of Chapter 7

This chapter describes the three-phase, 4 Kw, 4 poles induction motor model. This mathematical model explains the voltage equations and flux linkage equation. Furthermore, it introduces the equations required for mechanical dynamic system modelling. In addition, it develops the healthy induction motor mathematical model in full. After that the mathematical model is described for one broken rotor bar and two broken bars and under zero, 25%, 50% and 75% of full load. Finally, the mathematical equations are solved numerically in a MATLAB environment to predict motor current signals. These predicted results are then compared with the equivalent measurements taken during the experimental tests. The achieved results allow the conclusion that the predicted results based on the model are very similar to the experimental results and so the motor current can play a significant role in the detection of motor faults such as stator and motor bearing faults under different operation conditions.

CHAPTER 8
CONCLUSION AND FUTURE WORK

In this chapter, a review of the objectives and achievements is presented. It starts by describing the achievements one by one by comparing them to the objectives for this study presented in Chapter 1. Next, a summary of the novel features is given, and then it describes the contributions to knowledge made by this research. Finally, the author presents his conclusions on the condition monitoring of Induction motor using motor current signature analysis and makes recommendations for future work.

8.1 Review of the Aims, Objectives and Achievements

This section describes how well this research project has met its original aim and objectives, and the new contributions to knowledge that it has made. The major achievements of this research are explained and linked with the original aim and objectives set out in Section 1.3.

Aim: The aim of the research in this thesis was to detect and diagnose faults in an induction motor using the MCSA of the electrical driving motor. The aim has been met, and it has been demonstrated that MCSA is a possible means to detect and distinguish between common electrical and mechanical faults in the induction motor. A novel procedure for the induction motor fault detection using modulation signal bispectrum analysis of motor power supply parameter has been developed. The key achievements of the research work recognised in this thesis are detailed below.

- ***Objective one***: To design and build a comprehensive motor test facility in which to seed faults and gain experimental data on subsequent system behaviour. This work will allow CM of the induction motor using such MCSA monitoring techniques as dynamic motor current signals. It will also allow specific faults to be seeded into the induction motor: broken rotor bar, open and short circuit on stator windings and motor bearing faults.

- ***Achievement One*****:** The test rig facility and data acquisition software were developed as detailed in Chapter 5. The system consists of an induction motor, variable speed controller, supporting bearings, couplings and DC generator as a load. The test motor is a three-phase induction motor with rated output power of 4 kW at speed 1420 rpm (two-pole pairs), 28 rotor bars and 36 stator slots. Six motors were used in this research with the same specification and different health conditions. Consequently the atmosphere in which the practical research work conducted was similar to an industrial environment and practical induction motor applications. A number of measurement transducers were used on the test rig to monitor the function of the motor CM. Furthermore, the test rig was used to provide experimental data for testing the mathematical model of the induction motor (Chapter 7). Finally, designs for the motor test rig were provided for use in other research projects.

- ***Objective Two*****:** To enable the controlled seed of a variety of chosen fault conditions in a test facility and to seed each fault in a range of severities. These faults include the electrical and mechanical faults of induction motors, namely: broken rotor bar, stator winding fault and motor bearings fault. The effect of these faults on the performance of a three-phase squirrel cage induction motor was investigated.

- ***Achievement Two*****:** Three of the most common faults in induction motor were successfully seeded into the test rig. Firstly, Three BRB cases with different BRB severities and one baseline case were tested under the same operating conditions. As illustrated in Section 5.3.1, the first BRB case is a motor with half BRB which was created by drilling a hole into one of the 28 bars up to the half depth of a bar. The second is one complete bar breakage created by drilling the hole to the full depth of the bar. And the third is two continuous bar breakage which was induced by drilling two bars side by side to their full depth. These three fault cases were induced in three different motors with the same specifications and they were tested to have close baseline signatures before the faults were created on their rotors. Secondly, two stator faults were seeded for open and short circuit in Section 5.3.2.1 and 5.3.2.2 respectively. The open circuit on stator winding was made by Lawton Electrical Services LTD (LESL).

Two types of open circuit were achieved by removing one or two conductors of stator phase. Repeating the experiment with different fault severities (one and two conductors removal) and different operating conditions (speeds 100% and loads zero%, 25%, 50% and 75% of full load) were studied. The reproducibility of the results obtained was tested by repeating the experiment with the same faults many times under the same operating conditions. For short circuit in the stator winding current signals were collected under two different stator winding configurations, a healthy motor and two inter turn short circuit in first coil in phase A under two successive load conditions: 0% and 25% of full load. This allows the diagnostic performance to be examined at different loads and avoid any possible damages of the test system at the full load when the faults are simulated. Finally, two types of common bearing faults have been tested in this study as shown in Section 5.3.3. The first one, an abrasive wear in the outer race has been considered; which models that caused by friction between ball and outer race surfaces due to lack of lubrication, while the second case of fault is an inner race defect. To examine the influence of the operating condition on fault diagnosis performance, electrical current signals were measured under loads: 0%, 25%, 50% and 75% of the full operating load.

- ***Objective Three*****:** To collect and analyse motor current data from a healthy motor to establish a baseline profile for use in fault detection and then compare the spectral content of the motor current signal from a healthy motor with a known fault. To categorise the differences between MCSA with and without a fault, to establish a link between specific faults and the corresponding differences in the motor current signature.

- ***Achievement Three*****:** With the healthy Induction motor, the baseline motor current spectrum was established and discussed in Section 6.2. Effective experiments have been carried out to monitor the frequencies of the current spectra of a healthy motor. Frequencies at which they occur were predicted precisely. This method is believed to be one of the first successful attempts to establish a detailed baseline spectrum for the detection and diagnosis of faults within induction motor using motor current signature analysis.

- ***Objective four*****:** to evaluate motor temperature influence on motor current signal.

- ***Achievement Four*****:** To demonstrate the relationship between slip and temperature of the induction motor, motor temperature test was performed in the lab. The healthy motor ran at full speed and 50% of full load for ten minutes and data was collected each minute (see Figure 6.2). The results show the temperature and motor slip gradually increase during the test.

- ***Objective Five*****:** To examine the VFD operation mode on the motor current signals.

- ***Achievement Five*****:** the baseline motor and one broken bar were tested under slip compensation and non-slip compensation and under four load conditions as shown in Section 6.3.2. The results shown that the slip compensation technique of speed control does not monitor the actual shaft speed for speed adjustment; relatively it uses drive output current transducers to monitor the current drawn by the motor and alters the main frequency so that the motor speed can maintain desired speed as steady as possible. However, because of inevitable load fluctuations the main supply frequency realised in this way will have some fluctuations accordingly, or it is not as stable as that without slip compensation. Additionally, with the slip compensation operation it is not clear that the spectra under different loads have the sideband pattern, meaning that traditional MCSA techniques are not suitable for detecting the broken bar faults in these circumstances and hence new approaches have to be investigated.

- ***Objective Six***: To examine the motor current signature using different traditional signal processing techniques such as convention bispectrum (CB) and a new method which depends on side band estimation by using modulation signal bispectrum (MSB-SE).

- ***Achievement Six:*** In order to evaluate motor current signals, the three different datasets are processed for baseline and three different broken rotor bar cases and different loads to obtain CB and MSB-SE simultaneously for comparisons. In calculating DFT, a Hanning data window is applied to the data segment to minimise the side lobes of DFT and spectrum leakage. In addition, a 40% overlap between segments is used; the number of averages is set to more than 100, in order to effectively suppress noise and interference. Moreover, a single Matlab function is developed to calculate CB and MSB simultaneously according to Equation 4.3 and Equation 4.12 respectively, which ensures their performance to be compared under the same base. The results of CM and MSB-SE are examined with in a frequency range from 0 to 80Hz which is common for detection of rotor faults, and are presented as proper surface graphs, to give effective representation of the key features in the results (see Figure 6.8 and Figure 6.9). The results show that MSB-SE allows the three different cases of broken rotor bar to be detected and diagnosed by using the change of MSB-SE magnitudes. However, CB is unable to capture any of these faulty components by either its magnitude or coherence results and then it is not sufficient to diagnose motor faults with a motor current signal.

- ***Objective Seven*:** To analyse and examine the motor current signature by the application of MSB-SE and compare it with conventional PS.

- ***Achievement Seven:*** motor current signals were collected for baseline and different motor faults and under different loads. The results of PS and MSB-SE were tested at characteristic frequency of each fault which studied in Chapter 5. The results of broken rotor bar, stator faults and motor bearing faults show that MSB-SE demonstrates the faults much more clearly, and that makes it easier to identify. Furthermore, it is more accurate to quantify the characteristic frequency of different induction motor faults to produce more accurate diagnostic results as shown in Chapter 6.

- ***Objective Eight*:** To evaluate the possibilities of model-based fault detection and diagnosis using a mathematical model. A model for three-phase squirrel cage induction motor will be developed for normal and abnormal operating conditions. The abnormal conditions will include broken rotor faults. Each operating condition will be simulated at different load conditions.

- ***AchievementEight*:** the use of the motor current signature of broken motor bar has been studied using a numerical simulation based on construction of the three phase induction motor which used in the test rig. The model started with describing healthy motor and then applied this model on broken rotor bar. The model consists of thirty two equations (three equations describe stator volts, twenty nine describe rotor and end-ring volts) as shown in section 7.2. These equations were derived by Kirchhoff's law and presented in matrix forms. The inductances of the motor were calculated by using winding function theory as shown in section 7.2.2. Additionally the motor was modelled under one and two broken bars and different loads. Finally, the results of both predicted and experimental were compared and shown that the model predictions and experimental results were in agreement with one another (see Section 7.4)

- ***Objective Nine*:** To provide directions and guide lines for future research in this field.

- ***AchievementNine*:** Section 8.5, below gives a number of useful paths for future work on Condition Monitoring of induction motors using different seeded faults, and using the same techniques developed in this research.

8.2 Conclusions on the Induction Motor CM using MCSA

From the research work and results reported in this thesis it is possible to conclude the following:

8.2.1 Conclusion on Induction Motor Rotor Faults Current Signature

- ***Conclusion one:*** Faults on the rotor of electrical motors cause additional components which modulate the fundamental supply component and lead to a nonlinear phase current signal. In a power spectrum they exhibit as asymmetric sidebands around the supply frequency. To extract these components in noise signals, a new MSB-SE estimator can be applied to measured signals to suppress inevitable noise components and non-modulating components for obtaining a more accurate measure of the modulation. Because of its success on BRB this new method was applied on other motor faults such as stator faults and motor bearing faults.

- ***Conclusion Two:*** MSB-SE analysis is particularly effective as it takes into account the sideband phase information and results in a more accurate estimation of the sideband magnitudes by suppressing the random noise influences from the motor operation and the measurement process.

- ***Conclusion Three:*** The accuracy of MSB-SE is much higher when compared with that of CB and PS.

- ***Conclusion Four:*** MSB-SE allows the three different severities of BRB to be detected and diagnosed by using the change of MSB magnitudes. However, CB is unable to capture any of these faulty components by either its magnitude or coherence results and then it is not sufficient to diagnose motor faults with motor current signal.

- ***Conclusion Five:*** In the case of power spectrum, spectral peaks appear at frequencies at ($f_s \pm 2sf_s$) and increase as the load and fault increases. In a similar way, the phase current bispectrum also increase in amplitudes with load and fault severity but they appear at ($2sf_s$).

- ***Conclusion Six:*** A simple model of an induction motor has been developed to simulate squirrel cage rotor faults. The model represents an induction motor with one broken and two broken bars. The model was validated against a set of results obtained from the experimental measurements (see Sections 7.4). The achieved results allow the conclusion that the predicted results, based on the model, are very similar to the experimental results and so the motor current can play a significant role in the detection of motor faults such as stator and motor bearing faults under different operation conditions.

8.2.2 Conclusion on Induction Motor Stator Faults Current signature

- ***Conclusion One:*** The stator fault causes the amplitude changes and frequency shifts at the characteristic frequency which can be represented by diagnostic features: modulation ratio and slip respectively.

- ***Conclusion Two:*** MSB-SE modulation ratio produces a full separation of different motor cases whereas power spectrum can only separate the two-coil removal case. This shows that MSB has a better performance in diagnostic stator faults.

- ***Conclusion Three:*** Simultaneously, both MSB slip and power spectrum slip values can be used as a basis for diagnostic under high load conditions even if for the two coil removal case and for short circuit, showing that it performs relatively poorer and is not suitable to be used as a diagnostic feature under stator faults.

- ***Conclusion Four:*** n the case of power spectrum, spectral peaks appear at bar passing frequencies at ($f_s \pm N_b * f_r$) and increase as the load and fault increases. In addition, the frequency values decrease slightly as the fault severity increases because of changing in flux due to motor temperature. In a similar way, the phase current bispectrum sidebands also increase in amplitudes with load but they appear at ($N_b * f_r$).

- ***Conclusion Five:*** MSB-SE has no modulation influences which shows the faults more clearly, which would make it easier to identify and more accurate to quantify the characteristic frequency of different stator fault to produce more accurate diagnostic results.

8.2.3 Conclusion on Induction Motor Bearing Faults

- ***Conclusion one:*** MSB-SE analysis is evaluated using motor current signals to detect and diagnose motor bearing faults. From its spectrum presentations, it can be found that MSB shows a simpler spectrum structure compared with the power spectrum. It means that MSB shows peaks only at kf_o and kf_i for outer race and inner race faults respectively, whereas power spectrum shows peaks at ($f_s \pm kf_o$) and ($f_s \pm kf_i$) which can cause difficulty to identify them when the spectrum components are rich. Moreover, MSB produces a more accurate amplitude estimate due to its capability of noise reduction and non-modulation component removal.

- ***Conclusion Two:*** With MSB-SE analysis the motor current can be used to detect and diagnose bearing faults when the motor operates without VFD controller under no-load condition. The VFD induces too much noise into the system and it is not possible to discriminate the small bearing component for condition monitoring.

- ***Conclusion Three:*** The bearing fault causes amplitude increases at the characteristic frequencies corresponding to outer race and inner race faults. MSB-SE produces a reliable difference at these frequencies whereas PS only provides change evidences at some of the frequencies. This shows that MSB has a better performance in extracting small changes from the faulty bearing for fault detection and diagnosis.

8.3 Novel Feature Summary and Contribution to Knowledge

The research project presented in this thesis incorporated a number of important issues that were novel and not previously implemented by other researchers or practitioners. These aspects of novelty are summarised below.

- **Novelty One:**

The author of this thesis believes that the way in which motor current signal has been examined using advanced analysis techniques which are dependent on modulation signal bispectrum sideband estimation. This new method was applied on the motor current to detect and diagnose electrical and mechanical motor faults. After that it was compared with conventional power spectrum analysis under different loads as shown in Chapter 6.

- **Novelty Two:**

The motor current cannot be used to detect and diagnosis bearing faults when the motor operates with VFD controller. The VFD induces too much noise into the system and it is not possible to discriminate the small bearing component for condition monitoring. Therefore with small bearing fault severity detection the motor should be connected to main supply directly without control.

- **Novelty Three:**

Although VFD operation under slip compensation keeps the motor speed constant, it is unable to monitor motor current signal for motor fault detection. So a *v/f* open loop controller was used to drive the motor for motor fault detection using MCSA.

8.4 Contributions to Knowledge

❖ *First Contribution*

The application MSB-SE of motor current signal for recognition and diagnosis of induction motor faults has not been undertaken before and hence the research work developed in this thesis is believed to be the first to explore applications of MCSA to the detection of induction motor faults under steady state circumstances. The MCSA detection technique is able to detect reciprocating induction motor faults in a reliable style, at low cost, and rapidly.

❖ *Second Contribution*

The author of this research believes that the research work in this thesis is the first work to examine the specific changes in motor performance that take place when a fault occurs on rotor bars, stator winding or motor bearing and the impact on the motor current signal spectrum.

❖ *Third Contribution*

There are no previous reports in the literature of the use of the bispectrum based on sideband estimation for fault detection and fault diagnosis of an induction motor and which compare this new method with conventional power spectrum.

❖ *Fourth Contribution*

A mathematical model for motor current signals under rotor fault conditions and an effective method to decouple the BRB current which interferes with that of speed oscillations associated with BRB to provide theoretical supports for the new estimators and clarify the issues in using conventional bispectrum analysis has not previously been approached in this way.

8.5 Recommendations for Future Work

To monitor successfully an induction motor using MCSA, further development is needed of the detection of different types of faults with different levels of severity. This work should include three items: an investigational study, signal processing and modelling. The use of frequency, demodulation, and bispectrum analyses for MCSA has proved to be sufficient to detect faults in a motor fed by VFD, and can be depended on to provide information about the induction motor condition monitoring. The author of this thesis now makes a number of recommendations for research to enhance the CM of induction motors using MCSA.

- ***Recommendation One*****:** The research should be extended to other motor driven machinery such as pumps, fans, gearboxes, machine tools etc.

- ***Recommendation Two*****:** The MCSA spectrum of induction machines exhibits frequency components due, for example, to an inverter which may overlap with frequency components created by motor faults. An efficient method to separate these frequency components from each other needs to be investigated.

- ***Recommendation Three*****:** More study is needed to evaluate the sensitivity and consistency of the proposed detection technique on an induction motor fed by VFD, e.g. to achieve a better understanding of the effect of the inverter on the induction motor electrical power parameters.

- ***Recommendation Four*****:** The induction motor used in this research is fed by v/f controller. Therefore it is expected to get significant results by using motor voltage technique for motor fault detection.

- ***Recommendation Five*****:** a new statistical technique has been applied on motor current in this thesis to detect and diagnose induction motor faults as shown in Chapter 6. It is recommended that this method can be applied on motor current to diagnose other motor faults such as eccentricity.

- ***Recommendation Six*****:** The VFD induces too much noise into the system when it is used with the VFD controller to detect motor bearing faults and it is not possible to differentiate the small bearing component for condition monitoring (Section 6.5). It is recommended that a new method should be used to eliminate this noise when the tested motor is connected to the VFD.

- ***Recommendation Seven*****:** The modelling of induction motor in this research is for a broken rotor bar. However the model of VFD driver is not considered. It is recommended that this model should be extended to include stator fault, motor bearing faults with VFD model. It would also be possible to apply MSD-SE of motor current.

- ***Recommendation Eight*****:** It is recommended that further academic research should be conducted on the utilisation of the motor vibration to detect the induction motor faults. It would also be possible to apply MSB-SE to investigate the possibility of monitoring motor faults in a similar way that used in this thesis.

8.6 Publications

[1] A. Alwodai, F. Gu, and A. Ball, "Motor Current Signature Analysis of a Variable Speed Drive for Motor Fault Diagnosis," in *Proceedings of the 24th COMADEM2011*, 2011, pp. 884–892.

[2] A. Alwodai, F. Gu and A. Ball, "A Comparison of Different Techniques for Induction Motor Rotor Fault Diagnosis." vol. 364, ed: Journal of Physics: Conference Series, 364. 012066. ISSN 1742-6596, 2012.

[3] A. Alwodai, Y. Shao, X. Yuan, M. Ahmed, F. Gu, and A. D. Ball, "Inter-turn short circuit detection based on modulation signal bispectrum analysis of motor current signals," in In: Proceedings of the 19th International Conference on Automation and Computing (ICAC), Brunel University, London, UK. ISBN 978-1908549082, Brunel University, London, UK, 2013.

[4] A. Alwodai, X. Yuan, Y. Shao, F. Gu and A. D. Ball, "Modulation signal bispectrum analysis of motor current signals for stator fault diagnosis," in 18th International Conference on Automation and Computing (ICAC), Loughborough, UK, 2012, pp. 1-6.

[5] A. Alwodai, T. Wang, Z. Chen, F. Gu and A. Ball, "A Study of Motor Bearing Fault Diagnosis using Modulation Signal Bispectrum Analysis of Motor Current Signals," Journal of signal and information processing, vol. 4, p. 72, 2013.

References

[1] F. Gu, Y. Shao, N. Hu, and A. D. Ball, "Electrical motor current signal analysis using a modified bispectrum for fault diagnosis of downstream mechanical equipment," *Mechanical Systems and Signal Processing* vol. 25, pp. 360–372, 2011.

[2] A. Stefani, "Induction Motor Diagnosis in Variable Speed Drives," PhD, Electrical Engineering, University of Bologna 2010.

[3] A. Bellini, F. Filippetti, C. Tassoni, and G. A. Capolino, "Advances in Diagnostic Techniques for Induction Machines," *Industrial Electronics, IEEE Transactions on,* vol. 55, pp. 4109-4126, 2008.

[4] S. Nandi, H. AToliyat, and X. D. Li, "Condition Monitoring and Fault diagnosis of ElectricalMotors-A Review," *IEEE Trans. Energy Convers,* pp. 719-729, 2005.

[5] M. El Hachemi Benbouzid, "A review of induction motors signature analysis as a medium for faults detection," *Industrial Electronics, IEEE Transactions on,* vol. 47, pp. 984-993, 2000.

[6] R. M. Tallam, L. Sang-Bin, G. C. Stone, G. B. Kliman, Y. Ji-Yoon, T. G. Habetler, *et al.*, "A Survey of Methods for Detection of Stator-Related Faults in Induction Machines," *Industry Applications, IEEE Transactions on,* vol. 43, pp. 920-933, 2007.

[7] P. J. Tavner and J. Penman, *Condition monitoring of electrical machines*. Hertfordshire, England: Research Studies Press Ltd, 1987.

[8] W. Long, T. G. Habetler, and R. G. Harley, "A Review of Separating Mechanical Load Effects from Rotor Faults Detection in Induction Motors," in *Diagnostics for Electric Machines, Power Electronics and Drives, 2007. SDEMPED 2007. IEEE International Symposium on,* 2007, pp. 221-225.

[9] W. Li and C. K. Mechefske, "Detection of Induction Motor Faults: A Comparison of Stator Current, Vibration and Acoustic Methods," *Journal of Vibration and Control,* vol. 12, pp. 165-188, 2006.

[10] N. Mehala, "Condition Monitoring and Fault Diagnosis of Induction Motor using using Motor Current Signature Analysis," Electrical Engineering, National Institute of Technology Kurukshetra, India, 2010.

[11] P. Vas, *Parameter estimation, condition monitoring, and diagnosis of electrical machines*. Oxford : New York: Clarendon Press ; Oxford University Press, 1993.

[12] M. R. Mehrjou, N. Mariun, M. Hamiruce Marhaban, and N. Misron, "Rotor fault condition monitoring techniques for squirrel-cage induction machine—A review," *Mechanical Systems and Signal Processing,* vol. 25, pp. 2827-2848, 11// 2011.

[13] M. Seera, C. P. Lim, D. Ishak, and H. Singh, "Fault Detection and Diagnosis of Induction Motors Using Motor Current Signature Analysis and a Hybrid FMM–CART

Model," *IEEE Transaction on neural networks and learning systems* vol. 23, pp. 97-108, 2012.

[14] W. T.Thomson and M. Fenger, "Current signature analysis to detect induction motor faults," *IEEE Industry Applications Magazine* pp. 26-34, 2001.

[15] A. Bellini, F. Filippetti, G. Franceschini, C. Tassoni, R. Passaglia, M. Saottini*, et al.*, "On-field experience with online diagnosis of large induction motors cage failures using MCSA," *IEEE Transactions on Industry Applications,* vol. 38, pp. 1045-1053, 2002.

[16] W. T. Thomson and R. J. Gilmore, "Motor Current Signature Analysis to Detect Faults in Induction Motor Drive-fundamentals, Data Interpretation and Industail Case Histories " in *The Thirty_Second Turbomachinery Symposium*, 2003, pp. 145-156.

[17] C. Kar and A. R. Mohanty, "Monitoring gear vibrations through motor current signature analysis and wavelet transform," *Mechanical Systems and Signal Processing,* vol. 20, pp. 158-187, 1// 2006.

[18] M. E. H. Benbouzid and G. B. Kliman, "What Stator Current Processing-Based Technique to Use for Induction Motor Rotor Fault Diagnosis?," *IEEE Trans. Energy Convers,* vol. 18, pp. 238-244., 2003.

[19] J. Jee-Hoon, J.-J. Lee, and K. Bong-Hwan, "Online Diagnosis of Induction Motors Using MCSA," *Industrial Electronics, IEEE Transactions on,* vol. 53, pp. 1842-1852, 2006.

[20] M. Pineda-Sanchez, M. Riera-Guasp, J. Perez-Cruz, and R. Puche-Panadero, "Transient motor current signature analysis via modulus of the continuous complex wavelet: A pattern approach," *Energy Conversion and Management,* vol. 73, pp. 26-36, 2013.

[21] J. Antonino-Daviu, P. Jover, M. Riera, A. Arkkio, and J. Roger-Folch, "DWT analysis of numerical and experimental data for the diagnosis of dynamic eccentricities in induction motors," *Mechanical Systems and Signal Processing,* vol. 21, pp. 2575-2589, 2007.

[22] Z. Ye, A. Sadeghian, and B. Wu, "Mechanical fault diagnostics for induction motor with variable speed drives using Adaptive Neuro-fuzzy Inference System," *Electric Power Systems Research,* vol. 76, pp. 742-752, 2006.

[23] I. Tsoumas, G. Georgoulas, A. Safacas, and G. Vachtsevanos, "Empirical Mode Decomposition of the stator start-up current for rotor fault diagnosis in asynchronous machines," 2008, pp. 1-6.

[24] J. Cusidó, L. Romeral, J. A. Ortega, A. Garcia, and J. R. Riba, "Wavelet and PDD as fault detection techniques," *Electric Power Systems Research,* vol. 80, pp. 915-924, 2010.

[25] G. Didier, E. Ternisien, O. Caspary, and H. Razik, "A new approach to detect broken rotor bars in induction machines by current spectrum analysis," *Mechanical Systems and Signal Processing,* vol. 21, pp. 1127-1142, 2007.

[26] Y. C. Kim and E. J. Powers, "Digital Bispectral Analysis and Its Applications to Nonlinear Wave Interactions," *IEEE Transactions on Plasma Science,* vol. 7, pp. 120-131, 1979.

[27] T. W. S. Chow and F. Gou, "Three phase induction machines asymmetrical faults identification using bispectrum," *Energy Conversion, IEEE Transactions on,* vol. 10, pp. 688-693, 1995.

[28] N. Arthur and J. Penman, "Induction machine condition monitoring with higher order spectra," *Industrial Electronics, IEEE Transactions on,* vol. 47, pp. 1031-1041, 2000.

[29] L. Saidi, F. Fnaiech, H. Henao, G. A. Capolino, and G. Cirrincione, "Diagnosis of broken-bars fault in induction machines using higher order spectral analysis," *ISA transactions,* vol. 52, pp. 140-148, 2013.

[30] L. Saidi, F. Fnaiech, G. Capolino, and H. Henao, "Stator current bi-spectrum patterns for induction machines multiple-faults detection," in *IECON 2012 - 38th Annual Conference on IEEE Industrial Electronics Society*, 2012, pp. 5132-5137.

[31] F. Gu, T. Wang, A. Alwodai, X. Tian, Y. Shao, and A. D. Ball, "A new method of accurate broken rotor bar diagnosis based on modulation signal bispectrum analysis of motor current signals," *Mechanical Systems and Signal Processing,* vol. 50-51, pp. 400-413, 2014.

[32] A. Alwodai, F. Gu, and A. Ball, "A Comparison of Different Techniques for Induction Motor Rotor Fault Diagnosis," vol. 364, 2012.

[33] A. Alwodai, X. Yuan, Y. Shao, F. Gu, and A. D. Ball, "Modulation signal bispectrum analysis of motor current signals for stator fault diagnosis," in *18th International Conference on Automation and Computing (ICAC),* Loughborough, UK, 2012, pp. 1-6.

[34] Z. Chen, T. Wang, F. Gu, M. Haram, and A. Ball, "Gear Transmission Fault Diagnosis Based on the Bispectrum Analysis of Induction Motor Current Signatures," *Journal of Mechanical Engineering,* vol. 48, pp. 84-90, 2012.

[35] M. Haram, T. Wang, F. Gu, and A. Ball, "An Investigation of the Electrical Response of A Variable Speed Motor Drive for Mechanical Fault Diagnosis " *Proceedings of the 24th International Congress on Condition Monitoring and Diagnostic Engineering Management (COMADEM 2011).* pp. 867-874, 2011.

[36] T. Juggrapong, "Fault Detection and Diagnosis of Induction Motors Based on Higher-Order Spectrum," in *International Conference of Engineers and Computer Scientists*, Hong Kong, 2010.

[37] J. Treetrong, J. K. Sinha, F. Gu, and A. Ball, "Bispectrum of stator phase current for fault detection of induction motor," *ISA Transactions,* vol. 48, pp. 378-382, 2009.

[38] M. Blodt, P. Granjon, B. Raison, and G. Rostaing, "Models for Bearing Damage Detection in Induction Motors Using Stator Current Monitoring," *Industrial Electronics, IEEE Transactions on,* vol. 55, pp. 1813-1822, 2008.

[39] H. Çalış and A. Çakır, "Experimental study for sensorless broken bar detection in induction motors," *Energy Conversion and Management,* vol. 49, pp. 854-862, 4// 2008.

[40] A. Hughes, *Electric motors and drives: fundamentals, types and applications*. Oxford: Newnes / Elsevier, 2006.

[41] I. Boldea and S. A. Nasar, *Electric Drives*. Taylor & Francis Group, 2005.

[42] A. E. Fitzgerald, C. Kingsley, Jr., and S. D. Umans, *Electric Machinery*. London: McGraw-Hill Education - Europe, 2003.

[43] T. Wildi, *Electrical machines, drives, and power systems*. Upper Saddle River, N.J: Prentice Hall, 2006.

[44] A. H. Bonnett and T. Albers, "Squirrel-cage rotor options for AC induction motors," *Industry Applications, IEEE Transactions on,* vol. 37, pp. 1197-1209, 2001.

[45] B. S. Payne, "Condition Monitoring of Electric Motors for Improved Asset Management," PhD, Faculty of Science and Engineering., University of Manchester, University of Manchester, 2002.

[46] A. Vamvakari, A. Kandianis, A. Kladas, S. Manias, and J. Tegopoulos, "Analysis of supply voltage distortion effects on induction motor operation," *Energy Conversion, IEEE Transactions on,* vol. 16, pp. 209-213, 2001.

[47] M. G. Say, *Alternating current machines*. Harlow: Longman Scientific and Technical, 1986.

[48] R. Parekh, "AC Induction Motor Fundamentals," *Microchip Technology Inc,* 2003.

[49] D. Polka, "Motors and Drives - A Practical Technology Guide," ed: ISA, 2003.

[50] D. D. Reljić, D. B. Ostojić, and V. V. Vasić, "Simple Speed Sensorless Control of Induction Motor Drive," presented at the Sixth International Symposium Nikola Tesla, Belgrade, SASA, Serbia, 2006.

[51] B. I. Jeftenic, M. Z. Bebic, and N. N. Mitrovic, "A simple speed sensorless control for variable frequency induction motor drives," *Energy Conversion, IEEE Transactions on,* vol. 14, pp. 500-505, 1999.

[52] E. Babaei, S. H. Hosseini, G. B. Gharehpetian, M. T. Haque, and M. Sabahi, "Reduction of dc voltage sources and switches in asymmetrical multilevel converters using a novel topology," *Electric Power Systems Research*, vol. 77, pp. 1073-1085, 6// 2007.

[53] P. E. Randall L. Foulke, BCEE, "Principles and Applications of Variable Frequency Drives," presented at the NC AWWA-WEA Spring Conference, New Bern, North Carolina, 2009.

[54] A. Alwodai, F. Gu, and A. Ball, "Motor Current Signature Analysis of a Variable Speed Drive for Motor Fault Diagnosis," in *Proceedings of the 24th COMADEM2011*, 2011, pp. 884–892.

[55] D. M. Bezesky and S. Kreitzer, "NEMA Application Guide for AC adjustable speed drive systems," in *Petroleum and Chemical Industry Conference, 2001. IEEE Industry Applications Society 48th Annual*, 2001, pp. 73-82.

[56] B. Dhanya, S. Nagarajan, and S. Ramareddy, "Fault analysis of Induction Motor fed by a fault tolerant voltage source inverter," in *Computing, Electronics and Electrical Technologies (ICCEET), 2012 International Conference on*, 2012, pp. 51-58.

[57] J. Aguayo, A. Claudio, L. G. Vela, S. Lesecq, and A. Barraud, "Stator winding fault detection for an induction motor drive using actuator as sensor principle," in *Power Electronics Specialist Conference, 2003. PESC '03. 2003 IEEE 34th Annual*, 2003, pp. 1347-1351 vol.3.

[58] H. W. Penrose. *Variable Frequecy Drives Therory, Application and Troubleshooting*.

[59] Jon Gardell, Chairman Prem Kumar, and V. Chairman, "Adjustable Speed Drive Motor Protection Applications and Issues," ed, 2008, p. 39.

[60] A. Munoz-Garcia, T. A. Lipo, and D. W. Novotny, "A new induction motor V/f control method capable of high-performance regulation at low speeds," *Industry Applications, IEEE Transactions on*, vol. 34, pp. 813-821, 1998.

[61] B. Biswas, S. Das, M. P. Purkait, M. S. Mandal, and D. Mitra, "Current Harmonics Analysis of Inverter-Fed Induction Motor Drive System under Fault Conditions," in *the International MultiConference of Engineers and Computer Scientists IMECS*, Hong Kong, 2009.

[62] B. Drury and E. Institution of Electrical, *The control techniques drives and controls handbook* vol. 57. Stevenage: Institution of Engineering and Technology, 2009.

[63] Carrier, "Variable Frequency Drive," in *Technology Carrier Corporation Syracuse*, ed. New York, 2005.

[64] B. J. Sauer and P. A. Brady, "Application of AC Induction Motors with Variable Frequency Drives," in *Cement Industry Technical Conference Record, 2009 IEEE*, 2009, pp. 1-10.

[65] F. Filippetti, G. Franceschini, C. Tassoni, and P. Vas, "AI techniques in induction machines diagnosis including the speed ripple effect," *Industry Applications, IEEE Transactions on,* vol. 34, pp. 98-108, 1998.

[66] J. Cusidó, L. Romeral, J. A. Ortega, A. Garcia, and J. Riba, "Signal Injection as a Fault Detection Technique," *Sensors,* vol. 11, pp. 3356-3380, 2011.

[67] Z. Ye and B. Wu, "A review on induction motor online fault diagnosis," in *Power Electronics and Motion Control Conference, 2000. Proceedings. IPEMC 2000. The Third International*, 2000, pp. 1353-1358 vol.3.

[68] M. Iorgulescu and R. Beloiu, "Faults diagnosis for electrical machines based on analysis of motor current," in *Optimization of Electrical and Electronic Equipment (OPTIM), 2014 International Conference on*, 2014, pp. 291-297.

[69] A. H. Bonnett and G. C. Soukup, "Analysis of rotor failures in squirrel-cage induction motors," *Industry Applications, IEEE Transactions on,* vol. 24, pp. 1124-1130, 1988.

[70] G. Y. Sizov, A. Sayed-Ahmed, C.-C. Yeh, and N. A. O. Demerdash, "Analysis and Diagnostics of Adjacent and Nonadjacent Broken-Rotor-Bar Faults in Squirrel-Cage Induction Machines," *IEEE Transactions on Industrial Electronics,* vol. 56; 54, pp. 4627-4641, 2009.

[71] J. F. Bangura and N. A. Demerdash, "Effects of broken bars/end-ring connectors and airgap eccentricities on ohmic and core losses of induction motors in ASDs using a coupled finite element-state space method," *Energy Conversion, IEEE Transactions on,* vol. 15, pp. 40-47, 2000.

[72] G. Didier, H. Razik, and A. Rezzoug, "On the experiment detection of incipient rotor fault of an induction motor," in *Electric Machines and Drives Conference, 2003. IEMDC'03. IEEE International*, 2003, pp. 913-916 vol.2.

[73] C. Kral, H. Kapeller, F. Pirker, and G. Pascoli, "Detection of rotor faults under transient operating conditions by means of the Vienna Monitoring Method," in *Diagnostics for Electric Machines, Power Electronics and Drives, 2005. SDEMPED 2005. 5th IEEE International Symposium on*, 2005, pp. 1-6.

[74] C. Concari, G. Franceschini, and C. Tassoni, "Differential Diagnosis Based on Multivariable Monitoring to Assess Induction Machine Rotor Conditions," *Industrial Electronics, IEEE Transactions on,* vol. 55, pp. 4156-4166, 2008.

[75] M. Riera-Guasp, M. Pineda-Sanchez, J. Perez-Cruz, R. Puche-Panadero, J. Roger-Folch, and J. A. Antonino-Daviu, "Diagnosis of Induction Motor Faults via Gabor Analysis of the Current in Transient Regime," *Instrumentation and Measurement, IEEE Transactions on,* vol. 61, pp. 1583-1596, 2012.

[76] L. Zhenxing, Z. Xiaolong, Y. Xianggen, and Z. Zhe, "On-line squirrel cage induction motors' rotor mixed fault diagnosis approach based on spectrum analysis of instantaneous power," in *Intelligent Control and Automation, 2004. WCICA 2004. Fifth World Congress on*, 2004, pp. 4472-4476 Vol.5.

[77] O. M. E, B. F, and K. A, "Diagnostics of Broken Rotor Bars in Induction Machines Using the Neutral Voltage," in *ICEM'96*, Chania, 2006.

[78] R. Supangat, J. Grieger, N. Ertugrul, W. L. Soong, D. A. Gray, and C. Hansen, "Detection of Broken Rotor Bar Faults and Effects of Loading in Induction Motors during Rundown," in *Electric Machines & Drives Conference, 2007. IEMDC '07. IEEE International*, 2007, pp. 196-201.

[79] F. M. Janeiro, J. F. Martins, V. F. Pires, P. M. Ramos, and A. J. Pires, "Induction Motor Broken Bars Online Detection," in *Instrumentation and Measurement Technology Conference Proceedings, 2008. IMTC 2008. IEEE*, 2008, pp. 2137-2140.

[80] S. Guedidi, S. E. Zouzou, W. Laala, K. Yahia, and M. Sahraoui, "Induction motors broken rotor bars detection using MCSA and neural network: experimental research," *International Journal of System Assurance Engineering and Management*, vol. 4, pp. 173-181, 2013.

[81] I. P. Georgakopoulos, E. D. Mitronikas, and A. N. Safacas, "Detection of Induction Motor Faults in Inverter Drives Using Inverter Input Current Analysis," *Industrial Electronics, IEEE Transactions on*, vol. 58, pp. 4365-4373, 2011.

[82] K. Byunghwan, L. Kwanghwan, Y. Jinkyu, L. Sang Bin, E. J. Wiedenbrug, and M. R. Shah, "Automated detection of rotor faults for inverter-fed induction machines under standstill conditions," in *Energy Conversion Congress and Exposition, 2009. ECCE 2009. IEEE*, 2009, pp. 2277-2284.

[83] H. Niao Qing, X. Lu Rui, G. Feng Shou, and Q. Guo Jun, "A Novel Transform Demodulation Algorithm for Motor Incipient Fault Detection," *Instrumentation and Measurement, IEEE Transactions on*, vol. 60, pp. 480-487, 2011.

[84] S. H. Kia, H. Henao, and G. A. Capolino, "A High-Resolution Frequency Estimation Method for Three-Phase Induction Machine Fault Detection," *Industrial Electronics, IEEE Transactions on*, vol. 54, pp. 2305-2314, 2007.

[85] P. Ostojic, A. Banerjee, D. C. Patel, W. Basu, and S. Ali, "Advanced Motor Monitoring and Diagnostics," *Industry Applications, IEEE Transactions on*, vol. 50, pp. 3120-3127, 2014.

[86] A. Bellini, F. Filippetti, G. Franceschini, C. Tassoni, and G. B. Kliman, "Quantitative evaluation of induction motor broken bars by means of electrical signature analysis," *Industry Applications, IEEE Transactions on*, vol. 37, pp. 1248-1255, 2001.

[87] J. F. Martins, V. F. Pires, and T. Amaral, "Induction motor fault detection and diagnosis using a current state space pattern recognition," *Pattern Recognition Letters*, vol. 32, pp. 321-328, 1/15/ 2011.

[88] J. Penman, H. G. Sedding, B. A. Lloyd, and W. T. Fink, "Detection and location of interturn short circuits in the stator windings of operating motors," *Energy Conversion, IEEE Transactions on*, vol. 9, pp. 652-658, 1994.

[89] W. T. Thomson, "On-line MCSA to diagnose shorted turns in low voltage stator windings of 3-phase induction motors prior to failure," in *Electric Machines and Drives Conference, 2001. IEMDC 2001. IEEE International*, 2001, pp. 891-898.

[90] Z. Pinjia, D. Yi, T. G. Habetler, and L. Bin, "A Survey of Condition Monitoring and Protection Methods for Medium-Voltage Induction Motors," *Industry Applications, IEEE Transactions on*, vol. 47, pp. 34-46, 2011.

[91] D. Leggate, J. Pankau, D. Schlegel, R. Kerkman, and G. Skibinski, "Reflected waves and their associated current," in *Industry Applications Conference, 1998. Thirty-Third IAS Annual Meeting. The 1998 IEEE*, 1998, pp. 789-798 vol.1.

[92] A. Alwodai, Y. Shao, X. Yuan, M. Ahmed, F. Gu, and A. D. Ball, "Inter-turn short circuit detection based on modulation signal bispectrum analysis of motor current signals," in *In: Proceedings of the 19th International Conference on Automation and Computing (ICAC), Brunel University, London, UK. ISBN 978-1908549082*, Brunel University, London, UK, 2013.

[93] A. Siddique, G. S. Yadava, and B. Singh, "A review of stator fault monitoring techniques of induction motors " *IEEE Trans. Energy Conv*, vol. 20, pp. 106–114, 2005.

[94] J. Cusido, L. Romeral, J. A. Ortega, J. A. Rosero, and A. Garcia Espinosa, "Fault Detection in Induction Machines Using Power Spectral Density in Wavelet Decomposition," *Industrial Electronics, IEEE Transactions on*, vol. 55, pp. 633-643, 2008.

[95] M. J. Castelli, J. P. Fossati, and M. T. Andrade, "New methodology to faults detection in induction motors via MCSA," in *Transmission and Distribution Conference and Exposition: Latin America, 2008 IEEE/PES*, 2008, pp. 1-6.

[96] P. Neti, M. R. Shah, K. Younsi, J. Krahn, J. Y. Zhou, and C. D. Whitefield, "Motor current signature analysis during accelerated life testing of form wound induction motors," in *Power Modulator and High Voltage Conference (IPMHVC), 2010 IEEE International*, 2010, pp. 106-109.

[97] P. S. Barendse and P. Pillay, "The Detection of Unbalanced Faults in Inverter-Fed Induction Machines," in *Diagnostics for Electric Machines, Power Electronics and Drives, 2007. SDEMPED 2007. IEEE International Symposium on*, 2007, pp. 46-51.

[98] J. R. Stack, R. G. Hartley, and T. G. Habetler, "An amplitude modulation detector for fault diagnosis in rolling element bearings," *IEEE Transactions on Industrial Electronics* vol. 51 pp. 1097–1102, 2004.

[99] A. Shrivastava and S. Wadhwani, "Condition monitoring for inner raceway fault of induction motor ball bearings," *International Journal of Electrical Engineering*, vol. 5, pp. 239-244, 2012.

[100] J. R. Stack, R. G. Harley, and T. G. Habetler, "An amplitude modulation detector for fault diagnosis in rolling element bearings," in *IECON 02 [Industrial Electronics Society, IEEE 2002 28th Annual Conference of the]*, 2002, pp. 3377-3382 vol.4.

[101] A. Alwodai, T. Wang, Z. Chen, F. Gu, and A. Ball, "A Study of Motor Bearing Fault Diagnosis using Modulation Signal Bispectrum Analysis of Motor Current Signals," *Journal of signal and information processing,* vol. 4, p. 72, 2013.

[102] J. R. Stack, T. G. Habetler, and R. G. Harley, "Fault classification and fault signature production for rolling element bearings in electric machines," *Industry Applications, IEEE Transactions on,* vol. 40, pp. 735-739, 2004.

[103] B. Akin, U. Orguner, H. A. Toliyat, and M. Rayner, "Low Order PWM Inverter Harmonics Contributions to the Inverter-Fed Induction Machine Fault Diagnosis," *Industrial Electronics, IEEE Transactions on,* vol. 55, pp. 610-619, 2008.

[104] J. R. Stack, T. G. Habetler, and R. G. Harley, "Bearing fault detection via autoregressive stator current modeling," *Industry Applications, IEEE Transactions on,* vol. 40, pp. 740-747, 2004.

[105] A. Ibrahim, M. El Badaoui, F. Guillet, and F. Bonnardot, "A New Bearing Fault Detection Method in Induction Machines Based on Instantaneous Power Factor," *Industrial Electronics, IEEE Transactions on,* vol. 55, pp. 4252-4259, 2008.

[106] R. R. Schoen, T. G. Habetler, F. Kamran, and R. Bartheld, "Motor bearing damage detection using stator current monitoring," *IEEE Trans. Ind.Appl.,* vol. 31, pp. 1274–1279, 1995.

[107] D. M. Yang, "Induction Motor Bearing Fault Diagnosis Using Hilbert-Based Bispectral Analysis," in *Computer, Consumer and Control (IS3C), 2012 International Symposium on*, 2012, pp. 385-388.

[108] E. C. C. Lau and H. W. Ngan, "Detection of Motor Bearing Outer Raceway Defect by Wavelet Packet Transformed Motor Current Signature Analysis," *Instrumentation and Measurement, IEEE Transactions on,* vol. 59, pp. 2683-2690, 2010.

[109] R. R. Obaid, T. G. Habetler, and J. R. Stack, "Stator current analysis for bearing damage detection in induction motors," *in Proc. SDEMPED,Atlanta, GA,* pp. 182–187, Aug 2003.

[110] R. I and A. R. (2006) Bearing Damage Detection of the Induction Motors using Current Analysis. *Transmission & Distribution Conference and Exposition: Latin America,TDC '06*. 1-5.

[111] L. Frosini and E. Bassi, "Stator current and motor efficiency as indicators for different types of bearing faults in induction motors," *IEEE Transactions on Industrial electronics* vol. 57, pp. 244-251, 2010.

[112] O. Vitek, M. Janda, V. Hajek, and P. Bauer, "Detection of eccentricity and bearings fault using stray flux monitoring," in *Diagnostics for Electric Machines, Power Electronics & Drives (SDEMPED), 2011 IEEE International Symposium on*, 2011, pp. 456-461.

[113] I. Ozelgin, "Analysis of Magnetic Flux Density for Air-gap Eccentricity and Bearing Faults," *International Journal of Systems Applications, Engineering & Development* vol. 2, pp. 162-169, 2008.

[114] M. Drif and A. J. M. Cardoso, "Airgap eccentricity fault diagnosis, in three-phase induction motors, by the complex apparent power signature analysis," in *Power Electronics, Electrical Drives, Automation and Motion, 2006. SPEEDAM 2006. International Symposium on*, 2006, pp. 61-65.

[115] H. Jongman, H. Doosoo, L. Sang Bin, and C. Kral, "Monitoring of airgap eccentricity for inverter-fed induction motors based on the differential inductance," in *Energy Conversion Congress and Exposition (ECCE), 2012 IEEE*, 2012, pp. 3000-3007.

[116] D. Morinigo-Sotelo, L. A. Garcia-Escudero, O. Duque-Perez, and M. Perez-Alonso, "Practical Aspects of Mixed-Eccentricity Detection in PWM Voltage-Source-Inverter-Fed Induction Motors," *Industrial Electronics, IEEE Transactions on,* vol. 57, pp. 252-262, 2010.

[117] S. Nandi, H. A. Toliyat, and A. G. Parlos, "Performance analysis of a single phase induction motor under eccentric conditions," in *Industry Applications Conference, 1997. Thirty-Second IAS Annual Meeting, IAS '97., Conference Record of the 1997 IEEE*, 1997, pp. 174-181 vol.1.

[118] N. Halem, S. E. Zouzou, K. Srairi, S. Guedidi, and F. A. Abbood, "Static eccentricity fault diagnosis using the signatures analysis of stator current and air gap magnetic flux by finite element method in saturated induction motors," *International Journal of System Assurance Engineering and Management,* vol. 4, pp. 118-128, 2013.

[119] J. Cusido, J. Rosero, E. Aldabas, J. A. Ortega, and L. Romeral, "Fault detection techniques for induction motors," in *Compatibility in Power Electronics, 2005. IEEE,* 2005, pp. 85-90.

[120] H. Jongman, H. Doosoo, L. Sang Bin, and C. Kral, "Offline Monitoring of Airgap Eccentricity for Inverter-Fed Induction Motors Based on the Differential Inductance," *Industry Applications, IEEE Transactions on,* vol. 49, pp. 2533-2542, 2013.

[121] A. Ghoggal, S. E. Zouzou, H. Razik, M. Sahraoui, and A. Khezzar, "An improved model of induction motors for diagnosis purposes – Slot skewing effect and air–gap eccentricity faults," *Energy Conversion and Management,* vol. 50, pp. 1336-1347, 5// 2009.

[122] J. Faiz and M. Ojaghi, "Different indexes for eccentricity faults diagnosis in three-phase squirrel-cage induction motors: A review," *Mechatronics,* vol. 19, pp. 2-13, 2// 2009.

[123] M. Sahraoui, A. Ghoggal, S. E. Zouzou, and M. E. Benbouzid, "Dynamic eccentricity in squirrel cage induction motors – Simulation and analytical study of its spectral signatures on stator currents," *Simulation Modelling Practice and Theory,* vol. 16, pp. 1503-1513, 10// 2008.

[124] H. Guldemir, "Detection of airgap eccentricity using line current spectrum of induction motors," *Electric Power Systems Research,* vol. 64, pp. 109-117, 2// 2003.

[125] M. Drif and A. J. M. Cardoso, "Airgap-Eccentricity Fault Diagnosis, in Three-Phase Induction Motors, by the Complex Apparent Power Signature Analysis," *Industrial Electronics, IEEE Transactions on,* vol. 55, pp. 1404-1410, 2008.

[126] D. G. Dorrell, W. T. Thomson, and S. Roach, "Analysis of airgap flux, current, and vibration signals as a function of the combination of static and dynamic airgap eccentricity in 3-phase induction motors," *Industry Applications, IEEE Transactions on,* vol. 33, pp. 24-34, 1997.

[127] W. B. Collis, P. R. White, and J. K. Hammond, "Higher-order spectra: The bispectrum and trispectrum," *Mechanical Systems and Signal Processing,* vol. 12, pp. 375-394, 1998.

[128] M. B. Rao, P. B. B. Rao, and P. S. Subramanyam, *Mathematical Methods*: Global Media, 2008.

[129] R. B. Randall, *Application of B&K Equipment to Frequency Analysis. Brüel & Kjær, ISBN: 8787355140*, 1977.

[130] X. Li, M. Yu, Y. Liu, and X. Xu, "Feature Extraction of Underwater Signals Based on Bispectrum Estimation," in *Wireless Communications, Networking and Mobile Computing (WiCOM), 2011 7th International Conference on*, 2011, pp. 1-4.

[131] W.B.Collis, P.R.White, and J.K.Hammond, "Higher-orderspectra:the bispectrum and trispectrum," *Mechanical Systems and Signal Processing,* vol. 12, pp. 375–394, 1998.

[132] A. Naid, F. Gu, Y. Shao, S. Al-Arbi, and A. Ball, "Bispectrum Analysis of Motor Current Signals for Fault Diagnosis of Reciprocating Compressors," 2009.

[133] S. E.-O. a. E. K. Fatih Karpat, "A Virtual Tool for Computer Aided Analysis of Spur Gears with Asymmetric Teeth, Applications of MATLAB " *in Science and Engineering, Prof. Tadeusz Michalowski (Ed.), InTech, Available from:* http://www.intechopen.com/books/applications-of-matlab-in-science-and-engineering/a-virtual-tool-for-computer-aided-analysis-of-spur-gears-with-asymmetric-teeth, 2011.

[134] G. C. Zhang, M. Ge, H. Tong, Y. Xu, and R. Du, "Bispectral analysis for on-line monitoring of stamping operation," *Engineering Applications of Artificial Intelligence,* vol. 15, pp. 97-104, 2002.

[135] R. Kakarala, "A Signal Processing Approach to Fourier Analysis of Ranking Data: The Importance of Phase," *Signal Processing, IEEE Transactions on*, vol. 59, pp. 1518-1527, 2011.

[136] F. Gu, Y. Shao, N. Hu, B. Fazenda, and A. Ball, "Motor current signal analysis using a modified bispectrum for machine fault diagnosis," 2009, pp. 4890-4895.

[137] J. Byungchul, S. Changyong, E. J. Powers, and W. M. Grady, "Machine fault detection using bicoherence spectra," in *Instrumentation and Measurement Technology Conference, 2004. IMTC 04. Proceedings of the 21st IEEE*, 2004, pp. 1661-1666 Vol.3.

[138] L. Arebi, "The Use Of Passive Telemetry In Rotor Fault Diagnosis," PhD, Engineering, University of Huddersfield, 2015.

[139] W. T. Thomson, "On-line current monitoring to detect electrical and mechanical faults in three-phase induction motor drives," in *Life Management of Power Plants, 1994., International Conference on*, 1994, pp. 66-73.

[140] O. V. Thorsen and M. Dalva. (1995, 5). *A survey of faults on induction motors in offshore oil industry, petrochemical industry, gas terminals, and oil refineries*.

[141] J. Milimonfared, H. M. Kelk, S. Nandi, A. D. Minassians, and H. A. Toliyat, "A novel approach for broken-rotor-bar detection in cage induction motors," *Industry Applications, IEEE Transactions on*, vol. 35, pp. 1000-1006, 1999.

[142] C. J. Verucchi, G. G. Acosta, and F. A. Benger, "A Review on Fault Diagnosis of Induction Machine," presented at the Latin American Applied Research, Aires, Argentina, 2008.

[143] S. M. A. Cruz and A. J. M. Cardoso, "Stator winding fault diagnosis in three-phase synchronous and asynchronous motors, by the extended Park's vector approach," *Industry Applications, IEEE Transactions on*, vol. 37, pp. 1227-1233, 2001.

[144] B. Vaseghi, N. Takorabet, and F. Meibody-Tabar, "Stator turn fault study and parameter extraction of induction machines using FEM," *COMPEL: The International Journal for Computation and Mathematics in Electrical and Electronic Engineering*, vol. 29, pp. 885-899, 2010.

[145] G. M. Joksimovic and J. Penman, "The detection of inter-turn short circuits in the stator windings of operating motors," *Industrial Electronics, IEEE Transactions on*, vol. 47, pp. 1078-1084, 2000.

[146] F. Zidat, L. J. P, F. Morganti, J. F. Brudny, T. Jacq, and F. Streiff, "Non Invasive Sensors for Monitoring the Efficiency of AC Electrical Rotating Machines," *Sensors*, vol. 10, pp. 7874-7895, 2010.

[147] W. T. Thomson and D. Morrison, "On-line Diagnosis of Stator Shorted Turns in Mains and Inverter Fed Low Voltage Induction Motors," *Proceedings of IEEE Power Electronics Machines and Drives Conference*, pp. 122-127, 2002.

[148] Sinocera Piezotronics I. (2011a). *V/IEPE Input Data Acquisitions, from http://www.china-yec.com/en/products_details.asp?id=218*.

[149] Sinocera Piezotronics I. (2011b). *YE7600 General Control & Analysis Software, from http://www.china-yec.com/en/products_details.asp?id=221*.

[150] D. Howitt and D. Cramer, *Introduction to research methods in psychology*, 2 ed. Harlow: Pearson, 2008

[151] IEEE, "IEEE Standard Test Procedure for Polyphase Induction Motors and Generators," in *IEEE Std 112-2004 (Revision of IEEE Std 112-1996)*, ed, 2004, pp. 1-79.

[152] C.-M. Ong, *Dynamic simulation of Electric Machinery Using Matlab/Simulink*. New Jersey: Prantice Hall 1998.

[153] H. Razik, "Modelling of double star induction motor for diagnosis purpose," in *Electric Machines and Drives Conference, 2003. IEMDC'03. IEEE International*, 2003, pp. 907-912 vol.2.

[154] S. J. Chapman, *Electric machinery fundamentals*. New York: McGraw-Hill, 2005.

[155] V. Devanneaux, B. Dagues, J. Faucher, and G. Barakat, "An accurate model of squirrel cage induction machines under stator faults," *Mathematics and Computers in Simulation*, vol. 63, pp. 377-391, 11/17/ 2003.

[156] M. Wieczorek and E. Rosolowski, "Modelling of induction motor for simulation of internal faults," in *Modern Electric Power Systems (MEPS), 2010 Proceedings of the International Symposium*, 2010, pp. 1-6.

[157] L. Alberti, N. Bianchi, and S. Bolognani, "Finite element modeling of induction motor for variable speed drives," *COMPEL: The International Journal for Computation and Mathematics in Electrical and Electronic Engineering*, vol. 29, pp. 1245-1256, 2010.

[158] H. A. Toliyat and T. A. Lipo, "Transient analysis of cage induction machines under stator, rotor bar and end ring faults," *Energy Conversion, IEEE Transactions on*, vol. 10, pp. 241-247, 1995.

[159] A. K. Ibrahim, M. I. Marei, H. S. El-Gohary, and S. A. M. Shehata, "Modeling of Induction Motor Based on Winding Function Theory to Study Motor under Stator/Rotor Internal Faults," in *Proceedings of the 14th International Middle East Power Systems Conference (MEPCON'10)* Cairo University, Egypt, 2010, pp. 494-500.

[160] M. Ojaghi, M. Sabouri, and J. Faiz, "Diagnosis methods for stator winding faults in three-phase squirrel-cage induction motors," *International transactions on electrical energy systems*, vol. 24, pp. 891-912, 2014.

[161] A. R. Munoz and T. A. Lipo, "Complex vector model of the squirrel-cage induction machine including instantaneous rotor bar currents," *Industry Applications, IEEE Transactions on*, vol. 35, pp. 1332-1340, 1999.

[162] S. Hamdani, O. Touhami, and R. Ibtiouen, "A Generalized Two Axes Model of a Squirrel-Cage Induction Motor for Rotor Fault Diagnosis," *Serbian Journal of Electrical Engineering*, vol. 5, pp. 155-170 2008.

[163] M. Arkan, D. Kostic-Perovic, and P. J. Unsworth, "Modelling and simulation of induction motors with inter-turn faults for diagnostics," *Electric Power Systems Research,* vol. 75, pp. 57-66, 2005.

[164] S. A. Al-Jufout, "Modeling of the cage induction motor for symmetrical and asymmetrical modes of operation," *Computers and Electrical Engineering,* vol. 29, pp. 851-860, 2003.

[165] Y. Soufi, T. Bahi, M. Harkat, and H. Merabet, "Detection of broken bars in squirrel cage induction motor," in *International Design and Test Workshop (IDT),* 2009, pp. 1-5.

[166] C. Mishra, A. Routray, and S. Mukhopadhyay, "Experimental Validation of Coupled Circuit Model and Simulation of Eccentric Squirrel Cage Induction Motor," in *Industrial Technology, 2006. ICIT 2006. IEEE International Conference on,* 2006, pp. 2348-2353.

[167] L. Swedrowski and J. Rusek, "Model and simulation tests of a squirrel - cage induction motor with oscillation of the air gap," in *Diagnostics for Electric Machines, Power Electronics and Drives, 2005. SDEMPED 2005. 5th IEEE International Symposium on,* 2005, pp. 1-6.

[168] Y. Soufi, T. Bahi, M.F.Harkat, and R.Rouaibia, "Diagnosis and Fault Detection in Induction Motor drive Fed by PWM Voltage Source Inverter," *J. Electrical Systems 6-2,* 2010.

[169] M. Riera-Guasp, M. F. Cabanas, J. A. Antonino-Daviu, M. Pineda-Sanchez, and C. H. R. Garcia, "Influence of Nonconsecutive Bar Breakages in Motor Current Signature Analysis for the Diagnosis of Rotor Faults in Induction Motors," *Energy Conversion, IEEE Transactions on,* vol. 25, pp. 80-89, 2010.

[170] B. Liang, B. S. Payne, A. D. Ball, and S. D. Iwnicki, "Simulation and fault detection of three-phase induction motors," *Mathematics and Computers in Simulation,* vol. 61, pp. 1-15, 2002.

APPENDIX

APPENDIX A: Time Domain Features

This section presents time domain features of MCSA under healthy and broken bar motor and comparison between them.

A1: Time Domain Features under Healthy Condition

Figure A1.1 shows the measured line voltages and phase currents for healthy motor operating at no load. The RMS values of voltage and current of phase (A) are 429.26 v and 4.51A, respectively

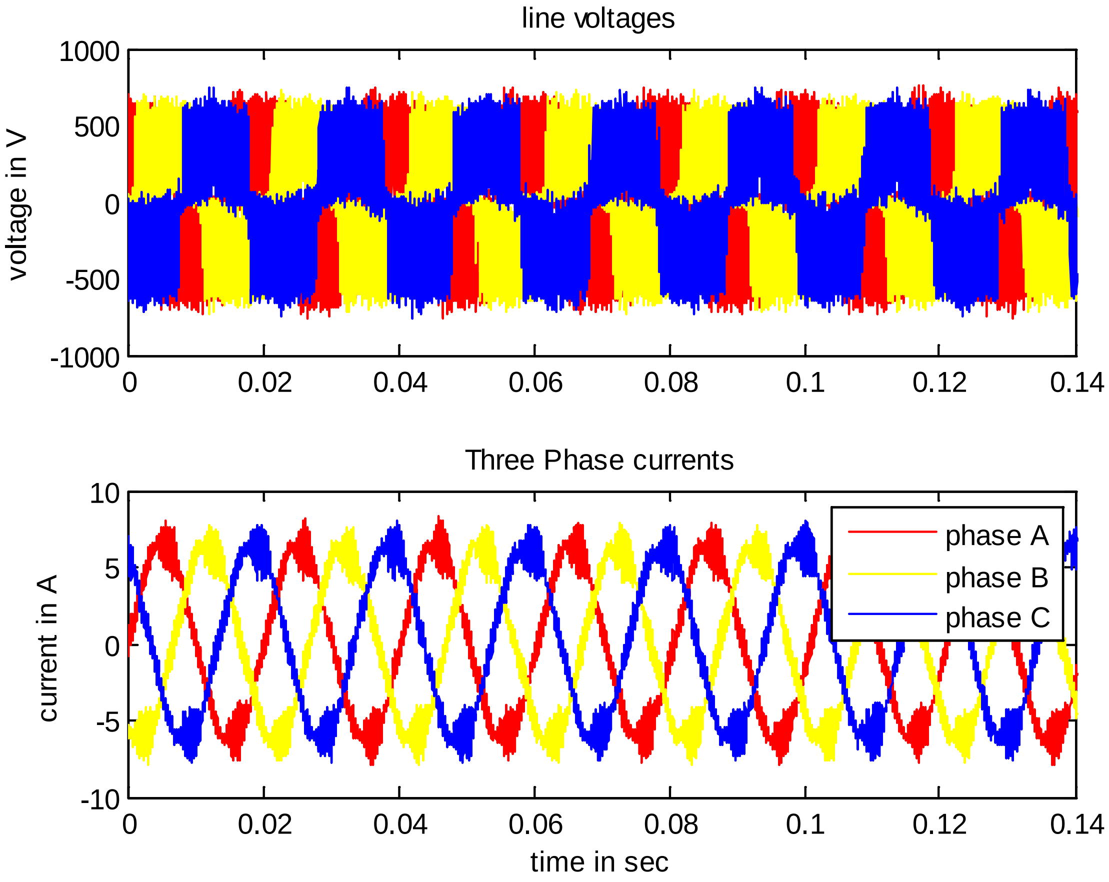

Figure A1.1 - Three phase voltages and currents in time domain

As can be seen from Figure A1.1 the voltage signal is not purely sinusoidal; this variation in the voltage signal is due to PWM invertor which supplies the motor.

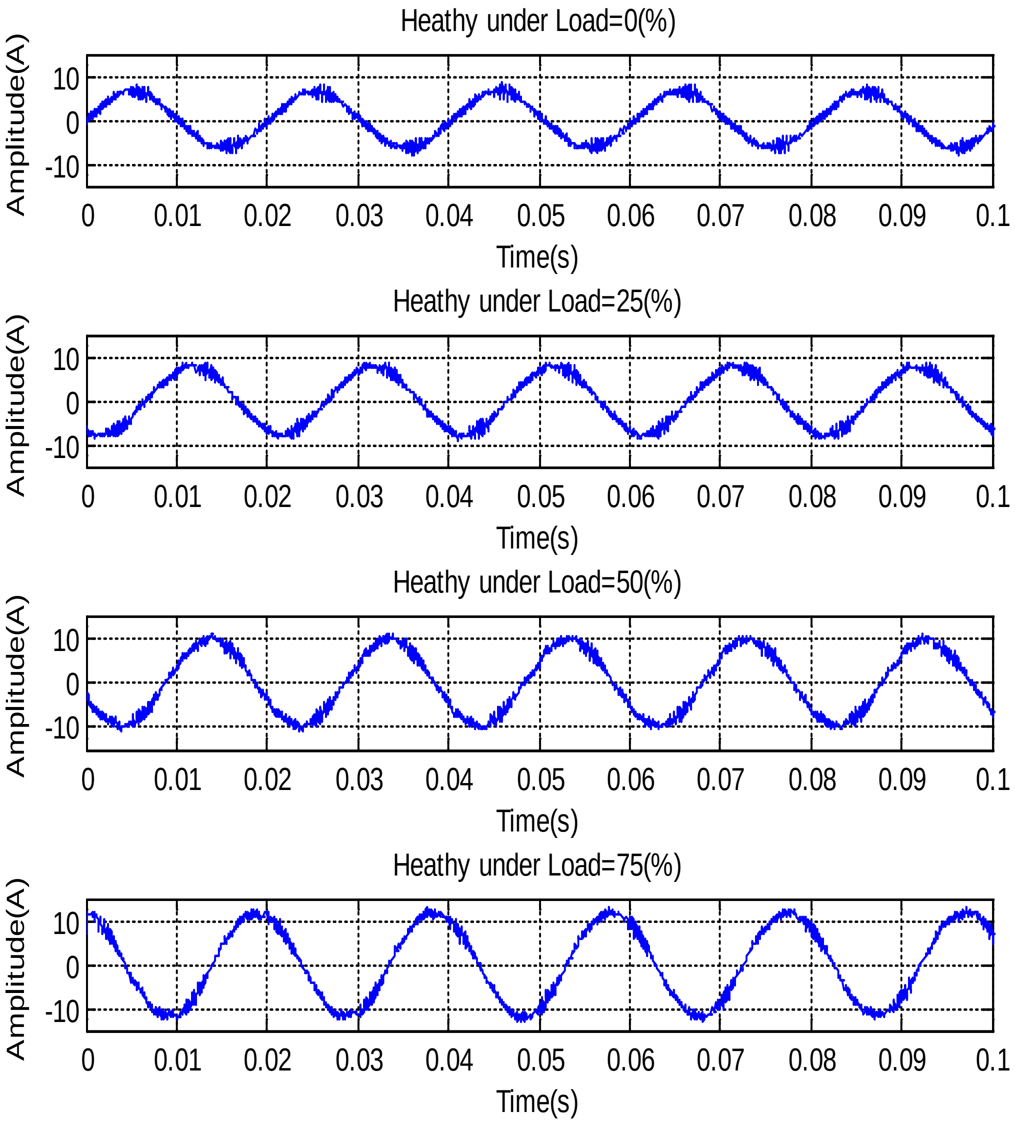

Figure A1.2-Phase Current in Time Domain under Healthy Condition

Figure A1.2 shows current signals of phases under healthy condition. It seems clear from the Figure the current value changes with load. This means that increasing in load leads to decreasing in current value (for example Peak value is 6.3817A at no load and 11.9371A at 75% of full load).

Figure A1.3 shows RMS value of stator phase current under healthy condition and at zero, 25%, 50% and 75% of full load. It can be seen from the figure the current signals have very small differences at three tests. This means that the measuring of signals is consistent at all tests and the average RMS value is very close to all values at the three tests. Therefore, the average value can be used to evaluate current signal under different operation conditions.

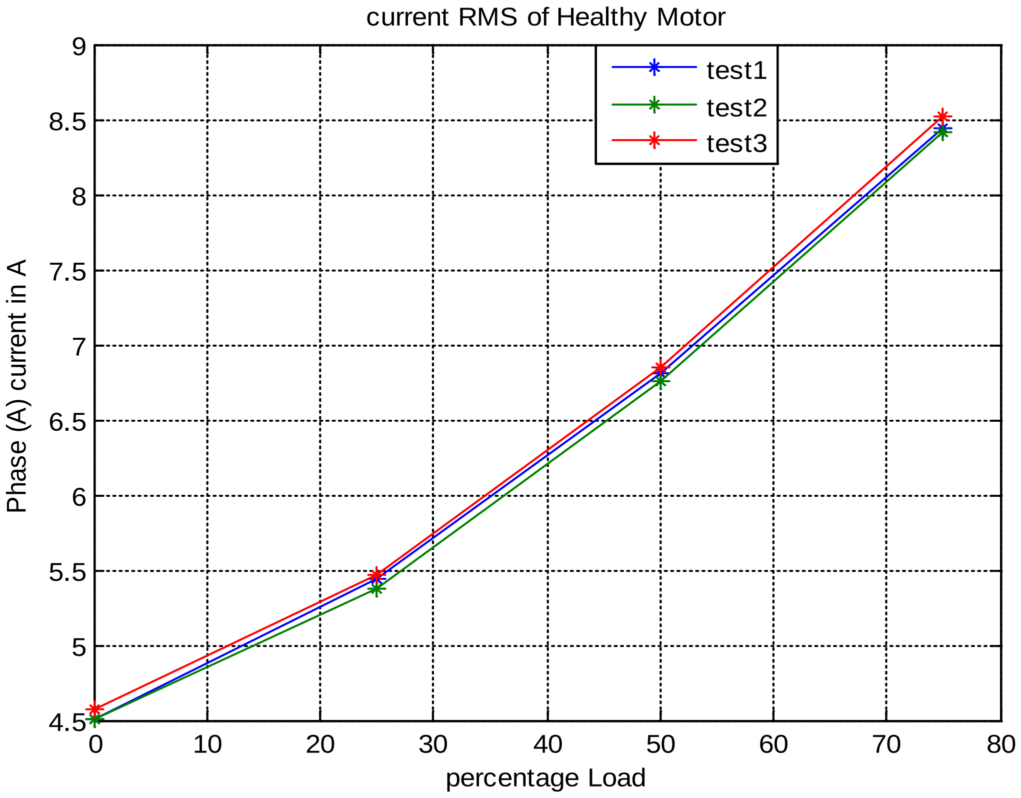

Figure A1.3- RMS Value of Phase Current under Healthy Condition

Figure A1.4 shows RMS average value of phase current under healthy situation and at different load conditions.

Figure A1.5 shows peak value of phase current signal at three tests and under healthy condition. Figure A1.6 shows average peak value of the current signal.

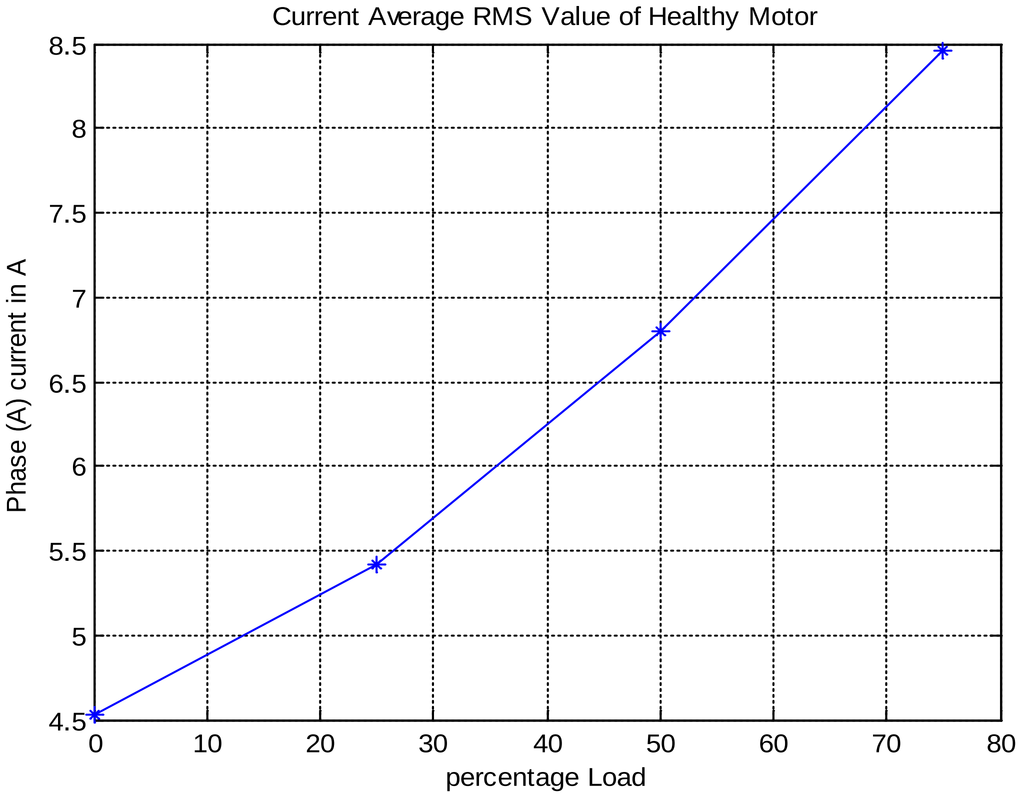

Figure A1.4-RMS Average Value of Phase Current under Healthy Condition

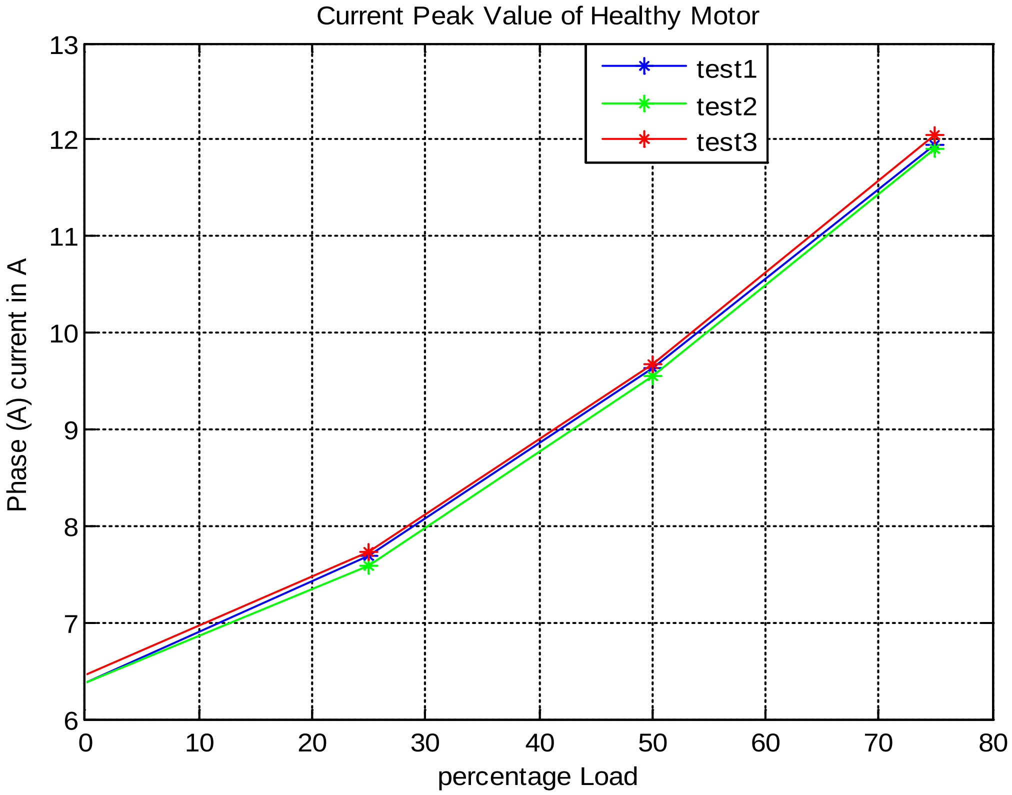

Figure A1.5-Peak Value of Phase Current under Healthy Condition

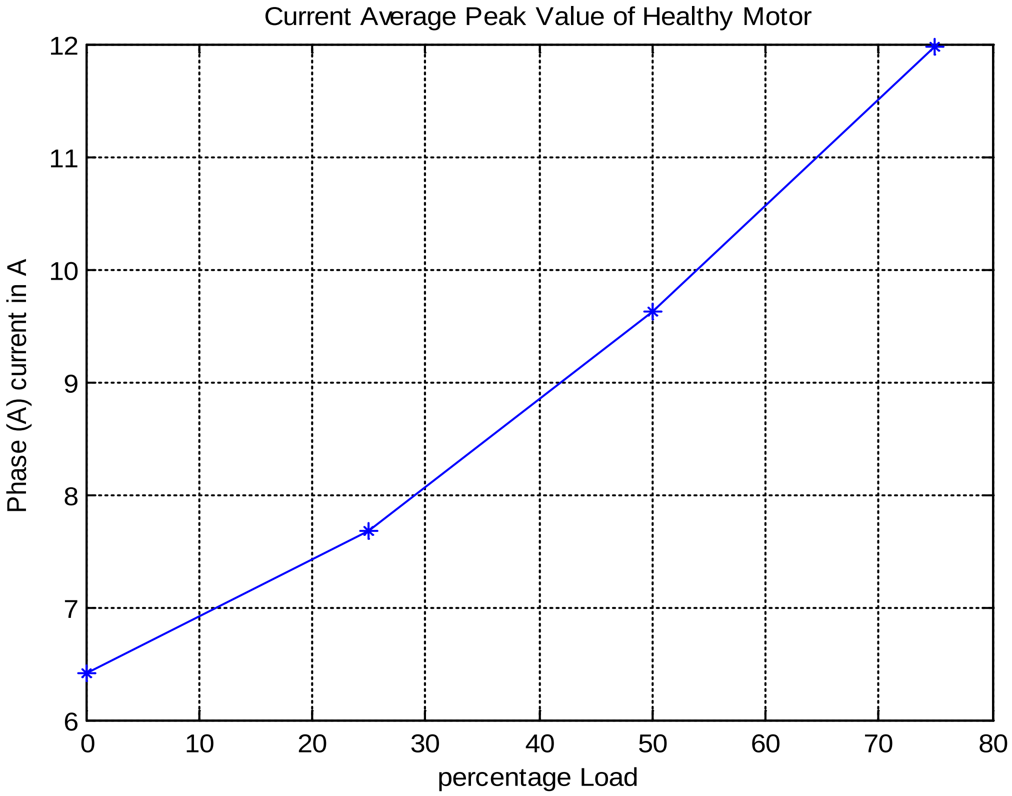

Figure A1.6-AveragePeak Value of Phase Current under Healthy Condition

A2: Time Domain Features under One Broken Bar condition

Figure A2.1 shows phase current under full broken rotor bar fault. As can be seen from the figure the peak value of the current increases with increasing in the load, for example, peak value of the current is 6.4111 A at no load and it is 12.2062 A at 75% load.

Figure A2.2 shows RMS value of phase stator current under broken bar fault and at deferent load conditions. The RMS value at no load is 4.5219 A while it is 8.5905 A at 75% load

Figure A2.3 shows peak value of phase stator current under broken bar fault and at deferent load conditions. The peak value at no load is 6.3950A while it is 12.1488A at 75% load.

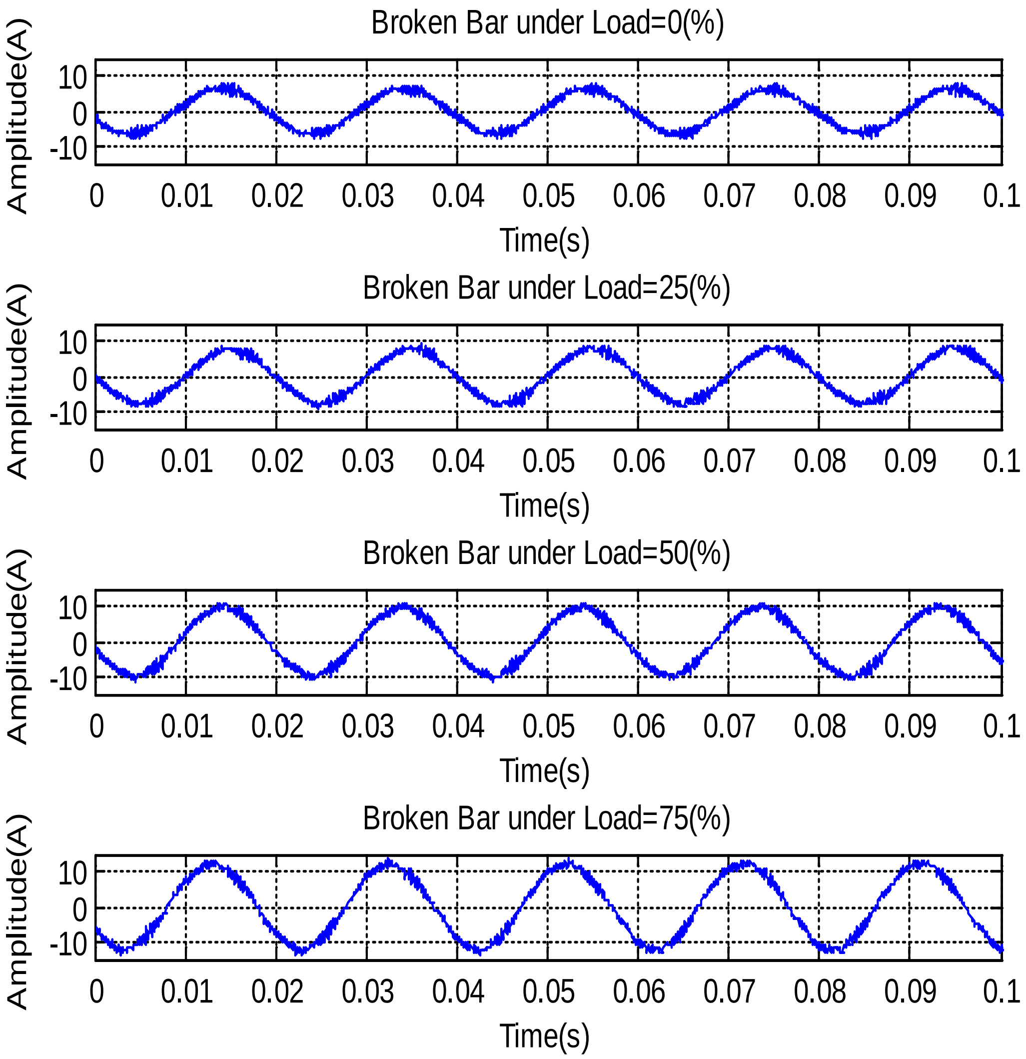

Figure A2.1-Phase Current under One Broken Bar

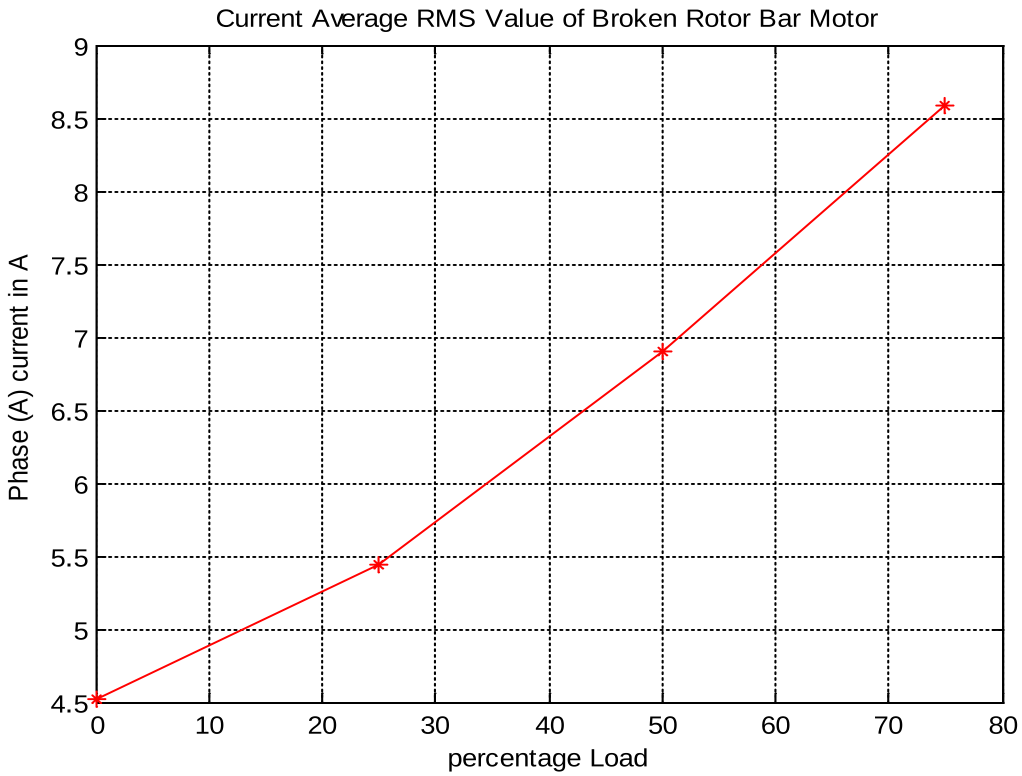

Figure A2.2-RMS Average Value of Phase Current under One Broken Bar

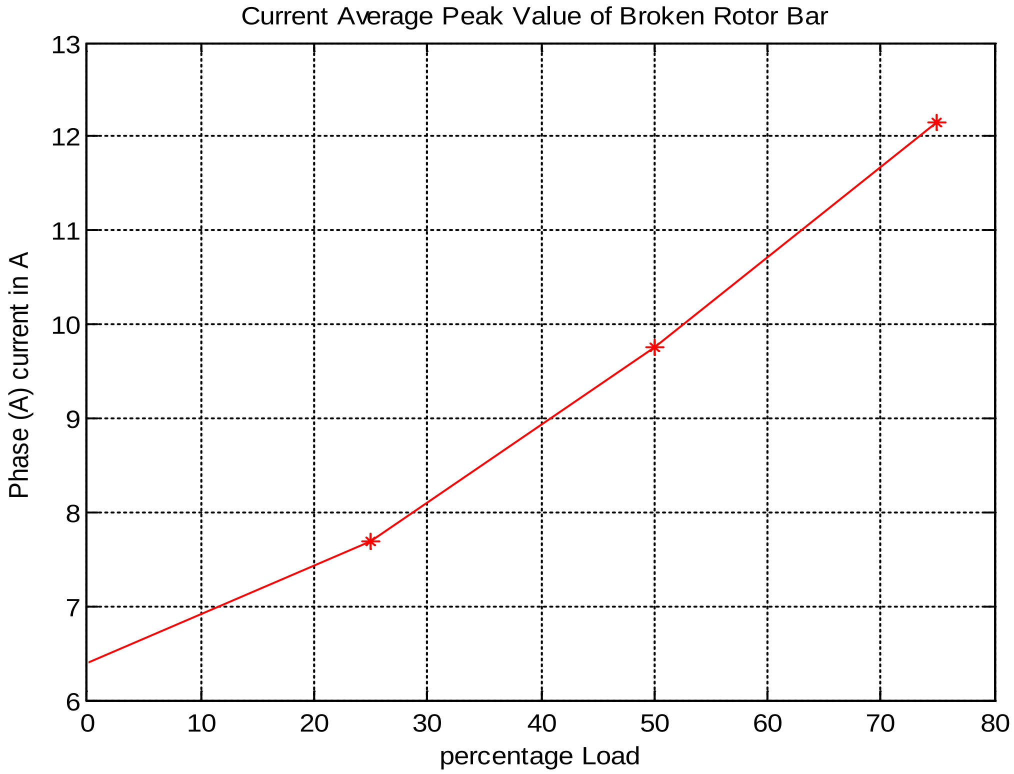

Figure A2.3-Peak Value of Phase Current under One Broken Bar

A3: Comparison between Healthy and faulty Condition in Time Domain Results

Figure A3.1 shows comparison between the current from Phase Current under healthy and one broken bar motor at 75% of full load. As can be seen from the figure broken bar fault causes increment in current value, for example, in case of 75% load, peak values of the current are 11.9371A and 12.2062 A under healthy and broken bar cases, respectively. As a result increase in the peak current value due to broken bar fault at 75% load is about 0.27 A.

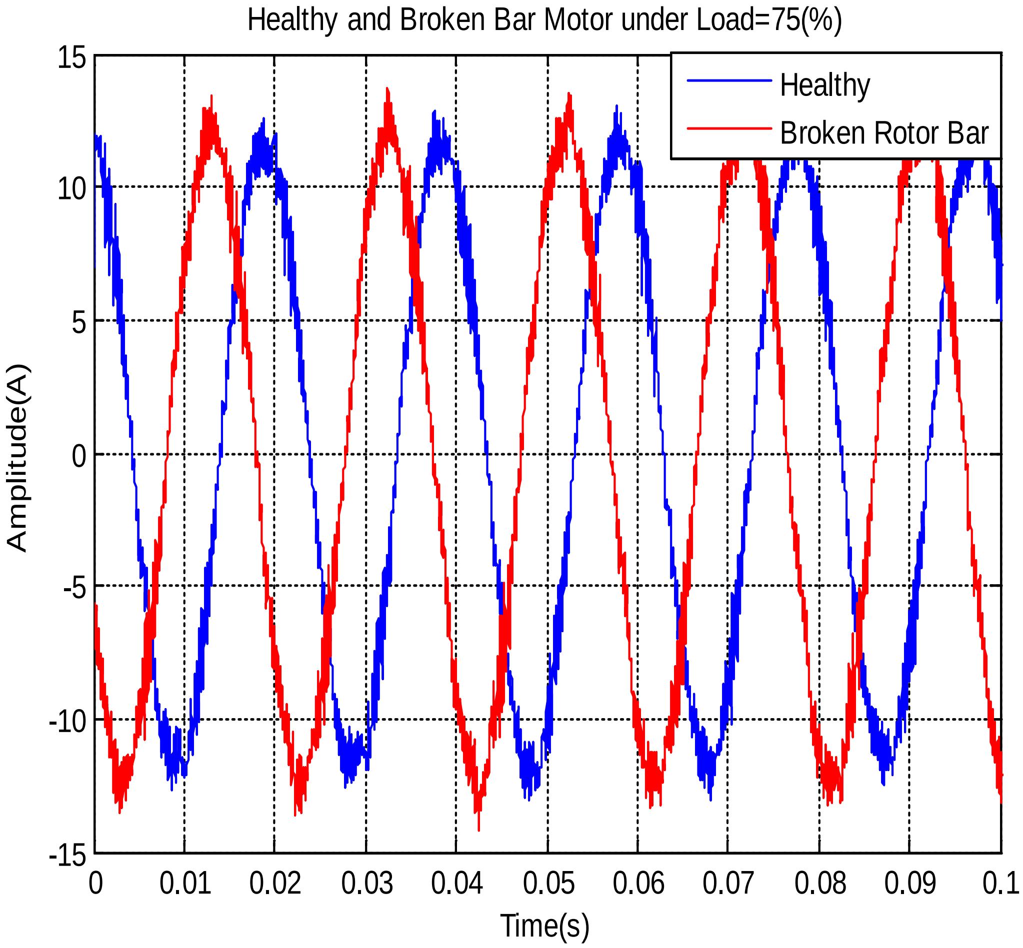

Figure A3.1-Phase Current of Healthy and One Broken Bar at 75% of Full Load

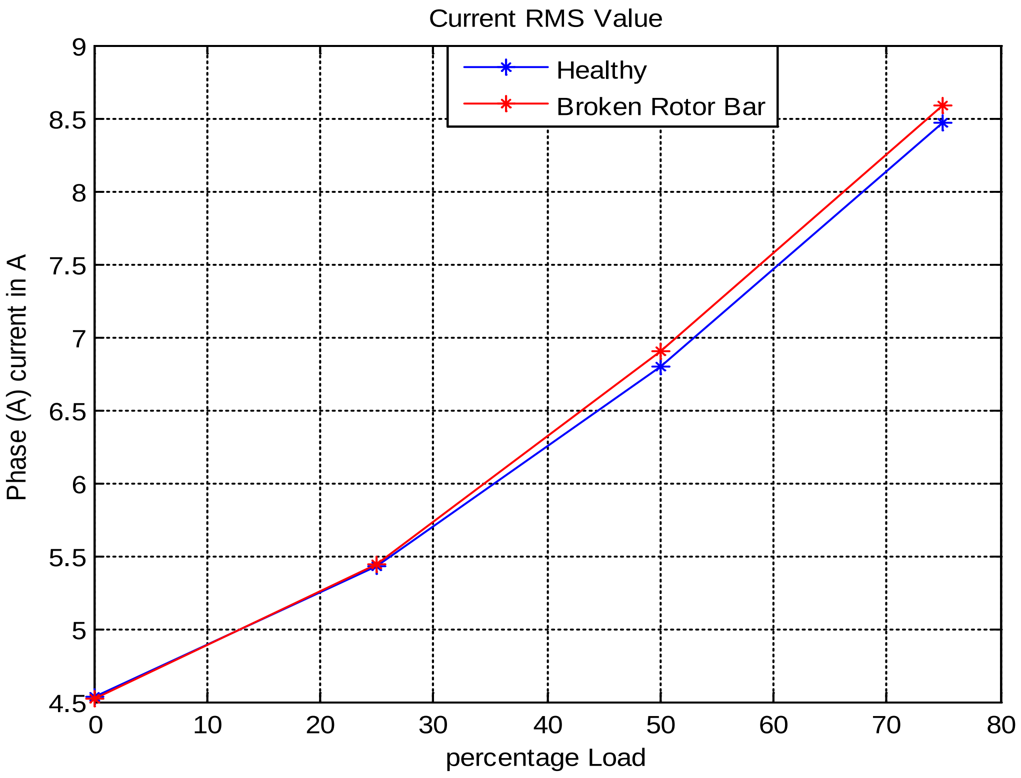

Figure A3.2-RMS Average Value of Phase Current

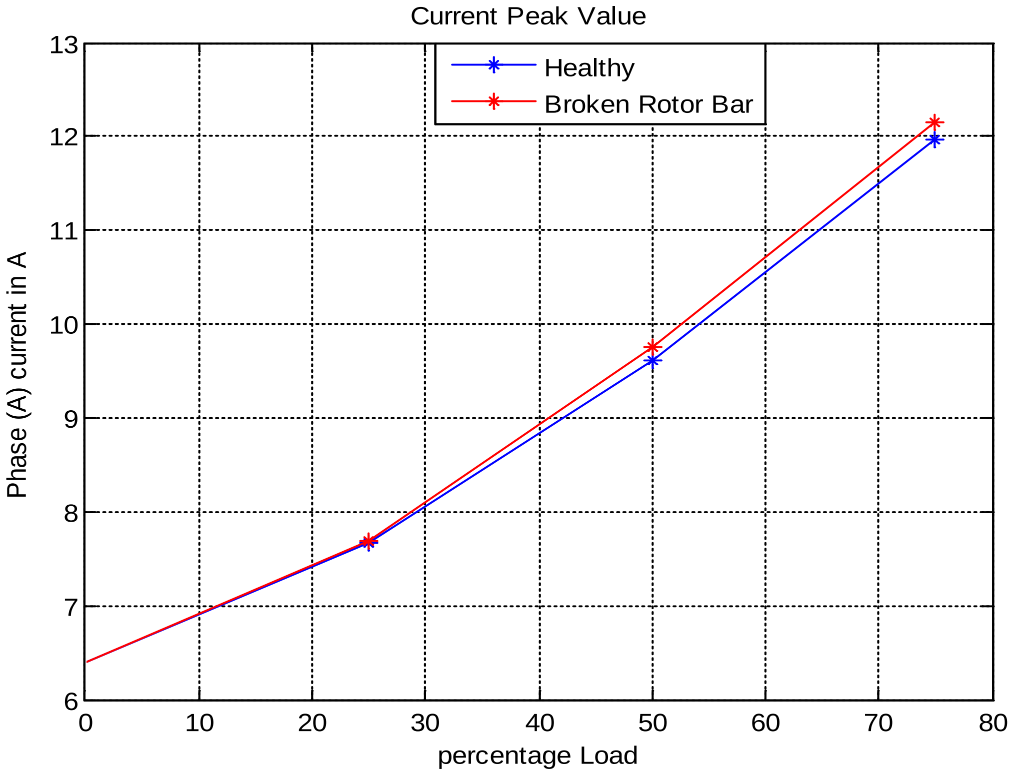

Figure A3.3-Peak value of Phase Current

In comparing the RMS values of current signal of healthy and full broken bar fault in Figure A3.2 one can see the increase in the RMS value in the case of a broken rotor bar, however the difference is small. Although the RMS values of current signals presented in Figure A3.2 show small differences, they do not reveal useful information about the motor s health.

Figure A3.3 shows peak value of phase current signal under healthy and broken rotor bar. As can be seen from the Figure the difference is small and similar RMS value, peak value does not give a significant feature to detect the broken bar fault.

A4: Summary of MCSA Time Domain Features

It can be seen from the results presented in Section A3 that the current changes as the operating conditions change. The deference of current signals under broken rotor bar and healthy condition is very small. Therefore, presenting the current as waveforms is not useful for the extraction of information about the motor health. For this reason the values of two statistical parameters for the current under four load conditions were presented and then healthy and faulty conditions were compared.

Based on the above discussion, it can be concluded that the MCSA does not have an enough capability in the detection of broken rotor bar fault of the induction motor in the time domain, and it is not capable of diagnosing this fault as well. However to overcome this problem, this thesis presented some faults of an induction motor in frequency domain.

APPENDIX B: Features of MSB-SE and CB

Figure B1, Figure B2 and Figure B3 present typical MSB results under half broken bar, one broken bar and two broken bars respectively. As it can be seen in Figure B1 (a), Figure B2 (a) and Figure B3 (a) MSB-SE shows a distinctive peak at bifrequency (3.4,50) Hz in the bispectrum domain. Clearly, this peak is relating to $2sf_s$ and can be relied on to detect and diagnose BRB. In addition, this peak is also distinctive in MSB-SE coherence in Figure B1(c),

Figure B2(c) and Figure B3(c) confirming that it is from modulation processes between $2sf_s$ and f_s

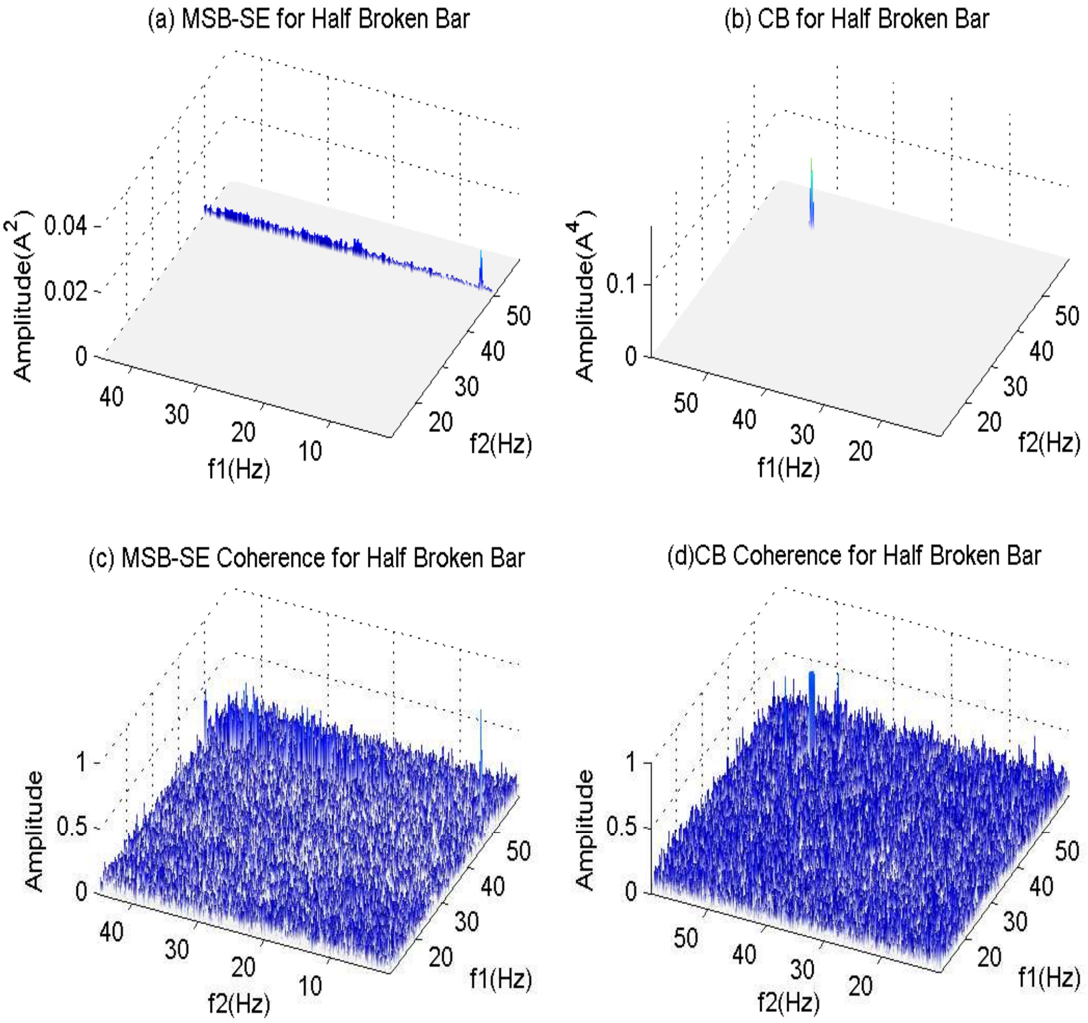
(a) MSB-SE for Half Broken Bar

(b) CB for Half Broken Bar

(c) MSB-SE Coherence for Half Broken Bar

(d)CB Coherence for Half Broken Bar

Figure B1-Characteristics of MSB-SE and CB for Half Broken Bar Case at 75% Load

On the other hand, the CB in Figure B1 (b), Figure B2 (b) and Figure B3 (b) show a single peak at bifrequency (50, 50) Hz. This frequency does not show any connections to BRB at $2sf_s$. Moreover, CB coherence in Figure B1(d), Figure B2(d) and Figure B3(d) are predominated by background noise in the whole domain. It means that the peak at (50, 50) Hz is not from real nonlinear coupling, but is due to the very high amplitudes at 50Hz in the original signal.

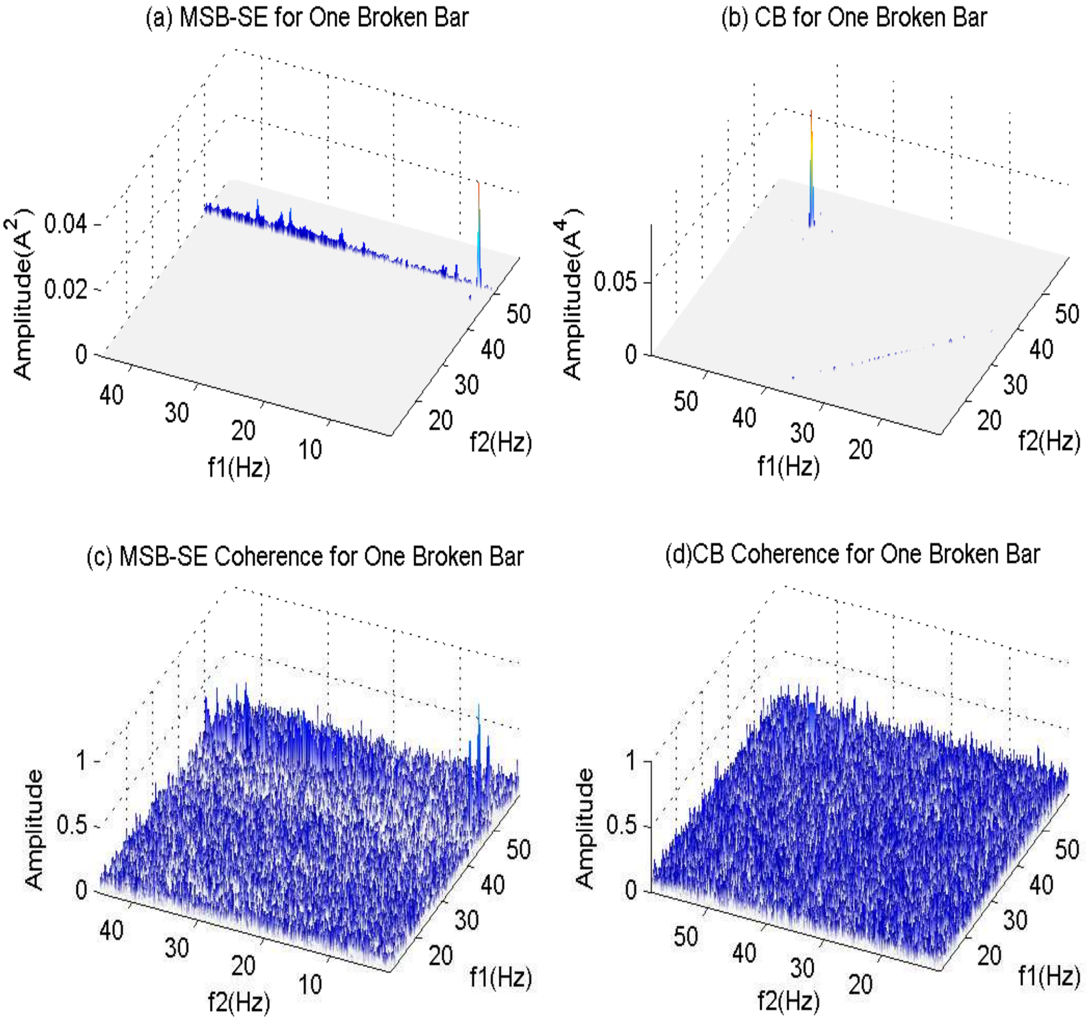

Figure B2-Characteristics of MSB-SE and CB for One Broken Bar Case at 75% Load

From the above discussions it can be concluded that MSB-SE allows the three different severities of BRB to be detected and diagnosed by using the change of MSB magnitudes. However, CB is unable to capture any of these faulty components by either its magnitude or coherence results and then it is not sufficient to diagnose motor faults with motor current signal.

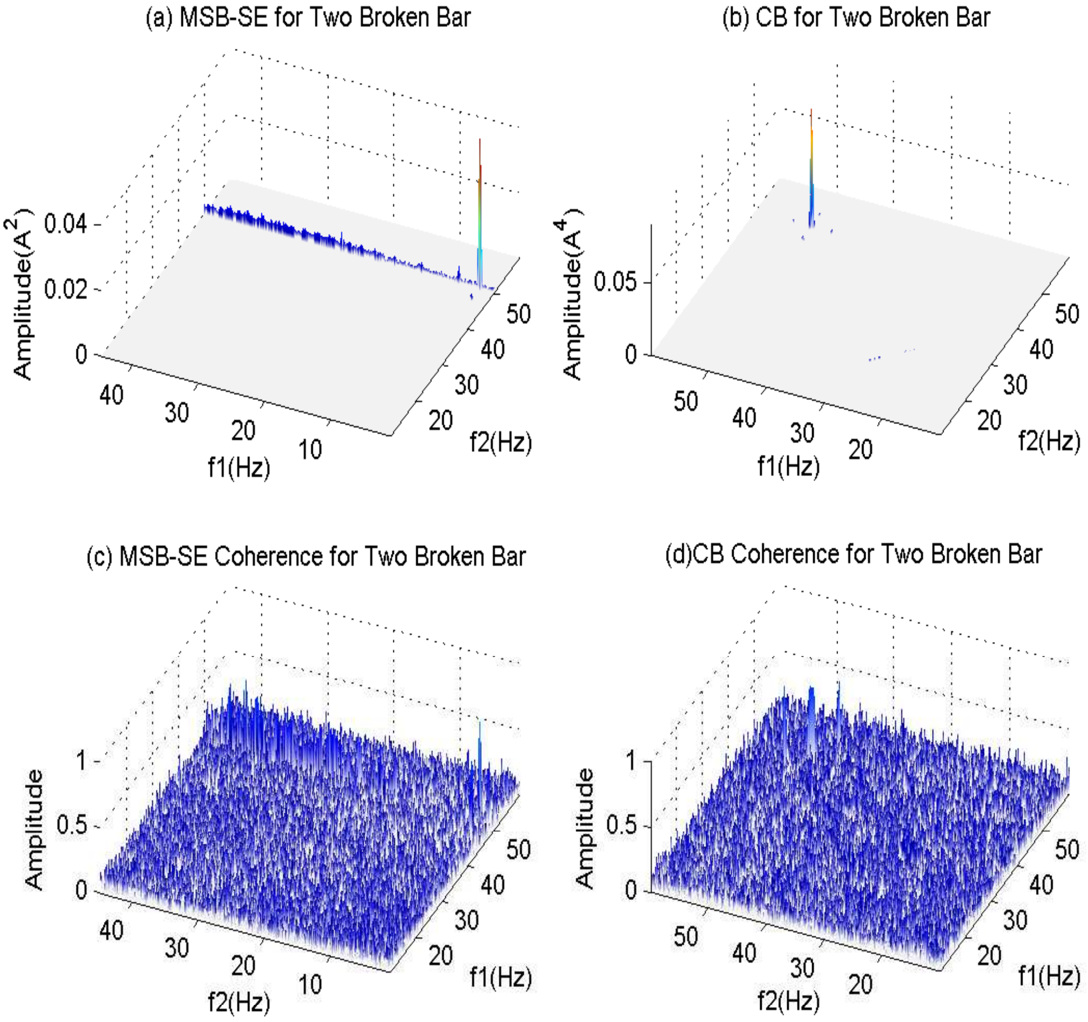

Figure B3-Characteristics of MSB-SE and CB for Two Broken Bar Case at 75% Load